Investigation into methods for the calculation and measurement of pulverised coal boiler flue gas furnace exit temperature

Prepared by:

Naeem Ebrahim Tootla

TTLNAE001

Department of Mechanical Engineering

University of Cape Town

Supervisor:

Professor Louis Jestin

February 2016

Submitted to the Department of Mechanical Engineering at the University of Cape Town in partial fulfilment of the academic requirements for a Master of Science degree in Mechanical Engineering

Key Words: Boiler furnace exit temperature, Mass and energy balances, Acoustic pyrometer

Abstract

The boiler flue gas furnace exit temperature (FET) is a key operating parameter of coal fired steam boilers. From the design perspective, the FET is vital for materials selection and sizing of heat transfer surfaces. From an operating perspective, it is a major indicator of the rate of combustion and heat transfer that is occurring within the furnace. Downstream of the furnace, the FET has a significant impact on both the performance and reliability of the boiler heat exchangers, which ultimately impacts on both boiler efficiency and availability. Monitoring of the FET can advise operating and engineering corrective actions which will ultimately result in better efficiency, reliability and availability together with the associated economic benefits. Therefore, methods of determining FET are investigated. Two methods are focused on for this study, one indirect and one direct.

The indirect method studied is a mass and energy balance method which begins with a global boiler mass and energy balance to calculate the major boiler flow rates of coal, air and flue gas which are difficult to measure online. These parameters are then used as inputs into a furnace or backpass mass and energy balance to calculate the furnace exit temperature. The method is applied to a case study, and is evaluated in terms of the measurement uncertainties which are propagated on the intermediate parameters calculated, as well as on the final calculated FET. The main conclusions are that this indirect method contains various uncertainties, due to parameters which have to be assumed such as (i) the distribution of ingress air (also called tramp air) in the different sections of the boiler and (ii) the estimation of the share of water evaporation heat transfer occurring in the water walls of the furnace part of the boiler. The method is however still useful and can be easily applied to any boiler layout and can be used as a reference tool to verify other measurements.

The direct method studied is acoustic pyrometry. The work specifically focuses on the sources of error in determining the temperature from the measurement of the time of flight of sound, the impact of particle concentration on the speed of sound through a gas-particle mixture, and the temperature profile reconstruction from acoustic time of flight measurements. A limited set of physical testing was also carried out using one acoustic generator and receiver to take measurements on a real coal power plant. As part of this physical testing, the detection of time of flight from acoustic signals was explored.

Already installed radiation pyrometers were also used as a reference for interpreting the acoustic measurements. The indications are that the acoustic pyrometer provides a more representative temperature measurement than the radiation pyrometers. The uncertainty of the acoustic measurement for the same case study as the indirect method was determined and compared with

the calculated result. While many aspects still need to be researched further, this initial study and experimental testing produced very promising results for future application of acoustic pyrometry for better monitoring of the coal combustion processes in power plant boilers.

Declaration

I, Naeem Ebrahim Tootla, know the meaning of plagiarism and declare that all the work in the document, save for that which is properly acknowledged, is my own.

Signed by candidate

Naeem Ebrahim Tootla

Acknowledgements

Firstly, I would like to thank the Eskom Power Plant Engineering Institute as well as my managers at Eskom, Morris Maroga and Alton Naidoo, for affording me the funding and opportunity to pursue this Masters study.

I would like to thank my supervisor Professor Louis Jestin whose expertise, experience, guidance and drive were critical in completing this project.

I would like to thank Chris du Toit, Wico Nigrini, and the Camden Performance and Testing team for assisting with all of the logistical aspects of my experimental testing.

I would also like to thank Enertechnix, Mike Anna, Nelson Lopes and Nick Scheepers for making available both their time and equipment for testing, as well as being readily available to provide support and information at various stages during the course of the project.

I would also like to make mention of the Eskom Research, Testing & Development department who provided laboratory results and support.

I would like to extend my gratitude to my fellow students at UCT for making the office an interesting, enjoyable and pleasant working environment.

I would also like to acknowledge the staff members at UCT, namely Dr Wim Fuls, Prof Pieter Rousseau, Prof Hennie Mouton and Julian Mayer, all of whom offered me guidance and assistance at various times during my project.

I also would like to thank my family for all their support. Without them, I would not be who I am today.

Last, but certainly not least, I would like to thank my loving wife Meagan. All endeavours in life are easier, with you by my side.

Table of Contents

List of Figures vii
List of Tables xi
List of Nomenclature xii
1. Introduction 1
1.1. Project rationale 1
1.2. Project objectives 2
1.3. Scope and limitations of Project 2
1.4. Outline of dissertation 3
2. Background 4
2.1. Pulverised coal boiler in the overall power plant cycle 4
2.2. The pulverised coal boiler and its auxiliaries 5
2.3. The importance of the FET 11
3. Indirect methods 14
3.1. Literature study on indirect methods 14
3.2. Overview of application of an indirect method 15
3.3. Global boiler mass and energy balance (BMEB) methodology 17
3.4. Furnace and Backpass MEB 29
3.5. Sensitivity Analysis and uncertainty propagation method 34
3.6. Case study MEB implementation 35
3.7. MEB Results and Discussion 38
3.8. Radiation from furnace to convective pass 49
3.9. Summary of indirect methods 57
4. Direct Methods 60
4.1. Literature study on direct methods 60
4.2. Practical and theoretical topics of interest 72
4.3. Direct methods experimental testing 101
4.4. Direct methods testing results and analysis 115
5. Conclusions and Recommendations 129
5.1. Conclusions 129

5.2. Recommendations for future work 132
6. List of References 134
Appendix A. Mathcad equation writing benefits 140
Appendix B. MEB calculations with primary boundary 141
Appendix C. Uncertainty propagation programme 155
Appendix D. Calculation of emissivity of furnace exit surface 156
Appendix E. Temperature reconstruction code 160
Appendix F. Time of flight detection code 165
Appendix G. Detailed time of flight measurement data 168
Appendix H. Radiation pyrometer results 171
Appendix I. Calculation of flue gas-particle mixture properties 173
Appendix J. EBE Faculty: Assessment of Ethics in Research 175

List of Figures

Figure 1: Typical overall power plant Rankine cycle 4

Figure 2: Relationship between different coal analytical bases [2] 5

Figure 3: Example of a vertical roller type mill showing internal details [3] 7

Figure 4: Example of a regenerative air heater [4] 9

Figure 5: Primary and Secondary A/H configurations 9

Figure 6: Example of slagging on the tubes on the left and severe distortion of a tube after failure12

Figure 7: Example of a boiler tube which failed by long term overheating 12

Figure 8: FMEB and BPMEB control volumes for tower boiler (left) and 2-pass boiler (right) 16

Figure 9: High level relationship between Boiler MEB (BMEB), furnace MEB (FMEB) and backpass MEB (BPMEB) 17

Figure 10: Mass and energy balance inputs, outputs and boundaries 19

Figure 11: Global boiler MEB calculation flow 21

Figure 12: Boiler energy balance inputs 23

Figure 13: Boiler energy balance outputs 24

Figure 14: FET_f and FET_b boundaries 29

Figure 15: Dimbo model geometry 31

Figure 16: Plant X operating data for load, steam pressure, steam flow rate and air flow rate 35

Figure 17: Plant X operating data for steam, air and flue gas temperatures 36

Figure 18: Boiler air flow schematic 39

Figure 19: Coal mass flow rate sensitivity analysis 43

Figure 20: Uncertainty propagation on coal mass flow rate 43

Figure 21: Air mass flow rate sensitivity analysis 44

Figure 22: Uncertainty propagation on air mass flow rate 44

Figure 23: Flue gas mass flow rate sensitivity analysis 45

Figure 24: Uncertainty propagation on flue gas mass flow rate 45

Figure 25: FET sensitivity analysis 46

Figure 26: Uncertainty propagation on FET 46

Figure 27: Graphical representation of problem showing dimensions of Plant X boiler 50

Figure 28: Graphical representation of the zonal method showing surfaces and volumes 51

Figure 29: Variation of particle extinction coefficient with particle concentration for different particles sizes 53

Figure 30: Temperature profile of flue gas over a vertical plane in the middle of the enclosure 55

Figure 31: Variation of FET for varying extinction coefficients 56

Figure 32: Impact of roof temperature on zonal model results of FET and heat transfer 57

Figure 33: General magnitude of error when measuring gas temperature in boiler cavities using thermocouples [1] 61

Figure 34: High velocity thermocouple [24] 61

Figure 35: Electromagnetic spectrum [28] 63

Figure 36: Example configuration of the main components of a radiation pyrometer [28] 64

Figure 37: Basic acoustic pyrometer set up from boiler top view 67

Figure 38: Diagram of a spark gap generator [25] 69

Figure 39: Example of a pneumatically driven acoustic pyrometer [44] 70

Figure 40: (a) SEI Boilerwatch MMP Transceiver unit [52]. (b) Typical 8 transceiver setup of the MMP system [53] 72

Figure 41: Enertechnix PyroMetrix Acoustic Pyrometer. (a) Generator. (b) Receiver. (c) Example layout with zones [44] 73

Figure 42: Systematic error in temperature measurement resulting from unknown combustion mixture [33] 74

Figure 43: Graphic representation of Fermat's principle 75

Figure 44: Depiction of how a higher frequency results in lower potential for error 77

Figure 45: Speed of sound in air-magnesia mixture [56] 79

Figure 46: Speed of sound in a typical boiler flue gas mixture with m_p=0.035 and ζ=3333 80

Figure 47: Speed of sound ratio versus gas volume fraction for a sound frequency of 500Hz and density ratio ζ=3333 which is typical of SA coal boiler. 81

Figure 48: Speed of sound ratio using homogenous conditions for ζ=3333 83

Figure 49: Typical boiler flue gas range using homogenous conditions for ζ=3333 83

Figure 50: Speed of sound ratio for ζ=3333 84

Figure 51: Speed of sound ratio for the 0% excess air condition 85

Figure 52: Co-ordinate arrangement of a horizontal plane in boiler furnace 86

Figure 53: Bilinear profile used in the method described by Kleppe et al [49] 88

Figure 54: Temperature plane discretization for least squares method 89

Figure 55: Example of temperature grid of a circular plane [45] 91

Figure 56: AP layout consisting of 4 generators and 8 receivers producing a total of 24 paths 93

Figure 57: Temperature profile 1. One peak symmetrical distribution with the peak at the centre of the furnace and a gradual gradient from walls to centre 94

Figure 58: Temperature profile 2. One peak symmetrical distribution with the peak at the centre of the furnace and a steep gradient from walls to centre 95

Figure 59: Temperature profile 3. One peak asymmetrical with the peak skewed from the centre of the furnace 95

Figure 60: Temperature profile 4. Two peak profile with different peaks 96

Figure 61: Comparison of original (left) and reconstructed (right) 1 peak profile with gradual temperature increase from wall to centre 97

Figure 62: Comparison of original (left) and reconstructed (right) 1 peak profile with steep temperature increase from wall to centre 97

Figure 63: Comparison of original (left) and reconstructed (right) 1 peak asymmetrical profile 98

Figure 64: Comparison of original (left) and reconstructed (right) 2 peak profile 98

Figure 65: Depiction of outer frame where there are only inner points for interpolation 99

Figure 66: Siemens Ardometer radiation pyrometer [61] 102

Figure 67: Boiler top view depicting furnace acoustic paths 103

Figure 68: Boiler 3D view depicting furnace acoustic paths 104

Figure 69: Testing location at Plant X unit 2 economiser 105

Figure 70: Example of AST and ASR signals processed through PyroMetrix software showing examples of AST and ASR event detections 106

Figure 71: Example of AST Signal Zoomed in on the time scale 107

Figure 72: TOF detection procedure 108
Figure 73: Example of ASR spectrogram 108
Figure 74: Example of ASR time domain signal with high signal to noise ratio 109
Figure 75: Example of FFT of signal with high signal to noise ratio 110
Figure 76: Example of ASR time domain signal with low signal to noise ratio 110
Figure 77: Example of FFT of signal with low signal to noise ratio 111
Figure 78: Example of spectrogram of low signal to noise ratio 111
Figure 79: Example of a time domain signal overlaid with the filtered signal 112
Figure 80: Example of threshold detection 113
Figure 81: Acoustic sound generator [62] 114
Figure 82: Acoustic sound receiver [62] 114
Figure 83: Unit 2 economiser acoustic pyrometer temperature results 117
Figure 84: Unit 2 furnace front acoustic pyrometer results compared with radiation pyrometers 118
Figure 85: Unit 6 furnace front acoustic pyrometer results compared with radiation pyrometers 119
Figure 86: Siemens Ardometer MPZ20 standard lens optical characteristics [61] 120
Figure 87: CFD temperature profiles of Plant X boiler along a vertical plane and horizontal plane at the top row of burners 121
Figure 88: Unit 6 furnace diagonal acoustic pyrometer results compared with radiation pyrometers, at boiler full load 123
Figure 89: Unit 6 furnace diagonal acoustic pyrometer results compared with radiation pyrometers, at boiler 3/4 of full load 123
Figure 90: Uncertainty ranges on FET from both the MEB and acoustic pyrometer 128

List of Tables

Table 1: Comparison between Excel sheet and Mathcad models 28

Table 2: Test plant MEB measurements 36

Table 3: MEB Assumptions 37

Table 4: Final Coal Analysis 38

Table 5: Main results of Plant X MEB calculations 38

Table 6: Impact of ingress air distribution on calculated FET 40

Table 7: Input values for MEB sensitivity analysis and uncertainty propagation study 41

Table 8: Uncertainty propagation comparison between MEB models with and without the A/H 49

Table 9: Boundary conditions for zonal model 52

Table 10: Particle properties used as inputs to calculate particle radiative properties 53

Table 11: Remaining inputs to the zonal model calculation 54

Table 12: Zonal model results 54

Table 13: Comparison between popular acoustic pyrometers 73

Table 14: Path numbering 94

Table 15: Errors of reconstructed profiles 99

Table 16: Errors of reconstructed profiles excluding outermost 1.75m on all sides 100

Table 17: Band-pass filter parameters 112

Table 18: Time of flight offset values 114

Table 19: Comparison between raw TOF determined from the 2 detection methods 116

Table 20: Inputs required to calculate the gas-particle mixture properties with their associated uncertainties 127

List of Nomenclature

General symbols

$\%Air_{ing}$	Mass percentage of ingress air in total humid air	% m/m
$\%Ash$	Mass percentage ash content of coal	% m/m
$\%BA$	Mass percentage of bottom ash in total ash	% m/m
$\%C$	Mass percentage carbon content of coal	% m/m
$\%C_{ba}$	Mass percentage of carbon in bottom ash	% m/m
$\%C_{fa}$	Mass percentage of carbon in fly ash	% m/m
$\%FA$	Mass percentage of fly ash in total ash	% m/m
$\%H$	Mass percentage hydrogen content of coal	% m/m
$\%H_2O$	Mass percentage moisture content in coal	% m/ m
$\%Ingress_{backpass}$	Mass percentage of backpass ingress air in total ingress air	% m/m
$\%Ingress_{furnace}$	Mass percentage of furnace ingress air in total ingress air	% m/m
$\%N$	Mass percentage nitrogen content of coal	% m/m
$\%O$	Mass percentage oxygen content of coal	% m/m
$\%S$	Mass percentage sulphur content of coal	% m/m
A_{kl}	Fourier coefficients	-
c	Speed of sound	m/s
c_g	Speed of sound in pure gas	m/s
c_m	Speed of sound in gas-particle mixture	m/s
C'	Unburnt carbon per kg of coal	kg C/kg coal
C'''	Energy of unburnt carbon per unit energy in coal	kJ C/kJ coal
C_D	Drag coefficient	
C_p	Specific heat at constant pressure	kJ/kgK
C_{solid}	Specific heat of solid	kJ/kgK
$C_{v.gas}$	Specific heat of gas at constant volume	kJ/kgK
CV	Calorific value	kJ/kg
d_p	Diameter of particle	μm
$EA_{A/H.fg.in}$	Excess air at air heater flue gas inlet	% m/m
E_{in}	Energy inputs	MW
E_{out}	Energy outputs	MW
f	Slowness	s/m

FET_b	Furnace exit temperature calculated from backpass MEB	°C
FET_f	Furnace exit temperature calculated from furnace MEB	°C
g	Gravitational constant	m/s^2
h	Enthalpy	kJ/kg
$h_{air.A/H.out}$	Enthalpy of air at air heater outlet	kJ/kg
$h_{air.amb}$	Enthalpy of air at ambient temperature and pressure	kJ/kg
$h_{air.leak.out}$	Enthalpy of leakage air ait air heater flue gas outlet	kJ/kg
h_{BA}	Enthalpy of bottom ash	kJ/kg
$h_{FA.A/H.in}$	Enthalpy of fly ash at air heater flue gas inlet	kJ/kg
$h_{FA.A/H.out}$	Enthalpy of fly ash at air heater flue gas outlet	kJ/kg
HAR	Humid air required	kg air/kg coal
$HAR_{inc.leak}$	Humid air required for secondary boundary	kg air/kg coal
h_{coal}	Enthalpy of coal	kJ/kg
$h_{fa.FE}$	Enthalpy of fly ash at furnace exit	kJ/kg
$h_{fg.FE}$	Enthalpy of flue gas at furnace exit	kJ/kg
$h_{fg.A/H.in}$	Enthalpy of flue gas at air heater inlet	kJ/kg
$h_{fw.econ.in}$	Enthalpy of feedwater at economiser inlet	kJ/kg
$h_{fw.econ.out}$	Enthalpy of feedwater at economiser outlet	kJ/kg
$h_{H_2O.vap}$	Latent heat of vaporisation of water	kJ/kg
$h_{rh.in}$	Enthalpy of steam at reheater inlet	kJ/kg
$h_{rh.att}$	Enthalpy of reheater attemporator water	kJ/kg
$h_{steam.drum}$	Enthalpy at steam drum	kJ/kg
$h_{steam.rh.out}$	Enthalpy of steam at reheater outlet	kJ/kg
$h_{steam.sh.out}$	Enthalpy of steam at superheater outlet	kJ/kg
K	Constant	-
L	Path length	m
L_m	Mean beam length	m
m_p	Mass loading ratio	
$\dot{m}$	Mass flow rate	kg/s
$\dot{m}_{air.A/H.leak}$	Mass flow rate of air heater leakage air	kg/s
$\dot{m}_{air.A/H.in}$	Mass flow rate of air at air heater inlet	kg/s

$\dot{m}_{air.A/H.out}$	Mass flow rate of air at air heater outlet	kg/s
$\dot{m}_{air.ingress}$	Mass flow rate of ingress air	kg/s
$\dot{m}_{air.total}$	Total mass flow rate of air inside control volume	kg/s
$\dot{m}_{coal}$	Mass flow rate of coal	kg/s
$\dot{m}_{fa}$	Mass flow rate of fly ash	kg/s
$\dot{m}_{fg.A/H.in}$	Mass flow rate of flue gas at air heater inlet	kg/s
$\dot{m}_{fg.FE}$	Mass flow rate of flue gas at furnace exit	kg/s
$\dot{m}_{fw.econ.in}$	Mass flow rate of feed water	kg/s
$\dot{m}_{seal.air}$	Total mass flow rate of seal air into mills	kg/s
$\dot{m}_{rh.att}$	Mass flow rate of reheater attemporator water	kg/s
$\dot{m}_{rh.in}$	Mass flow rate of reheater inlet steam	kg/s
$\dot{m}_{rh.out}$	Mass flow rate of reheater outlet steam	kg/s
$\dot{m}_{sh.att}$	Mass flow rate of superheater attemporator water	kg/s
$\dot{m}_{sh.out}$	Mass flow rate of superheater outlet steam	kg/s
$\hat{m}_{fg}$	Mass flow rate of flue gas per kg of coal	kg fg/kg coal
$\hat{m}_{fg.A/H.out}$	Mass flow rate of flue gas per kg of coal at A/H outlet	kg fg/kg coal
M	Molar mass	g/mol
M_{fg}	Molar mass of flue gas	g/mol
N_{ω}	Dimensionless parameter	-
p_{atm}	Atmospheric Pressure	kPa
p_{fw}	Pressure of feed water	kPa
$p_{sh.att}$	Pressure of superheater attemporator spray water	kPa
$p_{steam.drum}$	Pressure of steam/water inside drum	kPa
$p_{steam.sh.out}$	Pressure of steam at final superheater outlet	kPa
P_{mills}	Power to mills	MW
$P_{PA.fans}$	Power to PA fans	MW
$P_{seal.fans}$	Power to mill seal air fans	MW
$\dot{q}_{rad}$	Radiative heat flux	W/m^2
$Q_{insul.loss}$	Losses to the surroundings as a percentage of input energy	%
$\dot{Q}_{credits}$	Energy of credits	MW
$\dot{Q}_{econ}$	Energy transferred to economiser	MW

$\dot{Q}_{fg.A/H.in}$	Energy of flue gas at A/H inlet	MW
$\dot{Q}_{heat.transfer}$	Sum of heat transfer to heat exchangers in boiler backpass	MW
$\dot{Q}_{in}$	Energy input from coal	MW
$\dot{Q}_{loss}$	Sum of energy losses	MW
$\dot{Q}_{loss.ash}$	Energy losses in ash	MW
$\dot{Q}_{loss.ba}$	Sensible heat loss in bottom ash	MW
$\dot{Q}_{loss.evap}$	Energy loss due to evaporation of fuel moisture	MW
$\dot{Q}_{loss.fa}$	Sensible heat loss in fly ash	MW
$\dot{Q}_{loss.humidity}$	Energy loss in flue gas humidity	MW
$\dot{Q}_{loss.rad}$	Energy losses due to radiation to surroundings	MW
$\dot{Q}_{loss.UBC}$	Energy losses due to unburnt carbon	MW
$\dot{Q}_{out}$	Energy recovered by steam	MW
$\dot{Q}_{rad.top}$	Radiation from furnace to convective pass	MW
$\dot{Q}_{superheaters}$	Energy transferred to superheater circuit	MW
$\dot{Q}_{walls}$	Energy transferred to furnace walls	MW
$\dot{Q}_{walls.bp}$	Energy transferred to evaporator walls upstream of the furnace	MW
R	Universal gas constant	J/molK
R'	Ideal gas constant for gas-particle mixture	J/kgK
R_{fg}	Ideal gas constant for flue gas	J/kgK
RH	Relative humidity	%
SAR	Stoichiometric air required	kg air/kg coal
sk, sl	maximum wavenumber of estimated Fourier series in x and y directions	-
t	Time	s
T	Temperature	°C
$T_{air.A/H.out}$	Temperature of air at air heater exit	°C
T_{amb}	Ambient temperature inside boiler house	°C
T_{atm}	Atmospheric Temperature	°C
$T_{BA.exit}$	Temperature of bottom ash leaving boiler control volume	°C
$T_{fg.A/H.in}$	Temperature of flue gas at air heater inlet	°C
$T_{fg.A/H.out}$	Temperature of flue gas at air heater outlet	°C

$T_{fw.econ.in}$	Temperature of feedwater at economiser inlet	°C
$T_{fw.econ.out}$	Temperature of feedwater at economiser outlet	°C
$T_{steam.sh.out}$	Temperature of steam at final superheater outlet	°C
$T_{sh.att}$	Temperature of attemporator spray water	°C
TOF	Time of flight	ms
u	Uncertainty	various
$\%_v O_{2.A/H.fg.in}$	Volume percentage of oxygen in flue gas air heater flue gas inlet	% V/V
$\%_v O_{2.A/H.fg.\text{out}}$	Volume percentage of oxygen in flue gas air heater flue gas outlet	% V/V
$\%_v O_{2.air}$	Volume percentage of oxygen in ambient air	% V/V
v_{mk} , v'_{mk}	Average sound velocity along path k	m/s
v_{slip}	Slip velocity	m/s
$V'_{seal.air}$	Volumetric flow rate of seal air	m^3/s

Greek symbols

α	Percentage of evaporation taking place in the furnace	%
β_g	Extinction coefficient of gas	m^{-1}
β_m	Extinction coefficient of gas particle mixture	m^{-1}
β_p	Extinction coefficient of particles	m^{-1}
γ	Specific heat ratio	-
γ'	Specific heat ratio of gas-particle mixture	-
γ_{fg}	Specific heat ratio of flue gas	-
ε	Emissivity	-
ε_g	Emissivity of gas	-
ζ	Density ratio	
η	Boiler efficiency	%
η_{direct}	Boiler efficiency calculated using the direct method	%
η_{losses}	Efficiency calculated using the losses method	%
κ_g	Absorption coefficient of gas	m^{-1}
κ_p	Absorption coefficient of particles	m^{-1}
λ	Relaxation parameter	-
μ	Dynamic viscosity	Ns/m2
ν	Kinematic viscosity	m^2/s

ρ	Density	kg/m^3
ρ_g	Density of gas	kg/m^3
ρ_m	Density of gas-particle mixture	kg/m^3
ρ_p	Density of particles	kg/m^3
σ	Stefan-Boltzmann constant	W m^{-2} K^{-4}
σ_p	Scattering coefficient	m^{-1}
υ	Velocity of gas phase	m/s
υ_p	Velocity of particle phase	m/s
ω	Specific humidity of ambient air	kg H_2O/kg dry air
Ω	Angular frequency	rad/s

Acronyms and Abbreviations

A/H	Air heater
AP	Acoustic pyrometer
ASG	Acoustic signal generator
ASR	Acoustic signal receiver
AST	Acoustic signal trigger
BET	Boiler exit temperature
BMEB	Boiler mass and energy balance
BPMEB	Backpass mass and energy balance
CFD	Computational fluid dynamics
CV	Calorific value
DCS	Digital control system
EA	Excess air
EPPEI	Eskom Power Plant Engineering Institute
FD	Forced draught
FES	Furnace exit surface
FET	Furnace exit temperature
FFFR	Fossil fuel firing regulations
FFT	Fast Fourier Transform
FMEB	Furnace mass and energy balance
GCV	Gross calorific value
HHV	Higher heating value
ID	Induced draught

IR	Infrared
JCGM	Joint Committee for Guides in Metrology
LHV	Lower heating value
MEB	Mass and energy balances
NCV	Net calorific value
OCGT	Open cycle gas turbines
OEM	Original equipment manufacturer
P&T	Performance and testing
PA	Primary air
PF	Pulverised fuel
RP	Radiation pyrometer
SA	Secondary air
SPC	Signal processing computer
STFT	Short time Fourier transform
TC	Thermocouple
TOF	Time of flight

1. Introduction

1.1. Project rationale

In a Rankine cycle coal fired power plant, the pulverised coal boiler is one of the major components. The boiler flue gas furnace exit temperature (FET) is a key operating parameter of coal fired steam boilers in terms of both the design and operation. From the design perspective, the FET is vital for materials selection and sizing of heat transfer surfaces [1]. From an operating perspective, it is a major indicator of the rate of combustion and heat transfer that is occurring within the furnace (which is also called the combustion chamber). It is sensitive in particular to the type of coal being burned, as well as the setup and performance of the entire combustion system such as the milling plant, air flows, burner settings, etc. Downstream of the furnace, the FET has a significant impact on the performance of the heat exchangers within the flue gas path. It affects both the performance and reliability of the boiler heat exchangers, which ultimately impacts on both boiler efficiency and availability.

If one delves deeper into the conditions mentioned above, it becomes clear that if the FET can be maintained within its designed values, it will improve performance and efficiency of the boiler as a whole, thereby producing economic benefits. Knowledge of the FET can enable operators to recognize that there are problems with the combustion system and can facilitate investigation and troubleshooting by engineering, maintenance and operating departments. Ideally, this would result in appropriate corrective action being taken.

Traditional invasive temperature measurement methods have been found to be problematic for continuous operation, mainly due to the physical conditions and geometry of the furnace. In an effort to address this problem, non-invasive methods using optical/radiation pyrometers and more recently, acoustic pyrometry, have been developed and have been purported to be capable of measuring the FET with a high level of accuracy.

In addition to these measurement devices, the FET can also be calculated using various modelling and calculation methods. The accuracy of these methods is, in most cases, still dependent on a vast array of other plant measurements, and the suitability of these methods for online monitoring depends on the availability of plant measurements as well as the solving time of the calculations.

From the South African perspective, no sustainable and reliable method of FET monitoring has been fully developed or implemented. Existing mass and energy balance calculation methods do exist in Eskom; however the application of these to the calculation of FET has not been fully

implemented. In terms of measurement devices, all Eskom boilers are fitted with some form of radiation pyrometers. Their primary function, however, is detection of flame presence for combustion safety and control in accordance with Fossil Fuel Firing Regulations (FFFR), as opposed to temperature measurement. Newer technologies such as acoustic pyrometry have not been implemented in Eskom as confidence in the instrumentation has not yet been established, particularly due to the operating conditions of South African boilers which operate with high ash content coals.

Taking all of this into account, it can be seen that there is a need for a thorough assessment of these methods, which will advise future investment decisions and will be a vital step in the development of an online boiler FET monitoring tool.

1.2. Project objectives

The primary objective of the project is to investigate the different methods and techniques that can be used to measure or monitor the FET and the different types of benefits that they can provide to improve overall boiler condition monitoring.

These methods will be analysed and compared in terms of:

- their capabilities, benefits and limitations.

- feasibility regarding installation and maintenance aspects.

- on-line monitoring applicability.

- expected accuracy that can be achieved utilising uncertainty propagation studies.

These methods are classified, henceforth, as indirect and direct methods. Indirect methods refer to calculation methods based on mass and energy balances (MEB), while the direct methods refer to measurement of the FET, by means of specialised instrumentation. This project will first focus on the indirect methods, and then on the direct method based on acoustic pyrometry. Both of these methods will be investigated and applied on an actual Eskom plant, and compared with each other, as well as with the existing radiation pyrometry.

1.3. Scope and limitations of Project

The scope of this project is **not** to provide a thorough exposition of all the existing technologies applied in industry, but rather to focus on those relevant to Eskom, as mentioned above.

The project is also **not** intended to develop a new technology but rather to assess how existing methods can be applied and the quality of results that can be obtained.

One of the major limitations is the availability of acoustic pyrometer equipment. Thus, the experimental testing of the acoustic pyrometer should **not** be regarded as extensive but rather as a means of demonstrating the fundamental aspects of the technology.

1.4. Outline of dissertation

The next chapter, Chapter 2, briefly lays down some foundational and background information related to the study that is valuable for understanding the subsequent sections.

Thereafter, the bulk of the report is broken up between Chapters 3 and 4.

Chapter 3 documents the indirect methods, beginning with a short literature study documenting some of the common indirect methods. The chapter then delves into greater detail on the specific indirect mass and energy balances (MEB) method of interest, covering the development of global boiler, furnace and backpass MEB models. Thereafter, the implementation on the test case plant is described, and the results presented, analysed and discussed. Lastly, the chapter looks at the radiation from the furnace to the convective pass which the MEB method does not account for and incorporates it into the MEB.

Chapter 4 documents the direct methods, again beginning with a literature study documenting some of the common direct methods with a particular focus on the history and development of acoustic pyrometry. The chapter discusses at some length, the practical and theoretical aspects regarding the application of acoustic pyrometry, and goes into some detail on pertinent topics such as explaining and applying a method to reconstruct the temperature profile in the furnace using acoustic measurements The method for experimental testing done during this project is then detailed, followed by results, and the analysis and discussion thereof.

Chapter 5 eventually concludes the salient points from the project as a whole, and provides recommendations for future work.

2. Background

The objective of this chapter is to provide a brief background on relevant topics, which serves to lay the foundations to assist the reader to place into context the subsequent chapters.

2.1. Pulverised coal boiler in the overall power plant cycle

In the Rankine cycle, the primary function of the boiler is to convert the chemical energy of coal into heat in the flue gas and then transfer this heat to water in order to produce steam of a specified quality, temperature and pressure, to be delivered to the turbine.

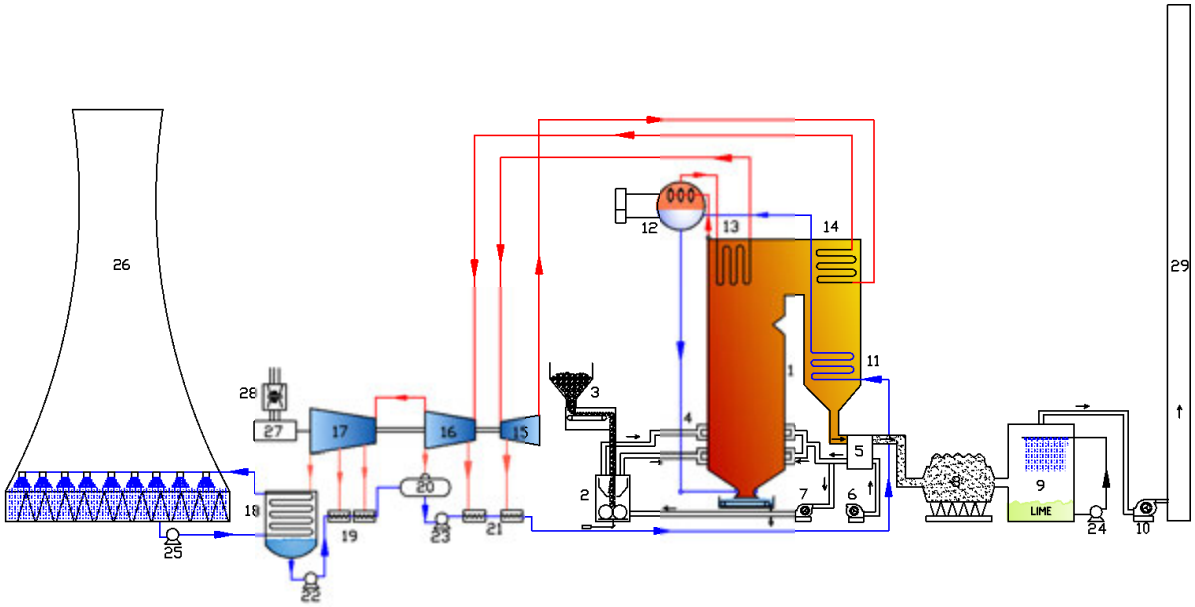

Figure 1: Typical overall power plant Rankine cycle

Essentially, the overall plant cycle involves a mixture of coal (3) and air (6) delivered as pulverised fuel (PF) to the boiler (4) where a combustion process takes place to release the chemical energy of the coal. The heat from the flue gas is transferred to the water which enters the boiler at the economiser (11) and passes through a series of heat exchangers (1, 11, 13, and 14) to produce and superheat steam. This superheated steam is thereafter delivered to a steam turbine (or a series of turbines operating at different pressure stages shown as 15, 16, and 17 in Figure 1) via an arrangement of high pressure steam pipework.

The steam delivered to the turbine is expanded to produce work to rotate the turbine which is coupled to a generator (27). The generator converts the mechanical work into electrical energy

which is delivered to the electricity grid. The expanded steam from the turbine is then fully condensed in the condenser (18) via the cooling water system (25, 26) and delivered back to the boiler at the economiser (11) via a series of pre heaters known as feed water heaters (19, 21). The pumps (22 and 23) generate the pressure to overcome the pressure losses of the whole circuit, as well as to enable expansion of steam in the turbine. Thus, the cycle continues.

2.2. The pulverised coal boiler and its auxiliaries

Since this project is focused on the boiler itself, it is important to understand a little bit more about the boiler and its auxiliary components.

2.2.1. Coal and the milling plant

i. **The composition and properties of coal**

The major constituents of coal are carbon, hydrogen, oxygen, nitrogen, sulphur, moisture and ash. Coal analysis is normally expressed in one of 2 ways, namely proximate analysis and ultimate analysis. In a proximate analysis of coal, the measured parameters are the inherent moisture of the coal, the ash content, the volatile matter, and the fixed carbon content by difference. In an ultimate analysis of coal, the quantities of carbon, hydrogen, nitrogen, and sulphur are determined and the oxygen found by difference.

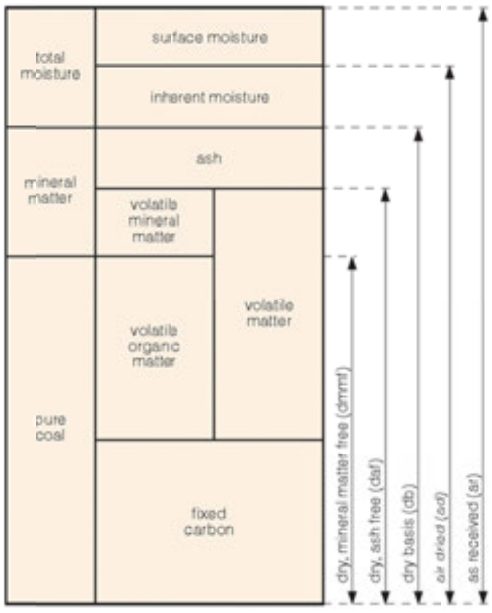

Figure 2: Relationship between different coal analytical bases [2]

As shown on Figure 2, coal analysis can be expressed in several different bases that can be converted from one to the other.

The chemical energy contained in the coal is expressed by its calorific value (CV). The CV is normally measured in a laboratory using a bomb calorimeter in which coal is oxidised with pure oxygen. The CV can be expressed as either the net calorific value (NCV) or the gross calorific value (GCV). When combustion takes place, the moisture in the coal experiences a phase change from liquid to vapour. The combustion products (i.e. the flue gas) also contain moisture generated by combustion of hydrogen in the coal. The difference between the NCV and the GCV is the latent heat of moisture from these 2 origins (coal and combustion of hydrogen). The NCV is also called the lower heating value (LHV) and the GCV is called the higher heating value (HHV). The HHV is higher than the LCV as it comprises the latent heat of water contained in the coal and the water generated by hydrogen combustion.

ii. The reason for using pulverised coal

As the name suggests, a pulverised coal boiler is designed to combust coal which is ground down to a very fine powder, normally in the region of 70 microns average mass diameter, also called d50, i.e. diameter at which 50% of the particles are above 70 µm and 50% below. The benefits of using pulverised coal are that it results in a greater surface area of the coal particle being exposed to the hot combustion air, thereby resulting in higher volumetric combustion rates [1], faster and more efficient combustion. This is desirable because it allows the physical dimensions of the boiler to be much smaller to produce the same output as can be achieved using larger particles, thus reducing the capital costs, which is the ultimate goal of boiler designers and manufacturers.

iii. The milling plant

The raw coal which is delivered to the power plant comes from coal mines and is in a variety of sizes, far too large to be used in the boiler. Before being fed to the boiler the raw coal is fed via the feeders to the mills, which dry the coal and grind it down to the required size.

a) Coal feeders

The function of the feeders is to control the rate at which coal is fed to the mills. There are two broad categories of feeders, namely volumetric feeders and gravimetric feeders. The difference between these 2 types is actually quite important with regards to accurately measuring and controlling the coal flow rate to the boiler, which is critical for the optimisation of combustion. Volumetric feeders control the volumetric flow rate of coal, without taking into account the bulk density of coal flow, which varies due to air spaces between the coal pieces and variations in moisture content. This means that the actual mass flow rate of the coal is not accurately measured

and controlled. This is actually the most commonly used type of feeder in Eskom. Gravimetric feeders, on the other hand, address this problem by measuring the weight of the coal along the feeder belt, thus providing a more accurate measurement of the coal mass flow rate.

b) <u>Mills</u>

The coal from the feeders is fed to the mills which pulverise the coal down to the desired fineness, typically about 70 µm as said above. There is normally one feeder to one mill. Mills come in a variety of configurations, such as tube mills (also called ball mills), vertical spindle roller mills (as shown in Figure 3), bowl mills, beater mills, etc. A full characterization of these different types is not relevant to this study.

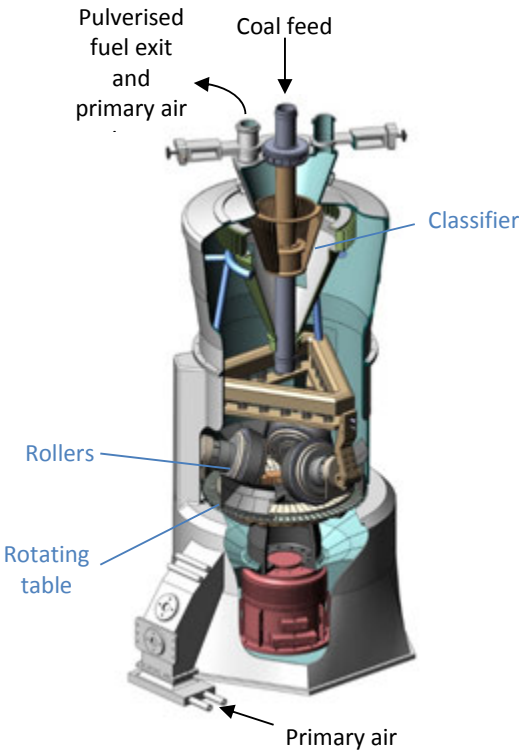

Figure 3: Example of a vertical roller type mill showing internal details [3]

One other aspect of coal mills that will be used later is seal air. Mills are pressurised by seal air which is supplied by a seal air fan, to prevent leaks of PF via the sealing elements and consequent external contamination of the air. This mass flow of seal air is relatively small in comparison to the total combustion air supplied to the boiler, but cannot be neglected.

2.2.2. Draught plant

The draught plant includes the forced draught (FD) fans, primary air (PA) fans, induced draught (ID) fans and the air heaters.

i. **Primary and secondary air**

Majority of the air flow into the boiler is via the left and right FD fans which draw atmospheric air from near the top of the boiler house where it is hotter than the ambient air and this saves energy by reducing the energy input to heat the air. The amount of air supplied is the amount of air required for stoichiometric combustion of the coal, plus a certain amount of excess air to ensure complete combustion. This air is delivered to the boiler, but first passes through the air heaters where it is heated by the hot flue gas leaving the boiler and entering the air heater at about 250-300°C. Some of this warm air is extracted by the PA fans, and is redirected to the mills, where it is used to dry the coal and pneumatically transport the pulverised coal to the burners on the boiler. This air which carries the PF is called the primary air, and the rest of the air from the FD fan which goes directly to the boiler after the air heater is called the secondary air (SA).

The secondary air and the primary air carrying PF are distributed to the burners. There are generally between 4 to 5 burners per mill, which translates to a total number of 20 or 25 burners for a unit with 5 mills. The quantities of the 2 air flows have to be controlled to ensure the correct air fuel mixture to each burner to achieve homogeneous combustion in the whole furnace. The burners are designed to ensure proper mixing of the air and fuel and to achieve stable combustion at different loads and with varying coal qualities. In low NOx burners, the secondary air flow is divided into additional streams such as tertiary air in order to achieve faster coal devolatisation close to the burner mouth, thereby creating a carbon rich area after combustion of volatile matter, thus enabling NOx reduction.

ii. **ID fans**

The function of the ID fans is to extract the flue gas and ash out of the boiler through the flue gas cleaning plant, which may be in the form of electrostatic precipitators or fabric filter plants, and out to the atmosphere via the flue gas stack. The ID fan also serves the critical function of maintaining the boiler enclosure slightly below atmospheric pressure, to ensure the safety of personnel and assets.

iii. **Air heaters**

One of the components which is quite influential for the calculation method presented in the next chapter is the air heater (A/H), thus it is imperative that some concepts are introduced here.

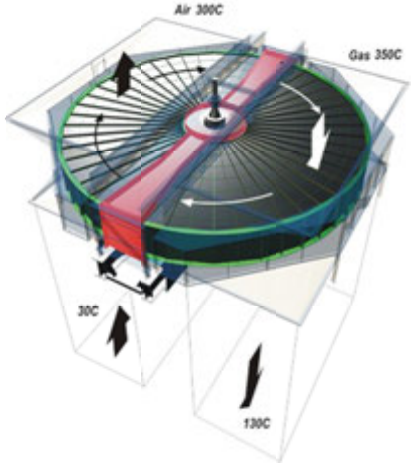

Figure 4: Example of a regenerative air heater [4]

Air heaters are found at the exit of the boiler on the flue gas path. Their function is to lower the temperature of the flue gas leaving the boiler by heating the air that is supplied to the boiler from the FD and PA fans. For every 22°C temperature drop of the flue gas in the air heater, the boiler efficiency increases by approximately 1% [1].

The designs of air heaters are mainly in 2 categories, namely regenerative or tubular A/H. The regenerative A/H consist of either a rotating wheel of heat exchanger packs in a stationary duct (Ljungström type shown in Figure 4) or a stationary wheel of heat exchanger packs and a rotating air and flue gas hood (Rothemuhle type). The primary air (which is less compared to secondary air), is at a higher pressure in order to overcome the mill and PF transport pressure losses, and there are typically one of the following two layouts. On the one hand, there is an A/H which heats all of the air from the FD fan prior to the split of SA and PA, as shown in Figure 5(a), while on the other hand the PA and SA have separate A/H (see Figure 5(b)).

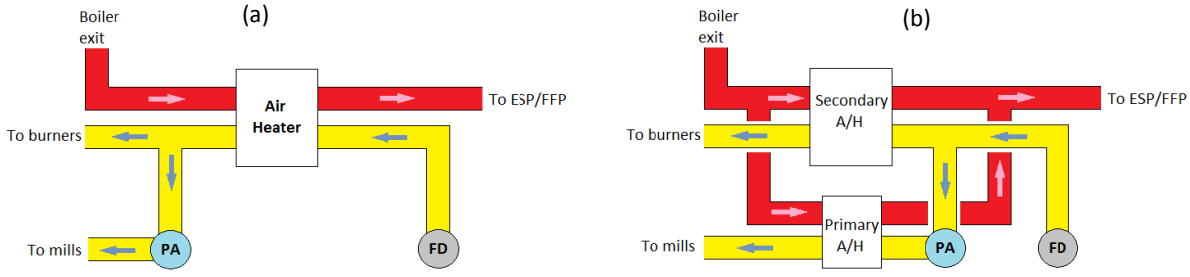

Figure 5: Primary and Secondary A/H configurations

In the case of separate A/H, the secondary A/H is typically a regenerative A/H and the primary A/H a tubular A/H.

Regenerative A/H have one very critical characteristic that will be mentioned again during the calculation methods studied in this report, and that is air heater leakage. Due to the physical construction of air heaters, there is leakage that occurs via the radial, axial and circumferential seals, from the higher pressure air side to the flue gas side. This results in a reduction of the air flow supplied to the boiler and a reduction of the flue gas temperature at A/H exit. With properly designed and fitted seals, A/H leakage should be less than 10% of the inlet air flow rate, although leakage is commonly in the 15-20% range and can even be as high as 30% [5]. This creates operational problems that can result in the FD and ID fans not having sufficient capacity to cope with the increased air and flue gas flow rates, and this limits the boiler steam output as the load has to be reduced. It also increases the power plant internal energy consumption thereby decreasing the energy efficiency.

2.2.3. Interface of flue gas system with water/steam system

All of the above components dealt with the coal, air and flue gas systems of the boiler, but the ultimate objective of all these systems is to produce steam from water which is fed through to the boiler from the boiler feed pumps. Water which has been pre-heated by the low pressure feed water heaters before the boiler feed pump and high pressure feed water heaters after the boiler feed pump, enter the boiler at the economiser. As the name suggests, the function of the economiser is similar to that of the air heater, in that it capitalises on the low temperature energy of the flue gas leaving the boiler, thereby improving boiler efficiency. The economiser is sometimes considered as the last stage of feed water heating since the water leaving the economiser is still in liquid phase.

The water from the economiser is fed to the boiler water walls. These water walls run from the bottom of the boiler along all the sides all the way up to the top. In some designs, there is even a 5^{th} wall called the division wall which runs up the middle of the boiler splitting the furnace into 2 halves, thereby increasing the surface area available for heat transfer between the flue gas and water. It also results in a more even flue gas temperature distribution across the cross section of the furnace.

The furnace refers to those tubes which are in the lower sections of the boiler closest to the flame, where the heat transfer is predominantly by radiation from the “fireball”. In a drum type boiler, the water in the water walls is heated at the saturation temperature of the water at drum pressure.

The drum contains a water/steam mixture and the water in the drum is recirculated into the water walls while the steam is fed to the superheaters. In a once-through boiler, there is no drum but rather separating vessels which behave similarly to a drum during start up. However, at higher loads, the water in the walls transitions into steam within the water walls and is therefore already slightly superheated at the separating vessels and thus goes straight to the superheaters.

The furnace exit is typically defined as the plane in space in the boiler which separates the predominantly radiative furnace volume (or combustion chamber), and what is called the "convective heat exchanger pass" which includes all of the tube bundles such as superheaters, reheaters and economisers. Even though it is called "convective heat exchanger pass", heat transfer still occurs by both radiation and convection, especially for the first "convective heat exchangers" on the flue gas path as the flue gas leaving the furnace section is typically upwards of 1200°C. There are a variety of configurations and arrangements of these heat exchanger bundles that are specific to certain designs, but essentially they are designed to find the best balance between the most optimum heat transfer characteristics, and lowest capital cost. This is achieved by minimising the material requirement both in terms of material volume and properties while achieving the steam temperature required by the steam turbine.

2.3. The importance of the FET

As mentioned above, the FET is a critical parameter in the design of the boiler heat exchangers. Thus, from an operating perspective, it is imperative that it is maintained within its design limits, both upper and lower, to ensure reliable and continuous operation of the boiler pressure parts.

One very important aspect of the design of the boiler is to ensure that the boiler FET does not exceed the ash fusion temperature limit. For a given ash quality content in the coal, the ash fusion temperature may range from about 900°C to 1350°C. For South African coals it is usually, and fortunately, towards the upper limit of that range. If the FET exceeds the ash fusion temperature, slagging occurs on the superheaters and reheaters, which adversely impacts on the performance of the heat exchangers. This reduction in heat transfer results in higher flue gas temperatures being experienced all along the flue gas path, ultimately causing a higher back end temperature of the flue gas at the outlet of the boiler, and thus a loss in boiler efficiency. The higher backend temperatures also seriously impact the performance of the dust cleaning plant.

As a result of this reduced heat transfer, the boiler has to operate at higher gas temperatures in order to achieve the desired steam outlet conditions. This exposes the boiler superheater and reheater tubes to metal temperatures higher than the design limits, accelerating age related boiler tube failure mechanisms such as long term overheating, fatigue and corrosion.

Figure 6: Example of slagging on the tubes on the left and severe distortion of a tube after failure

Boiler tube failures normally result in forced outages, and this plant unavailability incurs huge costs, due to the loss of production. In the Eskom case this coal power production often has to be supplemented by open cycle gas turbines (OCGT) which have a much higher fuel cost than coal plants.

Figure 7: Example of a boiler tube which failed by long term overheating

All of the above refers to high temperature issues, but a FET which is too low can also have other detrimental impacts, as this would also reduce the heat transfer in the boiler. The result can be phenomena like water carryover into the superheaters which can cause tube failures; and flue gas temperatures at the air heater which are below the dew point temperature, which can result in increased fouling of the air heater packs and corrosive damage mechanisms.

Proper control of the FET is possible by a number of different operating actions. For example, combustion can be adjusted by operating actions such as (i) changing the fuel quality, (ii) co-burning supporting fuel such as oil, (iii) adapting the PF particle size by adjusting the milling plant performance, (iv) tuning the burners settings like the burner secondary air swirl, (v) better distributing the air and fuel to different burners, (vi) changing the firing distribution to the different burners. Alternatively, furnace heat transfer can also be enhanced by cleaning the heat transfer surfaces by soot blowing. All of these corrective actions come with their own risks and costs, and they should be taken based only on well informed decisions that good knowledge of FET

will help to address. This is even more significant if the FET profile is known over the furnace exit cross section. With the introduction of low NOx burners and strict emission regulations, FET monitoring and in particular FET profile monitoring becomes even more important as the presence of hot spots increases the production of NOx gases [6]. Thus, the importance of the FET is clearly evident.

3. Indirect methods

This chapter details the indirect methods used in this study to determine the FET.

3.1. Literature study on indirect methods

Accurate estimation of FET by analytical methods is extremely complex [1]. At first glance, the problem appears to be a straight forward energy balance. The temperature of the flue gas at the furnace exit is calculated from its energy content, which is simply the energy supplied to the boiler in coal and air minus the energy transferred to the furnace walls plus any losses. One of the difficulties arises in estimating the amount of energy which is transferred to the furnace walls.

This is usually done by performing a calculation of the radiation heat transfer from the flame to the walls. The radiation mechanism is extremely complex, particularly in the case of the boiler furnace which consists of a particle laden gas medium. As a result, there is no analytical solution unless the problem is significantly simplified [7]. Many simplified radiation models have been described by authors such as Verbanck [8], Penninger et al [9] and Govindsamy [10]. The accuracy of the results from these simplified models has been found to be very dependent on certain assumptions, which can only be improved by reliable measurement data.

In light of this, many advanced numerical models have been discussed in literature. One of the most well-known methods is the zone (or zonal) method which was first introduced by Hottel and Cohen [11] in 1958. This method involves discretising the furnace into surface and gas volume zones. The core concept is the determination of direct radiation exchange areas between all of the surface-surface, gas-surface and gas-gas pairs, which are then used to develop a set of energy balance equations. The zone method has become widely used for modelling boiler furnaces [7]. Recently, Monnaemang [12] demonstrated the use of the zonal method, and her work will be used later. Some of the other popular numerical methods include the Monte Carlo method and heat flux method.

Chandok et al [13] avoided having to estimate radiation at all, by performing calculations upstream of the furnace exit to calculate the FET. The primary focus of their study was developing a neural network model to estimate the FET which required an analytical calculation to generate training data for the model. The analytical calculation was a MEB method that is completely independent of heat transfer theory. The method involves calculation of the FET by carrying out energy balances along all of the heat exchangers in the convective pass, beginning with 1 measurement of the flue gas temperature at the economiser outlet, working backwards to the furnace exit. All of the other temperatures along the flue gas path are calculated based on inlet

and outlet water/steam temperatures of the heat exchangers. The method is a lumped parameter analysis using averaged values.

While this method avoids the need to estimate radiative heat transfer, there still needs to be an indirect estimation of the energy transfer to the furnace walls. This aspect was not considered by Chandok et al. The difficulty arises in the fact that the water walls encompass a furnace section before and a section after the furnace exit in the convective pass. Due to the fact that all of the sections of the water walls are in the saturation state, there is no possibility of using water temperature measurement to determine the amount of energy transferred to the water walls in either section.

Hence, even with a MEB of the furnace (i.e. upstream of the furnace exit on the flue gas path), the above complication would arise. As mentioned by Govindsamy [10], the alternative to a radiation calculation, is to calculate the total amount of energy transferred to the entire water walls and estimate a factor which splits that amount between the furnace section of the walls, and the convective section of the walls.

All of the energy balance methods above have one additional level of uncertainty which is that they all require the mass flow rates of coal, flue gas and air as input parameters. These 3 parameters are not very accurately measured, if at all. They can, however, be calculated [10]. The Eskom mass and energy balance method [14] provides one such method of calculating these flow rates by performing a global MEB of the whole boiler and its auxiliaries, and this forms the basis for the calculation method described in this report.

Global MEB methods have typically been used for thermal performance evaluations and acceptance tests, where the primary objective is the calculation of boiler efficiency. The European standard EN12952-15 [15] and the American standard ASME PTC 4-2008 [16] both detail MEB methods used for performance evaluations that can be adapted for the calculation of the coal, air and flue gas flow rates. In fact, page 1 of the ASME standard explicitly mentions that the code can be used to determine these flow rates.

3.2. Overview of application of an indirect method

The indirect methods applied in this chapter involve the use of mass and energy balances (MEB) over particular control volumes within the boiler. It is possible for one to define any number of control volumes over which to do the MEB calculations. The choice of control volumes depends, to a large extent, on the objective of the calculation, the locations where plant measurements are available or where measurements can be more easily and accurately obtained.

Given the location of the furnace exit, it has been determined that the FET can be calculated either from a section upstream of the furnace exit by doing a furnace MEB (FMEB), and the temperature will be called FET_f, or from a section downstream of the furnace exit by doing a MEB over a section of the convective pass. This downstream MEB is referred to as the backpass MEB (BPMEB) and the temperature calculated from this direction will be referred to as FET_b. The principle can be applied to any boiler configuration, whether it is a tower type boiler or a 2-pass boiler. The convective pass above the furnace for a tower type will be referred to as the backpass in this study, for consistency. The power station which was used as a case study is a 2 pass boiler.

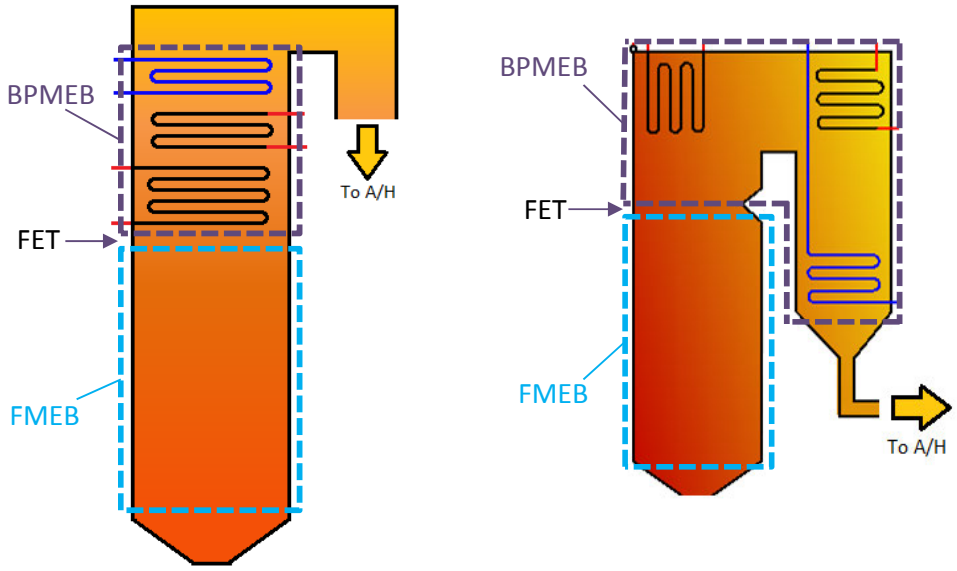

Figure 8: FMEB and BPMEB control volumes for tower boiler (left) and 2-pass boiler (right)

The MEB over any of these sections must surely require as inputs, the 3 large mass flow rates in the boiler, which are the coal, air and flue gas flow rates. These inputs are often very difficult to obtain or measure accurately online due to the large sizes and complex geometries of the ducts and pipes involved. The heterogeneities of the flows also don't allow for the installation of typical measurement instruments in the required standard conditions for which accuracy of the measurement can be guaranteed.

In some plants, there may be specialized measurement instrumentation that can be used to obtain these parameters, such as gravimetric feeders to determine the coal flow rate, mentioned in Chapter 2. In all other cases, these parameters can be calculated from a global boiler mass and energy balance (BMEB) provided that the required input parameter information is available. The high level relationship between the 3 control volumes is depicted in Figure 9.

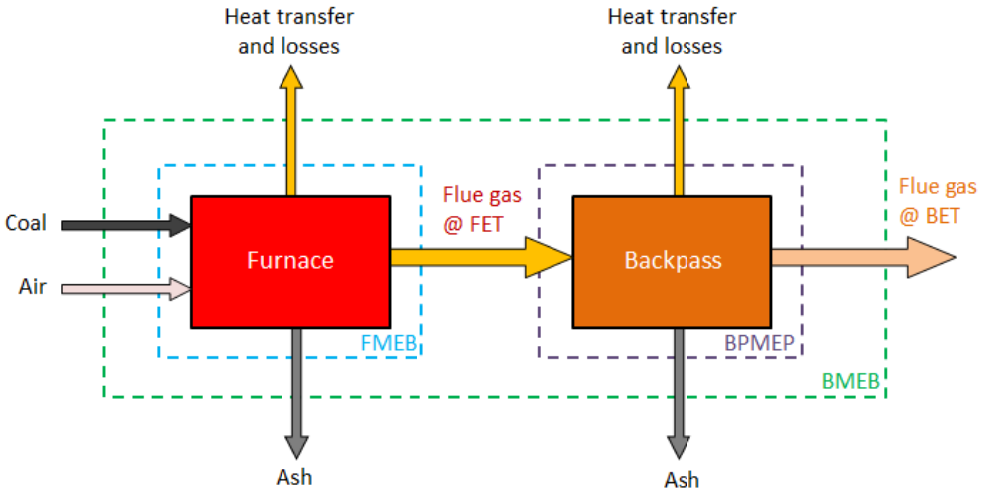

Figure 9: High level relationship between Boiler MEB (BMEB), furnace MEB (FMEB) and backpass MEB (BPMEB)

The method described here is derived from the Eskom Mass and Energy Balance manual [14] after having verified and refined certain calculations. The adapted and revised calculations of a new MEB model are developed in Mathcad. The FET_f and FET_b calculations are further developed and used to calculate the furnace exit temperature. Actual plant data is then applied as a case study to calculate the FET. Additionally, the radiation heat transfer from the furnace to the backpass is investigated as a correction factor into the MEB calculations using the zonal method. Later, the results from the indirect methods are compared to the direct measurements from pyrometers.

3.3. Global boiler mass and energy balance (BMEB) methodology

3.3.1. Development of Mathcad model

i. Reasons for revised model

As mentioned, there is already an existing Eskom Mass and Energy Balance Excel spreadsheet which was developed by previous Eskom Power Plant Engineering Institute (EPPEI) students, but it needed further validation and development, for the reasons explained below.

a) Understanding

The application of any mathematical model without fully understanding the development of it and the calculations contained within can result in incorrect application and misinterpretation of results. The development of the Mathcad model required a careful study of the Excel spreadsheet and the equations and rationale behind them, thus aiding in the overall understanding and traceability of the global boiler energy balance.

b) Customisation

Using an existing model does not allow any flexibility to modify the calculations as may be required for the specific application, e.g. adjusting the mass and energy balance control volume boundary. The original Excel spreadsheet was developed primarily for the BMEB in order to calculate the major boiler flow rates and verify their consistency. The calculation of the furnace exit temperature was not clearly documented and was only vaguely applied using the furnace control volume. Since the main objective here is the furnace exit temperature, it is only logical that this part of the calculation be clearly documented, and this is more easily accomplished in Mathcad. Refer to Appendix A for more details on why Mathcad in particular has been adopted.

ii. Boundary Selection

The first and perhaps most crucial step of any MEB calculation is to clearly define the boundary, or control volume. The schematic in Figure 10 shows control volumes that are typically used; and the inputs and outputs of the BMEB. The selection of these boundaries is naturally based on points in the system where the physical conditions of any mass flow stream crossing the boundary are well defined and can be either measured or calculated at that location. The boundary that is applied in [14] is shown by the dashed green line in Figure 10. This is also the boundary used for boiler mass and energy balances in the European [15] and American [16] standards to calculate the boiler efficiency for boiler acceptance tests. Of particular interest is to take note that there are 2 possibilities regarding the inclusion/exclusion of the air heater that can both be easily applied on most plants. This slight adjustment to the boundary is shown by the dashed red line at the air heater on Figure 10.

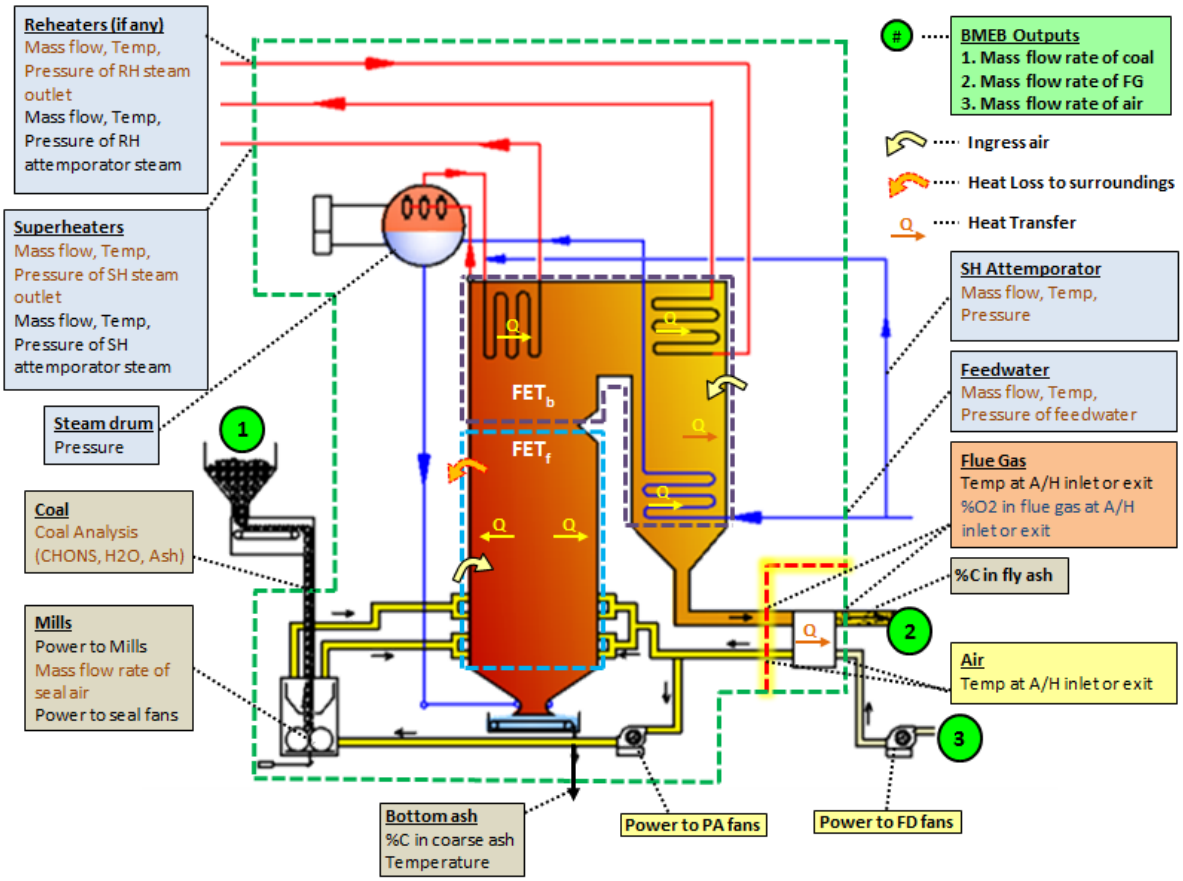

Figure 10: Mass and energy balance inputs, outputs and boundaries

Both boundaries do have pros and cons such as if one includes the air heater, then air heater leakage must be determined. A common method used to determine air leakage into the flue gas is to measure the increase of oxygen concentration in the flue gas between the inlet and outlet of the A/H. This leak can also be calculated from an air heater MEB by measuring the temperature drop in the flue gas across the air heater and the temperature increase of the air. Both methods have their own measurement issues. Both oxygen and temperature profiles in the ducts before and after the air heater are not homogenous and require integration of the mass weighted temperature and O_2 profiles, as was done in [17].

On the one hand, exclusion of the air heater removes the need for considering air heater leakage, thus simplifying the energy balance slightly and removing one source of inaccuracy. However, exclusion of the air heater also results in the need to use the flue gas temperature at the flue gas inlet to the A/H instead of the outlet in the energy balance calculations. Since the temperature here is much higher and less homogeneous than at the air heater outlet, the potential for inaccuracy becomes greater. Hence, sensitivity of the outputs to variations in the inputs is one

factor that must be considered. The implications of this selection from an error propagation perspective are discussed in subsequent sections.

The choice of the boundary is also driven largely by the availability of installed measurement instrumentation on site or access ports for taking ad-hoc measurements. In particular, some plants may only have O_2 in flue gas analysers installed at the flue gas inlet to the A/H. In that case the choice to exclude the air heater would be largely due to the unavailability of that measurement or the lack of access to obtain the measurement.

The overall structure of both MEB models (including and excluding the A/H) is the same. The model development presented in this document primarily focuses on the boundary excluding the A/H (and shall be referred to as the primary boundary). Areas where the differences would emanate due to inclusion of the A/H (referred to as the secondary boundary) will be pointed out, and shown in *italics* in the next sections.

iii. Model Inputs

All of the model inputs and typical locations on the boiler are depicted on Figure 10.

Note: The power to FD fan is only required as an input for the secondary boundary and only if the actual air temperature at the air heater air inlet is not known. In fact the FD fan power accounts for most of the temperature increase of the air through the fan.

iv. Calculation Flow

This section briefly explains the calculation flow of the BMEB. The main goal is to calculate the 3 unknown flow rates (coal, air and flue gas) using the measured input parameters. The 3 parameters are obviously related, since the amount of air supplied is a function of the coal composition, and the air and coal combine to produce the flue gas. Thus, by doing mass balances the air and flue gas mass flow rates can both be expressed in terms of the coal flow rate. Thereafter, these results are integrated into an energy balance to provide a third equation relating the 3 parameters. The calculation model is depicted in Figure 11.

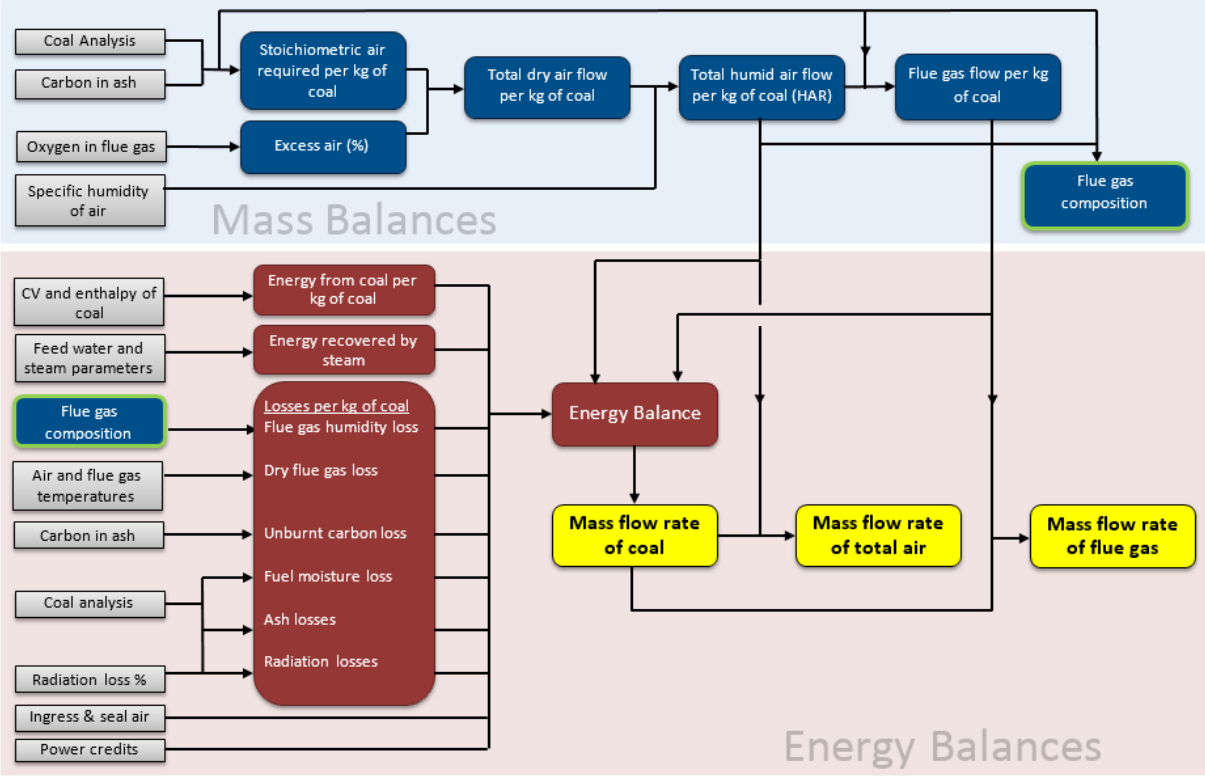

Figure 11: Global boiler MEB calculation flow

a) Mass balance

As can be seen from Figure 11, the starting point for the mass balance is the coal analysis. The coal analysis can be from any source, be it an online analyser or delivered offline from laboratory analysis of previously sampled coal. It should be noted whether the calorific value of the coal is in the form of the lower heating value (LHV) or the higher heating value (HHV). Either of the two can be used, so long as all of the subsequent calculations take into account which has been used. Also important is to take note of the moisture basis on which the coal analysis is determined.

Based on the chemical composition of the coal, and the fact that there is a percentage of unburnt carbon in ash (which is determined from the ash analysis), the theoretical air required for stoichiometric combustion can be calculated per kilogram of coal. Based on stoichiometric combustion reactions it can be shown that the theoretical air required for stoichiometric combustion is given by:

$$SAR = A:F_{stoich} = \frac{1}{0.23}\left[\frac{32}{12}(\%C - C') + \frac{32}{32}(\%S) + 8.\%H + 0.3\frac{32}{14}(\%N) - \%O\right] \quad (3.1)$$

Where C' = unburnt carbon in ash (kgC/kgCoal)

The above formula makes an assumption that 30% of the nitrogen in the coal is oxidized to NO_2. Even if this can vary substantially, it only makes a minor change to the total oxidizing air required.

Now, it is known that boilers need to be operated with a certain amount of excess air to ensure complete combustion. This is indicated by the presence of oxygen in the flue gas exiting the boiler. The excess air, as a percentage of the stoichiometric air is calculated as:

$$EA_{A/H.fg.in} = \left[\frac{SAR + 1 - \%Ash}{SAR}\right]\left[\frac{\%_v O_{2.A/H.fg.in}}{\%_v O_{2.\text{air}} - \%_v O_{2.A/H.fg.in}}\right] \times 100\% \tag{3.2}$$

If the A/H is included inside the control volume, this excess air calculation would be carried out at the A/H flue gas outlet, rather than at the flue gas inlet which is shown in equation (3.2).

So the amount of air that enters the boiler is thus the stoichiometric air plus a certain percentage of excess air. The total humid air (HAR) supplied to the boiler can then be expressed per kilogram of coal, taking into account the specific humidity (ω) of the air.

$$HAR = (1+\omega).SAR\left(1 + EA_{A/H.fg.in}\right) \tag{3.3}$$

The total air inside the control volume is thus:

$$\dot{m}_{air.total} = HAR.\dot{m}_{coal} \tag{3.4}$$

The flue gas is the sum of the coal flow and the air flow. As mentioned, the flue gas contains ash particles as well as unburnt carbon, meaning that not all of the coal mass flow is considered to form part of the flue gas. Hence, the mass flow rate of flue gas can then be expressed per kilogram of coal:

$$\hat{m}_{fg} = (1 - \%Ash) - C' + HAR \tag{3.5}$$

There is also further information that can be gained from the mass balance, such as the flue gas composition, which is shown in the full calculations in Appendix B and is also required for the furnace exit temperature calculation.

b) <u>Energy balance</u>

Equations (3.4) and (3.5) provide equations for 2 of the parameters (i.e. air and flue gas mass flow rates) in terms of the 3rd (i.e. coal mass flow rate). The energy balance provides the 3rd equation which relates all 3 parameters.

The energy balance calculation carried out over the global boiler boundary is the core of the mass and energy balance, and requires careful consideration of all the energy inputs and outputs to the boundary.

If one considers the sketch in Figure 12, the energy inputs into the boundary are shown. In this context, energy inputs refer to energy entering INTO the boundary, and not inputs to the calculation model as such.

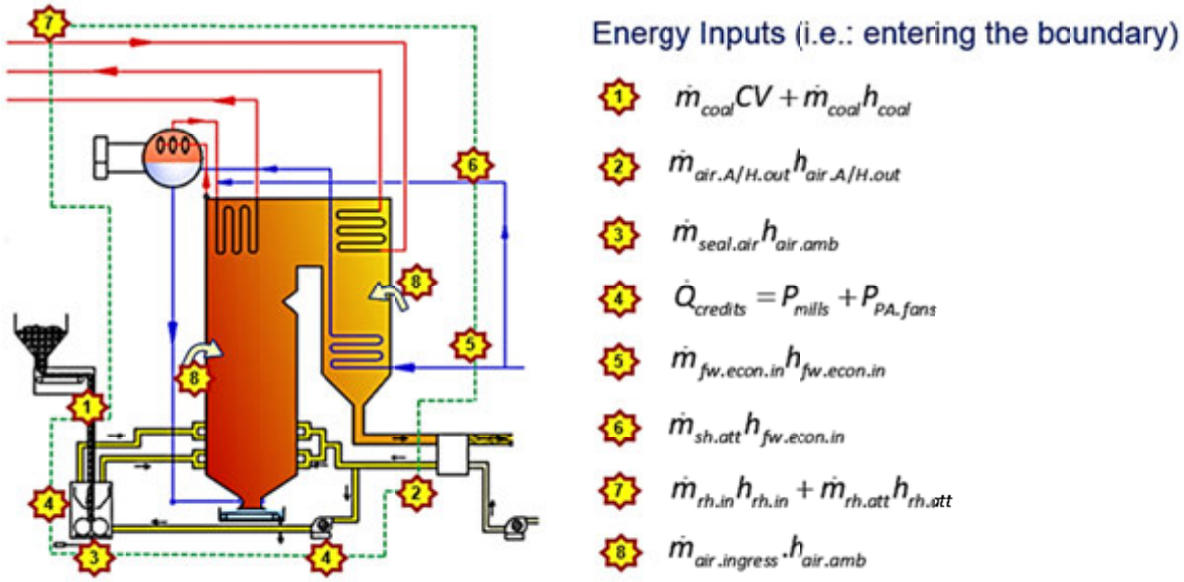

Figure 12: Boiler energy balance inputs

Each one can be looked at in a bit more detail:

1. Coal: Energy contained in the coal comes from the CV of coal and the enthalpy of coal. The enthalpy of the coal is expressed as $h_{coal} = \int_0^T C_p dT$ where the C_p of coal is taken as 1.38kJ/kgK. Of course the C_p of coal can vary with the coal quality, moisture content, etc.; however these variations are negligible in the context of the MEB.
2. Primary and secondary air: This refers to the energy of the air that goes to the boiler after being heated in the air heater. It includes the primary air and secondary air. As shown in Chapter 2, in some plants the primary air and secondary air may be heated in separate air heaters. In this case, the energy of both streams at the exit of the respective air heaters will have to be taken into account. *For the secondary boundary, this value would be at the air inlet to the A/H.*
3. Seal air: There is a small amount of energy from the air at ambient temperature being supplied directly to the mills in the form of seal air.

4. Electrical energy: The credits account for the power input of the motors driving the mills and the PA fans which are included inside the boundary, and are supplied in the form of electrical energy. This electrical energy is transferred to the coal and air directly in the mill and fans which are within the boundary. *In the case of the secondary boundary, if the A/H inlet temperature is not known, the FD fan power must also be included.*
5. Feedwater: The energy input is from feedwater entering the boiler.
6. Superheater attemporator: Depending on where the feedwater mass flow is measured, the energy of the attemporator water which taps off from the feed water line might have to be accounted for separately, as shown in Figure 12.
7. Reheater: If the plant has a reheater, there would also be energy input as a result of steam returning from the high pressure turbine entering the reheater, as well as from the reheater attemporator water entering the control volume.
8. Ingress air: While it cannot be exactly quantified where the ingress air enters the boiler, the BMEB is concerned with an overall amount of ingress air entering the boiler, accounted for as a percentage of *HAR*.

So the inputs can be expressed as:

$$E_{in} = \dot{m}_{coal}CV + \dot{m}_{coal}h_{coal} + \dot{m}_{air.A/H.out}h_{air.A/H.out} + \dot{m}_{seal.air}h_{air.amb} + \dot{Q}_{credits} + \dot{m}_{fw.econ.in}h_{fw.econ.in} + \ldots$$
$$\ldots\dot{m}_{sh.att}h_{sh.att} + \dot{m}_{rh.in}h_{rh.in} + \dot{m}_{rh.att}h_{rh.att} + \dot{m}_{air.ingress}.h_{air.amb} \quad (3.6)$$

The outputs consist of the energy recovered by steam and all of the losses, as shown in Figure 13. Again, outputs refer to energy exiting the boundary, not outputs of the model.

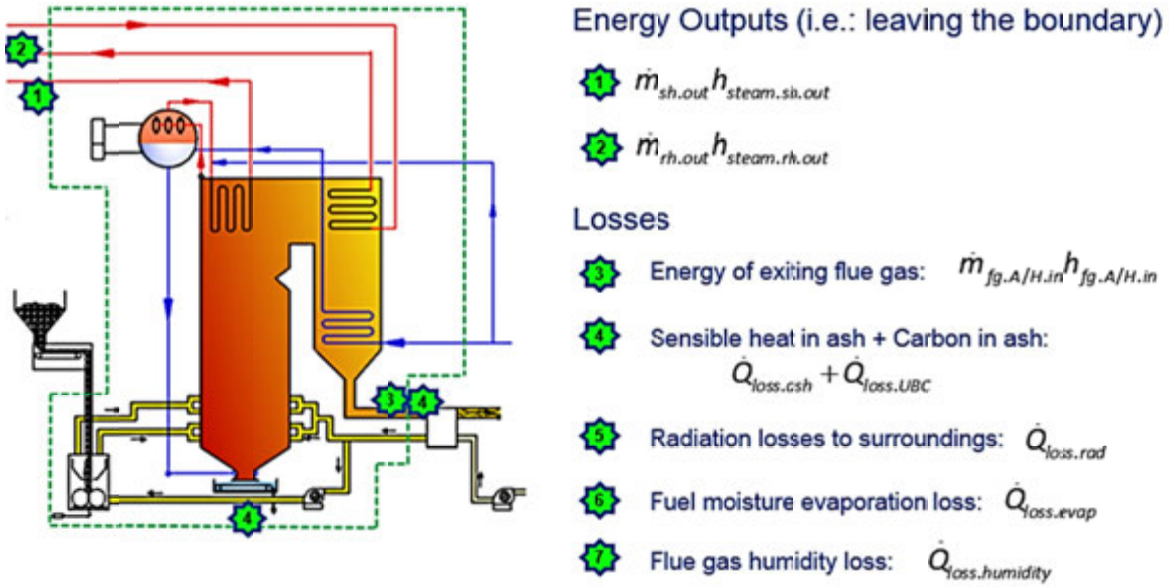

Figure 13: Boiler energy balance outputs

Looking at the outputs in more detail:

1. Superheater steam: The superheater outlet is considered as an energy output. The superheater outlet includes the superheater attemporator water tapped off from the feedwater line which exits the boiler as superheated steam.
2. Reheater steam: If the boiler contains a reheater, then the reheater outlet is an energy output. The reheater outlet steam also contains the reheater attemporator water.
3. Flue gas loss: This is the energy contained in the flue gas leaving the control volume. This quantity will depend on inclusion/exclusion of the A/H in the boundary *(Accordingly, it would be at either the air heater flue gas inlet or flue gas outlet).*
4. Ash losses: The loss associated with the ash is made up of 2 terms; the sensible heat lost and the unburnt carbon contained in the ash. These 2 terms are considered for both the fly ash and the bottom ash.
5. Radiation losses to surroundings: Even though the boilers are insulated, the insulation cannot be expected to be 100% efficient. This means that a certain amount of heat that is lost to the surroundings due to the temperature difference. The EN standard for boiler acceptance tests EN 12952-15 provides guidance of what this value should be estimated as. For a given boiler load capacity, a value can be estimated which is in the form of a percentage of the total heat input.
6. Fuel evaporation losses: During the coal drying process, the moisture in the coal experiences a phase change from liquid to steam, so the latent heat of vaporization is regarded as a loss since it cannot be utilised for heat transfer in the boiler.
7. Fuel humidity losses: If the coal CV used for the calculation is the higher heating value, then the fact that the outlet flue gas does not cool to a temperature low enough to condense the moisture results in that energy that would have been released during condensation being considered as a loss.

With all of the above taken into account, the outputs can be specified as:

$$E_{out} = \dot{m}_{sh.out} h_{steam.sh.out} + \dot{m}_{rh.out} h_{steam.rh.out} + \dot{m}_{fg.A/H.in} h_{fg.A/H.in} + \dot{Q}_{loss.ash} + \dot{Q}_{loss.UBC} + .\dot{Q}_{loss.rad} + \ldots \\ \ldots \dot{Q}_{loss.evap} \quad (3.7)$$

Equating the inputs to the outputs yields a fairly long equation that can be simplified slightly. The difference between the steam and water terms represents the total amount of energy recovered by the water/steam circuit, which is named $\dot{Q}_{out}$.

The air flow terms can be further broken down, since it is assumed that the amount of ingress air into the boiler is approximately a certain percentage of the total humid air.

$$\dot{m}_{air.total} = \dot{m}_{air.A/H.out} + \dot{m}_{air.ingress} + \dot{m}_{seal.air} \tag{3.8}$$

$$\therefore \dot{m}_{air.A/H.out} = \dot{m}_{air.total} - \%Air_{ing}\dot{m}_{air.total} - \dot{m}_{seal.air} \tag{3.9}$$

Using the mass balances done in the previous section, it is possible to write all of the mass flow rates of the air, ash and flue gas in the 2 above equations in terms of the mass flow rate of coal. All of the losses are also expressed in terms of the mass flow rate of coal. After some rearranging, the mass flow rate of coal can be expressed as:

$$\dot{m}_{coal} = \frac{\dot{Q}_{out} - \dot{Q}_{credits} - \dot{m}_{seal.air}h_{air.amb} + \dot{m}_{seal.air}h_{air.A/H.out}}{Denominator} \tag{3.10}$$

Where

$$\begin{aligned} Denominator = {} & CV(1 - C''' - Q_{insul.loss}) + h_{coal} + (HAR - HAR.\%Air_{ing})h_{air.A/H.out} \ldots \\ & \ldots + HAR.\%Air_{ing}.h_{air.amb} - \hat{m}_{fg}h_{fg.A/H.in} - (\%Ash).\%BA.h_{BA} - (\%Ash).\%FA.h_{FA.A/H.in} \ldots \\ & - \%H_2O.h_{H2O.vap} \end{aligned} \tag{3.11}$$

Once the coal flow rate is known, the total humid air and flue gas flow rates can also be calculated as:

$$\dot{m}_{fg.A/H.inlet} = \dot{m}_{coal}\hat{m}_{fg} \tag{3.12}$$

$$\dot{m}_{air.total} = \dot{m}_{coal}HAR \tag{3.13}$$

Thereafter, the air flow rates, specifically $\dot{m}_{air.A/H.out}$, can be calculated using equation (3.9).

At this point, it is pertinent to describe how this energy balance would differ in the case where the A/H is included INSIDE the control volume. As mentioned earlier, this would require the oxygen in flue gas measurement at the A/H flue gas outlet to be used to calculate the HAR and $\hat{m}_{fg}$. This new HAR value will be named as $HAR_{inc.leak}$ and includes all of the air from the FD fans including A/H leakage, seal air and ingress air. All of this air is assumed to be entering the control volume at ambient temperature. The power of the FD fan is also added to the credits to take into account the energy increase of the ambient air through the FD fans.

The HAR referred to in equation (3.11) must still also be calculated in order to quantify the air heater leakage in terms of the mass coal flow rate. Since the air heater leakage is simply the difference in the air flow at the air heater inlet and exit, the air heater leakage can be expressed as:

$$\dot{m}_{air.A/H.leak} = \dot{m}_{coal}(HAR_{inc.leak} - HAR) \tag{3.14}$$

Equations (3.10) and (3.11) must be adjusted accordingly for this alternate scenario.

$$Denominator = CV(1-C'''-Q_{insul.loss}) + h_{coal} + HAR_{inc.leak}h_{air.amb} - (HAR_{inc.leak} - HAR)h_{air.leak.out} \ldots$$
$$\ldots - \left[\hat{m}_{fg.A/H.out} - (HAR_{inc.leak} - HAR)\right]h_{fg.A/H.in} - (\%Ash).\%BA.h_{BA} - (\%Ash).\%FA.h_{FA.A/H.out} \ldots \quad (3.15)$$
$$\ldots - \%H_2O.h_{H2O.vap}$$

$$\dot{m}_{coal} = \frac{\dot{Q}_{out} - \dot{Q}_{credits}}{Denominator} \quad (3.16)$$

A point to take note of is that the leakage is assumed to leave the boiler with an enthalpy of air at the flue gas exit temperature.

Thereafter, as with the primary boundary, the desired flue gas and air flow rates can thus be calculated.

v. Model consistency verification

Before going further and deriving the furnace and backpass MEBs, the integrity of the calculations in the global boiler MEB were checked by some additional calculations of efficiency and by comparing the results with the existing Eskom MEB excel spreadsheet.

a) Calculation of efficiency

While not a direct objective of this methodology, the BMEB can be used to calculate the boiler efficiency. The efficiency can be calculated in 2 ways, namely the direct method, and the loss method.

Direct method:

$$\eta_{direct} = \frac{\dot{Q}_{out}}{\dot{Q}_{in} + \dot{Q}_{credits}} \quad (3.17)$$

$\dot{Q}_{out}$ is the "useful" energy recovered by the steam, and $\dot{Q}_{in}$ is the chemical energy of the coal expressed as its calorific value.

Losses Method:

$$\eta_{losses} = \frac{\dot{Q}_{in} + \dot{Q}_{credits} - Losses}{\dot{Q}_{in} + \dot{Q}_{credits}} = 1 - \frac{Losses}{\dot{Q}_{in} + \dot{Q}_{credits}} \quad (3.18)$$

For any given set of input data, if the energy balance equations are all logical, coherent and consistent, the efficiency calculated from equations (3.17) and (3.18) should be identical. It must be mentioned that this comparison of the 2 efficiency calculations is not a verification of the accuracy of the calculations, but rather serves as an integrity check of the model. An arbitrary set

of data was used to verify this. This can also be seen in the full detailed calculations in Appendix B which are for the case study which will be presented later.

b) Comparison with Eskom MEB model

The Eskom MEB model includes the air heater inside the control volume, therefore the secondary boundary model was used to perform a comparison with it. An arbitrary set of data was tested and the results checked. The table below shows test results obtained applying an arbitrary set of data to the excel spreadsheet and the Mathcad

Table 1: Comparison between Excel sheet and Mathcad models

Parameter	**Eskom Excel Sheet**	**Mathcad Incl. AH**	**% difference from Excel sheet**
Mass flow rate of coal (kg/s)	28.94	29.01	0.24%
Mass flow rate of air @ A/H air outlet (kg/s)	201.94	202.70	0.38%
Mass flow rate of flue gas @ A/H FG inlet (kg/s)	246.03	246.89	0.35%

The results in Table 1 are as expected. The Mathcad model with the air heater included correlates very closely with the Excel sheet, within 0.4%. This is to be expected since this secondary Mathcad model is essentially identical to the Excel model. The slight variations are attributed to:

- The Mathcad model uses linear interpolated enthalpy tables from Cengel and Boles [18] to determine enthalpies of air and flue gas. The Excel sheet uses specific heat capacity (C_p) table data from Rogers and Mayhew [19] which is then regressed to develop C_p polynomials, which when integrated gives the enthalpies.
- The Excel sheet has as an input, the A/H air inlet temperature, whereas the Mathcad document only has the ambient temperature as an input and includes FD fan power as a credit to account for any increase in the air temperature from ambient conditions to air heater inlet.
- Minor differences in constants applied, such as air composition, molecular weights, etc.

For the purposes of this Masters study, this slight difference is acceptable as it confirms the consistency of the calculations, but perhaps a future work should incorporate some study to reconcile the differences between the two to produce one consistent and completely validated tool to be used extensively in Eskom.

3.4. Furnace and Backpass MEB

The 3 main global boiler MEB outputs as obtained above, together with plant measurements and some carefully considered assumptions, make it possible to calculate the FET via either the furnace or the backpass sections. What is also important to note is that the methodology presented below can be utilised regardless of whether a global boiler MEB was done, provided that the required measurements of coal, air and flue gas flow rates are available. One should also take cognisance of the uncertainties of the plant measurements and factor it in to the results.

The rationale for calculating the FET from 2 different directions is that if the value calculated from both sides for a given set of data is identical, the coherence and integrity of the calculations can be confirmed.

3.4.1. Boundary selection

The boundaries for both the furnace and backpass calculations are depicted in Figure 14. The main consideration of the boundary selection is to have the furnace exit at the boundary, and extend the control volume in either direction of the furnace exit to a point where it is easiest to obtain input data.

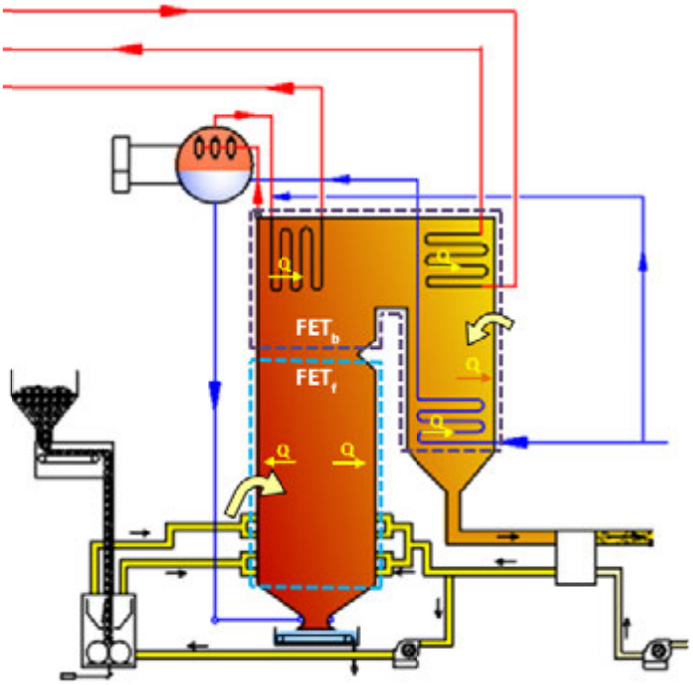

Figure 14: FET_f and FET_b boundaries

3.4.2. Input data and Assumptions

For the furnace and backpass MEBs, there are only two inputs required in addition to those used in the BMEB. The first is an estimation of energy transfer to the water walls in the furnace and backpass sections respectively. The second is the distribution of the ingress air between the furnace and backpass sections.

i. **Percentage of evaporation in furnace**

In the furnace section of the boiler, the only heat transfer occurring is from the flue gas to the furnace walls. On the gas side, the heat transfer to the walls results in a drop in temperature from the flame temperature (which can approach the adiabatic temperature in the burner region where the volatiles combust) to the furnace exit temperature. On the water/steam side within the membrane wall tubes, the heat transfer results in the temperature increasing from the economiser outlet temperature to the saturation temperature at boiler drum pressure for a drum type boiler. In the case of a once through boiler, the steam at the outlet of the evaporator can be slightly superheated at boiler full load. At full load in a supercritical boiler, the temperature of the supercritical fluid will continuously increase from the inlet of the water walls to the outlet without any “plateau” where phase change occurs in a sub-critical boiler.

In the water walls of a subcritical boiler, the water/steam conditions are only known at the inlet and outlet of the walls and thus only enable the determination of the total amount of heat transfer experienced by the walls. This means that the exact water/steam condition (specifically its enthalpy which is the parameter required) is not known in the water walls at the elevation corresponding to the furnace exit. This parameter obviously depends on global boiler operating conditions (e.g. load) as well as on combustion configuration (e.g. number of mills and burners in service). To estimate what percentage of the total heat transfer to the water walls is taken up in the furnace section under typical operating conditions requires some form of a boiler heat transfer model to be applied.

Every boiler in Eskom is being modelled using Dimbo, a boiler design code purchased by Eskom from a boiler manufacturer. So for this project, this Dimbo design code is used to determine the percentage of heat recovered in the furnace out of the total energy recovered by the water walls. Govindsamy elaborated on the use of Dimbo in detail [10]. A typical Dimbo model for the Eskom plant has the boiler evaporator wall broken up into convenient sections as shown in Figure 15.

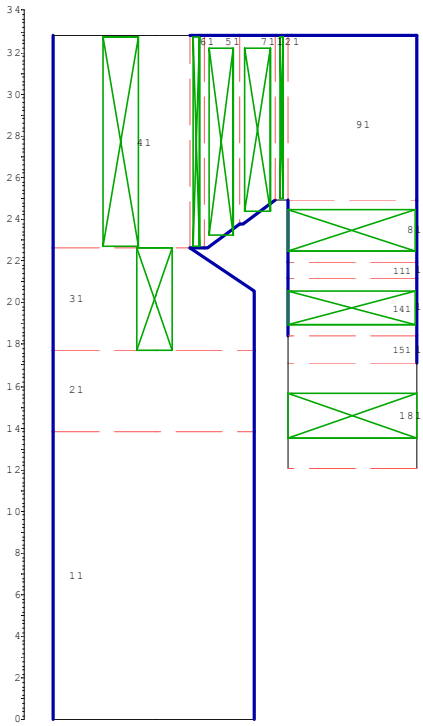

Figure 15: Dimbo model geometry

The Dimbo model provides values for the heat transfer take up by each of the sections. From Figure 15, it can be seen that the furnace section includes sections 11, 21 and 31. By comparing the heat transfer in those 3 sections to the total heat transfer in the water walls, the percentage evaporation in the furnace, labelled as α, is calculated.

Although in reality the furnace section does include the whole of section 31, for this calculation only half of section 31 is considered as part of the furnace, and the reason for this is to enable comparison with the direct method, which will become clear in the next chapter.

ii. Distribution of ingress air

In the global MEB, it was estimated that the ingress air accounts for a percentage, $\%Air_{ingress}$, of the total humid air entering the boiler. The assumption, if justified by supporting information, is a fair one and it is sufficient for the global balance since the entire boiler is inside the control volume. With the furnace and backpass mass and energy balances, there is a further complication. The question becomes: Where does this ingress air enter the boiler? One can imagine that quantifying all of the leaks in the boiler enclosure, while not impossible, would be extremely difficult. So for this analysis, the simplest case that 100% of the ingress air entering the boiler is in the furnace will be considered, and this parameter is varied to see the impact of this uncertainty on the result. Two new variables are introduced, namely $\%Ingress_{furnace}$ and $\%Ingress_{backpass}$.

3.4.3. Furnace MEB calculation method

The furnace MEB can be summarised as follows. The energy of the flue gas at the furnace exit is equal to the energy input to the furnace, minus heat transfer to the walls and the furnace losses. It is also anticipated that there is radiative transfer from the furnace to the backpass, $\dot{Q}_{rad.top}$, which will be ignored for the MEB at this stage and looked at independently as it requires a different approach.

$$\dot{m}_{fg.FE} h_{fg.FE} = E_{in} - \dot{Q}_{loss} - \dot{Q}_{walls} - \dot{Q}_{rad.top} \tag{3.19}$$

The $\dot{m}_{fg.FE}$ may not be the same as the flue gas flow rate calculated in the BMEB. Taking into account that some ingress air may only enter the flue gas downstream of the furnace exit:

$$\dot{m}_{fg.FE} = \dot{m}_{fg.AH.in} - \%Ingress_{backpass} \cdot \dot{m}_{air.ingress} \tag{3.20}$$

The energy inputs to the furnace are almost the same as for the BMEB except that it does not include the feedwater, and the ingress air in the furnace is now a percentage of ingress in the boiler. The water into the evaporator walls is accounted for in the $\dot{Q}_{walls}$ term.

$$\begin{aligned} E_{in} &= \dot{m}_{coal} CV + \dot{m}_{coal} h_{coal} + \dot{m}_{air.A/H.out} h_{air.A/H.out} + \dot{m}_{seal.air} h_{air.amb} + \dot{Q}_{credits} + \ldots \\ &\ldots \%Ingress_{furnace} \dot{m}_{air.ingress} . h_{air.amb} \end{aligned} \tag{3.21}$$

The heat transfer to the walls is calculated from the percentage of total evaporation that occurs in the furnace. The α value is as was defined in the preceding section 3.4.2.i.

$$\dot{Q}_{walls} = \alpha \times \dot{m}_{fw.econ.in} \left(h_{steam.drum} - h_{fw.econ.out} \right) \tag{3.22}$$

The losses are expressed as:

$$\dot{Q}_{loss} = \dot{Q}_{loss.ba} + \dot{Q}_{loss.fa} + \dot{Q}_{loss.UBC} + (2/3)\dot{Q}_{loss.rad} + \dot{Q}_{loss.evap} + \dot{Q}_{loss.humidity} \tag{3.23}$$

It must be noted that some of the losses are identical to the way in which they were calculated in the global BMEB. It is assumed that the heat lost to the environment from the BMEB is divided into 2 thirds for the furnace and 1 third for the backpass. It is a reasonable assumption given that the furnace is the hottest part of the boiler.

As with the BMEB, the losses due to sensible heat in ash are broken up into losses in bottom ash and fly ash. The fly ash sensible heat loss for the furnace section is calculated at the temperature of the fly ash at the furnace exit.

$$\dot{Q}_{loss.fa} = \dot{m}_{fa} h_{fa.FE} \tag{3.24}$$

It is assumed that the fly ash and flue gas at furnace exit are at the same temperature (i.e.: ash and flue gas are in thermodynamic equilibrium which is a reasonable assumption if combustion is complete at furnace exit as it normally should be), hence the fly ash temperature is actually the furnace exit temperature.

Therefore, by substituting equation (3.24) and the results from (3.20), (3.21), (3.22) and (3.23) into equation (3.19), the enthalpy and thus temperature of the flue gas (and fly ash) at furnace exit can be solved for iteratively.

3.4.4. Backpass MEB calculation method

The backpass MEB follows a similar methodology. In this case, however, the energy of the flue gas and fly ash at furnace exit are crossing INTO the boundary. There is also an energy input from the ingress air into the backpass section. Some of this energy is utilised for heat transfer to the water steam circuit, and some of it leaves the boiler in flue gas and fly ash at the boiler exit.

$$\dot{m}_{fg.FE}h_{fg.FE} + \dot{m}_{fa}h_{fa.FE} + \%Ingress_{backpass} \cdot \dot{m}_{air.ingress}h_{air.amb} = \dot{Q}_{heat.transfer} + \dot{Q}_{loss} \tag{3.25}$$

Again, the fly ash entering the boundary at the furnace exit is assumed to be at the same temperature as the flue gas.

There is heat transfer to the superheaters, reheaters, economsiers and the water walls.

$$\dot{Q}_{heat.transfer} = \dot{Q}_{superheaters} + \dot{Q}_{econ} + \dot{Q}_{walls.bp} \tag{3.26}$$

The energy to the water walls will be the (1-α) fraction of the total water walls heat transfer.

The only losses are the energy leaving the boundary in the flue gas and fly ash at the boiler exit as well as the remaining 1 third of the radiation losses. The rest of the losses from the furnace MEB are considered to be entering the backpass at the furnace exit and leaving at the air heater, and hence cancel out.

$$\dot{Q}_{loss} = \dot{Q}_{fg.AH.in} + \dot{Q}_{loss.fa} + (1/3)\dot{Q}_{loss.rad} \tag{3.27}$$

Once again, because equation (3.25) has 2 enthalpy functions (one for flue gas and one for fly ash) which are both a function of the variable of interest, the FET can be solved for iteratively.

3.5. Sensitivity Analysis and uncertainty propagation method

There are accepted methods for the evaluation of the systematic uncertainty/error propagated on a calculated result from the individual uncertainties of the input parameters. In this study, the words "error" and "uncertainty" are used interchangeably.

Consider a set of inputs (x_1, x_2,…, x_N) with uncertainties (u_{x1}, u_{x2},…, u_{xN}) respectively. If y is a function of these inputs, $y = f(x_1, x_2, \ldots, x_N)$, then the uncertainty of y is calculated as follows:

$$u_y = \sqrt{\left(\frac{\partial y}{\partial x_1}\right)^2 u_{x1}{}^2 + \left(\frac{\partial y}{\partial x_2}\right)^2 u_{x2}{}^2 + \left(\frac{\partial y}{\partial x_3}\right)^2 u_{x3}{}^2 + \ldots + \left(\frac{\partial y}{\partial x_N}\right)^2 u_{xN}{}^2} \tag{3.28}$$

The partial derivatives are approximated as follows:

$$\frac{\partial y}{\partial x_i} = \frac{y(x_i + u_{xi}) - y(x_i - u_{xi})}{2u_{xi}} \tag{3.29}$$

This can be done for any number of inputs and also any number of outputs.

These methods are described in greater detail in the Joint Committee for Guides in Metrology's Guide to the expression of uncertainty in measurement, JCGM 100:2008 [20].

A Microsoft Excel Visual Basic for Applications (VBA) programme was developed to perform this task. The programme allows the user to specify input data and their uncertainties into a Mathcad model and retrieve the desired outputs in Excel with the propagated uncertainties. Moreover, the programme is designed to be generic so that it can be applied to any Mathcad calculation model. More detail about the programme can be found Appendix C.

For the sensitivity analysis, the objective is to gain insight into which output parameters are sensitive to variations in the inputs. This is done by varying input parameters to the model independently, one at a time, and observing the impact on the outputs. Using the Excel program, the changes in an output variable as a result of independent changes in input variables are then ranked to determine the most sensitive parameters. In the case of the sensitivity analysis, a ± 1% variation is applied to each of the input parameters.

While the sensitivity analysis gives insight into how sensitive the outputs are to changes in the inputs, it does not account for what the actual uncertainties of the inputs are, which may be less or even more than ± 1%. So while an output may be very sensitive to a change in a certain input, in reality that input might be very accurately known and hence the potential for uncertainty in the output becomes very small. So for the uncertainty propagation study, the combined uncertainty of the outputs due to the propagation of uncertainties from all the inputs combined is calculated.

3.6. Case study MEB implementation

In order to use the MEB models to calculate furnace exit temperature as a comparison for the direct methods, a set of actual plant input data was required. The plant which was chosen shall be referred to henceforth as “Plant X”, and the unit used for this case study was unit 6. The reasons why Plant X was chosen is due to the large amount of combustion related work which was already undertaken within Eskom at this plant. It is also due to the fact that this plant was due to be retrofitted with new burners, so any testing done at this plant is also useful for other projects associated with the boiler combustion plant .

3.6.1. Plant measurements

A performance test programme was scheduled at Plant X prior to the installation of the new burners to establish a benchmark set of data for assessing the new burners. This performance test programme was used as an opportunity to collect the MEB data and to test the direct methods which are discussed in Chapter 4. The MEB data was collected with the plant operating at approximately full load in the region of 191-195MW. The plant operating parameters were maintained consistently during the 8 hour test period to ensure steady state conditions, which is a requirement for the MEB calculations. The average readings over a 1 hour period were used. The 1 hour period was chosen to coincide with the direct method testing period for comparative study. Figure 16 and Figure 17 depict how the operating data was maintained in a steady state condition for the entire performance test period. The period used for the MEB calculations is also shown.

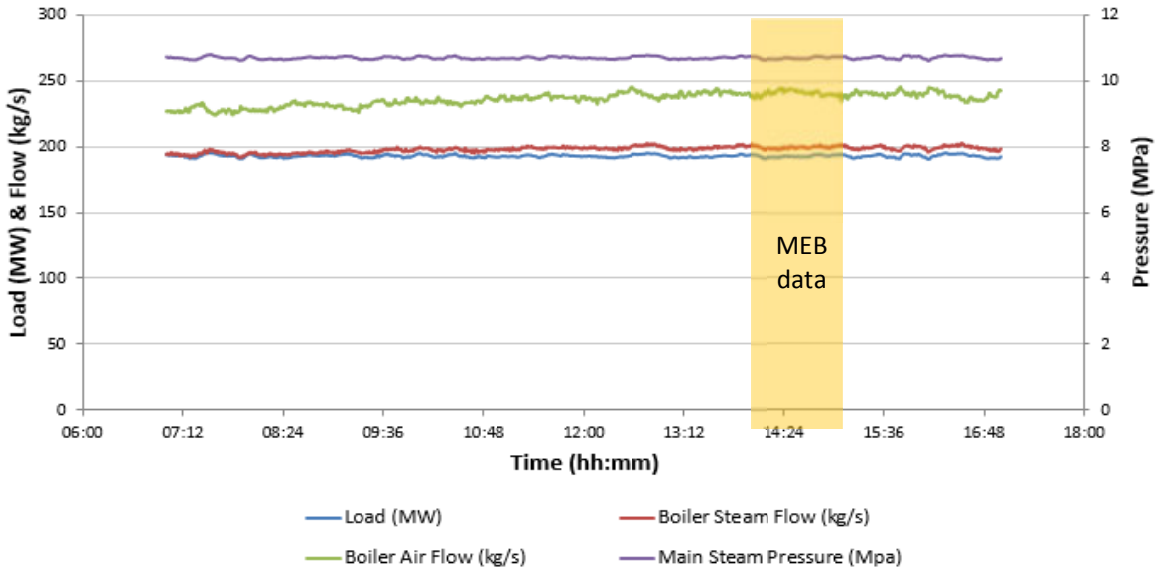

Figure 16: Plant X operating data for load, steam pressure, steam flow rate and air flow rate

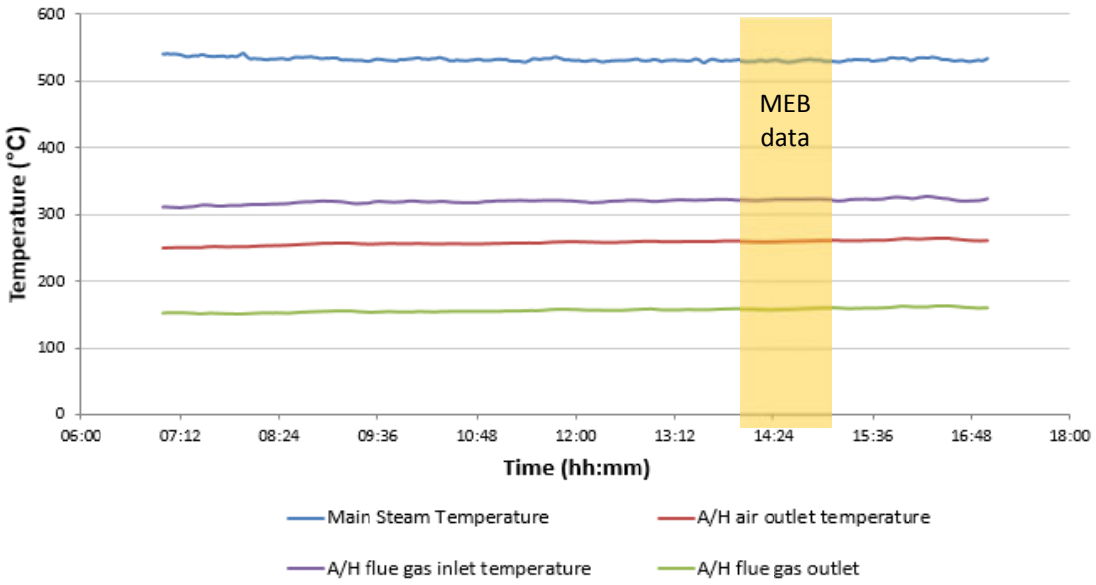

Figure 17: Plant X operating data for steam, air and flue gas temperatures

The list of plant measurements used for the BMEB is listed in Table 2 below:

Table 2: Test plant MEB measurements

Parameter	Description	Value	Unit	Source
p_{atm}	Atmospheric Pressure	83	kPa	Weather report
T_{atm}	Atmospheric Temperature	17	°C	Weather report
RH	Relative humidity	7	%	Weather report
T_{amb}	Ambient temperature inside boiler house	26	°C	Performance and Testing Total Air Flow Rate Report
$T_{air.A/H.out}$	Temperature of air at air heater exit	230	°C	DCS
$T_{fg.A/H.in}$	Temperature of flue gas at air heater inlet	322	°C	DCS
$T_{fg.A/H.out}$	Temperature of flue gas at air heater outlet	158	°C	DCS
$\%O_{2.A/H.fg.in}$	Volume percent oxygen in flue gas at air heater flue gas inlet	4.33	% v/v	DCS
$\%C_{fa}$	Carbon content in fly ash	3.416	% m/m	Ash Analysis Report
$\%C_{ba}$	Carbon content in bottom ash	3.416	% m/m	Assumed based on Ash Analysis Report of fly ash
$\dot{m}_{fw.econ.in}$	Mass flow rate of feed water	185.8	kg/s	DCS
p_{fw}	Pressure of feed water	15.71	MPa	DCS
$T_{fw.econ.in}$	Temperature of feedwater at economiser inlet	181.74	°C	DCS
$T_{fw.econ.out}$	Temperature of feedwater at economiser outlet	284.3	°C	DCS
$p_{steam.drum}$	Pressure of steam/water inside drum	11.43	MPa	DCS

Parameter	Description	Value	Unit	Source
$T_{steam.sh.out}$	Temperature of steam at final superheater outlet	534.0	°C	DCS
$p_{steam.sh.out}$	Pressure of steam at final superheater outlet	10.68	MPa	DCS
$\dot{m}_{sh.att}$	Mass flow rate of attemporator spray water	13.3	kg/s	DCS
$p_{sh.att}$	Pressure of attemporator spray water	15.71	MPa	DCS
$T_{sh.att}$	Temperature of attemporator spray water	181.74	°C	DCS
P_{mills}	Power to mills	831.6	kW	Operating Technical Specification Boiler Plant
$P_{PA.fans}$	Power to PA fans	1194.6	kW	Operating Technical Specification Boiler Plant
$P_{seal.fans}$	Power to mill seal air fans	37.58	kW	Operating Technical Specification Boiler Plant
$V'_{seal.air}$	Volumetric flow rate of seal air	1.035	m^3/s	Operating Technical Specification Boiler Plant
α	Percentage of evaporation in furnace control volume	68	%	Dimbo model calculation

In addition to the measured parameters and those sourced from technical specifications, a few assumptions need to be made.

Table 3: MEB Assumptions

Parameter	Description	Value	Unit	Source
$\%FA$	Percentage of fly ash in total ash	90	%	Assumed
$T_{BA.exit}$	Temperature of bottom ash	800	°C	Assumed
$Q_{insul.loss}$	Percentage of input energy to the boiler which is lost via radiation to the environment	0.8	%	EN 12952-15 [15]
$\%Air_{ing}$	Percentage of the air in the control volume which is made up by ingress air	10	%	Plant X Report [17]
$\%Ingress_{furnace}$	Percentage of ingress air that enters the furnace	100	%	Assumed for first calculation

3.6.2. Coal analysis

The coal analysis was carried out by Eskom's Research Technology & Development division. Coal samples were taken by Plant X Performance and Testing (P&T) personnel. The coal analysis data was provided by the laboratory on an air dried basis. The carbon content is iteratively adjusted until the laboratory measured CV matches the calculated CV. The oxygen content was calculated by difference. The resulting coal analysis used in the MEB calculations is shown in Table 4.

Table 4: Final Coal Analysis

Component	Value	Unit
Calorific Value (HHV)	19132.61	kJ/kg
Inherent Moisture	2.3	%
Ash	31.87	%
Carbon	47.27	%
Hydrogen	2.95	%
Oxygen	8.55	%
Nitrogen	1.07	%
Sulphur	0.99	%
Surface Moisture (As received)	5	%
Total	100	%

3.7. MEB Results and Discussion

The results of the MEB calculations for the Plant X test case are presented in this section, and put into context by further analysis and discussion.

3.7.1. Main results

The main results of the boiler MEB using the inputs listed in Table 2, Table 3, and Table 4, are listed below in Table 5.

Table 5: Main results of Plant X MEB calculations

Description	Symbol	Value	Unit
Mass flow rate of coal	$\dot{m}_{coal}$	30.55	kg/s
Mass flow rate of air at A/H outlet	$\dot{m}_{air.AH.out}$	209.12	kg/s
Mass flow rate of flue gas at A/H inlet	$\dot{m}_{fg.AH.in}$	253.94	kg/s
Efficiency (direct method)	η_{direct}	90.902	%
Efficiency (loss method)	η_{losses}	90.902	%
Furnace exit temperature (furnace MEB)	FET_f	1400.7	°C
Furnace exit temperature (backpass MEB)	FET_b	1400.7	°C

These main results can be put into context by some further analysis which follows.

3.7.2. Comparison between global MEB output and traverse flow rate measurements

Using actual data and measurements, one of the key assumptions can be tested for consistency with normal plant operation. It is assumed that ingress air accounts for 10% of the total air flow inside the boiler control volume [17].

As mentioned earlier, the MEB data was collected as part of a broader performance testing programme. One of the other measurements taken was the measurement of total air flow into the FD fans which represents the air flow into the air heater. This was taken by an external contractor and the results were made available. The test involved traverse measurements of air velocity and temperature across the ducts at the inlet side of the FD fan to determine the total air flow.

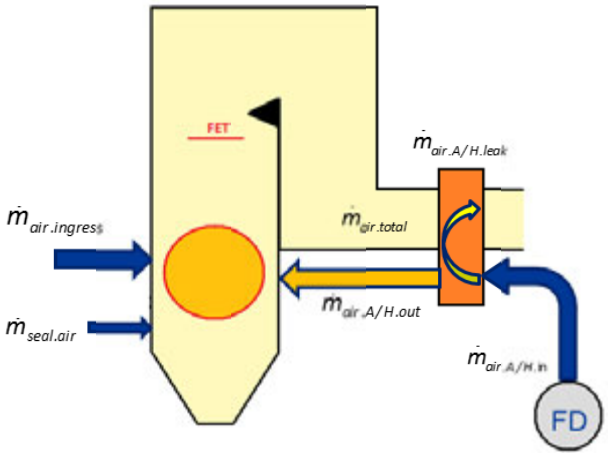

Figure 18: Boiler air flow schematic

Based on the traverse measurements, $\dot{m}_{air.A/H.in} = 242.5\,kg/s$.

From MEB, for 10% ingress air, using equation (3.9): $\dot{m}_{air.A/H.out} = 209.12\,kg/s$

However, from Figure 18**:**

$$\dot{m}_{air.A/H.leak} = \dot{m}_{air.AH.in} - \dot{m}_{air.A/H.out} \tag{3.30}$$

$$\Rightarrow \dot{m}_{air.A/H.leak} = 242.5 - 209.12 = 33.38\,kg/s \approx 13.8\%\ of\ \dot{m}_{air.A/H.in} \tag{3.31}$$

Thus, the assumption of 10% ingress air implies an air heater leakage of 13.8% of air heater inlet air flow which is consistent with the typical air heater leakages mentioned in Chapter 2.

3.7.3. The impact of ingress air distribution

The above calculation shows that from a global perspective, the total amount of ingress air seems to be a fair assumption. The second aspect of the ingress air that is assumed is the distribution of it between the furnace and the backpass, which are inputs to the FMEB and BPMEB respectively. To determine the impact of this assumption, the calculations were performed for a series of ingress air distribution scenarios. Table 6 shows how the calculated FET varies for these different scenarios.

Table 6: Impact of ingress air distribution on calculated FET

% of ingress air in furnace	**% of ingress in backpass**	**FET (°C)**
100%	0%	1400.7
75%	25%	1428.8
50%	50%	1458.2
25%	75%	1488.9
0%	100%	1521.0

The results in Table 6 show that the FET varies within a range of approximately ±60°C (i.e. from 1458.2°C for a 50% distribution between furnace and backpass, to 1400.7°C on the lower limit and 1521°C at the upper limit). This equates to ±4% uncertainty. This is significant, considering that this is the uncertainty caused by varying just one input parameter. It thus becomes evident that the unknown of ingress air, due to a lack of sufficient measurements or equations to solve for it results in a wide band of uncertainty on the final calculated furnace exit temperature. For simplicity sake in establishing a baseline for analysing the effects of all of the other input parameters, the FET calculation and all of the subsequent error propagation study presented hereafter is done with 100% of ingress air in the furnace, and the the overall amount of ingress air is varied, since the impact of the distribution on the FET has already been covered in this section

However, with the available information, there is no reason why one should gravitate towards any of the scenarios mentioned in Table 6. It is, however, very unlikely that the temperature could be as high as 1500°C. It must also be considered that there is also possibly a radiation component from the furnace to the backpass that is not accounted for by the MEB method which would reduce the FET. This will be looked at separately in section 3.8. Perhaps, the use of the direct methods to determine FET may also provide some insight as to which ingress air distribution is most likely in this case study. It should also be noted that in the subsequent sensitivity and error propagation studies, it.

3.7.4. Sensitivity Analysis and Error Propagation

When one looks at the impact that the ingress air parameter makes on the final calculated FET, it becomes only logical that the impact of variations/uncertainties of all of the parameters are assessed as well. Using the programme described in section 3.5, sensitivity analysis and uncertainty propagation is calculated for the test case.

The data used for these analyses is listed in Table 7. Each input is assigned a number shown in column 1. The values used are the input values used for the main calculations. For the sensitivity analysis, all of the inputs are varied by 1% of the value. For the uncertainty propagation, the last column on the right gives the percentage uncertainty for each input. These uncertainties are estimated considering both the expected accuracy of the measurement instrumentation as well as the variation of the measured parameters from the recorded test data from right to left and over time.

A note on percentage uncertainty:

For inputs which have percentage as the unit input value, the uncertainty is still given as a percentage of the input value. For example, the uncertainty for input x1, *%C*, is $\pm 0.0125 \times 47.27$, and not ± 1.25. It means that the last column of Table 7 needs to be multiplied by the value of the parameter to produce the uncertainty in the units of the parameter.

The outputs considered are the coal flow rate, the air flowrate, the flue gas flowrate, and the furnace exit temperature.

Table 7: Input values for MEB sensitivity analysis and uncertainty propagation study

Input number	**Input**	**Value**	**Unit**	**Sensitivity Analysis (% Variation)**	**Uncertainty Propagation Study (% Uncertainty)**
x1	*%C*	47.27	% m/m	1	1.25
x2	*%H*	2.95	% m/m	1	3.51
x3	*%N*	1.07	% m/m	1	0.66
x4	*%S*	0.99	% m/m	1	4.5
x5	*%H2O*	7.3	% m/m	1	4.5
x6	*%Ash*	31.87	% m/m	1	1.38
x7	*CV*	19123.77	kJ/kg	1	0.8
x8	P_{atm}	83	kPa	1	1
x9	T_{atm}	17	°C	1	10
x10	*RH*	7	% m/m	1	10
x11	T_{amb}	26	°C	1	10

Input number	Input	Value	Unit	Sensitivity Analysis (% Variation)	Uncertainty Propagation Study (% Uncertainty)
x12	$\%O_{2.A/H.fg.inlet}$	4.33	% v/v	1	10
x13	$\%O_{2.A/H.fg.inlet}$	5	% v/v	1	10
x14	$T_{fg.A/H.inlet}$	322	°C	1	3
x15	$T_{fg.A/H.outlet}$	158	°C	1	2.83
x16	$T_{air.A/H.outlet}$	230	°C	1	4
x17	$\%Air_{ingress}$	10	% m/m	1	50
x18	$\%C_{fa}$	3.416	% m/m	1	10
x19	$\%C_{ba}$	3.416	% m/m	1	10
x20	$\%FA$	90	%	1	10
x21	$T_{BA.exit}$	800	°C	1	15
x22	$\dot{m}_{fw.econ.in}$	185.85	kg/s	1	2
x23	P_{fw}	15.71	MPa	1	1
x24	$T_{fw.econ.in}$	181.7	°C	1	1
x25	$T_{fw.econ.out}$	284.2	°C	1	1
x26	$P_{steam.drum}$	11.43	MPa	1	1
x27	$T_{steam.sh.out}$	534.0	°C	1	0.375
x28	$P_{steam.sh.out}$	10.68	MPa	1	1
x29	$\dot{m}_{sh.att}$	13.3	kg/s	1	1
x30	$P_{sh.att}$	15.71	MPa	1	1
x31	$T_{sh.att}$	181.7	°C	1	1
x32	$Q_{insul.loss}$	0.8	%	1	50
x33	P_{mills}	831.6	kW	1	1
x34	$P_{pa.fans}$	1194.6	kW	1	1
x35	$P_{seal\ fans}$	37.583	kW	1	10
x36	$V'_{seal.air}$	1.035	m^3/s	1	10
x37	α	68	%	1	10

For each output, both a sensitivity analysis graph and an uncertainty propagation graph are presented. The results graphs focus on the top 10 most influential inputs on each output parameter. For both the sensitivity analysis and the uncertainty propagation graphs, the blue bars represent the absolute change in the output value if only that input is varied by the percentage listed in column 5 and column 6 of Table 7 respectively. On the uncertainty propagation graphs,

the top right hand corner of the graphs also gives the combined uncertainty propagated on the output as a result of the individual uncertainties of the inputs.

i. Coal Mass Flow Rate

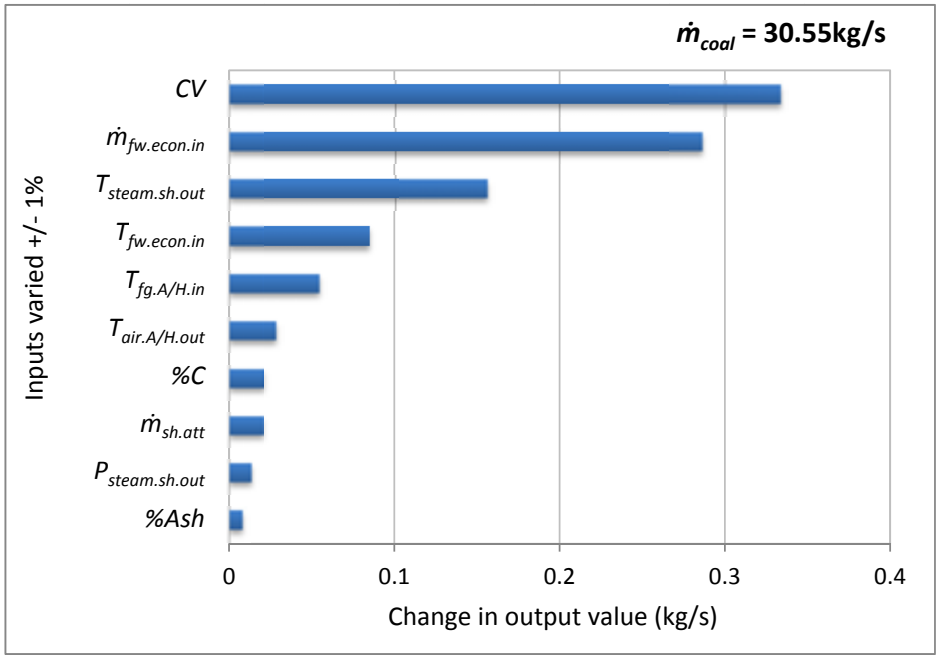

Figure 19: Coal mass flow rate sensitivity analysis

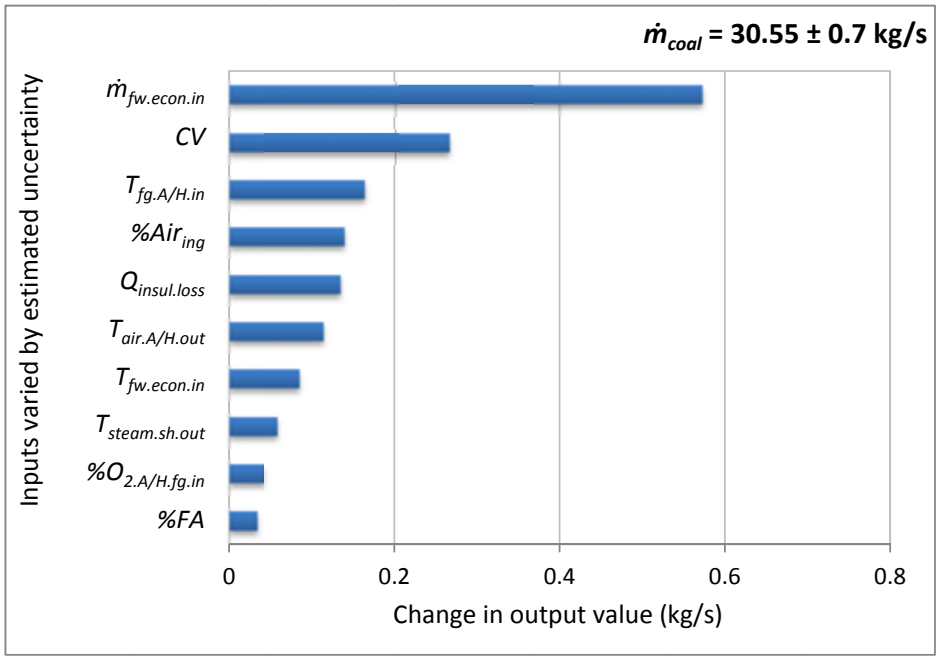

Figure 20: Uncertainty propagation on coal mass flow rate

ii. Air Mass Flow Rate

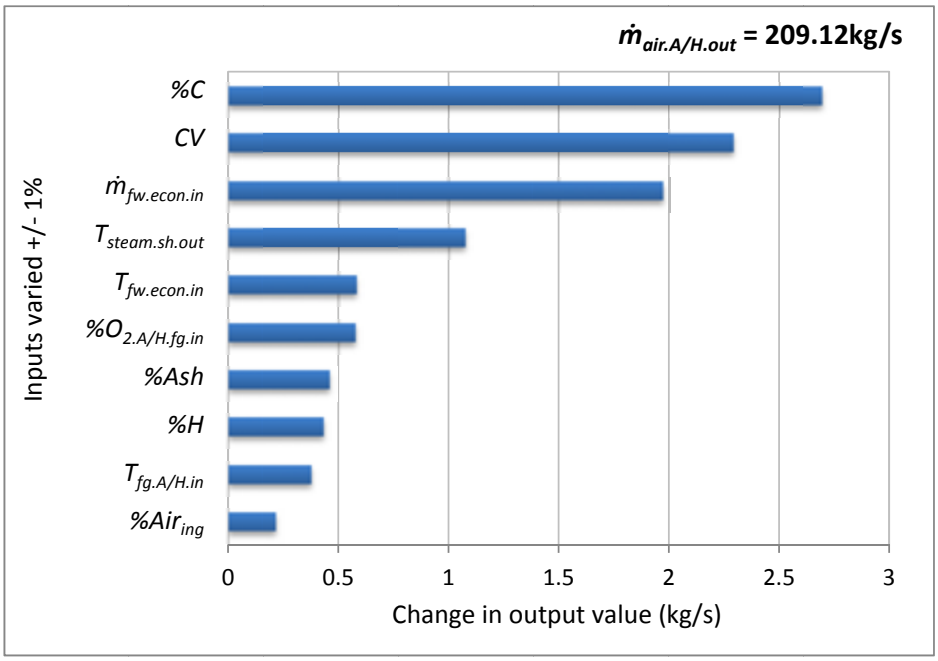

Figure 21: Air mass flow rate sensitivity analysis

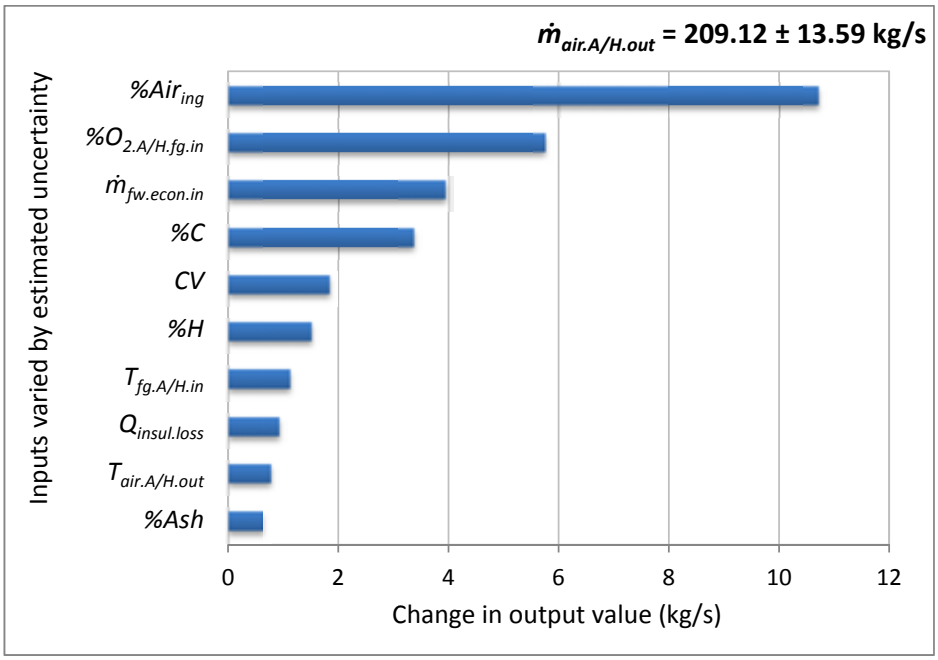

Figure 22: Uncertainty propagation on air mass flow rate

iii. Flue Gas Mass Flow Rate

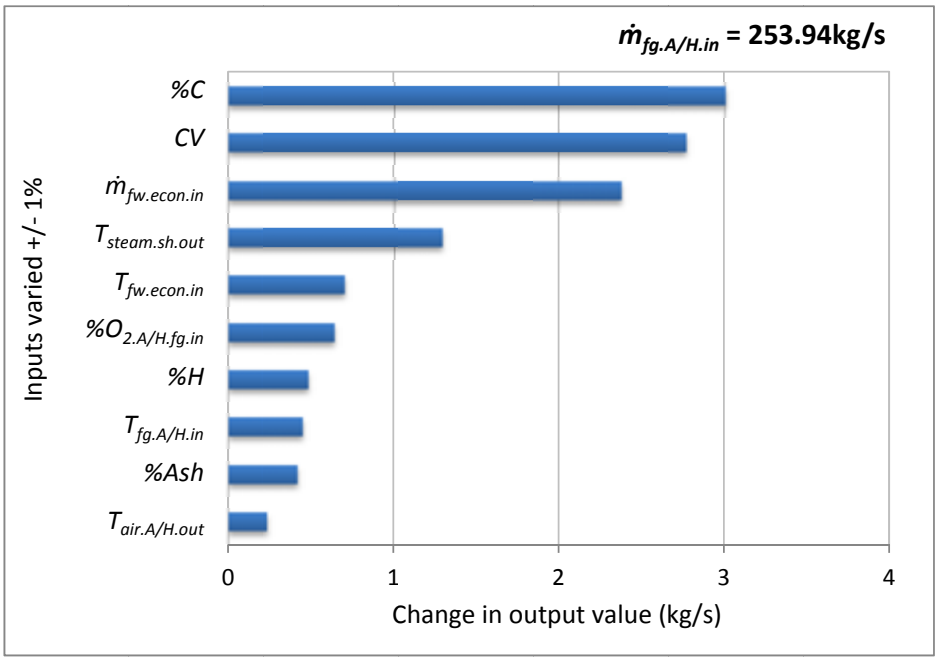

Figure 23: Flue gas mass flow rate sensitivity analysis

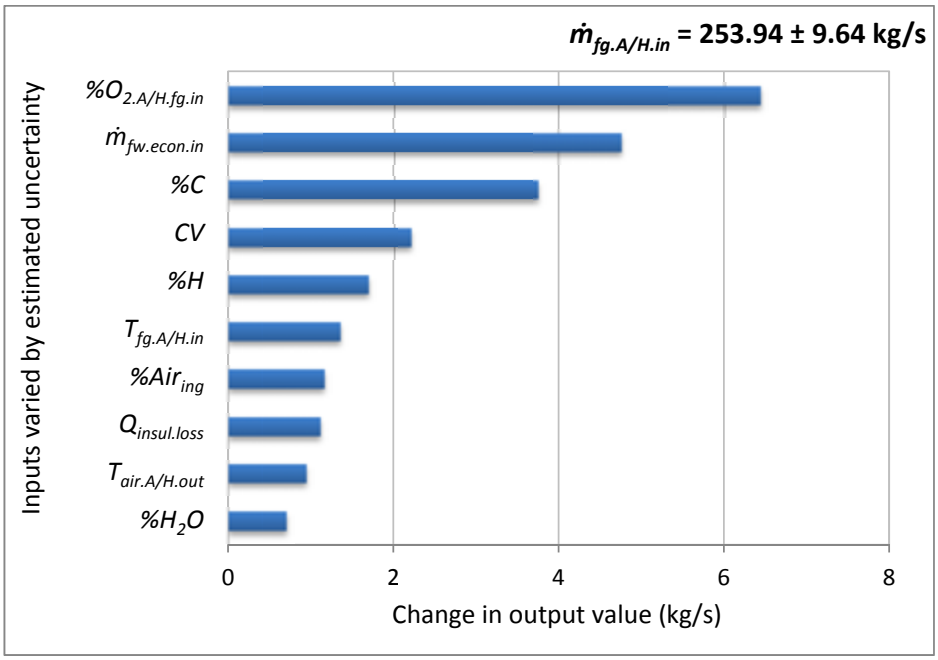

Figure 24: Uncertainty propagation on flue gas mass flow rate

iv. Furnace Exit Temperature

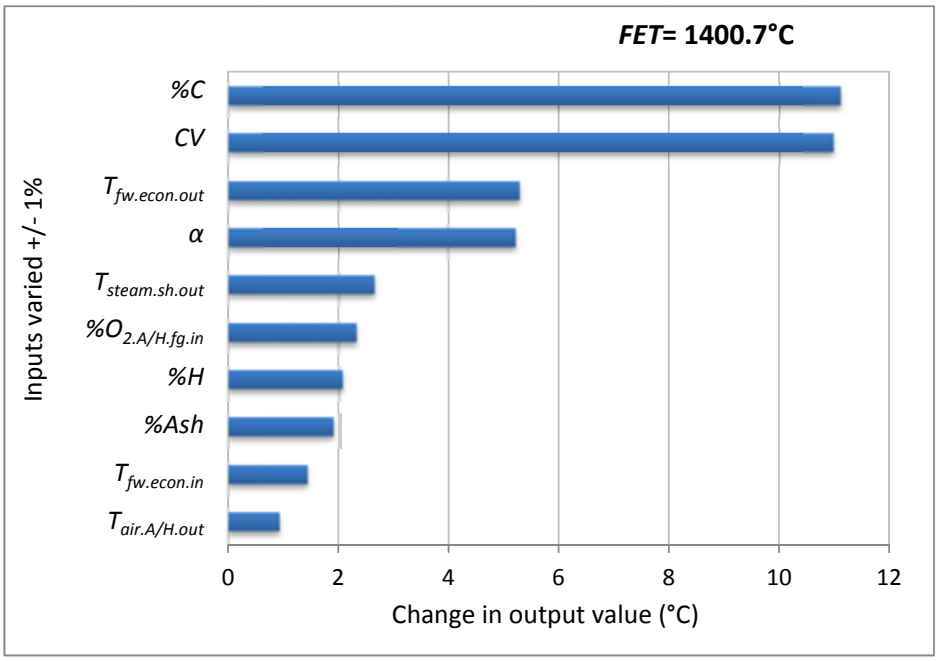

Figure 25: FET sensitivity analysis

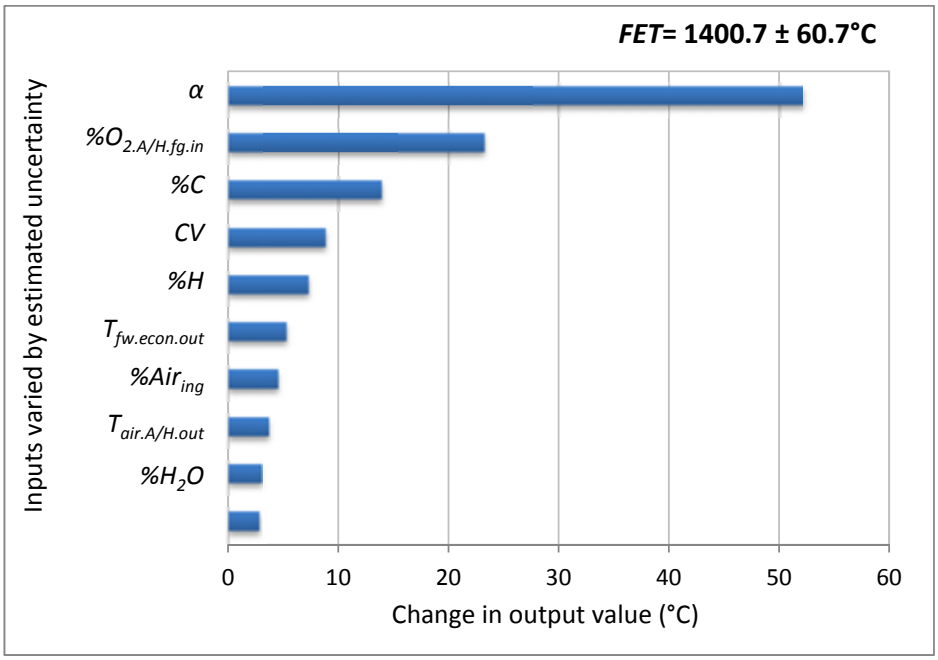

Figure 26: Uncertainty propagation on FET

3.7.5. Discussion of MEB Results

i. Main results

The main results from both the BMEB and the FET calculated from the FMEB (FET_f) and BPMEB (FET_b) are given in Table 5. When these BMEB results were further analysed in conjunction with traverse air flow measurements, it implies an air heater leakage of 13.8%, which is consistent with typical air heater leakage expectations.

The main results also illustrate 2 concepts which relate to the consistency of the calculation models. The efficiency is calculated using both the direct method and the losses method. Both methods produce the same value of 90.9%. As was mentioned previously, this indicates consistency in the BMEB calculations.

The FET_f and FET_b were both calculated as 1400.7°C. This same value calculated from both directions of the furnace exit (i.e. FMEB and BPMEB) is another form of verification for these calculations. It must also be noted, that this value is for the case where all of the ingress air is assumed to enter the boiler in the furnace section. Varying the distribution of the ingress air between the furnace and the backpass has a significant impact on the calculated FET. The difficulty in measuring or estimating this distribution is a shortcoming of the FMEB and BPMEB method. This is particularly significant for boilers with large amounts of ingress air such as the older boiler design technologies without tight furnace membrane walls or the 2-pass boilers more prone to ingress air in the boiler inter-pass ceiling.

The calculated FET is notably quite high, particularly if compared with the furnace exit temperature quoted in the Plant X C-Schedules, which is 1166°C. However, this calculated value may be overestimated by not accounting for some radiation aspects, which will be discussed in section 3.8. Also, as mentioned before, the actual point referred to as FET for this case study is a bit lower in the furnace where it would be slightly hotter than what is typically referred to as FET. This was mentioned at the outset, as a deliberate choice to be in line with the level used for direct method testing, which will be seen in Chapter 4.

ii. Sensitivity and uncertainty propagation

The results for the sensitivity of the intermediate outputs (i.e. the BMEB flow rates) are given in Figure 19, Figure 21 and Figure 23, for the 1% variation of the inputs. In all 3 cases, the most sensitive parameter does not have more than a ±1.2% effect on the output.

Considering then the effect of the realistic uncertainties of the inputs, the uncertainty propagation on the intermediate outputs is shown in Figure 20, Figure 22 and Figure 24 respectively. For these

results, the highest combined uncertainty is on the air flow rate shown on Figure 22, which is calculated to within ± 13.6 kg/s (≈6.5%). It is not surprising that of the 3 intermediate outputs, the highest uncertainty is found on the air flow rate, as the air flow rate is largely dependent on the major unknown of ingress air.

On the furnace exit temperature, which is the main focus of this study, the sensitivity to the inputs is shown on Figure 25. It can be seen from the figure that the FET is most sensitive to the CV of the coal. The 1% variation of the CV generates 11˚C (<1%) impact on the FET. So even in the case of the FET, it is not particularly very sensitive to any individual parameter. However, this does not mean that the final uncertainty on the calculated result is also low.

The uncertainty propagation of the FET is shown on Figure 26. It can be seen on the figure that the largest uncertainty is propagated from the α value. The α value was specified to have a 10% uncertainty, due to the fact that it was estimated from Eskom Dimbo model results, which itself can be influenced by a number of factors. As a result, the combined uncertainty on the FET is ±60.7°C. At first glance this seems like a significant number, but it should be considered that it only equates to an error of ± 4.34%. Further improvement in the estimation of α could reduce this value.

iii. Boundary selection revisited

In section 3.3.1, the boundary selection for the BMEB was discussed from a practical perspective based on the example of how the inclusion and exclusion of the A/H can affect a calculated result. Now that the uncertainty propagation methodology has been introduced, this boundary selection idea can be re-visited from this perspective.

In order to specifically compare the uncertainties, it is important that both the primary and secondary models produce the same calculated results. The calculated results for the primary boundary model can be used as has been presented thus far. The secondary boundary requires additional input data at the flue gas outlet and air inlet to the A/H. Now, unless all of the measurements around the air heater are 100% accurate such that A/H leakage calculated from both an O_2 mass balance and an energy balance across the A/H is equal, these 2 models will never produce identical results. Therefore, the data surrounding the A/H was reconciled as follows.

A measurement of oxygen of flue gas at air heater outlet was not available and was assumed to be 5.2%, based on Plant X C-Schedules. This was used to calculate a certain A/H leakage. Using this calculated leakage and the calculated flow rates from the primary boundary model; the A/H flue gas exit temperature was reconciled by a mass and energy balance across the A/H. All of the other

input data and their uncertainties were the same as was used for the case study on Plant X. The uncertainty propagation results are shown below in Table 8.

Table 8: Uncertainty propagation comparison between MEB models with and without the A/H

Output	**Results from model including air heater (kg/s)**	**Results from model excluding Air Heater (kg/s)**
$\dot{m}_{coal}$	30.55 +/- 0.67	30.55 +/- 0.70
$\dot{m}_{air.A/H.out}$	209.12 +/- 9.02	209.12 +/- 13.59
$\dot{m}_{fg.A/H.in}$	253.94 +/- 9.29	253.94 +/- 9.64

It can be seen from the table that the accuracy ranges of the 2 BMEB models are very similar. Thus the choice of boundary does not have any major ramifications from a pure uncertainty propagation perspective. Perhaps above all and in a more general sense, any calculation should be done in a way that most easily achieves the objective. The main objective of the Eskom MEB spreadsheet is to calculate the overall global air, coal and flue gas flow entering and leaving the plant to serve as a tool to verify plant measurements. For that application it is probably better to include the air heater.

In the case of calculating the furnace exit temperature, however, the flow rates required for the calculation are the air and flue gas flow rates in the boiler itself, so it makes sense to simplify the boundary to calculate the parameters of interest. The inclusion of the air heater adds an additional level of complexity that is simply not required for the calculation of FET, so provided that the required measurements are available, it is proposed that the primary boundary is used if the objective is to calculate FET.

3.8. Radiation from furnace to convective pass

Before concluding the chapter on the indirect methods, there is one more aspect to consider. Although no actual radiation heat transfer theory is used in the MEB calculations, the energy transfer to the water in the furnace walls calculated in the FMEB by equation (3.22) is effectively made up predominantly of radiative heat transfer from the fireball to the furnace walls. This calculation, however, only takes into account the radiation to the section of the water walls that is contained within the FMEB control volume, specified by α. It is, however, clear that there is radiative heat transfer FROM the furnace TO the heat transfer surfaces downstream of the furnace exit.

As a result, the MEB presented in the previous section needs to account for this radiation heat transfer to calculate the FET. The problem is depicted graphically below.

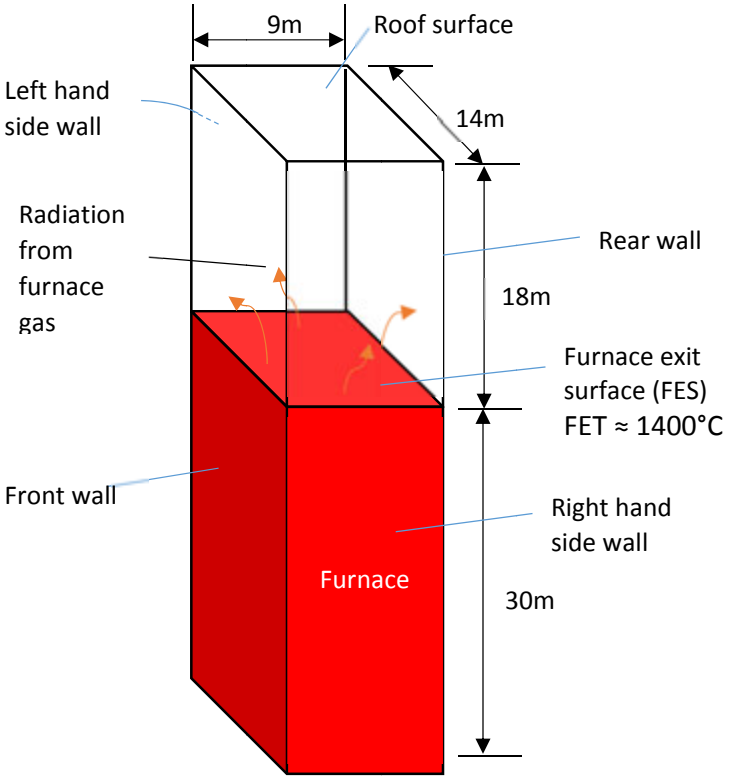

Figure 27: Graphical representation of problem showing dimensions of Plant X boiler

i. Analysis Methodology

A thorough detailed study of the theory of radiative heat transfer is beyond the scope of this study, and hence will not be done here. However, there are already existing models to calculate radiation in boilers, as was described by Monnaemang [12]. The Monnaemang model is based on the zonal method introduced by Hottel and Cohen [11], and is utilised hereafter.

The analysis consists of applying the zonal method, not to the furnace for which it has been primarily developed, but rather to the "cavity" above the furnace, shown by the transparent block in Figure 27. The geometry of the cavity is simplified here to be an enclosure containing no superheaters or platen tubes. All faces of the enclosure are considered to be surfaces operating at uniform temperatures and emissivities, and these form the boundary conditions for the model.

The cavity is discretized into gas volumes and surfaces (an example of which is shown in Figure 28). For every surface-to-surface, surface-to-volume, and volume-to-volume pair, direct exchange

areas are calculated. The radiation exchange between every surface/volume with every single other surface/volume is thus calculated, and the net radiative heat transfer to/from all surfaces and volumes can then be determined. For this analysis, the objective is to determine the total heat transfer from what will be referred to as the furnace exit surface (FES). This refers to the bottom surface of the enclosure, and would thus be determined as the sum of the net radiative heat transfer from all the discretized bottom surfaces of the enclosure.

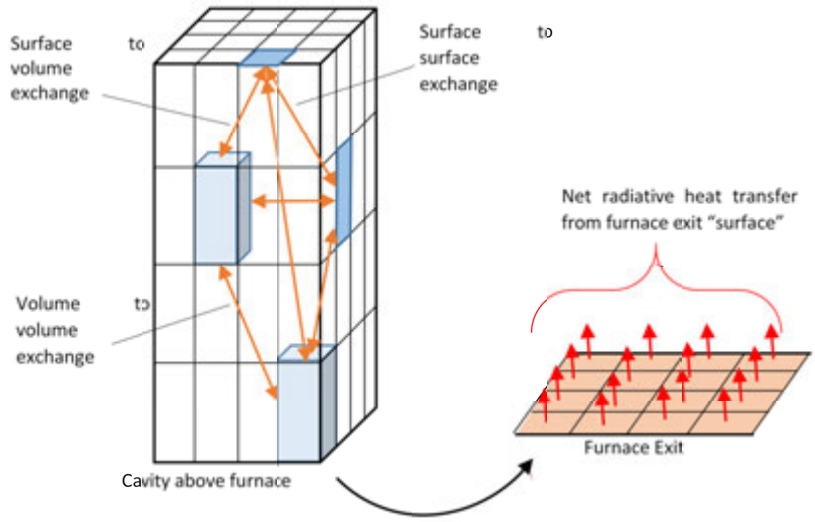

Figure 28: Graphical representation of the zonal method showing surfaces and volumes

The water walls make up all the sides of the enclosure and are assumed to be at a temperature of 350°C. The roof of the enclosure is also considered as a surface though it is not a water cooled wall, therefore its temperature shall be estimated to be in the range of the flue gas temperature in the superheater region and the effect of this estimation will also be investigated. These 5 surfaces are assumed to operate at emissivity of 0.7 which is typical in boilers.

The furnace section itself (red block in Figure 27) is not part of the analysis. However, the furnace exit is, and it is considered to be a surface with uniform temperature and emissivity, although in truth it is actually a gas particle mixture. Its temperature is initially the FET calculated from the MEBs, and thereafter iterated between the MEB and the zonal model, with the heat transfer from the zonal model being included as an energy loss to the FMEB. The emissivity of the FES, since it is not physically a wall, needs to be considered independently. The emissivity was investigated and found to be close to that of the water walls, 0.658. This calculation can be found in Appendix D.

The boundary conditions for the model can be summarised as follows:

Table 9: Boundary conditions for zonal model

Surface	Temperature (°C)	Emissivity
Front wall	350	0.7
LHS wall	350	0.7
RHS wall	350	0.7
Rear wall	350	0.7
Roof surface	600	0.7
Furnace exit "surface"	1400 (Initially)	0.658

The other inputs to the model are the enclosure dimensions, the chosen discretisation scheme, and the radiative properties of the 2-phase medium inside the enclosure which consists of ash and flue gas. The radiative properties required are the scattering coefficient (σ_p) and absorption coefficient (κ_p) of the ash particles, and the absorption coefficient (κ_g) of the gases. These coefficients combined are referred to as the extinction coefficient of the 2 phase mixture, β_m.

$$\beta_m = \beta_p + \beta_g = \left(\sigma_p + \kappa_p\right) + \kappa_g \tag{3.32}$$

For the gas phase, the extinction coefficient is equal to the absorption coefficient and can thus be related to the emissivity as follows:

$$\varepsilon_g = 1 - e^{-\beta_g L_m} \tag{3.33}$$

where L_m is the mean beam length of the enclosure.

A method for calculating the gas phase emissivity was mentioned above and used in Appendix D for the calculation of the furnace exit emissivity. This method can also be applied to the enclosure volume, accounting for the temperature of the gas in the volume. For this, the temperature of the gas volume is assumed to be 1000°C, estimated as the average between the roof surface and the furnace exit surface. Hence the gas emissivity and thereafter the gas extinction coefficient can be determined to be β_g=0.059m^{-1}.

Appendix D also provides a method to calculate particle emissivity and thus particle extinction coefficient, similarly to equation (3.33). It does not, however, offer a method to determine σ_p and κ_p that make up this value, and these are required to be known, as both are required as inputs to the model. Fortunately, Monnaemang [12] provided a secondary model that can be used to determine these radiative properties and this model was applied to determine the particle properties in the enclosure. Monnaemang's secondary model uses the physical properties of the particles as inputs, namely the particle density, diameter and number density (concentration).

Figure 29 shows how the particle extinction coefficient varies with the particle volume fraction for 3 different particle sizes.

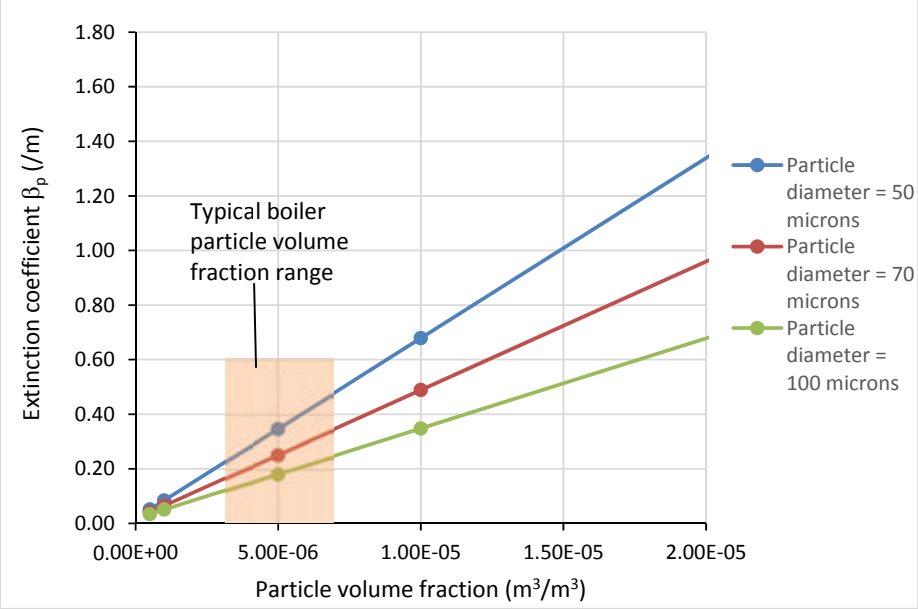

Figure 29: Variation of particle extinction coefficient with particle concentration for different particles sizes

The particle volume fraction calculated from the mass and energy balance is in the range of $5x10^{-6}m^3/m^3$. As can be seen on Figure 29, in this range the β_p value does not vary substantially for different particle sizes. Thus an average particle diameter of 70 microns is a satisfactory assumption. For the calculated particle volume fraction, this translates to a particle concentration of $2.755x10^7$ particles/m^3. The chosen particle properties used to calculate the particle radiative properties are summarised in Table 10.

Table 10: Particle properties used as inputs to calculate particle radiative properties

Parameter	**Value**	**Unit**
Ash particle density	1500	kg/m^3
Ash particle diameter	70	μm
Ash particle concentration	2.755×10^7	particles/m^3

Using these values, the extinction coefficient of the particles, β_p, is calculated from Monnaemang's secondary model to be $0.251m^{-1}$, which is made up by the scattering coefficient, σ_p=$0.191m^{-1}$, and absorption coefficient, κ_p=$0.06m^{-1}$.

Using the above values the overall extinction coefficient for the mixture is calculated:

$$\beta_m = \beta_p + \beta_g = 0.059 + 0.251 = 0.31m^{-1} \quad (3.34)$$

Thus, the remaining inputs to the zonal model in addition to the boundary conditions in Table 9 are as follows:

Table 11: Remaining inputs to the zonal model calculation

Parameter	**Value**
Dimensions	14m x 9m x 18m
Discretisation scheme	10 x 10 x 10
Extinction coefficient, β_m	0.31m^{-1}
Absorption coefficient, κ_m	0.119m^{-1}
Scattering coefficient, σ_m	0.191m^{-1}

The zonal model of Monnaemang [12] is then used to calculate the net radiative heat transfer from the furnace exit surface. This net radiative heat transfer was then included in the FMEB as an energy loss to calculate the new FET. As the Zonal model calculation depends on the FET as an input parameter, the calculation had to be iterated to ensure convergence between the MEB FET result and the Zonal model FET input. As the 2 models are coded separately in different software, the iteration was done manually, and it was found that 3 iterations provided sufficient convergence, within 0.3K in FET.

ii. Zonal model results

The main results of the zonal model and the new furnace exit temperature calculated from the MEB with the inclusion of this radiation loss from the furnace are listed below in Table 12.

Table 12: Zonal model results

Description	**Value**	**Unit**
Net radiative heat transfer on front wall	-7184.4	kW
Net radiative heat transfer on rear wall	-7184.4	kW
Net radiative heat transfer on LHS wall	-4297.5	kW
Net radiative heat transfer on RHS wall	-4297.5	kW
Net radiative heat transfer on roof surface	1198.2	kW
Net radiative heat transfer from furnace exit surface	21765.7	kW
Furnace exit temperature	1338.3	°C

The phenomenon driving these results can be best expressed graphically by the following plot.

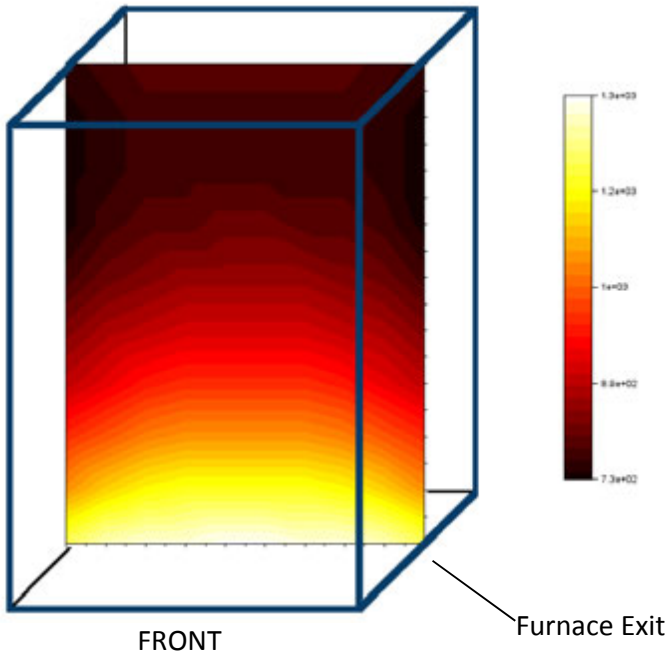

Figure 30: Temperature profile of flue gas over a vertical plane in the middle of the enclosure

Figure 30 shows the temperature distribution of the flue gas over a vertical plane through the middle of the enclosure. This profile demonstrates how the flue gas temperature drops with the height in the boiler as a result of the heat transfer to the walls without any gas flow and only through radiation. The profile also shows that the heat transfer is greatest at the walls since the temperature is the lowest at the walls, which is as expected.

With the values specified above, the radiative heat flux to the enclosure reduces the FET by ≈62°C, which is approximately 4.4% of the initial MEB result. In other words, a FET of 1338°C is obtained after accounting for the radiative heat transfer of 21.8 MW to the cavity compared to 1400C without accounting for this heat transfer.

So, considering the other sources of uncertainty already discussed in the MEB calculations, it shows that this radiation must be considered. The calculation described above has been carried out merely to provide an estimate, and as a result, some assumptions and simplifications have been made. In practice, it should be carried out more meticulously. With this in mind, it stands to reason that before closing this discussion, the sensitivity of these models to some of the inputs is investigated, especially since the model and the related theory was not covered in depth for this particular study.

The critical parameter that needs to be considered is the extinction coefficient of the 2 phase medium. Figure 31 shows how the calculated FET varies with the extinction coefficient.

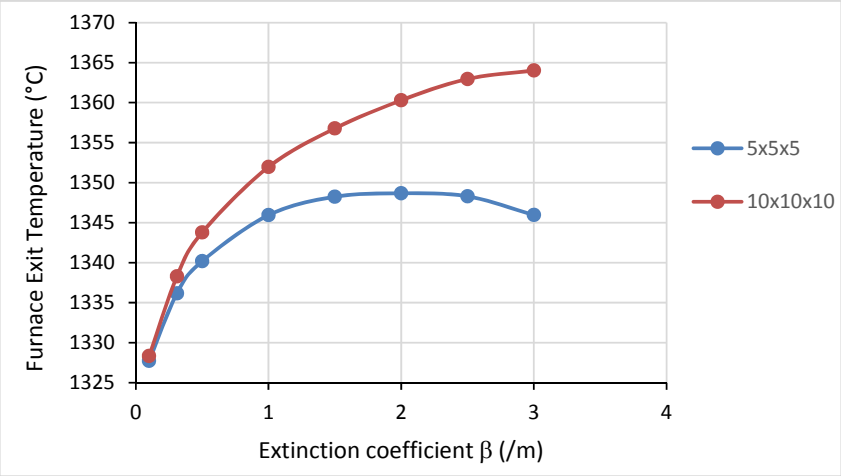

Figure 31: Variation of FET for varying extinction coefficients

As the extinction coefficient is a negative exponential coefficient in the heat transfer model, an increase in the extinction coefficient is expected to cause a decrease in the radiative transfer. In the case being considered, decreased radiative heat transfer implies an increase in FET, and this is seen in Figure 31. Moreover, the figure shows how the discretization scheme selected for the analysis can impact the results, particularly at the higher values of β. In the range for this calculation, the impact of the discretisation is minor, so the 10x10x10 discretisation is sufficient for the purposes of this analysis. It provides a good balance between resolution and solving time.

The other inputs of particular interest are the temperatures used for the boundary conditions. The water wall temperature assumption of 350°C is an informed assumption, based on the fact that the water in the water walls operates at saturation, in that temperature range. The roof temperature on the other hand should be investigated further. Figure 32 shows the impact of the roof temperature on the FET and the heat transfer.

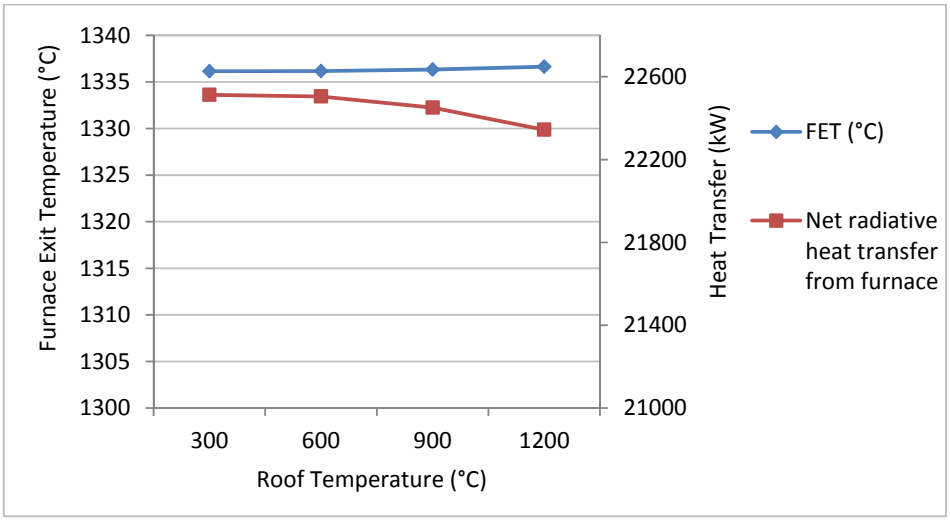

Figure 32: Impact of roof temperature on zonal model results of FET and heat transfer

As can be seen from Figure 32, the roof temperature does not have a major influence on the results. This is in fact due to its relatively large distance from the furnace exit as well as the relatively large extinction coefficient which is due to the high amount of ash in the flue gas. .

iii. **Remarks**

The zonal method applied in this section is typically used to analyse the radiation heat transfer in the furnace itself, and can be used in isolation as a means of calculating the FET. In this case, it has been applied to an enclosure of a simplified geometry to determine an estimate of the radiation heat transfer that occurs from the furnace to the convective pass. It shows that the MEB applied without consideration of this radiative heat transfer can result in an overestimation of the FET in the region of 60°C in this particular case.

3.9. Summary of indirect methods

It has been shown that by using a systematic, coherent and consistent approach, the furnace exit temperature can be calculated using mass and energy balances combined with a radiation model. It has also been seen that the calculation contains uncertainty from a number of different sources. This uncertainty is largely driven by the parameter which is renowned as difficult to accurately estimate, and that is the amount of energy transferred to the water walls; both in the furnace section itself, and also as a result of the radiation from the flue gas in the furnace exit zone towards the upper zone which is completely independent of the defined MEB control volumes.

The influence of these 2 parameters on the FET, (i.e.: (i) due to α coefficient and (ii) radiation from the furnace exit zone to the cavity) have respectively been found to be 52°C and 60°C respectively. While the inaccuracy on the determination of α coefficient can really be considered as a measurement error, the radiation from the furnace exit zone should rather be considered as a correction factor. A fair assumption would be to consider that this radiation also has its own uncertainty in the range of 20% meaning that the uncertainty it propagates on the FET would be in the range of 20% of 60°C, i.e.: 12°C.

There are also other uncertainties introduced by the fact that quite a large number of other variables are taken into account in the FET calculation. The sheer volume of measurements is one aspect, but the problem is further compounded by the fact that measurements are averaged over both time and space (e.g. right hand and left hand side measurements are averaged over time and then arithmetically between left and right). When gathering plant measurements, the calibration of the installed instrumentation is not always verified and this provides further potential for error.

With a certain amount of effort and deeper investigation, it should be possible to significantly reduce these sources of uncertainty. The problem is, however, compounded further by the need for assumptions such as the distribution of ingress air. This problem can best be addressed by striving for a global reduction of the total ingress air, which essentially reduces the impact of not knowing the distribution. It is also expected that the ingress air will be much less in boilers which have tight membrane water walls, as they are less prone to large amounts of ingress air than the type that was studied for this case study, which have refractory in between the water wall tubes to provide the seal.

So the mass and energy balance methodology shown in this chapter is a sound methodology, but to be used confidently, it requires plant performance and test activities with well determined measurement reliability and accuracy. One of the main positive aspects of the MEB is that most power plants should already have most, if not all, the required input data available to utilise it immediately, in some form, even if not in real time.

It should also be noticed that in addition to tight membrane wall furnaces (and thus less ingress air), the newer boilers also operate at supercritical conditions (at least at full load) meaning that the heat transfer to furnace walls can be more easily determined. As a result, MEB calculations of the FET for these boilers will certainly show much better accuracy than what was possible in the older Plant X that was used as a reference case in this study.

In terms of its online applicability, the MEB method is attractive compared to other complex numerical models, as it does not require complex and extensive calculation time. The calculation models are not complicated to incorporate into existing condition monitoring packages such as

EtaPro. That being said, the limitations of the MEB should not be discounted as well, the major one being that it can only be applied to steady state operation of the plant. If the objective of using it is general boiler performance testing or for verification of a set of measurements, the MEB is a very useful tool, but if the focus is to monitor the furnace exit temperature online, perhaps a more dedicated instrument is required. This direct approach will be discussed further in the next chapter, and later compared with the MEB approach.

4. Direct Methods

The direct methods refer to the methods which utilise a direct measurement of a physical property of the medium to determine the parameter of interest. This chapter details the direct methods looked at as part of this study.

4.1. Literature study on direct methods

The direct methods can be broadly grouped into contact (or intrusive) methods and non-contact (or non-intrusive) methods. There are a vast number of measurement techniques and instrumentation within each of these categories; however, a thorough exposition of all of these is not within the scope of this study. Therefore, the subsequent sections will first briefly describe the most popular contact and optical methods used in Eskom (namely suction and radiation pyrometers), with a particular focus on boiler furnace operation and the associated challenges. Thereafter, the acoustic method will be studied in more detail as it is the primary focus of this project.

4.1.1. Contact methods

Contact temperature measurements include various devices such as thermocouples, resistance temperature devices, bi-metallic strips, and silicon p-n junctions. Of these, thermocouples are by far the most commonly used in industry in a wide range of applications. Measurement of the boiler furnace exit temperature, however, presents specific challenges due to the high temperature (in some cases >1600K) and corrosive environment.

In a broad sense, the measurement obtained from a bare thermocouple is the equilibrium temperature reached by the probe with its environment. This equilibrium temperature is driven by the various heat transfer components that are in effect, such as the convection from the hot gas-particle mixture and the radiation between the thermocouple and its surroundings [21]. The equilibrium temperature, however, may not always be representative of the actual gas-particle temperature [22]. Of critical importance, is the radiation loss or gain experienced by the thermocouple, noting that from the Stefan-Boltzmann law in equation (4.1), the radiative flux varies by the fourth power of the temperature [23].

$$\dot{q}_{rad} = \varepsilon \sigma T^4 \tag{4.1}$$

As a result, the error due to radiation effects has been estimated to be quite substantial, particularly in high temperature applications, as shown in Figure 33.

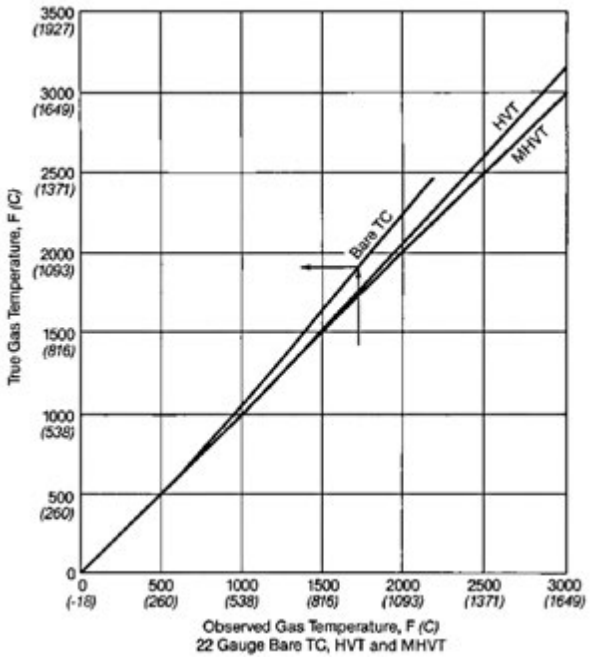

Figure 33: General magnitude of error when measuring gas temperature in boiler cavities using thermocouples [1]

The figure above also shows typical errors of 2 thermocouple measurement devices which have generally been employed to address the issue of radiation losses; high velocity thermocouples (HVT) and multiple high velocity thermocouples (MHVT). These devices utilize a system which extracts the flue gas via a radiation shielded tube and passes it over the thermocouple/s. They are also commonly referred to as suction pyrometers. The gas is extracted at a velocity higher than the flue gas velocity, thus increasing the convective heat transfer to the probe; while the shield reduces the radiative heat transfer, thereby reducing the radiation error. Figure 34 shows a schematic of a typical water cooled HVT.

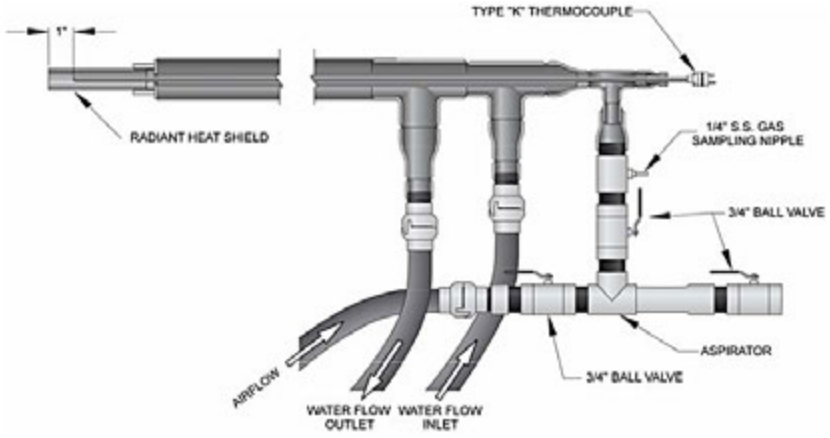

Figure 34: High velocity thermocouple [24]

Excellent accuracy can be achieved with HVT probes, provided that the effects of the gas velocity and radiation can be adequately mitigated. For a long time, they were regarded as the most widely accepted method of measuring gas at high temperatures [25]. Even today, they are commonly used during commissioning of boilers as well as for ad-hoc performance tests where they are used for traverse measurements via existing boiler inspection ports. They have, however, never found widespread use for continuous monitoring for a number of reasons, namely:

- The measurement obtained from the probe is a single point measurement [26]. This means that in order to gain sufficient information to determine the temperature profile in a flue gas section, multiple traverses are required. The increased time to collect temperature measurements over the entire furnace section [25], and the required probe length, becomes impractical, particularly in large furnaces. It also results in errors in estimating the temperature profile due to temperature variations with time.
- The procedure is very expensive and difficult to apply because of the complex equipment and labour involved [25], as the probe needs to be cooled to withstand the high flue gas temperatures.
- The suction process results in ash particles collecting inside the probe. This can result in blockages and extended exposure of the probe without maintenance would result in a degradation of the measurement accuracy [26].
- Thermal shocks during boiler transients can result in damage to the probes [27]. This results in the probes requiring regular maintenance.
- Slagging on the probe can also happens which can lead to complete probe destruction due to the weight of the slag.

For the reasons above, non-intrusive methods are sought after for continuous furnace exit temperature monitoring.

4.1.2. Radiation pyrometry

As seen above, the geometry and physical conditions of the boiler furnace makes direct measurement difficult. Hence, the use of non-contact techniques is very attractive, and many efforts have been made to develop systems which can address this particular need. One widely used measurement technique that has been applied to boilers, and is also used on all Eskom boilers, is radiation pyrometry. However, on Eskom boilers, temperature measurement from the radiation pyrometers is a secondary function and the temperature reading is not used in the boiler control systems. The primary function of the radiation pyrometers is to detect the presence of the flame for combustion safety.

Radiation pyrometry consists of a variety of different types of devices, with the underlining principle being that they utilise the principle that all bodies with a temperature >0K emit radiation. The intensity of this radiation is a function of the temperature of the body. The visibility of this radiation is dependent on its wavelength which determines where it is categorised on the electromagnetic spectrum.

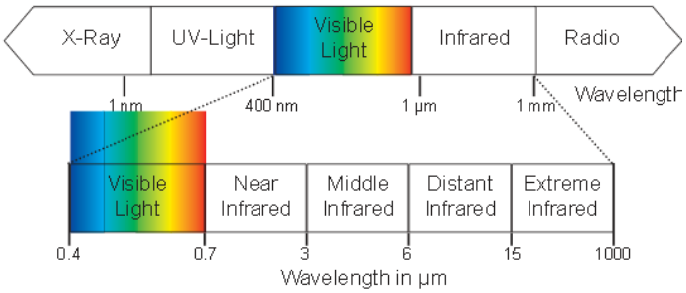

Figure 35: Electromagnetic spectrum [28]

i. Optical Pyrometers

The early forms of radiation pyrometers were a manual form of pyrometer that depended on the human eye to differentiate the temperature. The term “optical pyrometer” is often used to refer to this particular type of device. The most common form is the disappearing filament pyrometer which essentially consists of visually comparing the colour/brightness of a hot body with that of a calibrated heated filament [29]. The electrical current through the filament is the indicator of temperature and is adjusted until the filament is no longer visible against the backdrop of the radiation from the hot body. This indicates that they are at the same temperature. While these have wide spread applications for heating furnaces and steel and iron industries, it is not suitable for gas temperature measurement as clean gases do not radiate in the visible range [30].

ii. Radiation pyrometers

Newer radiation pyrometers on the other hand, do not require manual visual comparison. While there is a wide variety of configurations, all radiation pyrometers consist of a few key components, namely some form of detector (as opposed to the human eye), some form of optical lens system for focusing the radiation, and a filtering system to allow transmission of selected wavelengths. Of course, there is also the signal acquisition and processing components.

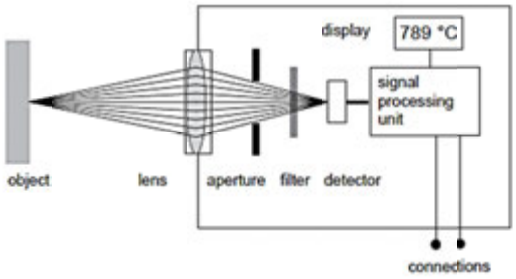

Figure 36: Example configuration of the main components of a radiation pyrometer [28]

The radiation pyrometer (RP) detects all of the radiation within its field of view, which is determined by the optical components, i.e. the lens system. The field of view is a conical volume that extends outwards from the aperture of the device, and is normally specified as the ratio of measuring distance to measuring spot size (Distance/Spot size). The spot size refers to the diameter of the cone at the distance of the target object. The minimum spot size occurs at the focal length of the lens.

The other function of the lens is to focus the radiation onto the detector, which is normally in the form of 2 broad types, namely thermal detectors and quantum detectors [31]. Quantum detectors include devices such as photodiodes which interact directly with photons with a fast response time, while thermal detectors include devices such as thermopiles which require time to reach equilibrium temperature.

The defining component of radiation pyrometers which results in the main classification of the distinct types is the type of filtering that is used. As mentioned, the reason for filtering is to allow detection of only specific wavelengths of radiation, and this choice of wavelength is based on the object being measured, the temperature range, and the environmental conditions [31].

Total radiation pyrometers (or broadband pyrometers) are designed to detect all wavelengths of radiation, regardless of wavelength. These are not commonly used due to large measuring errors that can result [28]. Spectral pyrometers are the most common type and are designed to filter only a specific narrow band of wavelengths. The wavelength band selected for filtering depends on a number of factors such as the temperature range, the object being measured, as well as the environmental conditions [32]. This is particularly useful in scenarios where there are multiple sources of radiation emission in the field of view of the pyrometer, but the different sources emit at different wavelengths. The spectral pyrometer's range is commonly in the infrared band of the spectrum leading to the common instrument called Infrared (IR) pyrometers. Two colour pyrometers (also called ratio pyrometers) measure the intensity of radiation at 2 distinct wavelengths. If the variation of emissivity with wavelength is known for the target object or if the

wavelengths are close enough to assume constant emissivity, the temperature can be estimated using the ratio of the 2 measurements without the need to estimate the emissivity of the target [29].

iii. Advantages and disadvantages of radiation pyrometers in the boiler furnace application

From the high level overview of the fundamental concepts presented above, it can be surmised that radiation pyrometry is particularly effective for the measurement of temperature of solid objects; particularly in a clean air environment, where the target is clearly defined and there are no physical obstructions between the target and the detector. The measurement of gas temperatures, however, is a much more complex issue.

Compared with contact methods, radiation pyrometry offers the following advantages:

- Thermocouples require a certain amount of time to reach equilibrium with its surroundings. Radiation pyrometers which use photodiode detectors have a much faster response time, which is dependent perhaps more on software than on physical conditions. [28]
- It allows measurements to be taken in difficult to access areas without the need for long cumbersome probes as is the case with HVT probes.
- This also means that the device is not directly exposed to the harsh furnace environment, meaning no physical damage of the components due to erosion and high temperatures.

However there are also some potential difficulties and undesirable features.

- Reconstruction of a temperature profile over different depths in a boiler is only possible with variable focal distance lenses.
- Fouling can obstruct the lens, but this can be mitigated somewhat by using a purge air system, as is done on some Eskom boilers.
- The accuracy of the measurements is highly dependent on the estimation of the optical characteristics of the target, such as emissivity, reflectivity and fluorescence [32].
- Gases are inherently optically thin, thus there is not a clearly defined field of view and target. In addition to the emission from the flue gas, there is strong emission from the ash and soot particles, emission from the surrounding water walls and possibly from the superheaters above the furnace, all of which can influence the measurement [33]. There has been development of infra-red radiation pyrometers, which are narrow band spectral pyrometers configured to only detect infra-red radiation, specifically in the wavelength range of CO_2 emission, ≈3.9µm. In this way, radiation from the tubes and particles is ignored. While this is a

logical concept, filtering of the correct wavelength is only one of the challenges in the furnace environment as the presence of the particles results in more challenges.

- As was discussed earlier in chapter 3, the physical presence of particles in the boiler has a significant influence on the radiative heat transfer. Solid particles have the effect of absorbing, emitting and scattering radiation. This can result in radiation being scattered out from the view of the pyrometer, or even being scattered into the field of view of the pyrometer [34]. Ultimately the depth of the pyrometer measurement into the boiler becomes very dependent on the concentration of particles which influence optical characteristics of the gas particle flue mixture, which in itself is a very complex phenomenon to estimate.

With specific filtering methods, and emissivity corrections applied, radiation pyrometers are proposed to be suitable for furnace gas temperature, however, in principle, radiation pyrometers are not designed for the measurement of gas temperature [34] .

4.1.3. Acoustic Pyrometry

Acoustic pyrometry is a relatively new technology in the field of temperature measurement and is an alternative technique that can possibly address some of the difficulties associated with the other technologies. In its simplest form, an acoustic pyrometer system measures the transit time of a sound wave travelling across the boiler, taking advantage of the fact that the speed of sound through a gas, varies with the temperature of the gas [25]. Furthermore, if the system is extended to measure the time of flight of sound waves on several acoustic paths on a horizontal plane, the temperature map, or profile, of the entire plane can be determined using a suitable reconstruction algorithm [6].

i. **Basic principle of operation**

In its simplest form, an acoustic pyrometer consists of an acoustic source (or acoustic generator) and an acoustic receiver. A sound wave is transmitted from the acoustic generator positioned at one wall of the boiler to a receiver located at a known measured distance from the generator, on one of the other walls of the boiler. This distance from the generator to the receiver is referred to henceforth as the path length, and the time taken for the sound wave to travel from the generator to the receiver is referred to as the time of flight (TOF).

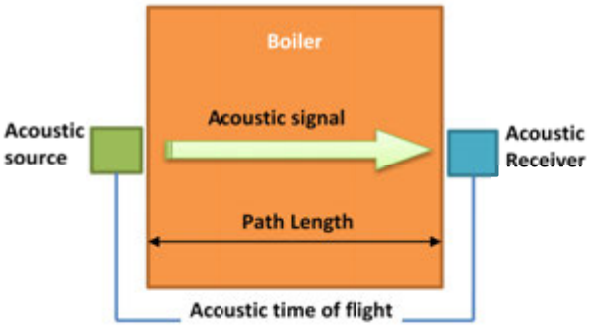

Figure 37: Basic acoustic pyrometer set up from boiler top view

From rudimentary physics, the average velocity, c, of the sound wave over a given distance is:

$$c = \frac{distance}{time} \tag{4.2}$$

Considering the case in figure 1:

$$c = \frac{Path\,Length}{Time\,of\ flight} = \frac{L}{TOF} \tag{4.3}$$

It is also known that the speed of sound in a gaseous medium is given by

$$c = \sqrt{\left(\frac{dP}{d\rho}\right)_s} \tag{4.4}$$

Furthermore, for an ideal gas, equation (4.4) can be manipulated to relate to the temperature of the gas as follows [35]:

$$c = \left(\gamma \frac{R}{M} T\right)^{\frac{1}{2}} \tag{4.5}$$

where

γ = specific heat ratio

R = universal gas constant (J/molK)

M = molar mass of gas (kg/mol)

T = temperature of gas (K)

Simple manipulations yield:

$$T = \frac{L^2}{\gamma_{fg} R_{fg} \left(TOF\right)^2} \tag{4.6}$$

Where $R_{fg}=R/M_{fg}$ and M_{fg} is the molar mass of flue gas.

Equation (4.6) provides an equation for the average temperature of the flue gas over a single path for a particular medium of known molar mass and specific heat ratio. Thus for any acoustic path, if the length of the path and gas properties are known, the time of flight measurement is all that is needed to determine the average gas temperature along the path.

Further complexities can arise if the intention of the acoustic pyrometer system is to map the temperature profile of the furnace using multiple acoustic path measurements. Individual path temperatures which may already contain inaccuracies due to errors in the time of flight detection have to then be used to produce a temperature map, meaning that the application of appropriate reconstruction algorithms is another very important aspect of the acoustic pyrometer in practice.

ii. History of acoustic pyrometer research and development

Acoustic pyrometry as a concept can be traced back as far as 1873, when Mayer [36] proposed the use of acoustics for temperature measurement, however the idea didn't gain much traction until the mid-1980s. Applications using acoustic time of flight measurements were already established, however the applications were generally in range finding systems, wherein the objective is to determine distance based on the known acoustic velocity in air. Conversely, in the case of acoustic pyrometry, the distance is known and the objective is to determine the acoustic velocity and consequently the temperature [25].

Although the literature on acoustic pyrometry is by no means voluminous, the research conducted thus far has been sufficient such that the technology has been developed into several commercial products, some of which will be touched on later. The early research work focused primarily on the development of adequate acoustic sources and the practical application thereof in terms of signal treatment and processing, in order to achieve the most accurate time of flight measurements.

One of the first detailed and perhaps most definitive studies was carried out by Green and Woodham [37] in 1983 and this laid the groundwork for much of the future developments. This study investigated the application of an acoustic pyrometer consisting of a spark gap discharge system as an acoustic source, based on concepts described by Wyber [38].

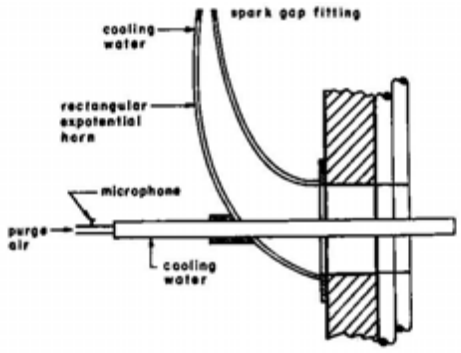

Figure 38: Diagram of a spark gap generator [25]

The system was capable of producing sound with SPL (sound pressure level) of 170dB, high enough to overcome typical boiler background noise and sound attenuation characteristics. One of the limitations of the experiments, however, was that no automated time of flight detection method was applied. Instead, a visual inspection technique was utilised to determine the time of flight, meaning the detection point was not clearly defined [39].

Although it was not a real time measurement, it still adequately demonstrated the idea that time of flight can be used as a measure of temperature. The other issues regarding the spark discharge source were related to safety due to the requirement of high voltages to produce the necessary sound intensity as well as the long term reliability of the system [25].

One of the prominent aspects of the study, and later restated by Green [40] and Kleppe [25], was the extensive list of potential sources of error associated with the time of flight measurements. The potential sources of error were identified and estimated. Based on this error study, they proposed that the mean temperature along a path could be determined within ±1%. They also demonstrated the application of a multiple path acoustic pyrometer system, utilising a deconvolution technique for the reconstruction of the temperature profile within the furnace.

Kleppe [25] and Nuspl et al [41] reported on a different type of acoustic pyrometer, using electrodynamic transducers as the acoustic source; essentially a loudspeaker that transmits a specific acoustic tone. The system provided a decent sound level of 126dB, but that limited its applicability to only certain boiler operating conditions and a shorter maximum path length.

The lower sound level could be countered by the application of improved digital signal processing methods [42], utilising Fourier transforms and cross correlation functions for time of flight detection. These types of signal processing techniques would also enable the acoustic pyrometer system to produce real time measurements, since the time of flight determination was not based on visual inspection.

Great strides were also being made in applying and adapting image processing methods and computer tomography ideas commonly associated with medical imaging applications. In addition to those mentioned above, authors such as Bramanti et al [6], Sielschott and Wübbeling [43], and Lu et al [26] expanded the literature regarding temperature reconstruction, demonstrating various temperature field reconstruction techniques.

With the greater interest, research and technology improvements in microprocessors, the initial problems associated with data processing and thermal mapping were largely addressed; however one of the outstanding problems repeatedly experienced in practical application was the high level of background noise in the boiler environment, which compromises the signal detection and processing accuracy. What was still required was an acoustic source that produces a high enough intensity to overcome this problem, while still being practicable. This led to the development of pneumatically driven sound sources which deliver powerful air blasts which can produce sharp wave front, high intensity sound waves in the region of 170dB [27]. The air blasts produced are essentially wide band random noise [42] as opposed to the tonal devices used previously.

Figure 39: Example of a pneumatically driven acoustic pyrometer [44]

Pneumatic types of generators have come to the fore due to their ease and simplicity of operation. They require only a pressurised air source, minimal modifications to the furnace enclosure and minimal maintenance. As a result, these are now the most common type of commercially available acoustic generators and have been successfully applied using appropriate time-of-flight detection and temperature field reconstruction methods. The acoustic pyrometer tested for this study is also of this type.

Some of the more recent research work includes the work of Shen et al [35] and further built upon more recently by Shen et al [45], which demonstrated the use of cross correlation analysis as a time of flight detection method, and temperature reconstruction based on a least squares method combined with multiquadratic or bicubic interpolation algorithms. Zhang et al [46] further

expanded upon the least squares method by incorporating an iterative component in the form of algebraic reconstruction technique.

While the use of pneumatically driven active acoustic sources has become the norm, some authors have also started looking at alternative acoustic sources. Srinivasan et al [47] investigated the use of an aero acoustic device with no moving parts called a Hartmann whistle as an acoustic source that can be tuned to deliver specific sound frequencies.

There is no doubt that acoustic pyrometers are currently accepted as a reliable source of furnace temperature measurement and are being widely used on boilers globally. They provide a means of monitoring furnace temperatures, enabling the identification of combustion deficiencies, optimizing burner operation, optimizing soot blower cycles, preventing slagging problems and preventing excessive furnace exit temperatures. It has also found a role as a means of validation for CFD simulation models as was carried out at Rybnik Power Plant in Poland [48].

In addition to fossil fuel boilers, acoustic pyrometer systems have also been tested and applied to chemical recovery and waste-to-energy boilers [49], as well as to the cement manufacturing pyroprocess [27]. Acoustic pyrometry techniques have also been applied to determine flue gas flows as well as velocity fields in furnaces, as reported in [50] and [30] respectively.

iii. Advantages of acoustic pyrometry

Acoustic pyrometry has been adopted as a measurement tool because of the numerous benefits it offers over the contact and optical measurement systems.

- It is a non-intrusive technique [33] so it is not required to be in contact with the flue gas stream and is therefore also not subject to radiation impacts as is the case with contact methods.
- As a result of not being in direct contact with the flue gas, there are no limitations on the exposure time.
- It is also not vulnerable to slagging and corrosion. The pneumatic generators have the added benefit of being self-cleaning in the event of any slag formation.
- It is not dependent on emissivity or visibility through the flue gas as opposed to optical methods.
- It has been reported to be accurate to within ± 1%. [40]
- In terms of installation, it does not require major modifications to the plant. Only minor boiler tube manipulations may be required to accommodate the components.

- It is not limited to point by point measurements. It can produce the temperature profile over an entire plane of the boiler, and in real time, thus enabling combustion optimization by operators and engineers.
- In theory, there is no limitation on the temperature range. However, the higher the temperature the shorter the time of flight resulting in a higher sensitivity to time of flight measurement errors. Commercially, it is specified to measure temperatures up to 3500°F [51] which is ≈1927°C.

4.2. Practical and theoretical topics of interest

These section looks at some relevant practical and theoretical aspects of acoustic pyrometry with applied examples where relevant.

4.2.1. Existing commercial acoustic pyrometers

The goal of this study is to investigate acoustic pyrometry as an overarching concept, not to rank or rate variations between different commercial acoustic pyrometer products. It is, nonetheless, still of interest to identify the products which are on the market. A scan of the available options revealed 2 of the most popular acoustic pyrometer concepts. There is the generator-receiver transceiver unit concept used by the SEI Boilerwatch MMP system and the agam MMP system; and there is the PyroMetrix system manufactured by Enertechnix which utilises separate generator and receiver components. Examples of these are shown in the following figures. Table 13 summarises the main characteristics of these acoustic pyrometers

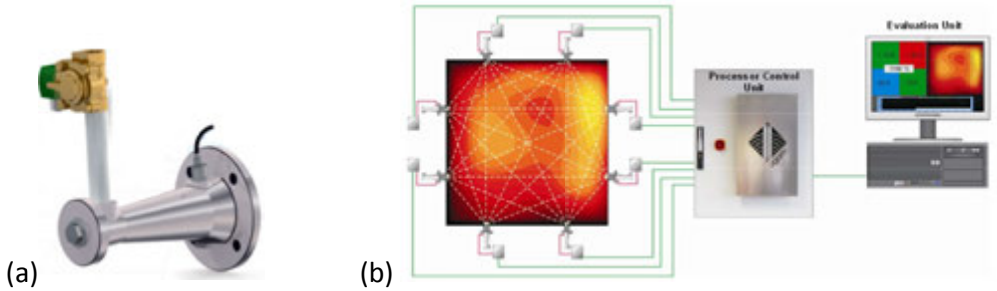

Figure 40: (a) SEI Boilerwatch MMP Transceiver unit [52]. (b) Typical 8 transceiver setup of the MMP system [53]

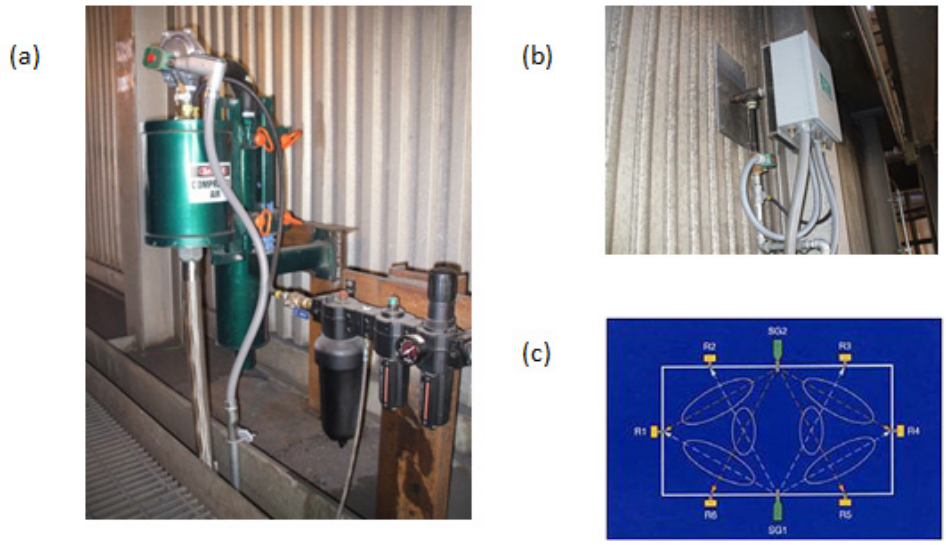

Figure 41: Enertechnix PyroMetrix Acoustic Pyrometer. (a) Generator. (b) Receiver. (c) Example layout with zones [44]

Table 13: Comparison between popular acoustic pyrometers

	SEI Boilerwatch MMP II/agam MMP	**Enertechnix PyroMetrix**
Acoustic Generator Type	Pneumatic	Pneumatic
Sound Level	126dB	170dB
Receiver configuration	Transceiver unit functions as both an acoustic generator and a receiver. Each unit acts as a generator in turn while all of the other units receive. Typical configuration of 8 units (2 per side of boiler).	Receivers are separate components. Several receivers are arranged to receive from a single generator. May be configured with more than 1 generator for better resolution. Typically 2 generators.
Boiler wall opening required	3” diameter penetration	1.5” diameter penetration for generators. 1/2” inch diameter penetration for receivers.
Air supply requirement	5.0 - 8.3 Bar	5.5 – 8.6 bar
Number of paths	Up to 24 paths for the typical 8 transceiver configuration.	Depends on number of generator-receiver combinations that can be achieved with layout.
Temperature range	Up to 1927°C	Up to 1927°C
Reported accuracy	Error <1.5%	Error < 1%
Temperature distribution information produced	Single path measurements. Zonal maps. Isothermal maps.	Single path averages and zonal temperature maps.

4.2.2. Errors in acoustic time of flight measurements

As mentioned earlier, most of the potential sources of error in an acoustic pyrometer system were quite well identified very early on. Based on those particular studies and a survey of the remaining literature, the potential sources of error on individual time of flight measurements that will need to be considered later when testing, are presented below.

It should be noted that the errors discussed in this section are generic and independent of the acoustic device. Any particular chosen equipment may also have specific errors inherent to its design and operation.

a) Gas composition

The impact of the gas composition on the temperature measurement emanates from the $\gamma_{fg}R_{fg}$ factor in equation (4.6). Young et al [33] quantified the typical systematic errors associated with acoustic pyrometer methods for various fuel types for which the exhaust gas composition is not known at all, and that this error is typically less than 2% on the temperature.

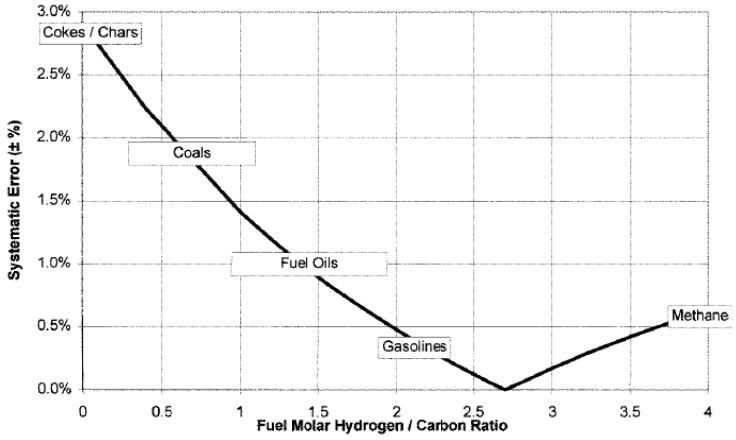

Figure 42: Systematic error in temperature measurement resulting from unknown combustion mixture [33]

This error is significantly reduced by better knowledge of the actual exhaust gas composition. Green [40] estimated that in a typical power plant furnace, the molar mass has a standard deviation of ≈ 0.4%, and the specific heat ratio (γ) in the temperature range of 300K-1800K, has a standard deviation of ≈ 0.4%. For these values, the error propagated will be 0.57% on temperature in K.

In the case of a power station, there should be a fairly accurate estimation of the flue gas composition, based on both the coal analysis as well as gas analysers in the flue gas stream, thus reducing this error. In any case, if it is deemed significant, this error is systematic and can thus be accounted for by applying an appropriate correction factor to the temperature calculation.

b) Path length measurement error

This refers to an error in the actual physical measurement of the path length. In a fixed installation, this error should be very small, and is mainly a function of the measurement device used to measure the path length. Typically this error should be as low as ± 1 cm. An error of ±1cm on a path of 13m results in ±0.15% error on the temperature in K. For a FET of 1300°C, this translates to approximately ±2.35K.

c) Path curvature

The preceding paragraph focused on the straight line path from generator to receiver. In reality, the actual path taken by the sound wave may be influenced by temperature and velocity gradients in the flue gas [54]. Therefore, the actual path may not be a perfect straight line, adding another potential source of error. Based on Fermat's principle of least time and refraction, the actual path of the sound wave will be the path that takes the shortest time. Due to the severe temperature and velocity gradients in the boiler which can be as high as 100K/m close to the walls [25], the shortest time is not necessarily along the shortest straight line distance as illustrated in Figure 43.

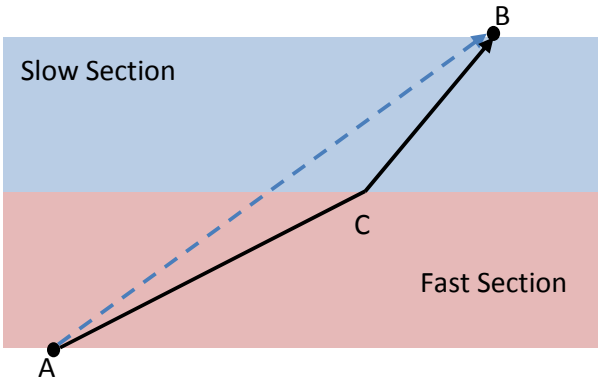

Figure 43: Graphic representation of Fermat's principle

If the time of flight between point A and point B is measured, the average velocity will be calculated as the time flight divided by the straight line distance AB depicted by the blue dashed line. However, if the sound wave travels faster in the red section than in the blue section, the actual path of the sound wave may actually be a path such as AC+CB, which results in the sound wave spending a shorter time in the slower section thus minimizing the overall flight time. So the true average velocity over the path is actually the time of flight divided by the distance along paths AC+CB.

The extent of the error caused by this phenomenon is dependent on the angle of the straight line path to the temperature gradient. Typically the worst case would be an error of 2% on the temperature measurement, but in most cases this error would be substantially lower, around

0.65% for typical paths [25]. This error could be accounted for by incorporating a correction factor into the temperature calculation if there is information regarding the temperature gradients. If it is known that the paths do not form large angles with the temperature gradients, then this error is small enough to be ignored [6] [50].

d) Gas velocity

If the flue gas flow has horizontal flow components, these would obviously impact on the time of flight. Horizontal gas velocity components are small, 1-2 % of the vertical gas velocity [25] which is itself in the range of 10 m/s and so comparatively low as regards the speed of sound which exceeds 500 m/s at FET. On the other hand, this source of error can be accounted for by taking all path measurements in both directions. This is most easily accomplished in acoustic pyrometer systems which have transceiver units which fulfil the functions of generator and receiver.

e) Particles in gas

It is well known that the speed of sound varies in different mediums and as a result of this the presence of solid particles in a gas medium has an impact on the speed of sound through the gas. This phenomenon is widely covered in various literatures, particularly those relating to the pneumatic conveying of solids; however, it has not been a focus of the existing research pertaining particularly to acoustic pyrometry. It is briefly mentioned in [40] and [25] citing Wallis's approximation that a 2 phase homogenous mixture can be treated as a kind of pseudo gas with modified gas properties [55].

It is known that South African power plants operate using coals consisting of a high proportion of ash, even as high as 30-40%, and thus for this project, a study of existing literature on the speed of sound in gas-particle flows has been conducted to ascertain if the high ash content in coal has a major impact on the speed of sound through the flue gas. Section 4.2.3 discusses this aspect in greater detail.

f) Timing error

Timing errors refer to errors relating to the actual detection of the time of flight and are dependent on the method that is used for detection. Some of the factors that influence this error are the frequency of the acoustic signal which determines the rise time of the signal. Acoustic signals with a sharp wave front reduce the amount of error that can be incurred due to incorrect time of flight detection. This is depicted on Figure 44.

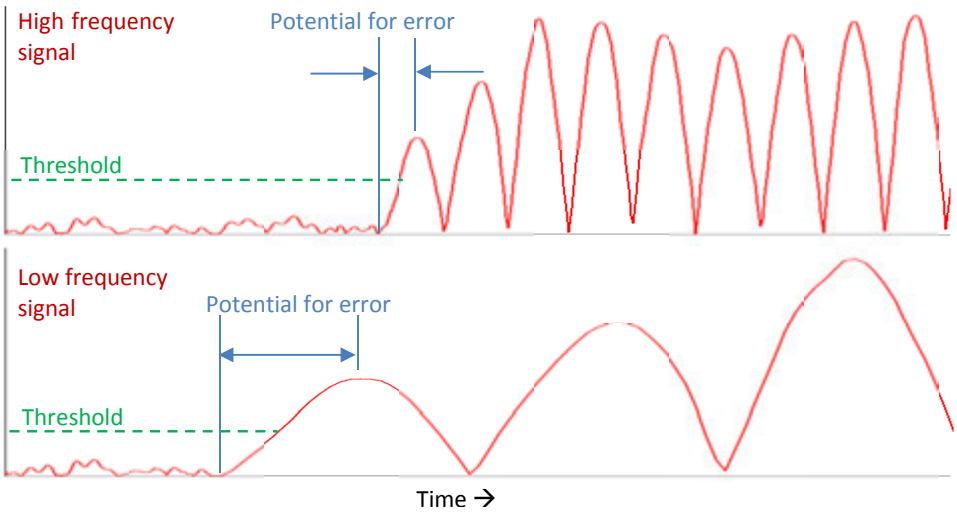

Figure 44: Depiction of how a higher frequency results in lower potential for error

A high signal to background noise ratio also makes accurate signal detection significantly easier. These aspects are revisited later during experimental testing.

g) Variation of gas temperature in mounting tubes

One of the key benefits of the acoustic pyrometer is that it is not intrusive and requires minimum plant modification to be installed, as the main components function externally to the boiler. However, this does come with a caveat, in that the sound waves have to be delivered and received to and from the furnace by some form of tubes or wave guides.

Now, the gas in these tubes is obviously at significantly lower temperature than the gas in the furnace, possibly even much closer to the ambient conditions. Ultimately, the nature and extent of this error is very dependent on the product design and configuration and it is something which the manufacturers should quantify and incorporate into their software during product development.

h) Speed of sound pulse

Green [40] made provision for correcting the time of flight due to the fact that the speed of the spark gap source pulse generally exceeds Mach 1, however this effect has been shown to be negligible over path lengths typically found on power boilers. [25]

i) Temperature variation with time

Temperature variations with time would not be relevant to individual path measurements but could perhaps have an impact when reconstructing the temperature map, if there is a time delay between the acquisitions of the various path time of flight measurements.

4.2.3. Impact of solid particles on the speed of sound through the flue gas

As mentioned earlier, the impact of solid particles in the flue gas flow on the speed of sound is of particular interest in this study. A study of the theoretical background on the subject of the speed of sound in gas solid flows was therefore carried out and applied with typical boiler parameters to see the impact.

This analysis begins with the derivation provided by Fan and Zhu [56]. By considering the interacting force between the particles and the gas phase, they described the oscillating motion of the particles. Combining this with the equation of a plane wave in a mixture, they showed that the ratio of the speed of sound in a 2 phase mixture with a solid to gas mass ratio m_p is related to the speed of sound in a pure gas by the following equation:

$$\frac{c_m^2}{c_g^2} = \left[1 + m_p \left(1 - \frac{\rho_g}{\rho_p} \right) \frac{(1+\xi)\xi + \phi^2}{(1+\xi)^2 + \phi^2} \right]^{-1} \tag{4.7}$$

Where

c_m = speed of sound in two phase mixture (m/s)

c_g = speed of sound in pure gas (m/s)

m_p = mass loading ratio

ρ_g = density of gas (kg/m^3)

ρ_p = density of particle (kg/m^3)

ξ and ϕ are functions of the densities and of the dimensionless parameter N_ω

$$N_\omega = \frac{\Omega d_p^2}{8\nu} \tag{4.8}$$

Where

Ω =angular frequency (rad/s)

d_p = diameter of solid particle (m)

v = kinematic viscosity (m^2/s)

This implies that for a given gas-particle mixture of known particle concentration, the speed of sound through the mixture is a function of the frequency of the sound.

An example of the application of the above relationship was shown by Soo [57] for an air-magnesia mixture with particle mass fraction m_p of 0.3 and density ratio ζ of 100 and 1000. The speed of sound ratio squared is plotted against N_ω.

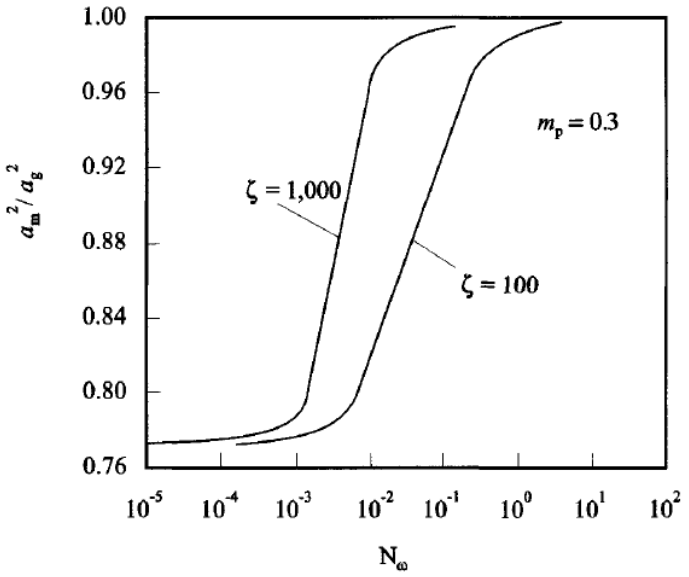

Figure 45: Speed of sound in air-magnesia mixture [56]

From the above figure, it is immediately apparent that at higher values of N_ω, and thus higher frequencies, the influence of the mixture on the speed of sound becomes almost negligible. Furthermore, the larger the density ratio (ζ) between the particle and the gas, the steeper the gradient of the curve and in that case, even at lower frequencies the particles have less of an impact.

While the figure above does provide useful insight into the relationship between the speed of sound and frequency as well as density ratio, it should also be applied to typical boiler conditions. Typical parameters are as follows:

Ash particle diameter: 70μm

Density of gas phase: 0.3kg/m^3

Density of ash particles: The ash particle density would be in the region of 1000kg/m^3. Thus the density ratio ζ = 3333

The mass fraction can be calculated using the typical South African coal ash content. The ash content is typically in the region of 30%. And the mass flow ratio of flue gas to coal is 8.5. So the particle to gas mass loading ratio is 0.3/8.5 = 0.035.

For these condition the graph of $\frac{c_m}{c_g}$ can be plotted as follows, versus the frequency of sound:

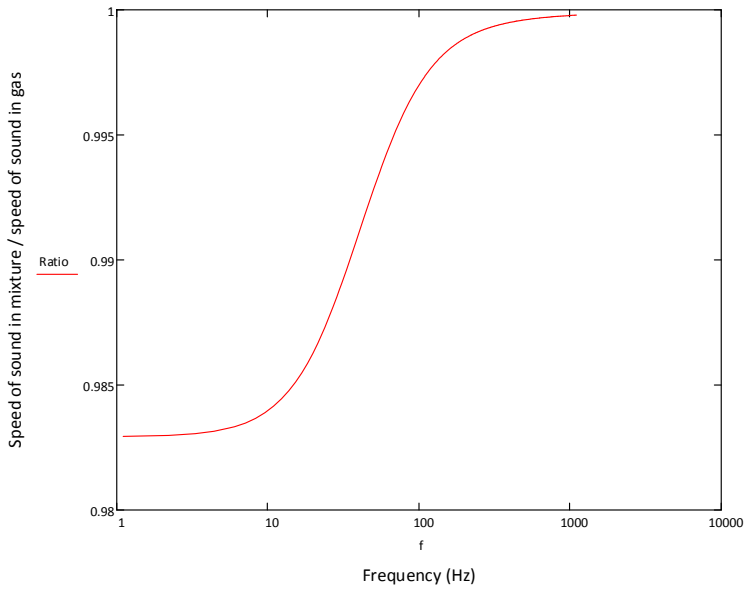

Figure 46: Speed of sound in a typical boiler flue gas mixture with m_p=0.035 and ζ=3333

From the above figure, it can be seen that in a typical boiler flue gas environment, even for extremely low frequencies, the speed of sound ratio is higher than 98%. The ash particles have very little influence on the speed of sound. This is not surprising, given that the flue gas is an extremely dilute 2 phase mixture and the impact of the particle phase is greatly dependant on the mass fraction and density ratio. In fact, the value used for the density of ash is quite conservative and it could even be closer to 1500kg/m^3, which would make the density ratio even larger, pushing the ratio in Figure 46 even closer to 100%.

In the above example, the particle concentration was fixed to see how the speed of sound varies with the frequency. The above shows that for a dilute mixture, as in a coal boiler even with high ash content as in SA, the velocity of sound in the 2 phase mixture is influenced by less than 0.2% for frequency above 100 Hz. So the analysis can be taken a step further to look at what the impact of the particle concentration is at a specific frequency.

If the frequency is fixed at an arbitrary value of 500Hz for example, and the solid particle mass fraction (and thus volume fraction since the density ratio does not change) is varied, then the speed of sound ratio can be plotted versus the gas volume fraction (aka “voidage”). The voidage, *eps*, is calculated by:

$$eps = 1 - m_p \frac{\rho_g}{\rho_p} \tag{4.9}$$

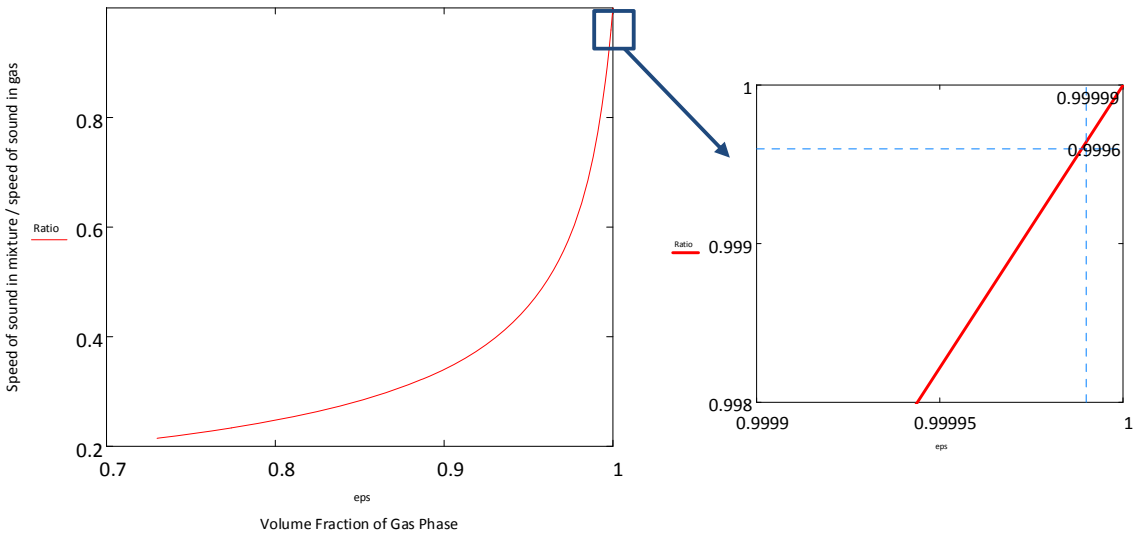

Figure 47: Speed of sound ratio versus gas volume fraction for a sound frequency of 500Hz and density ratio ζ=3333 which is typical of SA coal boiler.

Figure 47 further confirms that for dilute 2 phase mixtures (i.e. gas volume fraction approaching 1) the speed of sound in the mixture approaches the speed of sound in pure gas. For the boiler mass loading ratio of 0.035, the speed of sound ratio is approximately 1 (0.9996).

At this point, it is useful to compare these findings with other literature. Klinzing et al [58] provide an equation relating the speed of sound in the mixture to pure gas, based on the method described by Weber [59]:

$$\frac{c_m}{c_g}=\left(1+\frac{1-eps}{eps}\frac{\upsilon}{\upsilon_p}\frac{d\upsilon_p}{d\upsilon}\right)^{\frac{1}{2}}\left[\left(1+m_p\frac{d\upsilon_p}{d\upsilon}\right)eps\right]^{\frac{1}{2}} \tag{4.10}$$

Where

a_m = speed of sound in two-phase mixture (m/s)

a_g = speed of sound in pure gas (m/s)

m_p = mass loading ratio

υ = velocity of gas phase (m/s)

υ_p = velocity of solid phase (m/s)

It is immediately apparent that equation (4.10) contains additional information relating to the velocity and acceleration ratios of the 2 phases that was not part of the previous analysis. The previous analysis assumed homogenous conditions. To determine the velocity ratio between the 2

phases, the slip velocity has to be calculated. The slip velocity can be determined as follows, depending on the flow regime [58]:

$$v_{slip} = \frac{d_p{}^2(\rho_p - \rho_g)}{18\mu} g \qquad \text{(Stokes)} \tag{4.11}$$

$$v_{slip} = \frac{0.153 g^{0.71} d_p{}^{1.14} (\rho_p - \rho_g)^{0.71}}{\rho_g{}^{0.29} \mu^{0.43}} \quad \text{(Intermediate)} \tag{4.12}$$

$$v_{slip} = \left(\frac{4}{3} \frac{d_p(\rho_p - \rho_g)}{C_D \mu} g \right)^{1/2} \qquad \text{(Newton)} \tag{4.13}$$

The flow regime can be easily determined from the following criterion [58]:

$$K = d_p \left(g\rho \frac{\rho_p - \rho_g}{\mu^2} \right)^{1/3} \tag{4.14}$$

K < 3.3: Stokes

3.3 < K < 43.6: Intermediate

43.6 < K < 2360: Newton

It can be shown that for the typical boiler parameters as used above, the particle slip velocity is approximately 1% of the gas velocity. Thus it is actually fair to assume that in this case, the 2 phase flow is approximately homogenous i.e. particle velocity is equal to gas velocity.

This leads to the introduction of another method of dealing with the 2-phase flow. For a homogenous 2 phase mixture, Wallis [55] also provided a neat method of approximating the 2 phase mixture. He showed that the homogenous 2 phase mixture can be treated as a "pseudo-gas" with equivalent gas constant *R'* and specific heat ratio γ' :

$$R' = \frac{R_{gas}}{\left(1 + m_p\right)} \tag{4.15}$$

$$\gamma' = \frac{\left(\gamma + \frac{C_{solid} m_p}{C_{v.gas}} \right)}{\left(1 + \frac{C_{solid} m_p}{C_{v.gas}} \right)} \tag{4.16}$$

And the speed of sound in the homogenous 2 phase mixture is then:

$$c_m = c' = \sqrt{\gamma' R' T} \tag{4.17}$$

A comparison of the Weber and Wallis methods using a plot of speed of sound ratio vs voidage is shown below. For equation (4.7), the particle velocity and acceleration are assumed to be equal to that of the gas.

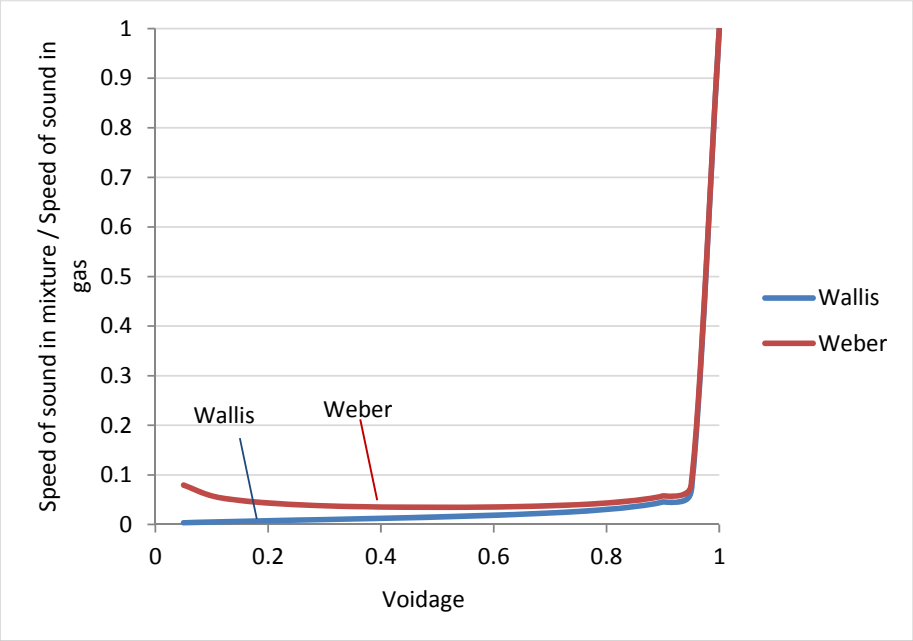

Figure 48: Speed of sound ratio using homogenous conditions for ζ=3333

Zooming in to the typical boiler operating range:

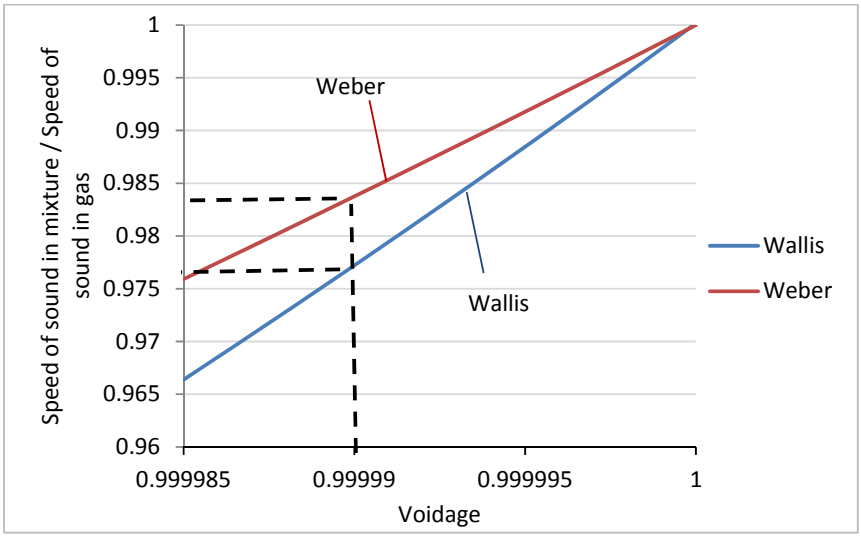

Figure 49: Typical boiler flue gas range using homogenous conditions for ζ=3333

From Figure 49, it can be seen that the speed of sound ratio is in the 97.75-98.35% range for both equations, for voidage of 0.99999. This is slightly lower than the >99% determined from the first analysis using the equation from Fan and Zhu. In this case, this implies that by not accounting for the 2 phase flow, a 2.25% error on the speed of sound can occur which results in a 4.5% error in

the calculated temperature. Accounting for the solid particles by using the "pseudo-gas" properties proposed by Wallis instead of the pure gas properties will mitigate the error when calculating the temperature from the sound velocity.

The natural follow up question to the above analysis, is whether this varies for different boiler operating conditions such as its load. This is considered hereafter. It has already been established that the speed of sound ratio can be expressed as a function of the voidage, which in turn, is a function of the mass loading ratio and the density ratio of the 2 phases of the mixture.

Consider first the density ratio. At a lower load condition, the furnace exit temperature will be lower and this will affect the density ratio since the gas density varies with the temperature but the solid density remains fairly constant. The curves plotted on Figure 48 and Figure 49 are specific to a particular density ratio, so new curves can be plotted for a different density ratio. Consider a drastically low gas temperature of 500°C. For such a gas temperature, the gas density would be in the region of 0.5kg/m^3, meaning that the density ratio (ζ) is 2000. The curve is plotted below for the typical boiler range, which in this case is a voidage of 0.999982.

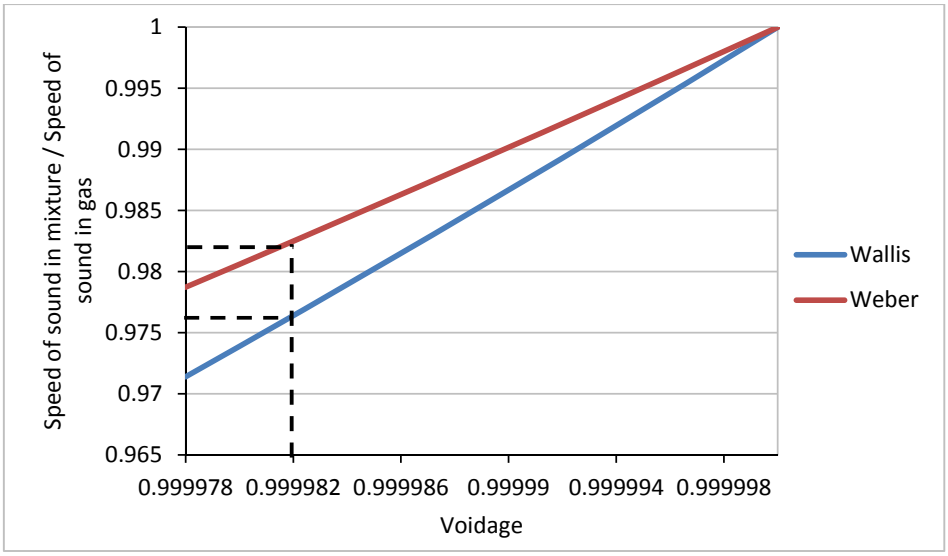

Figure 50: Speed of sound ratio for ζ=3333

It can be seen from Figure 50 that, even at a gas temperature of 500°C, the impact of density on the speed of sound ratio is negligible, as the ratio is still upwards of 97.5%.

The mass ratio, on the other hand, could also vary independently of the load as a result of the amount of excess air supplied to the furnace. On one extreme, any increase in excess air from the condition already considered, would lower the solid to gas mass ratio, and thus increase the voidage. The speed of sound in the mixture then approaches the speed of sound in the pure gas. On the other extreme, the lower limit for excess air is 0kg/s which would mean that only the

stoichiometric amount of air is supplied to the furnace. Boilers are never intended to be operated in this condition, so it can be considered as the absolute minimum excess air condition.

If the MEB calculations for Plant X from chapter 3 are used as a reference, the stoichiometric air requirement is 6 times the coal flow rate and the flue gas mass flow is approximately 7 times the mass flow of coal as opposed to 8.5 which was used in the examples above. Once again, the mass flow of the particles is actually the mass flow of ash, which is taken to be 30% of the mass flow rate of coal. Therefore, the mass loading ratio for the minimum excess air condition is then 0.3/7=0.043. This case is depicted in Figure 51.

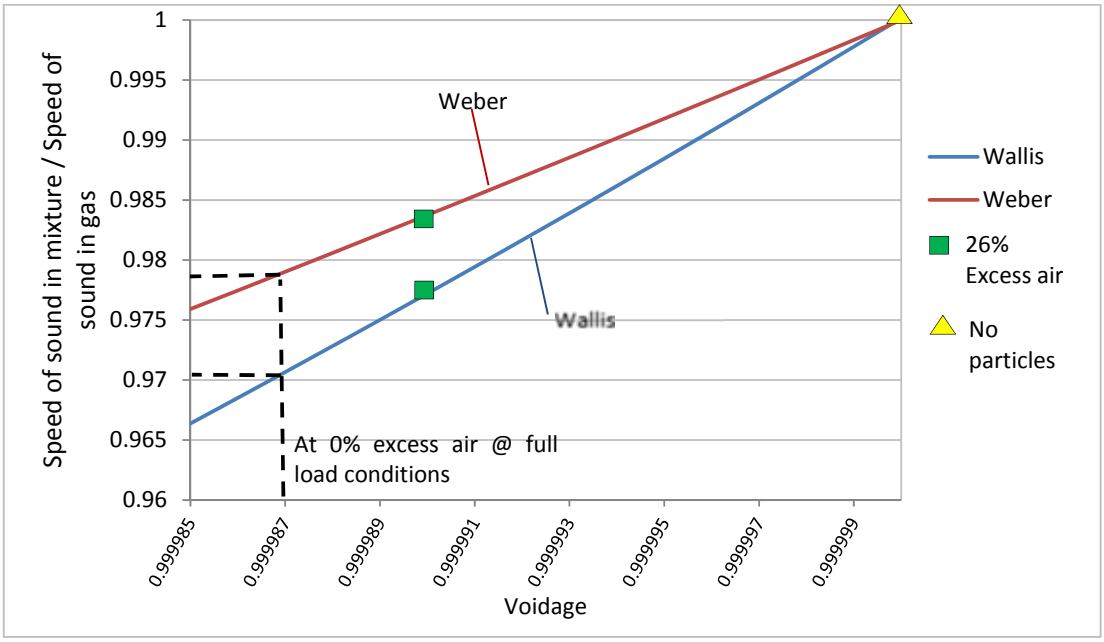

Figure 51: Speed of sound ratio for the 0% excess air condition

It can be seen that even in this extreme abnormal condition, the ratio does not drop lower than 97%. So of all the cases considered above, in the worst case the particles have a 3% impact on the speed of sound. Therefore, not accounting for the particles in the calculation of the temperature could result in an overestimation of temperature of up to 6%. Ultimately, there is sufficient information available at most power plants to allow for good estimates of the "pseudo-gas" properties to ensure that this overestimation is mitigated.

It was stated earlier that this subject is not a particular focus of acoustic pyrometry literature. Perhaps the apparent lack of attention given to the particular subject is due to the fact that for the desired applications, the solid particle concentration is so small that any impact on the speed of sound due to the presence of solid particles is almost negligible, and in the case of higher particle concentrations, can be relatively easily accounted for as shown above.

4.2.4. Temperature profile reconstruction

As mentioned previously, the individual time of flight measurements form one aspect of a typical acoustic pyrometry system. One of the stand out characteristics of the technology is that it affords the possibility of utilising multiple path time of flight measurements to map the temperature profile over an entire plane. The reconstruction of the temperature profile is essentially an inverse problem that requires some form of a deconvolution method to determine the profile. In other words, the time of flight measurements which vary as a result of the unknown temperature profile are used as a means of reconstructing the temperature profile. It is essentially a problem involving image reconstruction from projection data, a concept commonly encountered in fields such as medical imaging [6]. Several methods for the temperature profile reconstruction of acoustic pyrometer systems have been reported in literature. This section investigates this aspect of acoustic pyrometry with applied examples.

i. Overview of approaches in literature

The time of flight which is measured by the acoustic pyrometer is used as a representation of the total path length divided by the average velocity over the path as shown in equation (4.3). However the time of flight can also be expressed as the integral of the reciprocal of the velocity function (or slowness function) over the path length. If $f(x,y)$ is defined as the slowness function over a horizontal plane, then

$$t = \int_0^L \frac{dl}{c(x,y)} = \int_0^L f(x,y)dl \tag{4.18}$$

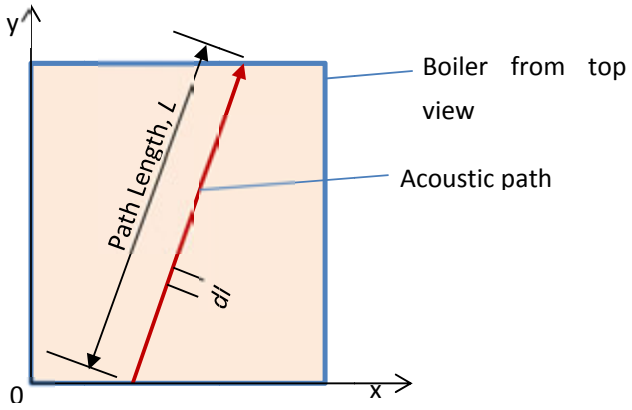

Figure 52: Co-ordinate arrangement of a horizontal plane in boiler furnace

In this sense, the total time of flight measured would be the sum of the times taken over each *dl*, which are in turn dependant on the gas velocity over that discretized segment. Thus, the goal of

the reconstruction is then to determine the slowness (i.e. reciprocal of the velocity) as a function of the x and y coordinates of the plane, using a set of time of flight measurements and known path lengths. Then, from equation (4.6), the temperature function would be given as:

$$T(\mathrm{x},\mathrm{y}) = \frac{1}{\left(f(x,y)\right)^2 \cdot \gamma^2 R^2} \tag{4.19}$$

The method described by Green [40] utilises a Fourier series with a finite number of terms to approximate the slowness function:

$$f(x,y) \simeq \sum_{k,l=0}^{sk,sl} A_{kl} \cos(k\pi X)\cos(l\pi Y) \tag{4.20}$$

where

A_{kl} = Fourier coefficients

k, l = index values in the x and y directions respectively

sk, sl = maximum wavenumber of estimated Fourier series in x and y directions respectively

X = fraction of the total furnace dimension in the x-direction travelled by the sound wave in the x-direction

Y = fraction of the total furnace dimension in the y-direction travelled by the sound wave in the y-direction

Substituting this definition of *f(x,y)* into equation (4.18) for a number of path measurements N_t, results in a set of linear equations to solve for the coefficients A_{kl} in terms of the path start and finish coordinates.

Bramanti et al [6] further discussed the Fourier series method and also introduced a section interpolation method which consisted of 2 primary steps: (i) iteratively determining the function for the temperature along each individual path, from which a sparse matrix can be produced; and (ii) applying an interpolation procedure to reconstruct the temperature over the entire plane.

In addition to the measured times of flight and path lengths, this method also required the temperatures at the start and end of each path. For the first iteration, the average velocity and mean temperature of the path is calculated as usual from equation (4.6). Thereafter, a new estimate of the average velocity can be made using the average value integral:

$$v'_{mk} = \frac{1}{L_k}\int_0^{L_k} \sqrt{\gamma \frac{R}{M} \cdot T(l_k)}\, dl_k \tag{4.21}$$

where

v'_{mk} = average sound velocity along path k (m/s)

L_k = length of path k (m)

$T(l_k)$ = temperature of the path as a function of the length (K)

Clearly, the temperature as a function of the path length needs to be determined to evaluate equation (4.21). In the example given in [6], the temperature function was assumed to be parabolic.

$$T(l_k) = A_k l_k^2 + B_k l_k + C_k \tag{4.22}$$

The coefficients (A_k, B_k, C_k) can be written in terms of the known path length, start and end temperatures and the previously calculated mean.

Thus the evaluation of equation (4.21) can be done. The new mean velocity, v'_{mk} , can be calculated and thus a new estimate of the mean temperature T'_{mk} is calculated This iterative process is repeated until the new estimate and the previous one are within a predefined threshold. The temperature functions for each path as a function of the path length is therefore produced in the form of equation (4.22). These temperature functions are used to produce a sparse temperature grid which is then applied with an interpolation algorithm to produce the complete temperature map.

The method reported by Kleppe et al [49] utilises a similar philosophy, with some slight differences. The temperature profile of each path is initially assumed to be bilinear with the maximum temperature at the peak and the minimum at the start and end points. Sufficient path measurements are taken to determine the maximum and minimum temperatures in terms of the standard deviation of the measurements.

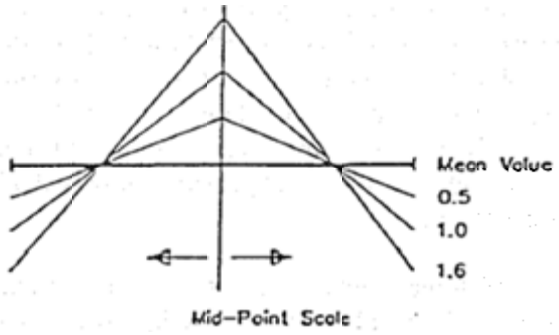

Figure 53: Bilinear profile used in the method described by Kleppe et al [49]

Noting that every endpoint may be the endpoint for a number of paths, the maximum and minimum temperatures are iteratively scaled by factors of standard deviations to converge to the

best fit for all of the measured path data. Once again, the temperature functions are used to form a sparse matrix which obviously does not contain any information in areas not traversed by a path. A Bezier function is used to produce a polynomial approximation of the temperature profile. Comparisons of line integrals of this reconstructed profile with measured data can be used to iteratively adjust the scale factors to continuously improve the reconstruction.

Another method which was mentioned by Bramanti et al [6] was a method utilising uniform sampling and a least squares solution. This method has also been demonstrated in more detail in [26], [35], [45] and [46]. The results of this method were deemed to be very similar to those using the Fourier technique. It is discussed in more detail below.

ii. Least squares method and Algebraic Reconstruction Technique (ART)

The least squares method involves dividing the temperature plane into an NxM grid as shown in Figure 54 where each block is assumed to be at a uniform temperature, i.e. a sound wave will travel at the same velocity at any point within a specific block. Thus for a number of blocks, N_i, the time of flight for path k would be given by the sum of the time of flights in each block that the path passes through, as shown by equation (4.23)

$$t_k = \sum_{i=1}^{N_i} f_i \Delta L_{ki} \tag{4.23}$$

f_i = reciprocal of the velocity of the sound in the i^{th} block

ΔL_{ki} = distance traversed by path k in the i^{th} block

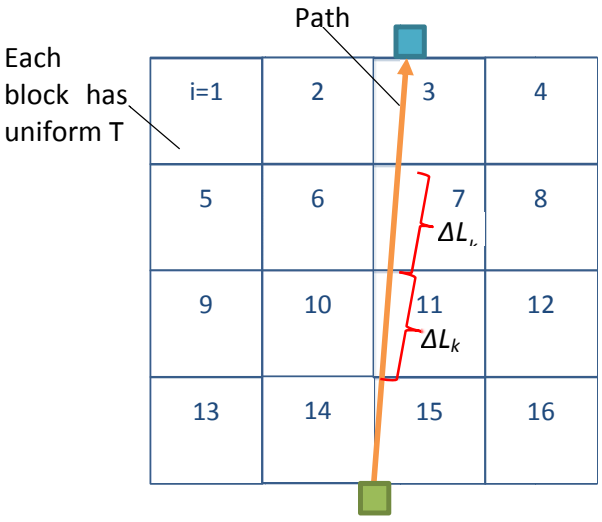

Figure 54: Temperature plane discretization for least squares method

A least squares solution is then usually applied to estimate the reciprocal of the velocity, f_i, for each block *i*. The least squares solution is solved as follows.

For each time of flight measurement, t_k, the error between the measured time of flight and the actual time of flight is:

$$error_k = t_k - t'_k = t_k - \sum_{i=1}^{N_i} f_i \Delta l_{ki} \tag{4.24}$$

For N_t TOF measurements, the total error would be the sum of the errors for each path. The objective of the least squares method is to determine the velocity distribution that minimizes this total error by taking the partial derivative and equating to zero. It follows:

$$\frac{\partial}{\partial f_i} \sum_{k=1}^{N_t} (t_k - \sum_{i=1}^{N_i} f_i \Delta l_{ki})^2 = 0 \tag{4.25}$$

It can be shown from linear algebra by a lengthy derivation that this minimum error is actually the projection of the vector **t**. It follows that, in matrix form:

$$\mathbf{L}^T \cdot \mathbf{L} \cdot \mathbf{f} = \mathbf{L}^T \cdot \mathbf{t} \tag{4.26}$$

And

$$\mathbf{f} = \left(\mathbf{L}^T \cdot \mathbf{L} \cdot\right)^{-1} \mathbf{L}^T \cdot \mathbf{t} \tag{4.27}$$

Where

$$\mathbf{L} = \begin{pmatrix} \Delta L_{11} & \Delta L_{12} & \cdots & \Delta L_{1i} \\ \Delta L_{21} & \Delta L_{22} & \cdots & \Delta L_{2i} \\ \vdots & \vdots & \ddots & \vdots \\ \Delta L_{k1} & \Delta L_{k2} & \cdots & \Delta L_{ki} \end{pmatrix}, \ \mathbf{f} = \begin{pmatrix} f_1 \\ f_2 \\ \vdots \\ f_i \end{pmatrix}, \ \mathbf{t} = \begin{pmatrix} t_1 \\ t_2 \\ \vdots \\ t_k \end{pmatrix}$$

The matrix **L** is easily populated based on the geometry of the chosen grid and path dimensions (as shown in Figure 54) and thus the vector **f** can be solved.

Thereafter, from equation (4.19), the temperature, T_i, of each block can be determined:

$$T_i = \frac{1}{f_i^2 \gamma R} \tag{4.28}$$

It should be noted that the temperature grid and the temperature plane do not have to be square. In fact they do not even have to be rectangular at all. This method has even been demonstrated with circular shapes [45] as shown in Figure 55.

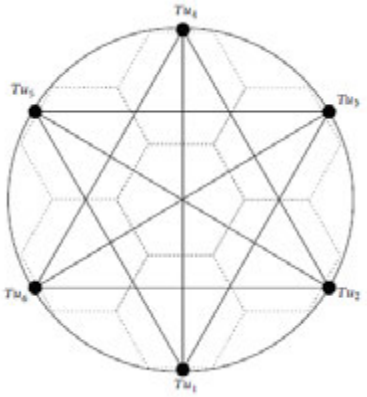

Figure 55: Example of temperature grid of a circular plane [45]

Zhang et al [46] expanded the least squares method, by pointing out that in cases where the matrix *L* is of full rank and M>N, then the problem is overdetermined and does not have an exact solution. They also stated that the problem is ill-conditioned and can sometimes produce negative temperature values, which are mathematically consistent but completely physically impossible. As a result, they employed the algebraic reconstruction technique (ART), which is an iterative method of solving systems of linear equations which was introduced in the field of image reconstruction by Gordon et al [60]. For the linear system above where **Lf=t**, the ART formula is given as:

$$f^{k+1} = f^{k} + \lambda \frac{t_j - \langle l_j, f^k \rangle}{\|l_j\|^2} l_j \tag{4.29}$$

Where

k=0,1,2,… is iterated until the difference between the solution of the current iteration (*k*+1) and the previous iteration (*k*) differ by a predefined threshold.

$j = k \mod \mathrm{M} + 1$ (M is the number of rows in matrix **L**)

f^{k+1} = vector **f** for the current iteration

f^{k} = vector **f** for the previous iteration

λ = relaxation parameter

l_j = *j*th row of matrix **L**

$\langle .., .. \rangle$ = vector inner product

Zhang et al [46] applied this ART method using the least squares solution as an initialisation vector to speed up the solution. The solution here is once again the vector **f** representing the 'slowness' in every *i*th block. And thereafter, as before, the temperature matrix can be calculated from (4.28).

For many practical purposes, the zonal temperature matrix of a resolution such as the one shown in Figure 54 may be adequate. It divides the furnace into 16 divisions, each represented by a single temperature value, which can be very useful to determine hotspots in the furnace. However, to reconstruct a more detailed temperature profile, there are generally 2 potential ways to do this. The obvious way to obtain better temperature profile resolution is to use a more finely discretized temperature grid. This does, however, mean that the number of paths would have to also increase since the solution to the linear system does not exist if $N_t<N_i$ (i.e. the number of paths must be at least equal to the number of discrete elements as there is one equation per path). Increasing the number of paths would obviously also come at a greater cost and so it would not be ideal.

What has been described in literature is the use of interpolation algorithms applied to the sparse matrix to produce the complete temperature profile. Examples of interpolation algorithms are bicubic [46] and multiquadratic radial basis function (RBF) interpolation [45].

The ART method applied together with multiquadratic RBF interpolation is demonstrated in this study. The multiquadratic interpolation is applied as per the work of Shen et al [45].

iii. Generation of simulated time of flight data

In order to demonstrate the application of the temperature reconstruction methods, multiple acoustic path time of flight measurements are required. Unfortunately, this was not possible for this project due to the limited equipment that was available to experiment with. However, it is possible to apply reconstruction algorithms to simulate time of flight data. The use of simulated time of flight data is not unique to this study. It is commonly done in literature.

Reconstruction using simulated TOF data involves defining a temperature function over a horizontal x-y plane. Of course if the temperature profile is defined, then for given flue gas properties, the profile of the reciprocal of the velocity, $f(x,y)$, is easily determined from equation (4.19). The acoustic paths are defined by their start and end x-y coordinates, determined for a chosen arrangement of acoustic pyrometer generators and receivers. The term “start and end coordinates” is used mainly for the mathematical consistency, but does not necessarily have any relevance to a physical direction of the path. Then, time of flight “measurements” are determined by taking line integrals of $f(x,y)$ over all the paths, as per equation (4.18). These integrated times of flights are then used as if they were actual measurements, as inputs to the reconstruction algorithm.

In order to generate the data, the path geometry must be established. Many of the literature sources that have been studied demonstrate the reconstruction for an AP layout that resembles

the 8 instrument, 24 path setup, typical of those products that use transceivers that functions as both a generator and a receiver.

For this study, a layout consisting of 4 generator instruments, and 8 receiver instruments is considered, which also consists of 24 acoustic paths. The size of the furnace to be considered is not critical as this is purely a mathematical exercise, so an arbitrary 14m x 14m furnace is chosen. The layout is depicted below on Figure 56.

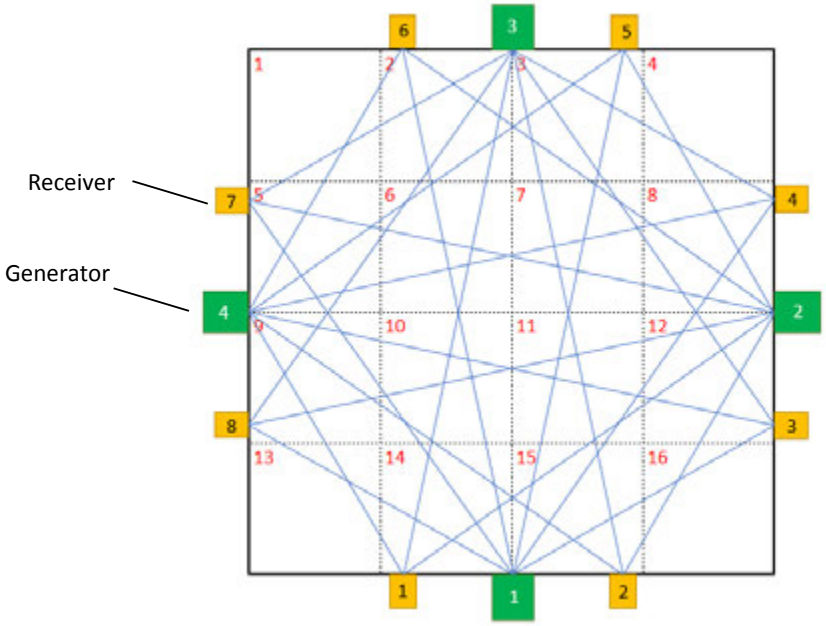

Figure 56: AP layout consisting of 4 generators and 8 receivers producing a total of 24 paths

The plane is discretised into a 4x4 grid, which divides the space into 16 blocks. The blocks are numbered as shown by the red numbers.

There is of course a multitude of different ways that this number of instruments could be arranged. One of the key factors in choosing this arrangement was to provide symmetrical coverage of the furnace, and to ensure the highest level of interdependency in the linear system, i.e. to have each path pass through at least 3 of the discretised blocks.

The numbering of the paths is not shown on Figure 56, for the sake of clarity, but is defined in the table below.

Table 14: Path numbering

Path	From Generator	To Receiver	Path	From Generator	To Receiver
1	1	8	13	3	4
2	1	7	14	3	3
3	1	6	15	3	2
4	1	5	16	3	1
5	1	4	17	3	8
6	1	3	18	3	7
7	2	2	19	4	6
8	2	1	20	4	5
9	2	8	21	4	4
10	2	7	22	4	3
11	2	6	23	4	2
12	2	5	24	4	1

With the geometry established, it can then be applied to a temperature distribution to obtain the line integrals. Because this is a purely mathematical reconstruction, the temperature needs to be expressed as a function of x and y. The temperature functions used here are adapted from the study by Shen et al [45]. Four temperature functions are considered:

$$T_1(x,y) = 1100 + 300 \times \sin\left(\frac{\pi}{14}x\right)\sin\left(\frac{\pi}{14}y\right) \tag{4.30}$$

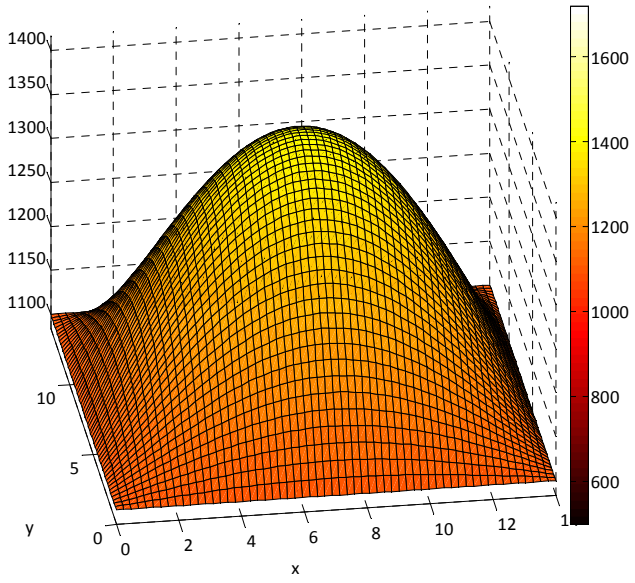

Figure 57: Temperature profile 1. One peak symmetrical distribution with the peak at the centre of the furnace and a gradual gradient from walls to centre

$$T_2(x,y) = 800 + 800 \times \sin\left(\frac{\pi}{14}x\right)\sin\left(\frac{\pi}{14}y\right) \tag{4.31}$$

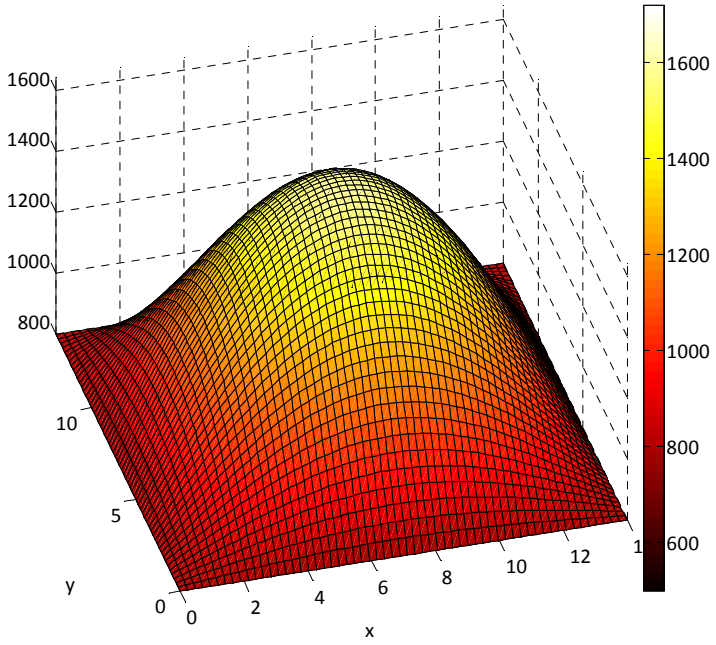

Figure 58: Temperature profile 2. One peak symmetrical distribution with the peak at the centre of the furnace and a steep gradient from walls to centre

$$T_3(x,y) = 1000 + 600 \times e^{(-((x-7)^2+(y-4)^2)/100)} \tag{4.32}$$

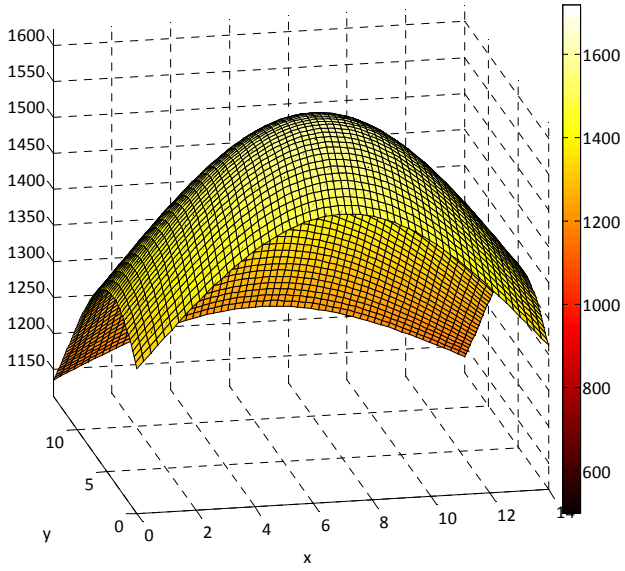

Figure 59: Temperature profile 3. One peak asymmetrical with the peak skewed from the centre of the furnace

$$T_4(x,y) = 800 + 800 \times e^{-20\left(\left(\frac{x}{14}-\frac{1}{3}\right)^2+\left(\frac{y}{12}-\frac{2}{3}\right)^2\right)} + 800 \times e^{-\left(20\left(\frac{x}{14}-\frac{2}{3}\right)^2+\left(\frac{y}{12}-\frac{1}{3}\right)^2\right)} \quad (4.33)$$

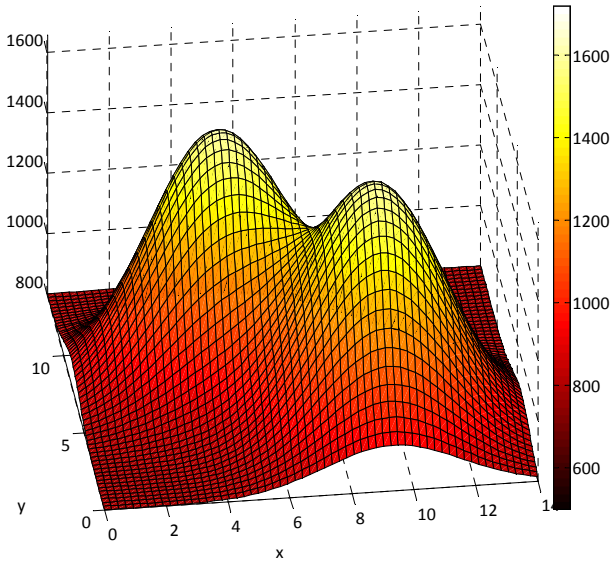

Figure 60: Temperature profile 4. Two peak profile with different peaks

Line integral time of flight data is simulated for all paths for each of these distributions and used as inputs to the reconstruction algorithm. The other parameters required for the reconstruction are the distance matrix **L** and the midpoints of the discretised blocks, all of which are calculated from the geometry. The results of the reconstruction together with the original profiles are depicted below. The generation of the simulated data and the reconstruction was performed by means of a Matlab code, which can be found in Appendix E.

iv. **Temperature reconstruction results**

a) Temperature Function $T_1(x,y)$

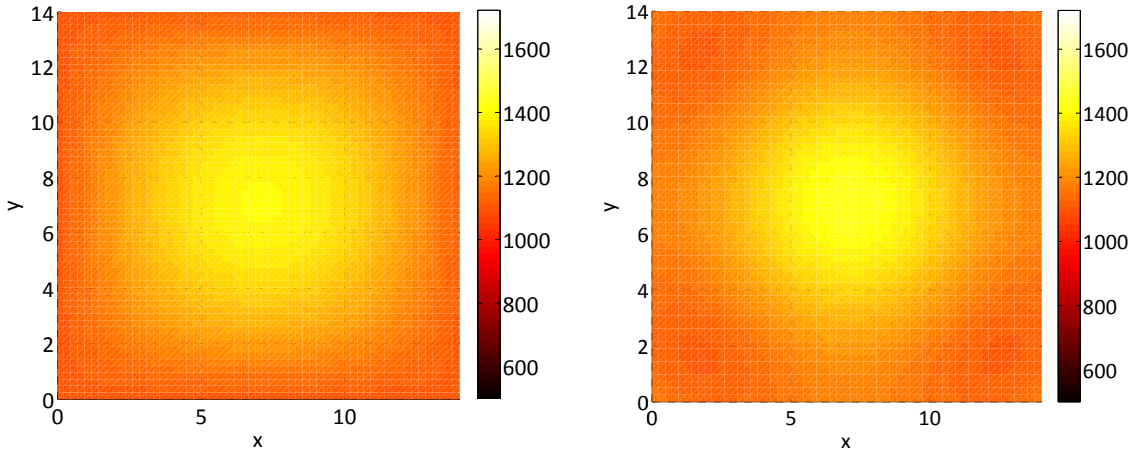

Figure 61: Comparison of original (left) and reconstructed (right) 1 peak profile with gradual temperature increase from wall to centre

b) Temperature Function $T_2(x,y)$

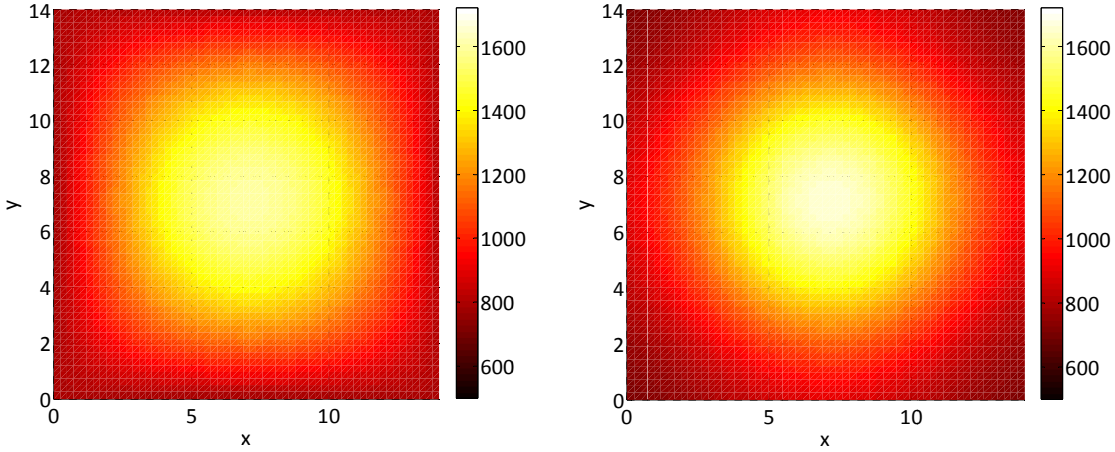

Figure 62: Comparison of original (left) and reconstructed (right) 1 peak profile with steep temperature increase from wall to centre

c) Temperature Function $T_3(x,y)$

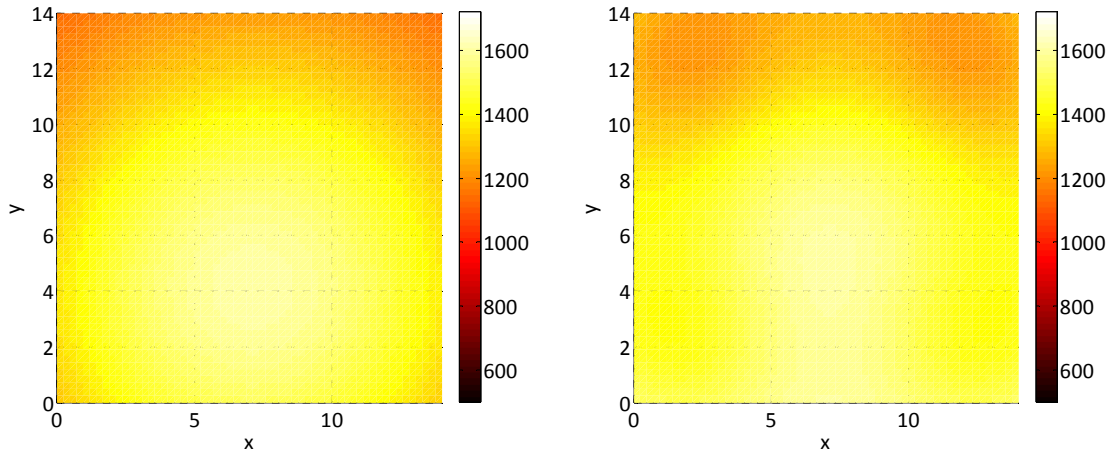

Figure 63: Comparison of original (left) and reconstructed (right) 1 peak asymmetrical profile

d) Temperature Function $T_4(x,y)$

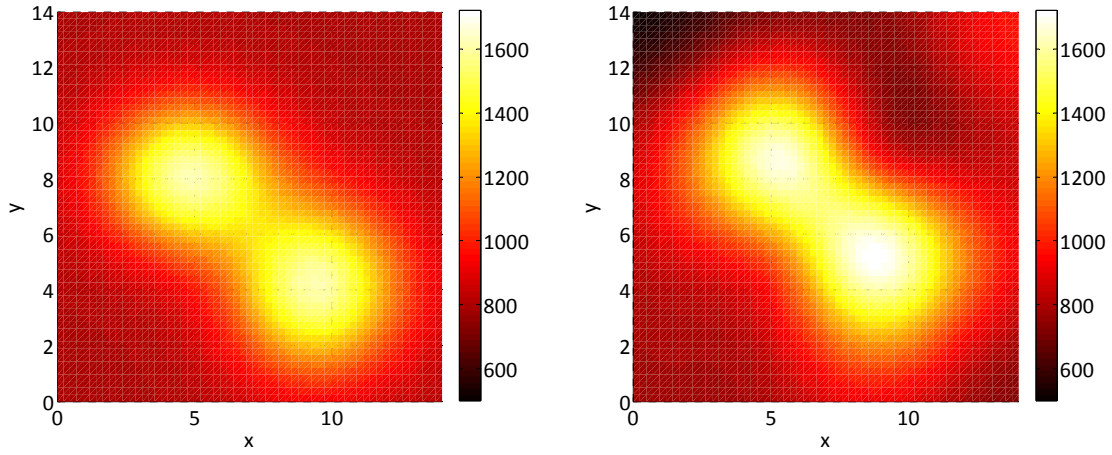

Figure 64: Comparison of original (left) and reconstructed (right) 2 peak profile

e) Analysis and discussion

In all 4 cases, from a first glance, the reconstructed profiles show a good visual correlation to the original profiles. This visual correlation must be further consolidated by determining the error in the reconstructed profile. A 15x15 point matrix is defined over the entire cross section providing 225 points of comparison between the original and reconstructed profile in each case. The mean absolute error is defined by:

$$E_{mean} = \frac{1}{225}\sum_{ii=1}^{225}\frac{\left|T_{recon.ii} - T_{original.ii}\right|}{T_{original.ii}} \times 100\% \quad (4.34)$$

The calculated errors are listed in Table 15.

Table 15: Errors of reconstructed profiles

Temperature profile	**Mean error E_{mean} (%)**	**Maximum error (%)**
$T_1(x,y)$	2.32	6.75
$T_2(x,y)$	4.80	13.08
$T_3(x,y)$	2.39	15.59
$T_4(x,y)$	7.08	22.17

As can be seen on Table 15, the mean error between the original and reconstructed profiles is between 2 and 7%. The highest mean error is 7.08% for the 2 peak profile. This is not surprising as it is the most intricate profile presented here. This does not necessarily mean that the method becomes inaccurate for this type of profile. The result is very specific to the arrangement of the acoustic paths and the specific position of the peak.

Of a greater concern is the fact that the maximum error increases from the simplest gradual gradient profile to the most complicated. What is noted is that the maximum error in all cases is actually along the edges of the reconstructed profile. This is a noteworthy observation because in terms of the interpolation method, there are 16 points from which the profile is reconstructed, which are the midpoints of the discretised elements. This means that the outermost points which are used in the interpolation are at coordinates (1.75;1.75), (1.75;12.25), (12.25;1.75) and (12.25;12.25). This means that the outermost 1.75m on all sides of the plane, is estimated based only on the inner points. This is depicted below.

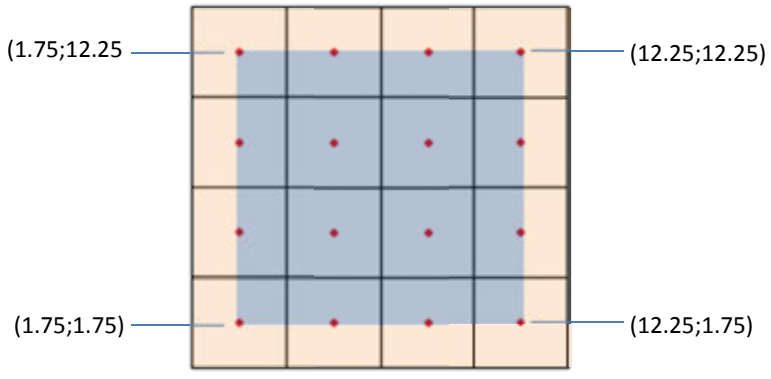

Figure 65: Depiction of outer frame where there are only inner points for interpolation

When this outermost area is not considered in the error analysis, a new 15x15 matrix is defined for x and y values from 1.75m to 12.25m. The results are as follows.

Table 16: Errors of reconstructed profiles excluding outermost 1.75m on all sides

Temperature profile	**Mean error E_{mean} (%)**	**Maximum error (%)**
$T_1(x,y)$	1.81	3.31
$T_2(x,y)$	4.00	9.59
$T_3(x,y)$	1.21	1.55
$T_4(x,y)$	6.38	20.67

On Table 16, it can be seen that with outermost area excluded, the mean and maximum errors for all cases improved, especially in the case of the single peak asymmetrical profile. However, for the 2-peak profile, the maximum error is still substantial. This can be a concern in practice, as in the real world, the original profile is not known. The reconstruction still provides a very useful qualitative result in terms of the general temperature distribution, which in and of itself can offer massive insight that can advise operating decisions in terms of balancing the combustion evenly.

One should be tentative in considering any specific actual value to be accurate, particularly if the profile is intricate like the one investigated. Overall, given that the furnace is discretised into only 16 blocks, it shows that the technique is quite effective at detecting abnormalities such as the hotspots of the 2 peak profile, even if the error on certain individual points can be quite high. A typical boiler profile is generally considered to be most similar to the first profile, and the results for this case are excellent.

There are 2 key geometrical factors that can be considered in an effort to improve the reconstruction accuracy. These are the number of paths and the number of discretised elements. These 2 factors are interrelated, with the number of paths being the limiting factor as the number of paths must be equal to or greater than the number of discretised elements for the linear system to have a solution. Perhaps a future more detailed study focused solely on temperature profile reconstruction can look at optimizing the geometry.

Another interesting further study would be to test these methods on a boiler and to compare the results with a temperature profile obtained by high velocity thermocouple traverse measurements. Unfortunately, there was only one acoustic generator and receiver available for this study, and thus the testing of the AP which follows focuses on the information that can be gained from individual path measurements.

4.3. Direct methods experimental testing

As per the objectives for this study, it was endeavoured to physically test an acoustic pyrometer on an actual boiler. The intention is also to compare the acoustic pyrometer measurements with those obtained from the MEB. Once again, the plant chosen for this testing is the same test case unit (Plant X Unit 6) as for the indirect methods.

In addition to the primary test unit, one of the other units, unit 2, at Plant X has been the subject of previous combustion projects which have resulted in the economiser location being modified with 6 ports along the side walls of the boiler backpass. These ports were installed for traverse measurements to enable access to flue gas velocity and temperature measurements. These ports can also be used for the acoustic pyrometer.

It must be noted that the results of all these tests are not exhaustive. Due to the fact that the available equipment was very limited, it was neither a complete nor a fixed installation of an acoustic pyrometer system. The intention of these tests was to be a form of preliminary testing, primarily to gain some insight into the operation of the acoustic pyrometer and to build some confidence in its capabilities, particularly considering the high ash content of the South African coals used in Eskom power plants.

4.3.1. Equipment setup

i. **Acoustic pyrometer**

The acoustic pyrometer used for the test was the PyroMetrix AP-204 acoustic pyrometer manufactured by Enertechnix, as mentioned in 4.2.1 and depicted in Figure 41.

A permanent full installation would be fixed in position and would consist of multiple generators and receiver combinations. In this case, the only equipment available for the test was a single generator and a single receiver, allowing for only 1 temperature path to be measured at a given moment in time. Another reason why the installation was not fixed was to allow it to be moved to different locations and units and also to avoid a laborious commercial process required for a permanent plant modification.

To use the acoustic pyrometer in this temporary installation, the following was also required:

- Scaffolding platforms for the generator and receiver
- Air supply to the generator, preferably >8 bar. A compressor was used.
- Openings on the furnace wall for the generator and receiver tubes.

The signal data was collected from the acoustic pyrometer OEM software already installed on the signal processing computer (SPC).

ii. Radiation pyrometers

The permanently installed radiation pyrometers (RP) at Plant X which are used for detecting flame presence did not require any additional setup. The temperature readings from these instruments are linked to the plant's DCS, thus making the data acquisition straight forward.

There are in total 8 RPs installed at the boiler. However for this study the 4 of interest are at 29m boiler elevation, 2 on the right hand side and 2 on the left hand side. The pyrometers are the Siemens Ardometer MPZ20 type as depicted below, fitted with the standard lens.

Figure 66: Siemens Ardometer radiation pyrometer [61]

iii. Thermocouples

At unit 2, two thermocouple grids have been installed; one above and one below the economiser. The thermocouple grids consist in total of 48 non-shielded and 36 radiation shielded type K thermocouples. Data from thermocouples was captured via a thermocouple data logger. The data logger used was a data Taker DT600 Series 3. The thermocouple data logger was limited to only 30 thermocouple readings, so the radiation shielded thermocouples were prioritized. The accuracy of the data logger itself was checked and verified by simulating a 300°C signal to each input using an ERO Electronic Memocal 2000, and the largest deviation was found to be 1.9°C, or 0.63%.

4.3.2. Testing Locations

i. **Furnace exit**

Given the temporary nature of the setup, the location was completely dependent on existing access ports on the boiler. The location on the furnace side most representative of the furnace exit and with available space to incorporate the acoustic generator was identified at 29m level, which is just above the highest row of burners, at the same level of the upper set of radiation pyrometers. It is not the ideal description of "furnace exit", which is normally considered to be just before the first superheater, but it provides the easiest access, given that the number of inspection ports on the boiler is very limited.

Figure 67 and Figure 68 depict the position of the acoustic generator, and the relative positions of the acoustic receivers for the 2 paths which were tested.

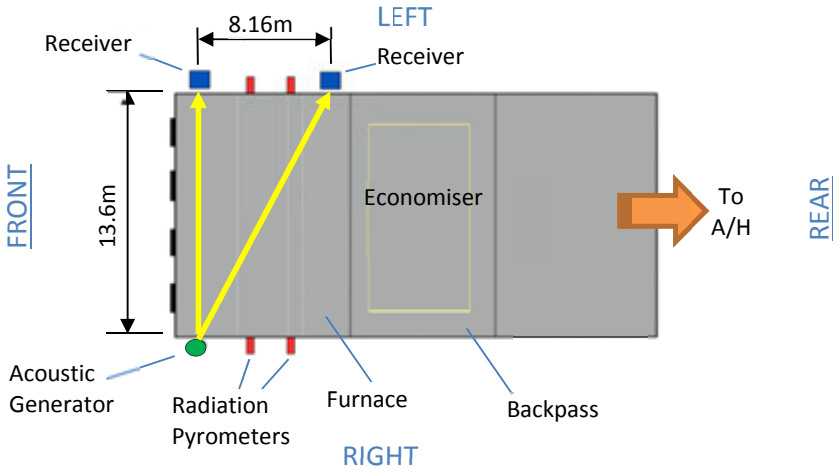

Figure 67: Boiler top view depicting furnace acoustic paths

The first path is a direct horizontal path from right to left hand side of the boiler very close to the front wall. The second is a diagonal across the boiler passing through the centre of the furnace, with the receiver also offset at a height of 3.57m above the generator. The front wall path was tested on both unit 2 and unit 6. The diagonal path was only tested on unit 6, but for 2 different loads, full load and approximately 75% of full load.

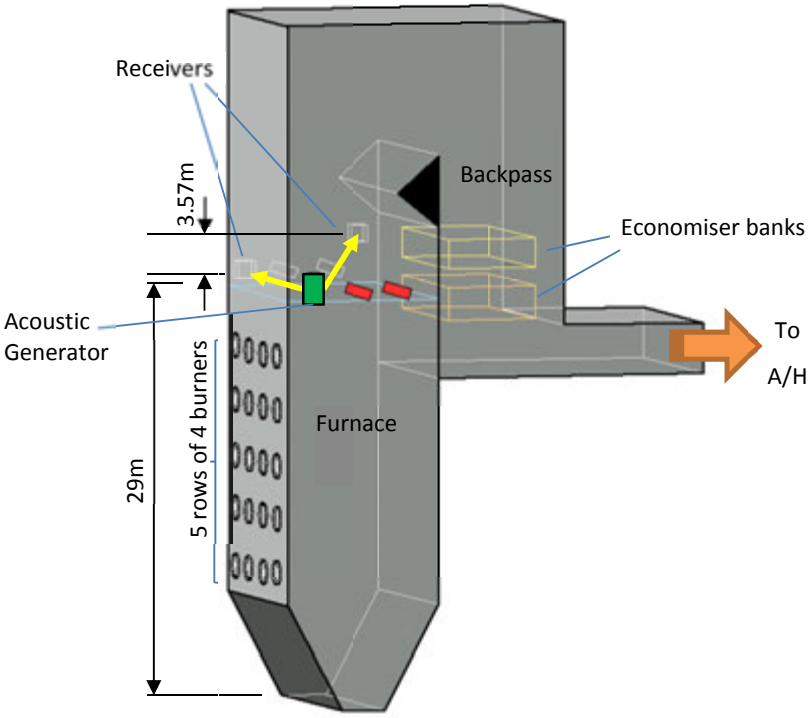

Figure 68: Boiler 3D view depicting furnace acoustic paths

ii. Economiser level

This location was only tested on unit 2. In order to make use of the traversing ports, the standard acoustic pyrometer barrel and receiver tubes had to be extended.

As can be seen on Figure 69, this economiser location on unit 2 also has two thermocouple grids installed, one above the economiser and one below the economiser. It would have been ideal if the ports were at the same level as one of the thermocouple grids. In this way, a direct comparison could have been made between the acoustic pyrometer and the thermocouples. With the existing layout, the temperature between the banks had to be estimated based on the thermocouple readings before and after the economiser, and then compared with the readings of the acoustic pyrometer.

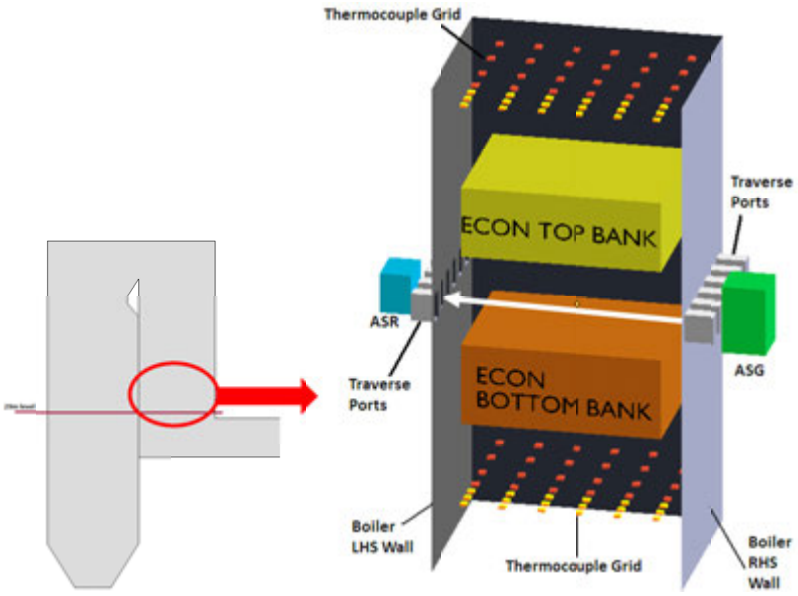

Figure 69: Testing location at Plant X unit 2 economiser

The rationale behind the installation of the 2 thermocouple grids is to determine the section averaged flue gas temperature above and below the economiser and then calculate the flue gas mass flow rate by performing an energy balance across the economiser. Although beyond the scope of this study, this is another reason to perform some testing in this location. It is envisaged that the AP may prove to be an alternative to the thermocouple grid for this application, which can be taken up in a future study.

4.3.3. Testing Limitations

The testing method was subject to the following limitations that must be considered when analysing the results:

- The AP equipment was not fixed to the boiler, but rather temporarily placed on a scaffold platform height adjusted so that the tubes line up with the boiler ports.
- Only 1 generator and receiver combination was available for the test.
- For the unit 2 economizer tests, only 30 of the thermocouple readings could be logged.
- The port used for the ASG for the furnace measurements was not ideally located as the port is very close to the front wall of the boiler. The OEM recommends that the ASG is positioned at least 1m from any wall to minimize impact of reflection of sound waves on the boiler walls.
- The location called the furnace exit is not the location typically defined as furnace exit. The testing location is actually much closer to the burners, where there is potentially much greater temperature fluctuation and gradients across the furnace.

4.3.4. AP Time of flight detection

Time of flight determination is the core of acoustic pyrometry, and for this experimental study time of flight was established in 2 ways: (i) by utilising the proprietary PyroMetrix software Version 255, and (ii) by means of an ad-hoc time of flight detection algorithm developed specifically for this study.

i. TOF detection using PyroMetrix Software

The signal processing computer (SPC) that is connected to the AP equipment records voltage signals from both the acoustic signal generator (ASG) and acoustic signal receiver (ASR) microphones during operation. The ASG signal input is called AST which refers to the Acoustic Signal Trigger. The SPC processes the signals utilising the built-in time of flight (TOF) detection algorithm. For the purposes of this study, the SPC connected to the pyrometer equipment was used just for the data acquisition of the raw AST and ASR signals. These acquired signals were later run through the latest version of PyroMetrix software to determine the time of flight. The software is designed primarily to be used for real time TOF detection; however it is also capable of post processing any recorded AST and ASR signal data offline. An example of the signals obtained from the software is shown on Figure 70.

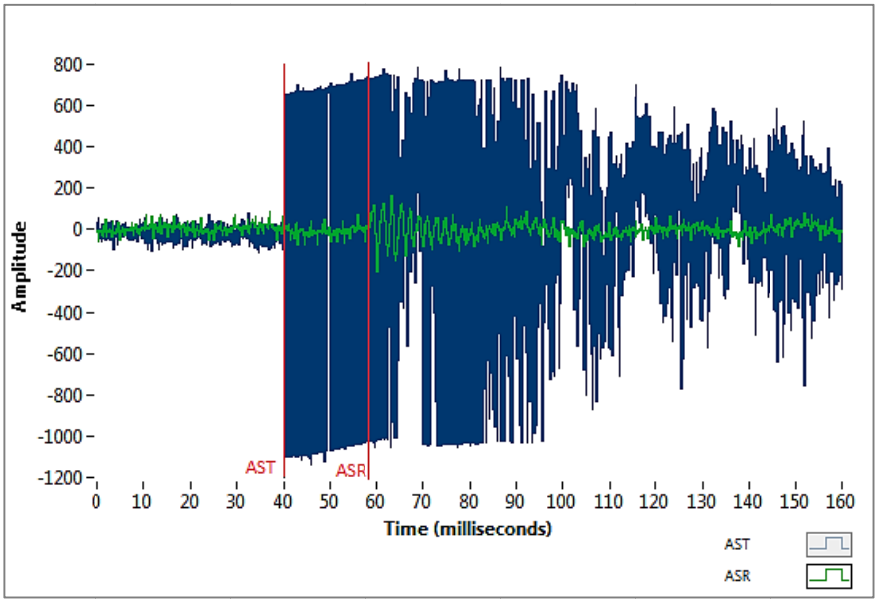

Figure 70: Example of AST and ASR signals processed through PyroMetrix software showing examples of AST and ASR event detections

What should also be noted is that it is the raw TOF that is obtained from the software. The raw TOF refers to the time of flight for the sound to travel from the AST microphone to the ASR

microphone. This raw TOF is higher than the actual time of flight in the furnace as it includes the time which the sound travels through the tubes delivering the sound into the boiler and to the receiver microphone. The software is able to accept inputs specifying the physical data for the connecting tubes, in order to determine the actual time of flight through the gas and subsequently the average temperature, however these calculations were done manually. The software was only used to obtain raw TOF measurements.

The time-of-flight algorithm is proprietary information, and was not explored in detail.

ii. Ad-hoc TOF detection method

Due to the fact that the PyroMetrix algorithm is not fully detailed, a time of flight detection method was developed specifically for this study. This serves to both demonstrate how such a system can be implemented, and also to provide a data set for comparison to determine whether similar time of flight values can be obtained via an independent method.

The cross correlation method mentioned in the literature study was considered as it has been previously applied to pneumatic acoustic pyrometers [42]. However, it becomes apparent that it is very difficult to obtain any sort of correlation between the AST and ASR signal with this type of method. This is due to the randomness and clipping of the AST signal as shown in Figure 71,

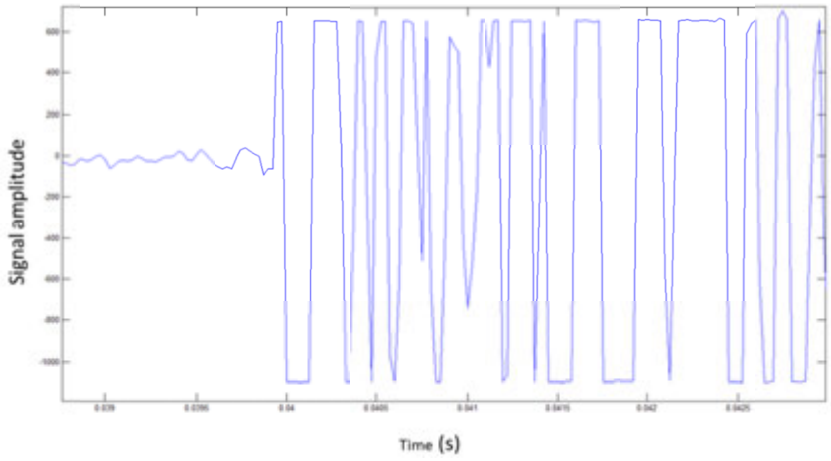

Figure 71: Example of AST Signal Zoomed in on the time scale

It is suspected that this signal is significantly altered due to the arrangement of tubes from the actual pneumatic cylinder to the microphone. The AST signal is only of use to determine the incident time of the ASG sound wave, as it contains a very distinct sharp rise wave front. This can be detected by straightforward threshold detection.

On the other end, the ASR event time needs to also be determined. A method involving the use of Fourier transform, signal filtering and threshold detection was developed that is used to

determine the event time of the ASR signal independently. This method is not fully automated but the steps are depicted in Figure 72. A Matlab code was developed to perform the analysis and is fully detailed in Appendix F.

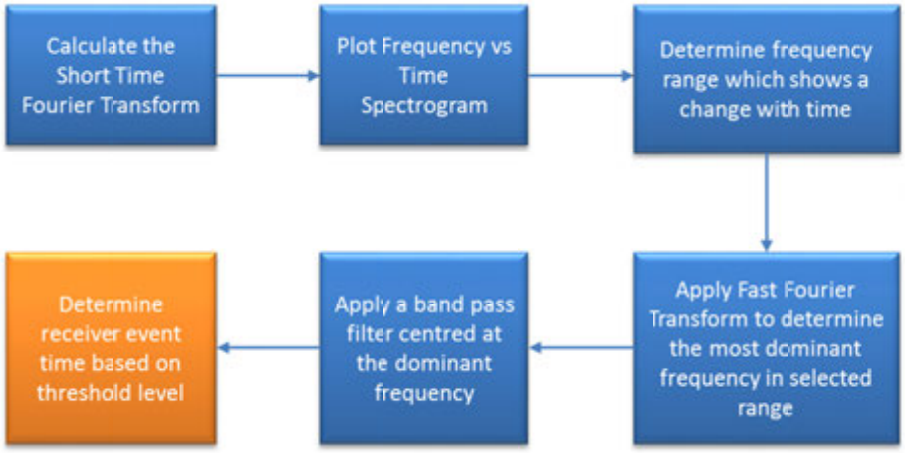

Figure 72: TOF detection procedure

The short time Fourier transform (STFT) is applied to the ASR signal in order to perform a frequency-time analysis. The STFT is plotted as a spectrogram, an example of which is shown in Figure 73.

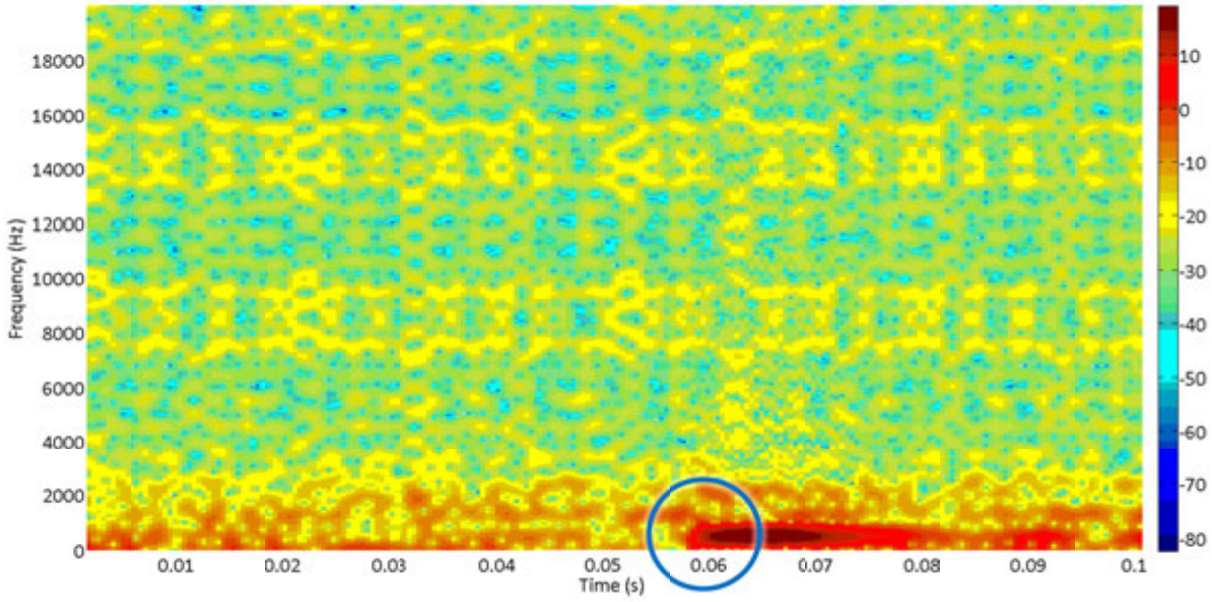

Figure 73: Example of ASR spectrogram

The y-axis of the spectrogram represents the frequency and the x-axis represents the time scale, with the colour map indicating the signal strength over both the time and frequency domain. It can be seen that over most of the frequency range, the signal seems to follow a somewhat recurring pattern. In other words, for most of the frequency range there is no significant change in

the magnitude of the signal over the entire time scale, which is indicative of consistent background noise.

The blue circle, however, towards the lower right of the figure highlights a frequency band in which the signal strength has clearly increased at a certain point in time indicating that the AP signal is being detected in this frequency range. So from the spectrogram, the frequency range for the analysis can be narrowed down, however this type of plot does not offer sufficient clarity and resolution in the time domain to establish the time of flight, thus further steps are required, using the Fast Fourier Transform (FFT).

In instances where there is a high signal to noise ratio, the STFT is not necessary, since the frequency band which has the highest magnitude would represent the frequency in which the acoustic pyrometer signal can be detected, as is the case for the signal depicted in Figure 73. Figure 74 shows this signal in the time domain demonstrating the high signal to noise ratio.

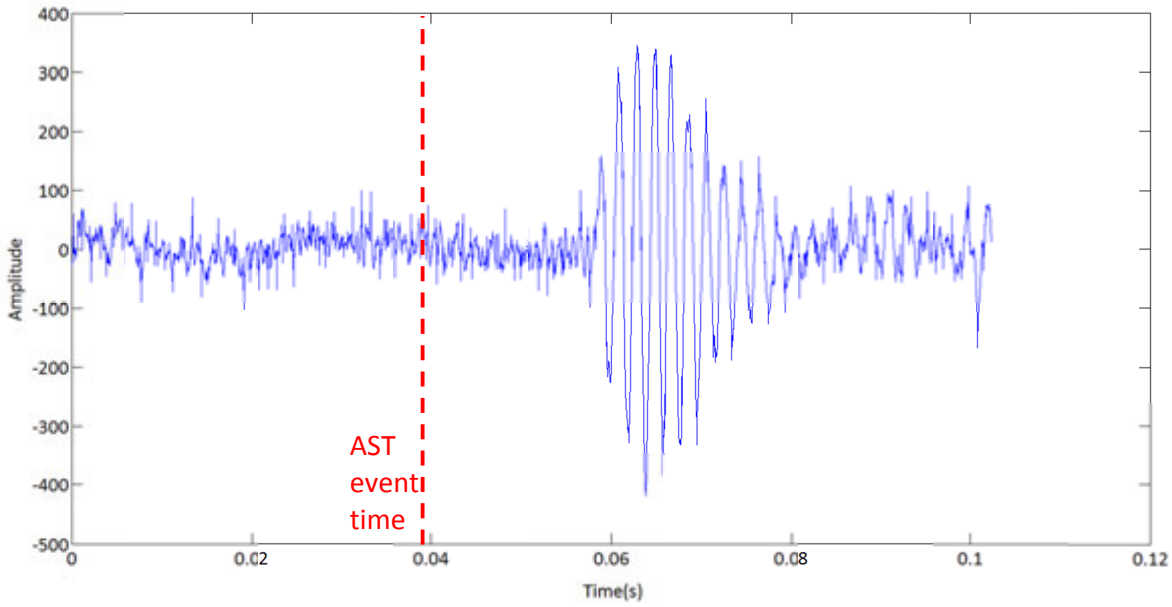

Figure 74: Example of ASR time domain signal with high signal to noise ratio

In this case one can jump straight to the FFT algorithm as it would immediately identify the frequency to be used for filtering. Figure 75 shows how the dominant frequency in the receiver signal can be easily identified from the FFT.

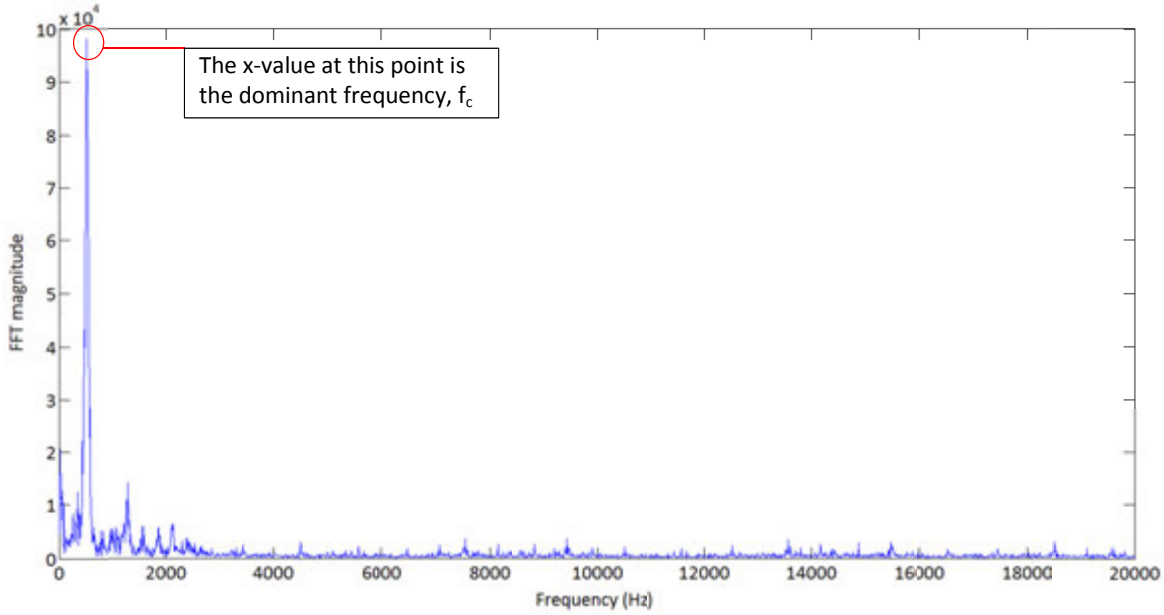

Figure 75: Example of FFT of signal with high signal to noise ratio

Consider now a case as depicted in Figure 76 and Figure 77, with a low signal to noise ratio.

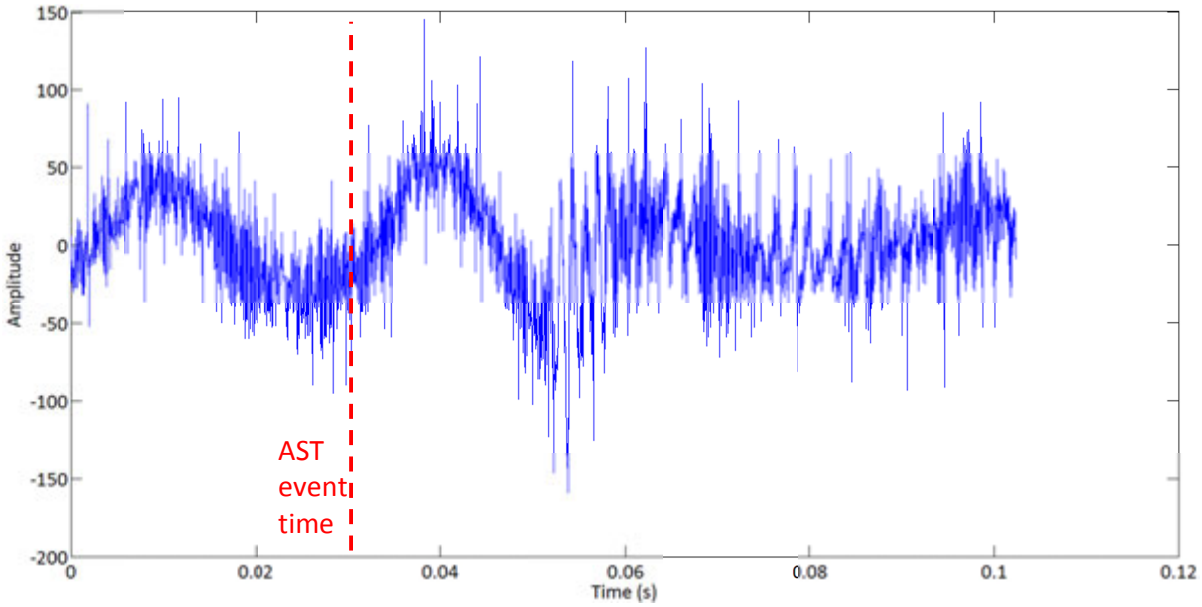

Figure 76: Example of ASR time domain signal with low signal to noise ratio

In Figure 76 above, one can immediately see that the AP signal is not distinct from the background noise. It is, in fact, almost completely unidentifiable. Figure 77 shows the FFT of this signal in the frequency domain.

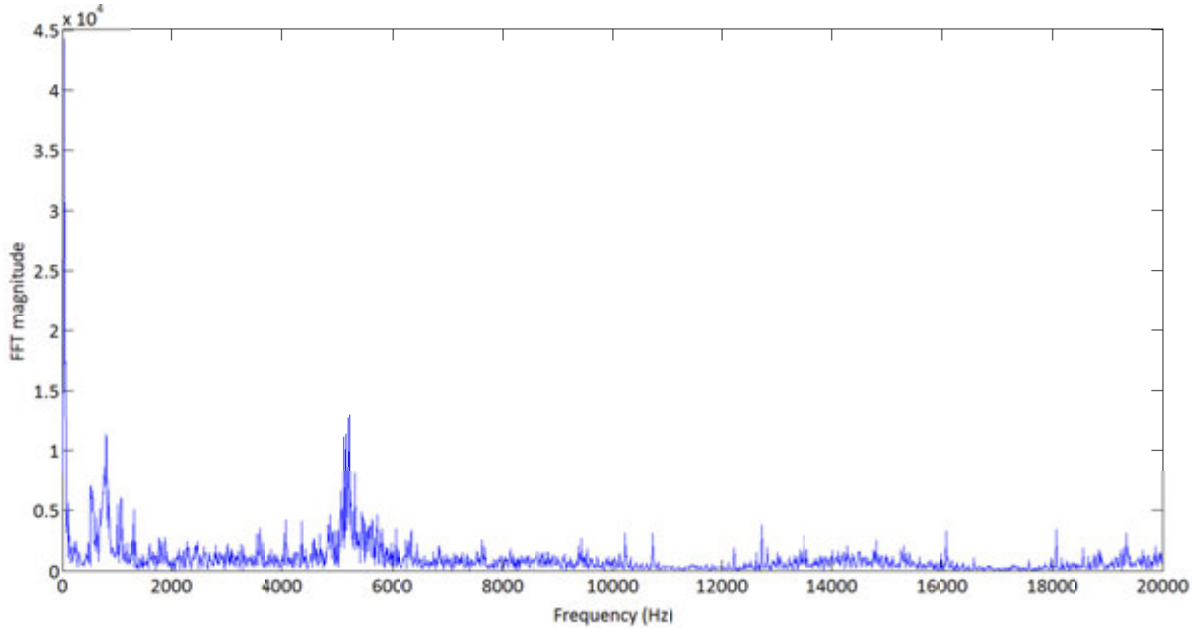

Figure 77: Example of FFT of signal with low signal to noise ratio

It can be seen on Figure 77 that there is more than 1 major frequency spike which have similar magnitudes. There is even a peak in the extremely low frequency range. It is in these cases that the first step of doing the STFT is very useful. From the STFT spectrogram it can be determined which frequency is most likely the acoustic pyrometer signal as it shows the most significant change in the time domain.

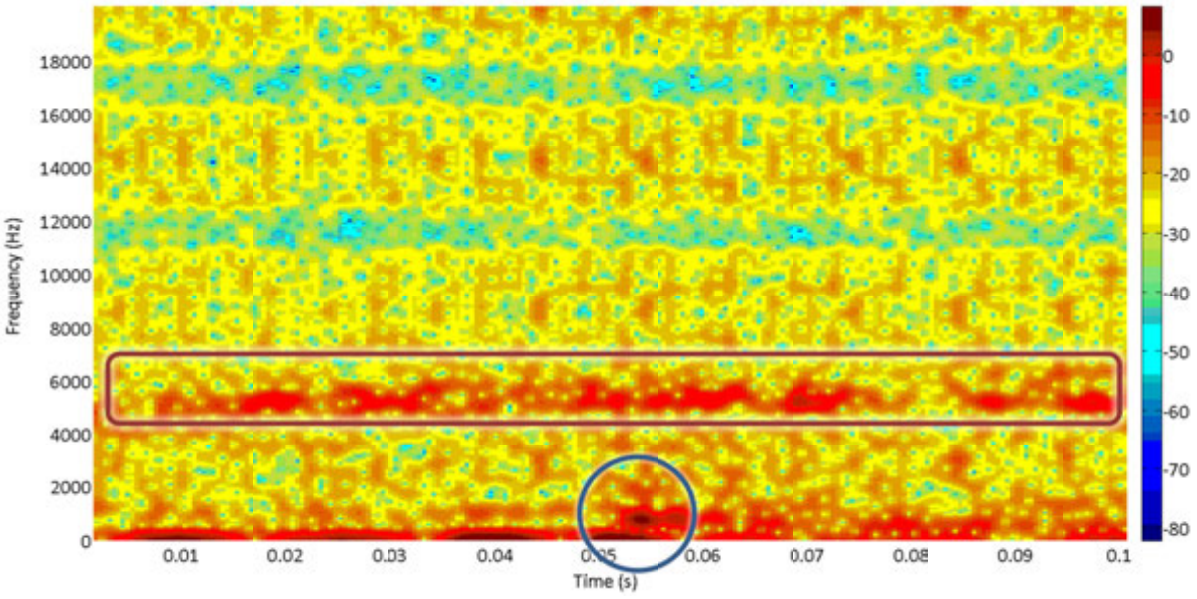

Figure 78: Example of spectrogram of low signal to noise ratio

From Figure 78, it can be seen that of the 2 dominant frequency ranges, only the one indicated by the blue circle shows a change in the time domain that could represent the AP signal. So this is the

manual aspect of the method, which requires an input of a frequency range in which to determine the specific frequency, f_c, to be used for filtering. The exact value of this frequency is then determined from the FFT.

Once the frequency has been identified, a band pass filter is applied centred at this frequency, f_c, using built-in Matlab filter design parameters. For each set of data (i.e. Unit 6 Furnace Front, Unit 6 Furnace Diagonal, Unit 2 Furnace Front, Unit 2 Economiser), the filter parameters were tuned to a value that is able to produce the most consistent values in terms of reducing the number of outliers, and achieving the least variance. Every signal in a data set was run through the exact same filter. The filter parameters used for each set of data are listed in Table 17.

Table 17: Band-pass filter parameters

Unit	Data set	Filter order	Pass band lower (Hz)	Pass band upper (Hz)	Ripple
6	Furnace Front	2	f_c – 1Hz	f_c + 1Hz	0.001
6	Furnace Diagonal	2	f_c – 1Hz	f_c + 1Hz	0.001
2	Furnace Front	2	f_c – 1Hz	f_c + 1Hz	0.001
2	Economiser	6	4000	5000	0.001

The same signal from Figure 76 is shown again on Figure 79, this time overlaid by the filtered and rectified signal. The signal is rectified, in order to prepare it for the threshold detection.

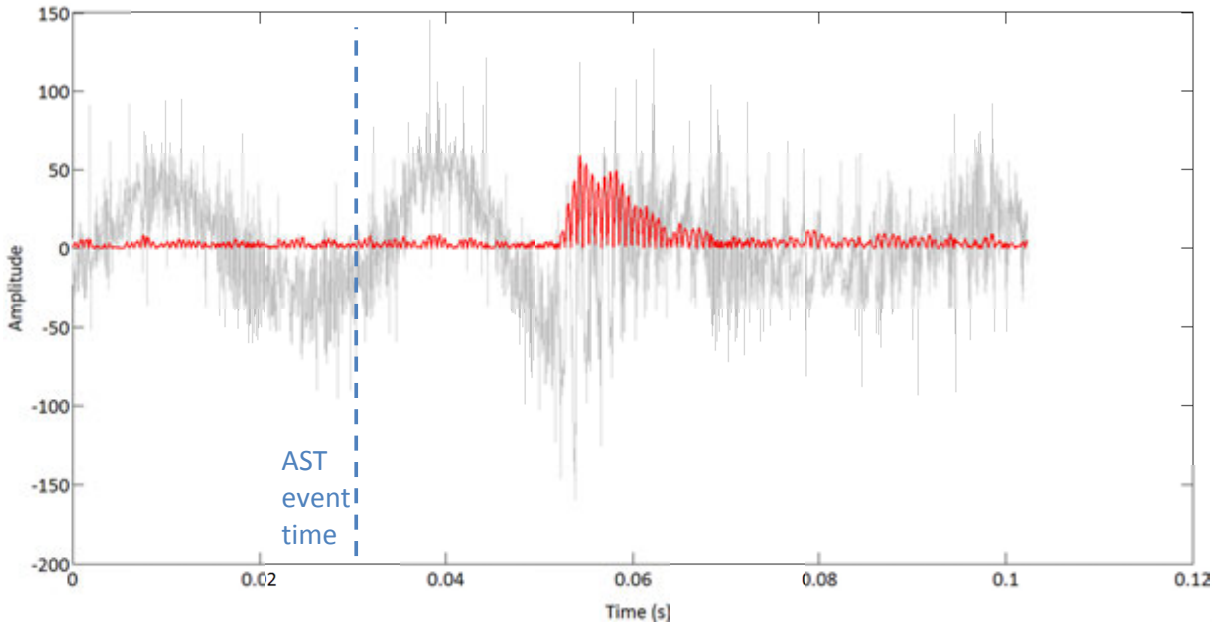

Figure 79: Example of a time domain signal overlaid with the filtered signal

The threshold detection for the time of flight is then applied to this type of filtered and rectified signal. Figure 80 provides a graphical representation of the threshold detection.

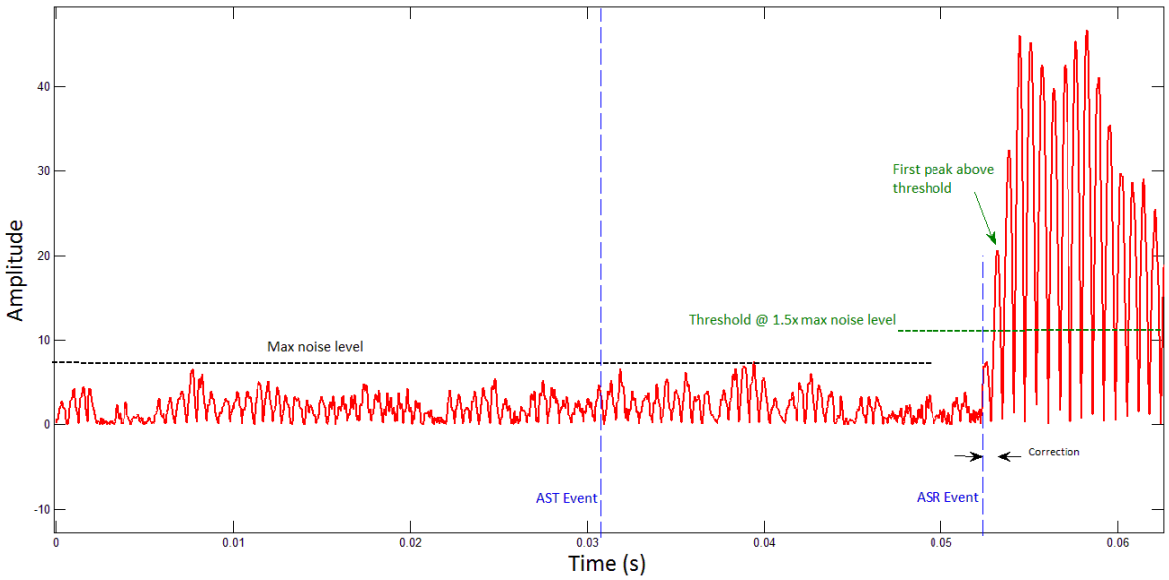

Figure 80: Example of threshold detection

The maximum noise level is determined from the first 40 milliseconds of the receiver signal (a range in which it is impossible for the receiver to detect the AP signal). This maximum noise level is then used as a threshold level. The point where the signal crosses a certain % above this threshold is recognised as the event time of the received signal. A correction is made by the code for one period of the signal. The reason for using a % above the threshold is to avoid false detection of slightly higher noise peaks that occur after the 40ms time range but before the actual signal. It is also usually the second peak which is detected more easily by the threshold crossing. Again, this % above the threshold was also tuned to achieve the most consistent results for each data set.

A similar threshold detection method is applied to the AST signal to determine the AST event time, and thus the time of flight is then the difference between the two.

4.3.5. AP temperature calculation methodology

As mentioned in the previous section, the signal analysis determines the total TOF of the signal including the time that it spends in the connecting tubes. However, in order to calculate the average velocity of the flue gas, this offset of the time spent by the sound wave in the sound generator barrel, trigger tube and the receiver tube has to be taken into account. All acoustic pyrometers have some sort of tube or wave guide arrangement in order to deliver the sound wave to the boiler, and these offsets are specific to the device. Therefore, for this aspect of the study,

OEM supplied correlations which were experimentally determined during product development were used to account for these offsets.

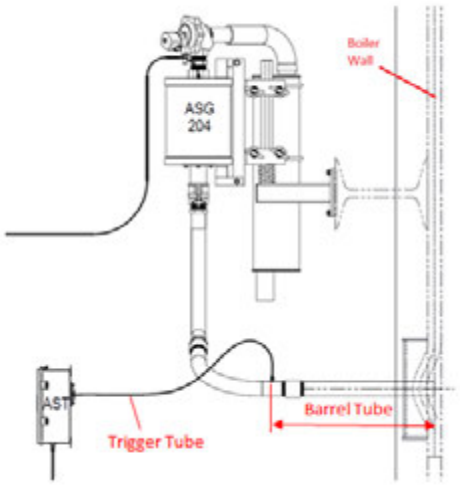

Figure 81: Acoustic sound generator [62]

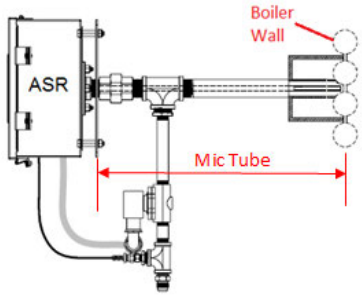

Figure 82: Acoustic sound receiver [62]

The actual TOF is then given by:

$$TOF_{actual} = TOF_{raw} - Offset \tag{4.35}$$

Where

$$Offset = t_{barrel} - t_{trigger} + t_{receiver} \tag{4.36}$$

The offsets used are as follows:

Table 18: Time of flight offset values

Test location	t_{barrel} **(ms)**	$t_{trigger}$ **(ms)**	$t_{receiver}$ **(ms)**	***Offset*** **(ms)**
Furnace	0.1995	2.9616	1.9603	-0.802
Economiser	3.0703	2.9616	4.193	4.302

Taking the above into account, as well as the "pseudo-gas" properties for the 2 phase flue gas mixture, equation (4.6) can be re-written as follows.

$$T = \frac{L^2}{\gamma' R' \left(TOF_{actual}\right)^2} \tag{4.37}$$

A full derivation of how the pseudo-gas properties are calculated is given in Appendix I. The calculated values are:

$\gamma' = 1.283$

$R' = 258.328 J / kgK$

4.4. Direct methods testing results and analysis

4.4.1. Comparison of the 2 TOF detection methods

The first result to be looked at is a comparison between the raw TOF measurements determined from the OEM software, and those determined from the ad-hoc method developed for this study.

In total, there are 5 sets of testing data which were taken for this study, all at Plant X. The data sets differ first by unit, then by location on the boiler, and thirdly by path orientation. For each set, several TOF measurements were taken. The full list of TOF measurements taken can be found in Appendix G. Table 19 shows the average TOF for each data set determined using both TOF methods, as well as the number of outliers for each set.

In all cases, outlying data points have been classified as any data points that have a deviation of more than 15% from the average for that set, which in most cases are totally erroneous detections as a result of signals from which the algorithm is unable to clearly distinguish the AP signal. The outlying range was chosen quite generously at 15%, to provide a holistic picture of the sort of variations that occur from measurement to measurement, while ignoring the aforementioned erroneous detections.

Table 19: Comparison between raw TOF determined from the 2 detection methods

Data set	Number of measure-ments	PyroMetrix average (ms)	Number of outliers	Ad-hoc TOF detection ave. (ms)	Number of outliers
Unit 2 economiser	22	21.059	4	21.282	3
Unit 2 furnace front	9	20.197	0	20.044	1
Unit 6 furnace front	14	18.420	3	19.132	3
Unit 6 furnace diagonal full load	13	21.059	2	21.282	1
Unit 6 furnace diagonal ¾ load	10	21.497	1	21.786	0

As can be seen from Table 19, on average, the ad-hoc TOF method agrees quite closely with the OEM software. It also produces less outliers overall, which is not surprising, because as mentioned in the description of the method, the filtering parameters were tuned for each data set to minimize the number erroneous detections in the set. Moreover, the fact that an independent ad-hoc method agrees so closely to the OEM method also begins to build confidence in the integrity of the acoustic pyrometer data. Since the ad-hoc method is the one which has been fully detailed and fully understood, it is the temperature values determined from these TOF measurements which are presented henceforth.

4.4.2. Main Results

This section shows the temperature results for all of the testing data. For each data set, the temperature for each measurement is plotted against the time the measurement was taken. Also plotted is the average temperature for the set, calculated with outliers excluded. Outliers are not plotted on the graphs for the sake of clarity but rather indicated by arrows showing that they are above or below the range of the graphs.

i. **Economiser results**

Figure 69 shows the results for the economiser testing carried out on unit 2.

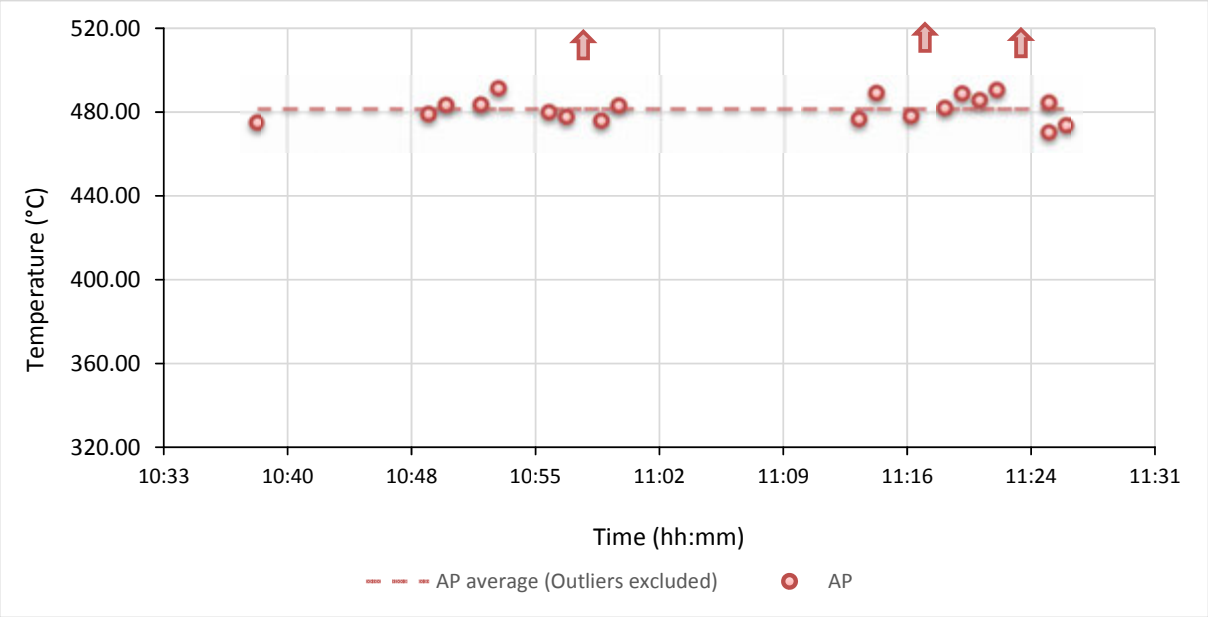

Figure 83: Unit 2 economiser acoustic pyrometer temperature results

There are a few key factors that must be taken into account when interpreting the results. The first thing that is apparent from the figure is that the readings are very consistent. If these results represented different measurements all taken at the same instant, then the variation of each measurement from the average would be a very critical parameter. In this case, variation from the average does not necessarily mean inaccuracy, as the boiler is a dynamic environment where even if load conditions are kept constant overall, there are plenty of dynamic phenomena that can vary along an individual path. Nevertheless, it is noted that all the measurements (with the exception of the outliers) are very close to the average, which does show consistency and repeatability.

The next step is to check whether, on average, the results are in the expected range. The average value over the testing period is ≈482°C.

Now, based on the limited thermocouple data available, the arithmetic average of the TCs at the top of the economiser is ≈520°C. The arithmetic average of the TCs at the bottom of the economiser is 352°C. A quick estimation of the temperature in between the banks can be made by considering that the surface area ratio of the bottom economiser bank to the top economiser bank is $\approx\frac{7}{6}$, as the bottom bank has 7 rows of tubes, while the top bank has 6. In this area of the boiler the heat transfer from the flue gas to the water is mainly by convection, and thus the heat transfer ratio between the banks should be approximately proportional to the heat transfer area ratio. Assuming this heat transfer relationship, the temperature between the banks based on the thermocouple readings is ≈442°C. Now, this is substantially lower than the acoustic pyrometer

reading, 8.3% less. In light of the comments above, the fact that the measurements are consistent but higher than expected suggests that perhaps there is a systematic error influencing the results.

As mentioned earlier, in order to make use of the traversing ports at the economiser level, the acoustic pyrometer barrel and receiver tubes had to be extended. This means that the offset time as a result of sound travel within the tubes is higher, meaning that the propagation of errors as a result of incorrect estimation of the offset is also higher. As the offset is applied to the entire data set, it produces a systematic error. The critical parameter to calculate the offset is the temperature of the barrel and receiver tubes. Because this area of the boiler is much cooler than the furnace, the barrel and receiver tubes were assumed to be at ambient temperature. If this assumption underestimates the temperature, the temperature reading of the AP increases, and this may be the source of the systematic error.

ii. Furnace front results

For all of the furnace measurements, the AP results together with the averages are plotted and compared with readings from the radiation pyrometers. Each data point of the radiation pyrometer plot represents the average value of 4 radiation pyrometers at 29m level on the boiler. The individual radiation pyrometer readings can be found in Appendix H. The results of the measurements taken close to the front wall of the boiler on units 2 and 6 are shown in Figure 84 and Figure 85 respectively.

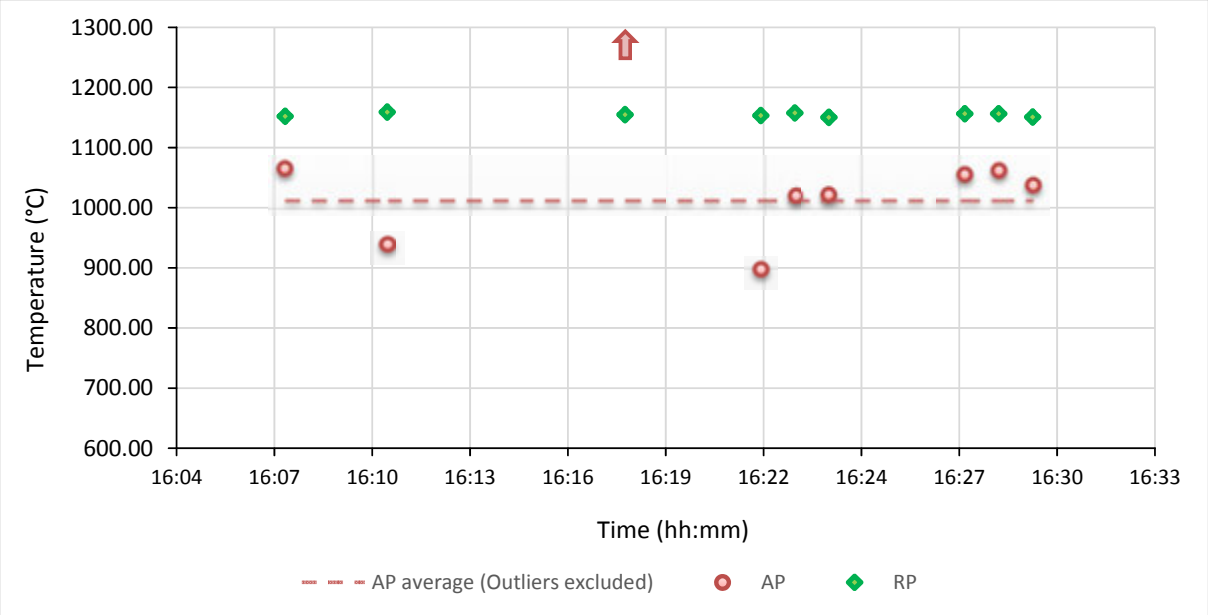

Figure 84: Unit 2 furnace front acoustic pyrometer results compared with radiation pyrometers

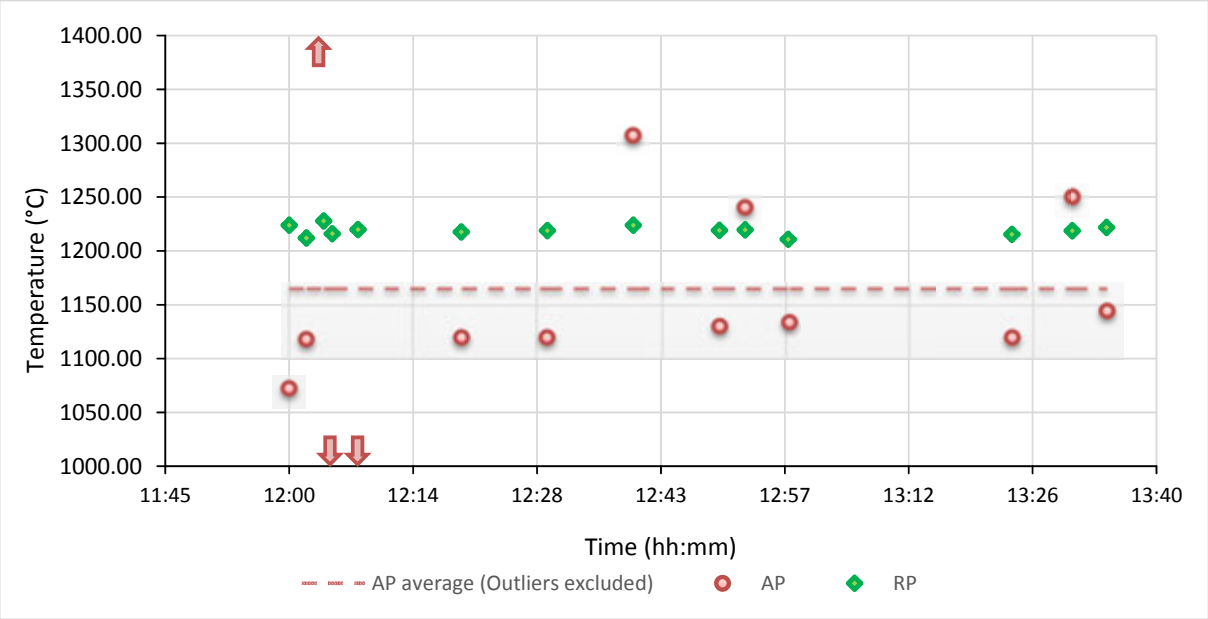

Figure 85: Unit 6 furnace front acoustic pyrometer results compared with radiation pyrometers

On unit 2, the average AP measurement is 1013°C and on unit 6 it is 1165°C. The unit 2 testing was carried out at a load of around 160MW, whereas the unit 6 furnace front test was carried out at a load of around 190MW. So the fact that the unit 6 value is higher than the unit 2 value corresponds with the boiler load for each test.

Now, all of the unit 6 furnace front testing was done at the same time that the MEB case study was done, but it is immediately noticeable that the value measured here is significantly less than that of the MEB case study in Chapter 3 even if the radiation aspects are taken into account in the MEB (the value was 1338°C). This is due to the fact that the MEB calculates an average value of the FET while the AP measurement in this location represents the average temperature on a path approximately 0.3m from and parallel to the boiler front wall. Now, because the boiler walls are water cooled, the flue gas temperature closer to the walls is much lower than the average temperature over the entire cross section of the furnace. Given that temperature gradients close to boiler walls can be as high as 100K/m [25], the lower temperature along the front wall path is reasonable. This concept is also important when comparing the AP results with the radiation pyrometers.

It was shown earlier on schematics of the testing locations that the radiation pyrometers are on the same boiler level that the AP was positioned on, but are positioned closer to the middle of the boiler on both the right and left hand side walls. While the flue gas temperature would also be low close to the left hand and right hand side walls, the results of the radiation pyrometer in each case are higher than the average AP measurement.

To understand why this is the case, the optical characteristics of the radiation pyrometer need to be considered. The radiation pyrometer does not measure the flue gas temperature right at the wall, but rather the average temperature as a result of all the radiation detected within its field of view. While the emitting, scattering and absorption characteristics of the particles in the flue gas have a major impact on the depth of this field of view into the boiler, this particular RP's lens is specified to have a minimum focusing range of 0.4m, as shown on Figure 86.

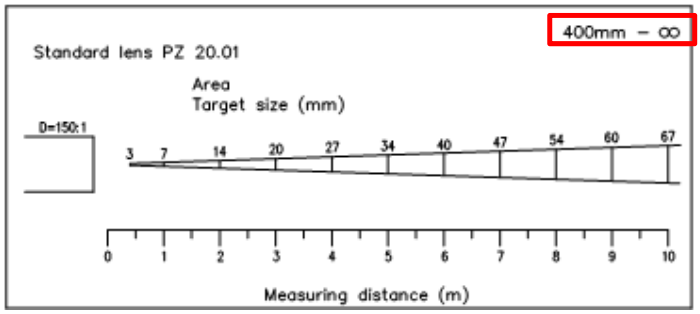

Figure 86: Siemens Ardometer MPZ20 standard lens optical characteristics [61]

From this, it can be deduced that the RP definitely measures the temperature in the boiler from the side wall at a depth into the boiler which is at least further from the side wall than the AP measurement is to the furnace front wall. If the temperature gradients along the side walls and the front walls are similar, it is expected that the RP should thus measure a higher temperature than that measured by the AP at the front wall. The question is then whether or not the temperature gradient near the different walls is the same. As mentioned at the outset, there is a substantial amount of boiler process and combustion work that has been previously undertaken at Plant X and this can perhaps provide a bit more insight to further interpret these results.

Peta et al [17] reported on CFD simulations of the entire boiler producing temperature profiles throughout the furnace on Plant X. While the actual values may not be directly comparable due to the variable operating conditions and input data, much insight can be gained about the general temperature profile. The figure below shows the temperature profile from that CFD of a horizontal plane at the level of last row of burners, and on a vertical plane close to the middle of the boiler perpendicular to the boiler front wall. The positions of the testing equipment for this current study are also marked on the figure.

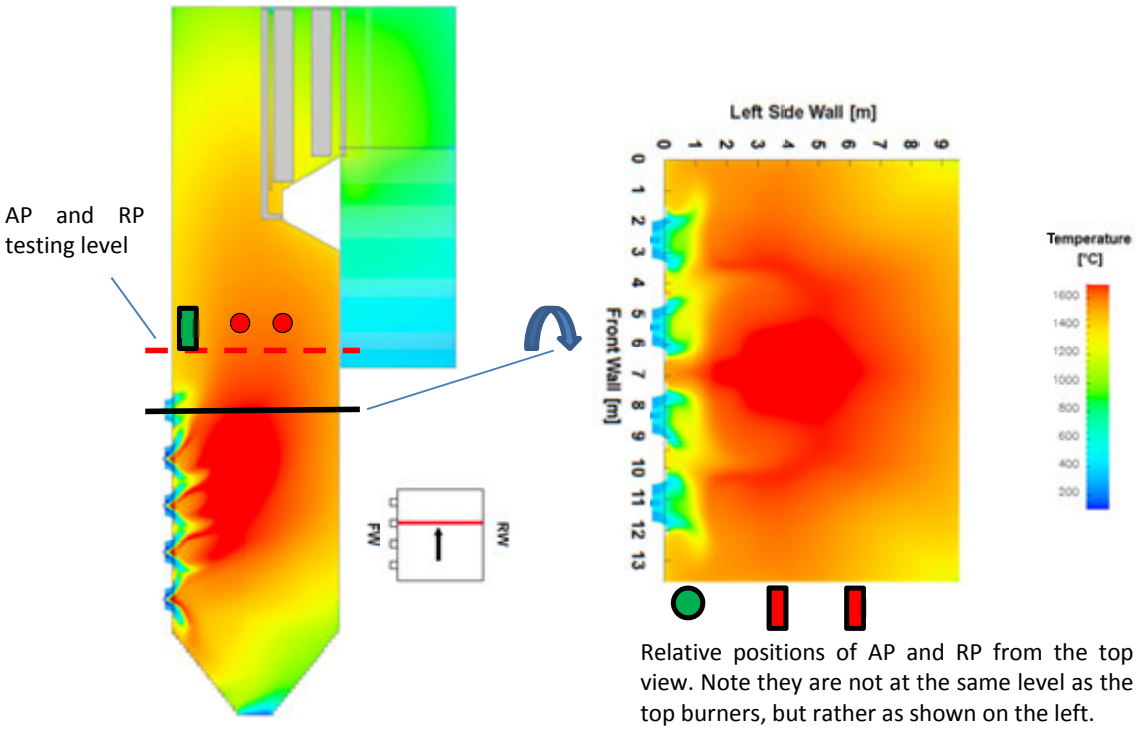

Figure 87: CFD temperature profiles of Plant X boiler along a vertical plane and horizontal plane at the top row of burners

From Figure 87, it can be seen that the temperature gradients are not the same near the front wall and near the side walls. In actual fact, these CFD profiles lend even more weight to the expectation that the RP should measure higher temperatures than the AP, since the temperatures from both the vertical and horizontal profiles depict the lowest temperatures close to the front wall. The profile on the right has drastically lower temperatures near the burners at the front but that profile is taken exactly at the burner level. The AP was actually positioned ≈4m higher than the burners as shown on the vertical profile. The vertical profile, however, also shows a 50-100°C lower temperature towards the front of the boiler, which is very similar to the measurement results obtained here.

Another aspect that can be looked at is the deviation from the average. While it was mentioned that deviation from the average is not a good indicator of accuracy since the measurements are taken over time, the deviation over time is interesting for these results. The RP measurements show very little variation over time, whereas the AP measurements in some cases show variations from point to point on the order of 100°C, and in one case on Figure 85, close to 200°C. Now one can simply argue that these 2 measurements are not directly comparable because they are measuring different areas, therefore the dynamic conditions experienced by the AP are simply not experienced by the RP.

To an extent, this may be a contributing factor. The area close to the burners is the most dynamic environment in the boiler. So perhaps, the AP measurement area is more prone to dynamic conditions and the measurements are actually reflective of real dynamic conditions. Also, the RP measurements shown here are averaged from 4 RPs. The individual RP measurements shown in Appendix H do show a bit more variation with time. However, the variation of the RP measurements is still not as drastic as the AP, which suggests that there may be other experimental factors at play here.

Closer inspection of the unit 2 results on Figure 84, show that 75% (6 out of 8) of the accepted results (by accepted results it is meant excluding the outliers), actually fall within a 45°C range between 1021°C and 1066°C. Similarly, on the unit 6 results on Figure 85, 8 out of 11 accepted results fall within a 73°C range. In fact, excluding the first measurement, 7 out of 11 fall within a very narrow range of just 27° between 1118°C and 1145°C. This shows that most of the measurements actually indicate that over the entire testing period the variation isn't as much. There are a few measurements, which although not classified as outliers, impact on the average value and seem to indicate large temperature fluctuations. So in addition to the fact that there may be some actual temperature fluctuation, the extent of this is most likely exaggerated by the experimental limitations which were identified at the outset, such as:

- For this path, the AP path was only 0.3m from the front wall, which is contrary to the manufacturer's recommendation of at least 1m.
- The equipment was not fixed in position which can result in movement during operation, which may affect the signal. Even though the equipment position was adjusted between shots, the fact that this positioning is done with the boiler on load, means that the positioning could not be perfect, thus the barrel and receiver tubes may not always have been in the best position to produce good signals.

iii. Furnace diagonal results

Figure 88 and Figure 89 show the results of the furnace diagonal measurements, for the full load and 75% load cases respectively. Again, the AP results with the averages are plotted and compared with the radiation pyrometers. Each data point of the radiation pyrometer plot represents the average of 4 radiation pyrometers at the 29m level on the boiler.

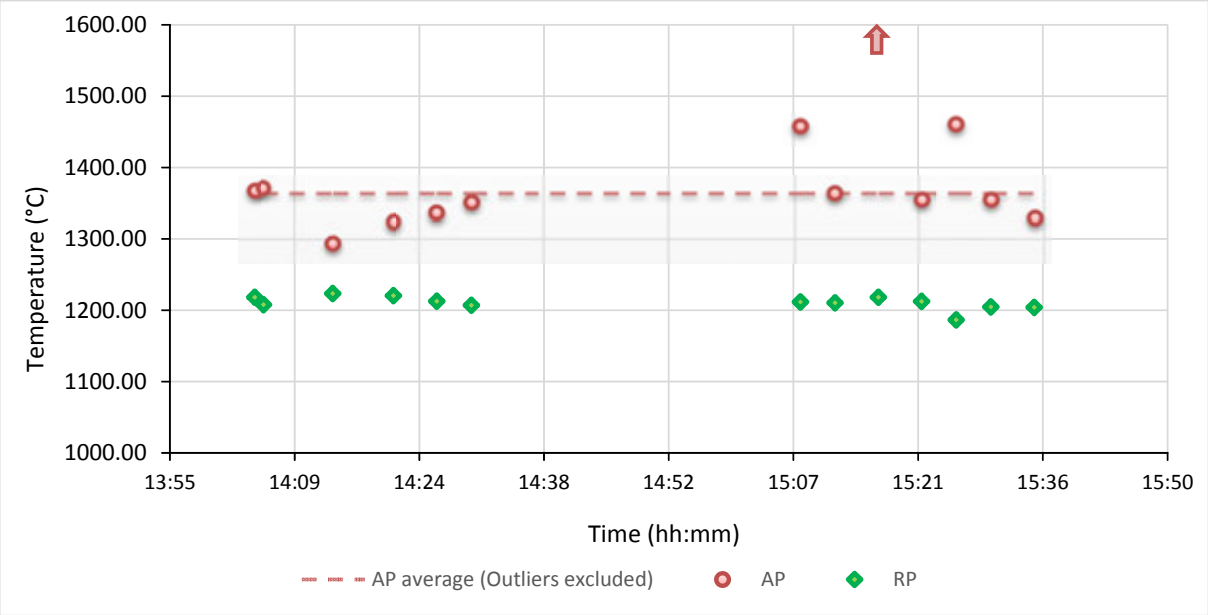

Figure 88: Unit 6 furnace diagonal acoustic pyrometer results compared with radiation pyrometers, at boiler full load

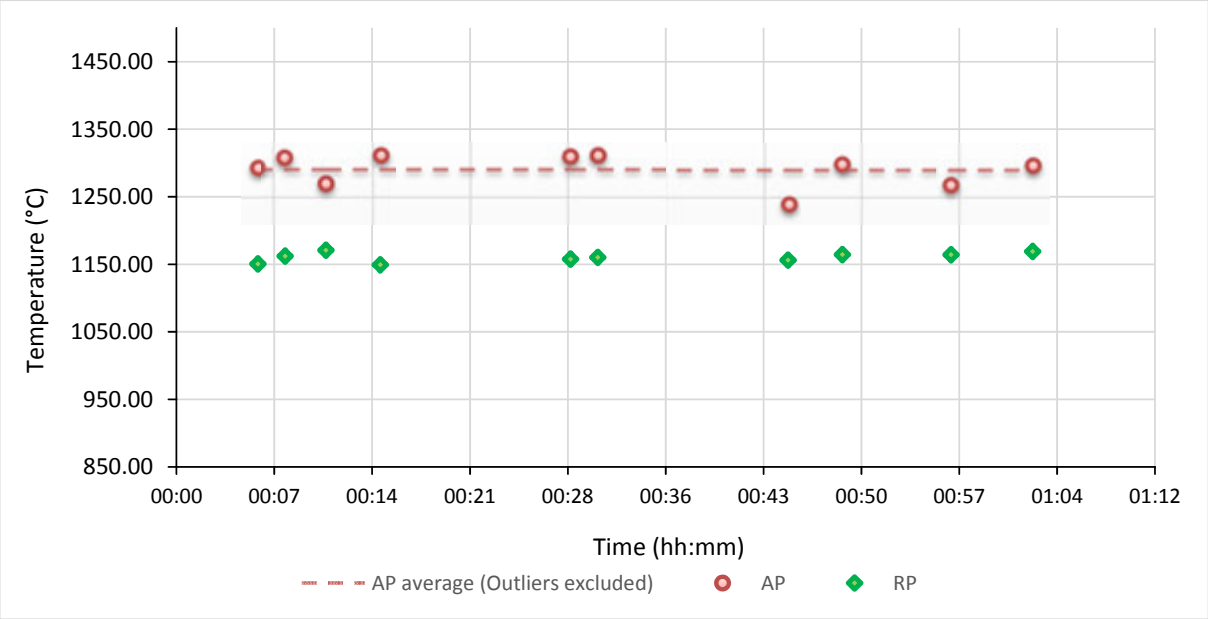

Figure 89: Unit 6 furnace diagonal acoustic pyrometer results compared with radiation pyrometers, at boiler 3/4 of full load

The full load test was carried out at the same load as the unit 6 furnace front test, approximately 190MW. The 75% load test was carried out at a load of approximately 140MW. The reasoning behind testing the same path but at different loads was that the furnace exit temperature is expected to be lower at lower loads, and it is thus a means of testing whether the AP results reflect this. From Figure 88, the average AP temperature measurement at 190MW is 1363.4°C,

and from Figure 89, the average AP temperature measurement at 140MW is 1290.5°C. Thus, the temperature at 140MW is measured to be lower than the full load temperature, which is as expected.

As with the furnace front tests, the AP results can be compared with the RP measurements sampled from the plant's DCS at the corresponding times. Comparing the RP results for the 2 load cases, the average RP reading is 1210.5°C at 190MW and 1160.4°C at 140MW. Therefore, similarly to the AP results, the RP temperature reading is higher for the full load case.

For these results, it can also be seen on Figure 88 and Figure 89 that, as before, the radiation pyrometer results do not display any substantial variation with time. The AP results do show some variation with time, however compared to the furnace front tests, the deviations are not as large. For the full load case, 9 out of 12 accepted results fall within a range of 48°C between 1323°C and 1371°C. For the 75% load case, all 10 results fall within a range of 72°C, between 1239°C and 1311°C. There a couple of point to point deviations close to 100°C, and as before, these may be as a result of the limitations of the test set up. For these tests the generator is in the exact same position as the furnace front test, and the receiver is again close to a wall, however it is the rear wall in this case.

There is one major contrast between these results and those from the furnace front result. For this diagonal path, at both load cases, it can be seen that the AP temperatures are, on average, higher than those measured by the RPs. The logic used to interpret the furnace front results does not apply here. Here the AP is measuring the average temperature along a path which passes through the centroid of the furnace cross section, and should thus give a good approximation of the average temperature in the furnace. The fact that the RP temperature reading is significantly lower than the AP, either points out a severe overestimation of temperature by the AP perhaps caused by a systematic error; or possibly a limitation of the optical characteristics of the RP to measure deep enough into the furnace to provide a representative measurement. Fortunately, there is an additional value available for comparison to provide greater clarity.

The measurements taken at full load on unit 6 are directly comparable to the calculated value from the MEB case study, presented in Chapter 3. In Chapter 3, the FET was calculated for various ingress air distributions between the furnace and backpass, and the lowest value was for 100% ingress air in the furnace. This value was ≈1400°C. A further indirect method was applied as it was proposed that this value may be overestimated by not accounting for radiation from the furnace to the backpass. A zonal model calculation was used to provide an estimate of the order of this overestimation, and the FET was then calculated to be 1338°C. This value agrees very closely to the AP measurement, as it is only ≈25°C (or 2%) less.

In addition to the full load MEB results presented in Chapter 3, the same MEB method combined with the zonal model correction was followed using input data from the 75% load test. For this calculation, the FET is calculated to be 1292.7 °C. Again, this value is very close to the corresponding average AP value (1290.5°C), just ≈2°C difference.

For each load case, the MEB provides a 3rd independent temperature value. Noting that the value calculated from the MEB represents an average FET over the furnace exit cross section, the similarity between the MEB results and the AP measurements suggests that perhaps the AP reading is more representative of the actual average temperature in the furnace than the RP. The CFD profiles displayed above on Figure 87 also support this, as it shows the hottest temperatures do occur towards the middle of the furnace. Although not studied in depth in this study, it is known that the RP measurements can be greatly influenced by radiation scattering into and out of its field of view. Thus, the lower RP reading is as a result of its limited "visibility" into the furnace due to the presence of the particles in the flue gas.

iv. Remarks on AP temperature results

From these experimental results, it shows that the acoustic pyrometer is able to provide temperature measurements in the expected ranges on average, and this has been further consolidated by the indirect MEB calculation method. The radiation pyrometers provided a good qualitative baseline from which to interpret the acoustic pyrometer results, although as has been pointed out more than once in this text, they also have their own inherent limitations.

The consistency and repeatability of the AP measurements for this study was brought into question in some cases, but should be considered in the light of the limitations of the testing setup. With a complete, fixed and calibrated installation, it is anticipated that these problems can be mitigated. That said, in normal operation, the acoustic pyrometer will take constant measurements automatically, much more frequently than was done here. This would provide a large amount of data which can be statistically treated in case of random variations.

The most direct available comparison data is the FET calculated from the MEB, and the AP temperature results are also compared hereafter with the MEB in terms of the uncertainty of the FET determined from both of these methods.

4.4.3. Uncertainty propagation on acoustic pyrometer temperature measurement

As uncertainty propagation was already presented for the MEB in Chapter 3, an uncertainty analysis of the acoustic pyrometer is presented here.

The temperature obtained from the acoustic pyrometer depends on the parameters contained in equation (4.37): $T = \frac{L^2}{\gamma' R' \left(TOF_{actual}\right)^2}$

Therefore, the uncertainty analysis for the temperature must evaluate the propagation of the uncertainty from the 4 parameters used to calculate temperature. The uncertainty of the temperature can be determined from the uncertainty propagation equation (3.28), which for the AP, can be expressed as:

$$u_T = \sqrt{\left(\frac{\partial T}{\partial \gamma'}\right)^2 u_{\gamma'}{}^2 + \left(\frac{\partial T}{\partial R'}\right)^2 u_{R'}{}^2 + \left(\frac{\partial T}{\partial L}\right)^2 u_L{}^2 + \left(\frac{\partial T}{\partial TOF_{actual}}\right)^2 u_{TOF_{actual}}^2} \tag{4.38}$$

In this case, there is an explicit equation that relates the output value (T) to the input values, so the partial derivatives can be expressed analytically, as opposed to the numerical approximation that is used in the uncertainty propagation programme. Substituting the partial derivatives and rearranging yields the uncertainty as a percentage:

$$\%u_T = \sqrt{\left(\frac{u_{\gamma'}}{\gamma'}\right)^2 + \left(\frac{u_{R'}}{R'}\right)^2 + 4\left(\frac{u_L}{L}\right)^2 + 4\left(\frac{u_{TOF_{actual}}}{TOF_{actual}}\right)^2} \tag{4.39}$$

The values of the inputs are the typical parameters of the furnace diagonal path, as this is the path which is most comparable to the MEB:

$L = 16.26m$

$\gamma' = 1.283$

$R' = 258.328 J / kgK$

$TOF_{actual} = 22ms$

The uncertainties of the inputs also need to be specified. The uncertainty of the path length is estimated based on the measurement device used, and would typically be ±1cm. For this case study, due to the temporary nature of the equipment setup, it is estimated to be ±5cm to account for any movement of the equipment between measurements. Therefore $u_L = 5cm$.

The uncertainty of the time of flight is derived from the timing error, which is dependent predominantly on the frequency of the received signal. The lower the frequency, the higher the uncertainty. Of all the testing that was done, the lowest detection frequency was in the region of 500Hz, which corresponds to a wavelength period of 2ms. This means that the worst case error is ±⅛th of this period, which is ±0.25ms. The potential error of the offset times, is not a random error but rather a systematic one and is thus not included here. Therefore $u_{TOF_{actual}} = 0.25ms$.

For the gas properties, previous studies have mentioned an uncertainty range of ≈0.4% [40]. Here, these properties are calculated in Appendix I. Therefore, the propagated uncertainty on these properties can be estimated by running the calculations of Appendix I through the uncertainty propagation programme that was introduced in Chapter 3. The inputs with their uncertainties to calculate the gas properties are listed in Table 20.

Table 20: Inputs required to calculate the gas-particle mixture properties with their associated uncertainties

Parameter	**Symbol**	**Value**	**Unit**	**% uncertainty**
Molar mass of flue gas	M_{fg}	31.15	g/mol	0.198
Specific heat ratio of flue gas	γ_{fg}	1.3	-	0.4
Mass percentage of ash in coal	$\%Ash$	31.87	% m/m	1.38
Mass of flue gas per kg of coal	$\dot{m}_{fg}$	8.642	kg fg / kg coal	2.854
Mass percentage of CO_2 in flue gas	$\%CO_{2.fg}$	20.375	% m/m	2.489
Mass percentage of N_2 in flue gas	$\%N_{2.fg}$	70.58	% m/m	0.259
Mass percentage of H_2O in flue gas	$\%H_2O_{.fg}$	4.168	% m/m	3.529
Mass percentage of O_2 in flue gas	$\%O_{2.fg}$	4.512	% m/m	9.894

All of the values in Table 20 are obtained from some part of the case study of Chapter 3. The ash content in coal is obtained from the coal analysis, while the rest of the parameters are outputs of the MEB calculations, and their uncertainties are propagated from the MEB inputs, determined during the uncertainty propagation study in Chapter 3.

For the values given in Table 20, the uncertainty propagated onto the gas properties is:

$u_{\gamma'} = 0.0049$

$u_{R'} = 0.575 J / kgK$

Therefore, the percentage uncertainty of the final temperature is calculated from equation (4.39):

$\%u_T = 2.387\%$

It should be emphasized that this uncertainty is not the same as the variation seen over time, but rather the uncertainty of any individual measurement.

Figure 90 now shows the MEB and AP results together with the respective uncertainty/error ranges for both the full load and the 75% load case. Since the uncertainty of the ingress air distribution was considered independently from the overall uncertainty propagation, the MEB results shown below here consider 2 ingress air distribution scenarios which cover the most realistic range: (i) 100% of the ingress air contained in the furnace, and (ii) 50/50 between furnace and backpass. These results also take into account the correction for radiation transfer from the furnace to the backpass.

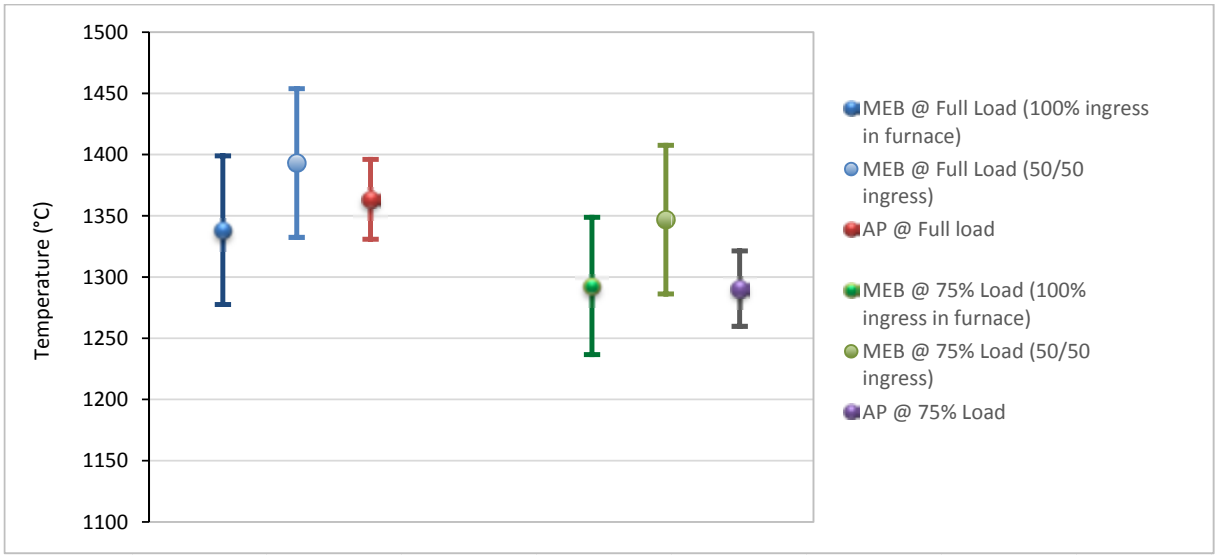

Figure 90: Uncertainty ranges on FET from both the MEB and acoustic pyrometer

As can be seen on Figure 90, the FET values from the 2 methods have been found to be very similar. This graph shows the final MEB calculated value including the radiation to the convective pass estimate. The uncertainty range of the AP is smaller than that of the MEB method. It is in fact, almost fully engulfed by the MEB's range for both load cases. The AP range shown in the figure is based on the operating conditions and set up of this experimental test, as well as the capabilities of the ad-hoc TOF detection method. In practice, the path length will be very precise, and the TOF detection accuracy can possibly be refined. With this in mind, the uncertainty of the AP for a permanent and fully optimized system may very well approach the ±1% range that was reported by Green [40] and Kleppe [25].

5. Conclusions and Recommendations

5.1. Conclusions

The primary objective of this study was to investigate the use of indirect and direct methods that can be used to measure and monitor the critical boiler furnace exit temperature, and compare them in terms of their benefits and limitations, feasibility, on-line monitoring applicability and expected accuracy ranges. The 2 methods which were singled out to be focused on were mass and energy balances and acoustic pyrometry. In order to meet these objectives, the following was undertaken.

At the outset, the fundamental concepts of the boiler and its auxiliaries were studied to lay the foundations and emphasize the importance of the boiler flue gas furnace exit temperature. From literature, the FET was found to be a critical parameter both in terms of boiler design and operation. Thereafter, the methods for determining it were studied.

5.1.1. Indirect methods

A brief literature survey was carried out on the indirect methods. It was found that most of the methods for the calculation of furnace exit temperature involve complex radiation models of the furnace. However, simpler methods do exist but require one to take cognisance of the inherent uncertainties brought about by the simplifications.

It has been shown that by using a systematic, coherent and consistent approach, the furnace exit temperature can be calculated using mass and energy balances. However, the calculation results do contain a certain level of uncertainty mainly due to the estimation of the amount of energy transferred to the water walls; both in the furnace section itself, and also as a result of radiation heat transfer which takes place across the defined MEB control volumes. Here, the MEB was combined with a simplified zonal model to account for the latter. It was found that the FET was overestimated by ≈60°C. For the furnace itself it was also mentioned that in once-through and especially supercritical boiler, the energy recovered by the water walls at a height above the end of vaporisation will be quite easy to determine by simple temperature measurements of the water walls external to the furnace.

There is also some uncertainty introduced by the fact that the calculations are dependent on a large number of variables. Naturally, a large number of variables increases the potential for errors. The potential for error is compounded by the fact that many of the measurements are averaged over both time and space, and also the calibration of the installed instrumentation is not always

verified and this provides further. With a concentrated effort, all these measurement errors can be significantly reduced.

Apart from measurement errors, the lack of a simple method for determining ingress air distribution is a major problem. This is particularly applicable older boilers like the type studied for this case study, which have refractory in between the water wall tubes to provide the seal. Newer boilers with membrane walls should experience much less ingress air. In both cases, the best way to reduce the impact of the ingress air distribution assumption would be to strive for a global reduction of ingress air into the boiler, by good maintenance activities.

The MEB method is attractive compared to complex numerical methods, as it does not require extensive solving time. It can also be easily implemented on most power plants which should already have most, if not all, the required input measurements. The straight forward nature of the calculations is also beneficial if the intention is to incorporate the methodology into existing condition monitoring packages such as EtaPro. While the methodology is sound, it should not be utilised without a consideration of the limitations. These limitations include the fact that the MEB can only be applied to steady state operation of the boiler. Moreover, to be used with confidence, the MEB requires a general improvement in performance testing activities, and measurement reliability and accuracy.

If the objective of using it is general boiler performance testing or for verification of a set of measurements, the MEB is a very useful tool, but if the focus is to monitor the furnace exit temperature online and inform real time operating decisions, perhaps a more dedicated instrument is required. Thus, the direct methods were investigated.

5.1.2. Direct methods

The harsh flue gas environment makes accurate and sustainable measurement of the flue gas furnace exit temperature difficult by traditional methods. Contact and optical methods do, however, have their place in boiler monitoring and performance improvement. As mentioned, the optical methods function as a flame detection tool at Eskom plants presently, and the contact methods are very useful if an ad-hoc combustion performance test, for example, needs to be carried out. The shortcomings of these common devices have made the acoustic pyrometry an attractive proposition.

As the acoustic pyrometer has not been used on power plants in South Africa, it was important to establish some fundamental concepts at the outset. Two aspects which were not tested experimentally but were studied and analysed based on the available literature, were the influence of solid particles on the speed of sound through the gas and the reconstruction of the

temperature profile. Based on these analyses, the particles do impact on the speed of sound through the flue gas, however the impact can be significantly reduced by accounting for the particles in the calculation of the gas properties, to produce pseudo-gas properties for the gas-particle mixture.

The reconstruction of the temperature profile over the furnace is one of the stand out features of acoustic pyrometry. It is an extensive and advanced subject, with many varied approaches which can be used. One such method using Algebraic Reconstruction Technique coupled with multiquadratic radial basis function interpolation was demonstrated briefly in this study for a typical equipment layout. The method was demonstrated using simulated time of flight data for 4 temperature profiles.

It was shown to be a very useful way to determine hotspots in the boiler from the sparse matrix. The final temperature profile produced after interpolation does contain a fair amount of error, particularly when the temperature profile is more intricate. Even with the high maximum error, the reconstructed profile still provides very useful qualitative information. For more simplistic single peak profiles, the reconstruction results are very close to the original profiles. It is possible to improve the accuracy of all reconstructions by increasing the resolution of the sparse matrix, which requires installing more equipment which brings with it a higher capital and maintenance cost.

From literature, it was found that the acoustic pyrometer does contain multiple sources of error/uncertainty, but most of these can be mitigated substantially to produce a very low uncertainty in the final result. For the conditions of the experimental testing in this study, the uncertainty of an individual time of flight measurement was found to be ≈2.4%. In spite of the limitations of the equipment and the testing locations, useful deductions could be made from the testing results. In all cases, the testing results, on average, produced data which was in the acceptable range, and in the case of the unit 6 diagonal path, in close agreement with the results of the indirect methods. The direct method was shown to have a sensitively narrower uncertainty range than the MEB for the old, subcritical drum type boiler tested.

In terms of installation and operation, the acoustic pyrometer does not require major modifications to the plant, however it would require a unit outage to install. The boiler wall would have to have holes drilled into the membrane walls or alternatively manipulated tubes installed to create openings for the generator and/or receiver depending on the device being used. The only other requirements are an air supply and a link to the plant's DCS, which should be readily available at most plants.

The online applicability of direct methods goes without saying, as it is designed to be an online tool, and in the case of acoustic pyrometers, most come with pre-loaded OEM software and hardware for data capture and processing. The ad-hoc maintenance requirements are minimal as the equipment is self-cleaning, and the manufacturer would most likely recommend certain periodic replacements.

In summary, several practical and theoretical aspects of acoustic pyrometry have been studied and the technology has been found to offer significant benefits over the contact and optical based methods. The experimental testing done for this study is the first on-site testing of acoustic pyrometry within the South African power industry, and while many aspects can still be researched further as will be mentioned below, this initial study and testing has been shown to be very promising.

5.2. Recommendations for future work

As the subject of this study is quite broad, it was not possible to address all possible approaches and methods. So the first recommendation would be to explore other measurement tools for determining boiler furnace exit temperature that have not been mentioned or explored in detail in this study. Some of these methods include radiation modelling methods such as the Monte Carlo and heat flux models; and direct methods such as laser spectroscopy and CCD (charged-coupled device) camera.

It was clear in the case of the MEB indirect methods that there are a number of aspects which can be improved to mitigate some of the negative aspects. Some of the future work on this subject could include the following:

- As it was presented here, there were small variations between the Mathcad model developed here, and the Eskom MEB Excel spreadsheet. These should be reconciled to produce one standard completely validated tool.
- Techniques to provide better estimation of ingress air should be investigated for the older Eskom boilers more prone to this ingress air.
- The entire MEB methodology (BMEB, FMEB, BPMEB) should be applied to develop standard models for power stations of different configurations.
- The method can be applied to the new supercritical boilers, utilising measurements of temperature of the furnace walls to better determine the furnace heat transfer, at least at high loads.

In terms of the direct methods:

- Further research should be done into the physical phenomena involved which influence the measurement of radiation pyrometers. These devices are already installed on Eskom boilers, so a method to optimally utilise the information they provide would be very beneficial, both from an academic and industrial perspective.
- In the short term, a minimal acoustic pyrometer system such as the one tested during this study can be installed permanently on a boiler, to provide some indication of furnace exit temperature (if not a full temperature profile) on plants which experience combustion problems. This simplistic system will already assist in plant monitoring, and also provide the opportunity for extended evaluation of acoustic pyrometry. This effort will demonstrate how the information obtained from the AP can be practically utilised during plant operation.
- Leading on from the previous point and with a longer term outlook, a full pilot installation of an acoustic pyrometer system should be implemented on a South African boiler and extensively tested, to experimentally verify the theoretical aspects of this study, such as the speed of sound in 2-phase gas-particle flow, as well as the reconstruction of the temperature profile from multiple acoustic path measurements. More advanced studies in the area of temperature profile reconstruction should be taken to study how the arrangement of acoustic paths and discretisation scheme can improve reconstruction accuracy.
- The possibility of using acoustic pyrometry as an alternative to the thermocouple grids installed at Plant X, for the determination of flue gas flow should also be investigated.
- The topics suggested above and the outcomes of these investigations can form a critical part of EPPEI's inter-university project to improve overall plant condition monitoring.

6. List of References

[1] J. Kitto and S. Stultz, Steam: its generation and use, Ohio: The Babcock & Wilcox Company, 2005.

[2] C. R. Ward, Coal Geology and Technology, Blackwell Scientific Publications, 1984.

[3] PT Hansa Pratama, "Products - Hansa Pratama," 2015. [Online]. Available: http://www.hansapratama.com/Production.php?id=ProdPower. [Accessed 07 November 2015].

[4] «Neftegazservis» Co.Ltd., "«Neftegazservis» Co.Ltd. - Rotary Heat Exchangers - Howden," 2014. [Online]. Available: http://ngs-hab.ru/ENG/hw_rotorheat.php#. [Accessed 07 11 2015].

[5] P. K. Ravulaparthy, "Air preheater leaks: Mind the gap," 19 02 2014. [Online]. Available: http://www.powerengineeringint.com/articles/print/volume-22/issue-2/features/air-preheater-leaks-mind-the-gap.html. [Accessed 07 11 2015].

[6] M. Bramanti, E. A. Salerno, A. Tonazzini, S. Pasini and A. Gray, "An Acoustic Pyrometer System for Tomographic Thermal Imaging in Power Plant Boilers," *IEEE Transactions on Instrumentation and Measurement ,* vol. 45, no. 1, pp. 159-167, 1996.

[7] M. H. Bordbar and T. Hyppänen, "Modeling of Radiation Heat Transfer in a Boiler Furnace," *Advanced Studies in Theoretical Physics,* vol. 1, no. 9-12, pp. 571-584, 2007.

[8] H. Verbanck, "Development of a Mathematical Model for Watertube Boiler Heat Transfer Calculations," in *Proceedings of the South African Sugar Technologists' Association Congress*, 1997.

[9] A. Penninger, F. Lezsovits and J. Rohaly, *Heat Engines and Boilers: Lecture Notes for the undergraduate BSc course,* Budapest: BME Department of Energy Engineering.

[10] R. Govindsamy, "Thermal Performance Evaluation of Heat Exchangers in Pulverised Coal Boilers," University of Witwaterstrand, Johannesburg, 2014.

[11] H. Hottel and E. Cohen, "Radiant heat exchange in a gas-filled enclosure: Allowance for nonuniformity of gas temperature," *AIChE Journal,* vol. 4, no. 1, pp. 3-14, 1958.

[12] W. O. Monnaemang, "A zonal model for radiation heat transfer in coal-fired boiler furnaces," University of Cape Town, Cape Town, 2015.

[13] J. Chandok, I. Kar and S. Tuli, "Estimation of furnace exit gas temperature (FEGT) using optimized radial basis and back-propagation neural networks," *Energy Conversion and Management,* vol. 49, no. 8, pp. 1989-1998, 2008.

[14] Eskom Power Plant Boiler Engineering, *Boiler Mass and Energy Balances Guideline and User Manual-V1.15,* Sunninghill: Eskom Generation Business Engineering, 2010.

[15] *Water-tube boilers and auxiliary installations - Part 15: Acceptance tests,* EN12952-15:2003, 2003.

[16] *Fired Steam Generators Performance Test Code,* ASME PTC 4-2008, 2008.

[17] S. Peta, "xxxxxx Combustion Reliability Improvement (CRI) Project," Eskom Generation Business Engineering, Middelburg, 2010.

[18] Y. A. Çengel and M. A. Boles, Thermodynamics: An Engineering Approach, McGraw-Hill, 2006.

[19] G. Rogers and Y. Mayhew, Thermodynamics and Transport Properties of Fluids, Wiley-Blackwell, 1995.

[20] Joint Committee for Guides in Metrology, *Evaluation of measurement data – Guide to the expression of uncertainty in measurement,* JCGM, 2010.

[21] J. Chedaille and Y. Braud, Industrial Flames Volume 1: Measurements in Flames, London: Edward Arnold (Publishers) Ltd., 1972.

[22] H. Jones, Radiation Heat Transfer, Oxford: Oxford Univeristy Press, 2000.

[23] T. A. Hanson, N. Yilmaz, P. Drozda, W. Gill, T. J. Miller and A. B. Donaldson, "Acoustic Pyrometry using Off-the-Shelf Range Finding System," *Journal of Fire Sciences,* vol. 26, pp. 287-308, 2008.

[24] Innovative Combustion Technologies, Inc., "1 - Furnace HVT Traverse Standard.pdf," [Online]. Available: http://www.innovativecombustion.com/pdfs/Furnace 20HVT%20Traverse%20Standard.pdf. [Accessed 30 September 2015].

[25] J. A. Kleppe, Engineering Applications of Acoustics, Norwood: Artech House, 1989.

[26] J. Lu, K. Wakai, S. Takahashi and S. Shimizu, "Acoustic computer tomographic pyrometry for two-dimensional measurement of gases taking into account the effect of refraction of sound wave paths," *Measurement Science and Technology,* vol. 11, no. 6, pp. 692-697, 2000.

[27] G. Kychakoff, A. F. Hollingshead and S. P. Boyd, "Use of Acoustic Temperature Measurements in the Cement Manufacturing Pyroprocess," in *2005 IEEE Cement Industry Technical Conference Record*, Kansas City, 2005.

[28] IMPAC Infrared GmbH, Pyrometer Handbook, Frankfurt: IMPAC Infrared GmbH, 2004.

[29] W. Gray and R. Müller, Engineering Calculations in Radiative Heat Transfer, Pergamon Press, 1974.

[30] J. Kleppe, "Adapt acoustic pyrometer to measure flue-gas flow," *Power,* vol. 139, no. 8, pp. 46-47, 1995.

[31] S. Udakara and G. Altangerel, "Basic Principles of Radiation Thermometry and Thermometer Calibrations," *Metrology Info,* vol. 14, no. 67, pp. 10-13, 2012.

[32] J. Nicholas and D. White, Traceable Temperatures, Chichester, England: John Wiley & Sons Ltd, 2001.

[33] K. Young, S. Ireland, M. Melendez-Cervates and R. Stones, "On the systematic error associated with the measurement of temperature using acoustic pyrometry in combustion products of unknown mixture," *Measurement Science and Technology,* vol. 9, no. 1, pp. 1-5, 1998.

[34] F. Rinaldi and B. Najafi, "Temperature Measurement in WTE Boilers Using Suction Pyrometers," *Sensors,* vol. 13, no. 11, pp. 15633-15655, 2013.

[35] G. Shen, L. An and G. Jiang, "Real-time Monitoring on Boiler Combustion Based on Acoustic Measurement," in *Power India Conference*, New Delhi, 2006.

[36] A. M. Mayer, "On an acoustic pyrometer," *Philosophical Magazine Series 4,* vol. 45, no. 297, pp. 18-22, 1873.

[37] S. Green and A. Woodham, "Rapid Furnace Temperature Distribution Measurement by Sonic Pyrometry," Central Electricity Generating Board, Southampton, 1983.

[38] R. Wyber, "The Design of a Spark Discharge Acoustic Impulse Generator," *IEEE Transactions on Acoustics, Speech and Signal Processing,* vol. 23, no. 2, pp. 157-162, 1975.

[39] S. P. Nuspl, E. P. Szmania, J. A. Kleppe and P. R. Norton, "Acoustic pyrometer". USA Patent US 4848924 A, 18 July 1989.

[40] S. Green, "An acoustic technique for rapid temperature distribution measurement," *Journal of the Acoustical Society of America,* vol. 77, no. 2, pp. 759-763, 1985.

[41] S. Nuspl, J. Kleppe, E. Szmania and P. Norton, "Acoustic Pyrometry Applied to Utility Boilers," in *Proceedings of Joint ASME/IEEE Power Generation Conference*, Portland, 1986.

[42] J. A. Kleppe, "The Application of Digital Signal Processing to Acoustic Pyrometry," in *IEEE Digital Signal Processing Workshop Proceedings*, Loen, 1996.

[43] H. Sielschott and F. Wübbeling, "Waveform Inversion in Acoustic Pyrometry," in *1st World Congress on Industrial Process Tomography*, Greater Manchester, 1999.

[44] Enertechnix, Inc., "Enertechnix, Inc. - PyroMetrix Acoustic Pyrometers," 2015. [Online]. Available: http://www.enertechnix.com/products_services_3.asp. [Accessed 01 October 2015].

[45] X. Shen, Q. Xiong, W. Shi, S. Liang, X. Shi and K. Wang, "A New Algorithm for Reconstructing Two-Dimensional Temperature Distribution by Ultrasonic Thermometry," *Mathematical Problems in Engineering,* vol. 2015, 2015.

[46] S. Zhang, G. Shen, L. An and Y. Niu, "Online monitoring of the two-dimensional temperature field in a boiler furnace based acoustic computed tomography," *Applied Thermal Engineering,* vol. 75, pp. 958-966, 2015.

[47] K. Srinivasan, T. Sundararajan, S. Narayanan, T. Jothi and C. Rohit Sharma, "Acoustic

Pyrometry in Flames," *Measurement,* vol. 46, no. 1, pp. 315-323, 2013.

[48] T. Janda, P. Madejski, K. Szczepanek, N. Modlinski and W. Kordylewski, "Verification of Computational Fluid Dynamics Pulverised Coal Boiler Simulation Using a System of Acoustic Temperature Measurement," in *12th International Conference on Boiler Technology*, Szczyrk, 2014.

[49] J. A. Kleppe, J. Maskaly and G. Bean, "The Application of Image Processing to Acoustic Pyrometry," in *International Conference on Image Processing*, Lausanne, 1996.

[50] H. Sielschott, "Measurement of horizontal flow in a large scale furnace using acoustic vector tomography," *Flow Measurement and Instrumentation,* vol. 8, no. 3-4, pp. 191-197, 1998.

[51] S. G. Deduck and D. Suplicki, "Advanced Technologies Provide New Insights for Assisting Energy from Waste (EfW) Boiler Combustion Monitoring, Operations and Maintenance," in *Proceedings of the 16th Annual North American Waste-to-Energy Conference*, Philadelphia, 2008.

[52] SEI Spain, "SEI Spain Acoustic Pyrometer," [Online]. Available: http://www.seispain.com/product.html. [Accessed 01 10 2015].

[53] Bonnenberg+Drescher, "Produkte und Entwicklungen," 2004. [Online]. Available: http://www.budi.de/produkte/frprodukt.html. [Accessed 01 10 2015].

[54] J. Kleppe, "High-Temp Gas Measurement Using Acoustic Pyrometry," *Sensors,* vol. 13, no. 1, pp. 17-22, 1996.

[55] G. B. Wallis, One-dimensional two-phase flow, New York: McGraw-Hill, 1969.

[56] L.-S. Fan and C. Zhu, Principles of Gas-Solid Flows, New York: Cambridge University Press, 1998.

[57] S. L. Soo, "Effect of Transport Process on Attenuation and Dispersion in Aerosols," *Journal of the Acoustical Society of America,* vol. 32, no. 8, p. 943, 1960.

[58] G. E. Klinzing, F. Rizk, R. Marcus and L. Leung, Pneumatic Conveying of Solids: A theoretical and practical approach, London: Chapman and Hall, 1997.

[59] M. Weber, Strömungs- Fördertechnik, Mainz: Krausskopf-Verlag, 1974.

[60] R. Gordon, R. Bender and G. T. Herman, "Algebraic Reconstruction Techniques (ART) for Three-dimensional Electron Microscopy and X-ray Photography," *Journal of Theoretical Biology,* vol. 29, no. 3, pp. 471-481, 1970.

[61] Siemens AG, *Siemens Operating Manual,* Erlangen, Germany: Siemens, 2010.

[62] Enertechnix inc., *Enertechnix PyroMetrix AP-204 Installation, Operation and Maintenance Manual,* Enertechnix, 2014.

[63] M. Anna, *Personal communication,* 2015.

[64] OMEGA Engineering, Inc., "Introduction to Infrared Pyrometers," [Online]. Available: https://www.omega.com/temperature/Z/InfraredPyrometers.html. [Accessed 01 12 2015].

[65] S. Peta, C. du Toit, R. Naidoo, W. Schmitz and L. Jestin, "Investigations of Operational Problems at a 200MWe PF Boiler," *Chemical and Process Engineering,* vol. 36, no. 3, pp. 305-320, 2015.

Appendix A. Mathcad equation writing benefits

While Microsoft Excel is a very powerful tool with a wide range of applications, as used in the error propagation program presented in this document, a detailed excel spreadsheet often does not allow for easy traceability of calculations. By this, it is meant that the calculation flow or methodology is difficult to trace, especially when different versions have to be produced to account for progress done during successive studies. As the model is meant to be used as a future reference tool for plant system engineers in the Eskom power plant fleet as well as for training purposes, it is not an easy task for the user to decipher which equations were used. The figure below is a basic example of more traceable equation writing in Mathcad compared with Excel.

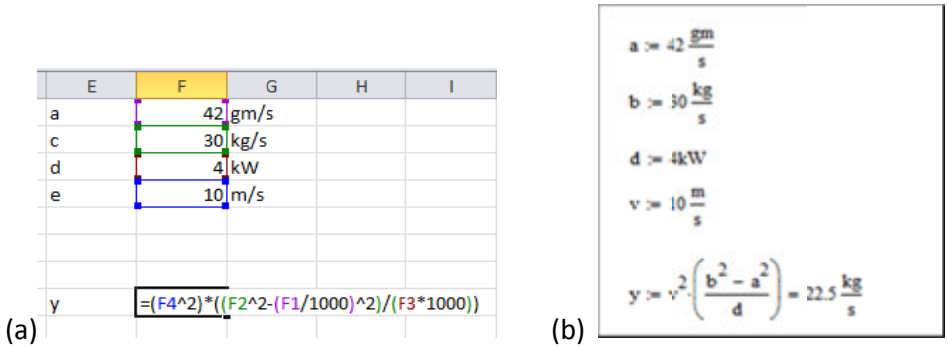

Figure: Comparison of Excel and Mathcad. (a) Excel (b) Mathcad

The figure above is a very rudimentary example but it points out the key differences which are:

- The visual difference is very clear. Mathcad equations are written in a normal mathematics notation format, whereas Excel requires formulas and cell references to write equations. The equation in (b) is instantly more legible than (a).
- Equations in Mathcad do not require any user effort for the conversion of units, thus removing one source of errors. The unit conversions are done internally, and calculation results can be displayed in any desired unit.
- Mathcad can also directly produce a calculation model as a legible document as can be seen by the full MEB calculation model in Appendix B.

This type of calculation models facilitates easier transfer of knowledge from student to student in the development of successive or connected topics. These are the main reasons why EPPEI has decided to generalise the use of Mathcad for its 8 specialisation centres at different universities.

Appendix B. MEB calculations with primary boundary

Inputs

Coal Analysis

	Mass Fraction	Calorific Value	Stoichiometric Coefficients	Molar Mass
Carbon	$mf_C := 47.27\%$	$CV_C := 32778.15 \frac{kJ}{kg}$	$St_C := 1$	$M_C := 12 \frac{gm}{mol}$
Hydrogen	$mf_H := 2.95\%$	$CV_H := 119931.72 \frac{kJ}{kg}$	$St_H := 0.5$	$M_H := 1 \frac{gm}{mol}$
Nitrogen	$mf_N := 1.07\%$	$CV_N := 0 \frac{kJ}{kg}$	$St_N := 0.3$	$M_N := 14 \frac{gm}{mol}$
Sulphur	$mf_S := 0.99\%$	$CV_S := 9257.524 \frac{kJ}{kg}$	$St_S := 1.0$	$M_S := 32 \frac{gm}{mol}$
Water	$mf_{H2O} := 7.3\%$	$CV_{H2O} := 0 \frac{kJ}{kg}$	$St_{H2O} := 0$	
Ash	$mf_{ash} := 31.87\%$	$CV_{ash} := 0 \frac{kJ}{kg}$	$St_{ash} := 0$	
Oxygen	$mf_O = 8.55 \cdot \%$	$CV_O := 0 \frac{kJ}{kg}$	$St_O := -0.5$	$M_O := 16 \frac{gm}{mol}$

$$mf_C + mf_O + mf_H + mf_N + mf_S + mf_{H2O} + mf_{ash} = 1.0000$$

Net calorific value of coal (calculated):

$$CV_{LHV.calc} := mf_C \cdot CV_C + mf_O \cdot CV_O + mf_H \cdot CV_H + mf_N \cdot CV_N + mf_S \cdot CV_S + mf_{H2O} \cdot CV_{H2O} + mf_{ash} \cdot CV_{ash} = 19123.87 \cdot \frac{kJ}{kg}$$

CV of coal (measured):

$$CV_{measured} := 19132.61 \frac{kJ}{kg}$$ (Coal analysis report gives HHV)

Converting this to LHV:

$$CV_{coal} := CV_{measured} - \left[212 \cdot mf_H + 24 \cdot \left(mf_{H2O} + 0.1 \cdot mf_{ash}\right) + 0.8 \cdot mf_O\right] \cdot \frac{kJ}{kg} = 19123.77 \cdot \frac{kJ}{kg}$$

Difference in Measured and Calculated CV values:

$$CV_{diff} := CV_{LHV.calc} - CV_{coal} = 0.096 \cdot \frac{kJ}{kg}$$

Adjust Carbon content so that the calculated value matches the measured CV.

Meteorological inputs

Atmospheric pressure:	$P_{atm} := 83kPa$	(approximate value for altitude in Ermelo)
Atmospheric air temperature:	$T_{atm} := 17\ °C$	(Weather report)
Relative humidity of air (m/m):	$RH := 7\%$	(Weather report)

Air/flue gas inputs

Ambient air temperature inside boiler house:	$T_{amb} := 26\ °C$	(Temperature inside boiler house from P&T Total air flow Report)
Oxygen concentration at A/H flue gas inlet (v/v):	$\%O_{2.A/H.fg.inlet} := 4.332874298\%$	
Oxygen concentration at A/H flue gas outlet (v/v):	$\%O_{2.A/H.fg.outlet} :=$ ▪ %	(No measurement available)
Flue gas temperature at A/H Inlet (Boiler exit temperature):	$T_{fg.A/H.inlet} := 322\ °C$	
Flue gas temperature at A/H outlet:	$T_{fg.A/H.outlet} :=$ ▪ °C	
Air temperature at A/H outlet:	$T_{air.A/H.outlet} := 230\ °C$	
Ingress air (% of total air):	$\%Air_{ing} := 10\%$	
Ingress air distribution to furnace:	$\%Ingress_{furnace} := 100\%$	
Ingress air distribution to backpass:	$\%Ingress_{backpass} := 0\%$	

Ash analysis

Unburnt carbon in fly ash (m/m):	$\%C_{fa} := 3.416\%$
Unburnt carbon in bottom ash (m/m):	$\%C_{ba} := 3.416\%$
Fraction of fly ash in total ash:	$\%FA := 90\%$
Fraction of bottom ash in total ash:	$\%BA := 100\% - \%FA = 10 \cdot \%$

Bottom ash exit temperature: $T_{BA.exit} := 800\ °C$

Enthalpy of ash: $h_{ash}(T) := 1.38 \cdot \left(\frac{T}{K}\right) \cdot \frac{kJ}{kg}$ (Assumed to have the same enthalpy as coal)

Feed water inputs

Mass flow rate of feed water to economizer: $\dot{m}_{fw.econ.in} := 185.84922 \frac{kg}{s}$

Pressure of feed water: $P_{fw} := 15.71199608MPa = 157.12 \cdot bar$

Temperature of feed water (economizer inlet): $T_{fw.econ.in} := 181.7398987\ °C$

Temperature of feed water (economizer outlet): $T_{fw.econ.out} := 284.2469025\ °C$

Superheater inputs

Pressure of Steam (drum outlet): $P_{steam.drum} := 11.43094444MPa = 114.309 \cdot bar$

Temperature of steam (final superheater outlet): $T_{steam.sh.out} := 534.0349731\ °C$

Pressure of steam (final superheater outlet): $P_{steam.sh.out} := 10.6794157MPa = 106.794 \cdot bar$

Mass flowrate of attemperator water: $\dot{m}_{sh.att} := 13.29690886 \frac{kg}{s}$

Pressure of attemperator water: $P_{sh.att} := 15.71199608MPa = 157.12 \cdot bar$

Temperature of attemperator water: $T_{sh.att} := 181.7398987\ °C$

Energy losses

Using the graph provided in EN 12952, boiler convective and radiative losses to the surroundings can be estimated as follows.

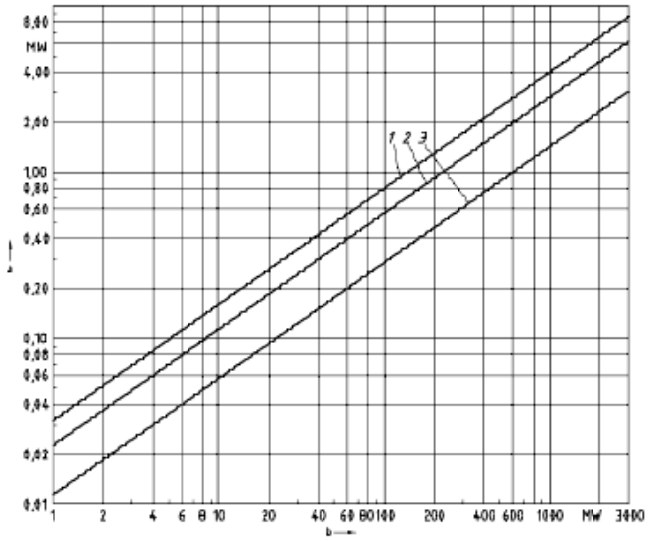

Key
a Radiation and convection losses, $\dot{Q}_{RC}$
b Maximum useful heat output, $\dot{Q}_N$

1 Brown coal, blastfurnace gas and fluidized-bed boilers
2 Hard coal boilers
3 Fuel oil and natural gas boilers

Credits

Any energy added to the fuid stream inside the control volume must be accounted for. Some of these energy sources can be considered as credits. The energy contribution from these components are quantified below using values from the Operating Technical Specification Boiler Plant Document and Boiler C-Schedules.

At full load, 4 mills are running. Using the rated power of the mills and the effciency of 90% the total power added to the fluid stream in the mills is as follows:

Power to mills: $P_{mills} := 231 \cdot kW \cdot 4 \cdot 90\% = 831.6 \cdot kW$

Primary air and forced draught fans all add energy to the air entering the boiler. The energy of the forced draught does not need to be taken into account if the air heater is excluded as the exact condition of the air at air heater exit is known. In the case where the inlet temperature of the air heater is taken to be ambient then the energy added to the air by the FD fan needs to be taken into account.

Power to primary air fans: $P_{pa.fans} := 445hp \cdot 4 \cdot 90\% = 1194.611 \cdot kW$

(1 PA fan per mill, therefore 4 PA fans in operation at full load)

Power to seal air Fans: $P_{seal.fans} := 15hp \cdot 4 \cdot 84\% = 37.583 \cdot kW$

(1 Seal Air fan per mill, therefore 4 Seal Air fans in operation at full load)

Power to forced draught fans: $P_{fd.fans} := 1150hp \cdot 2 \cdot 93.5\% = 1603.628 \cdot kW$

Total power to fans inside boudnary: $P_{fans} := P_{seal.fans} + P_{pa.fans} = 1232.194 \cdot kW$

The Boiler C-Schedule specifies that the seal air fans have a design duty of 1.035 m³/s per boiler.

Volumetric flow rate of seal air: $V'_{seal.air} := 1.035 \frac{m^3}{s}$

Any fuel sources other than Coal are not accounted for later and are accounted for below:

Oil and other energy inputs: $P_{other} := 0kW$

Constants

The following list of constants are needed for various calculations later in this document:

Molar mass of O_2: $M_{O2} := 32 \frac{gm}{mol}$

Molar mass of CO_2: $M_{CO2} := 44.01 \frac{gm}{mol}$

Molar mass of CO: $M_{CO} := 28.01 \frac{gm}{mol}$

Molar mass of N_2: $M_{N2} := 28.02 \frac{gm}{mol}$

Molar mass of SO_2: $M_{SO2} := 64.07 \frac{gm}{mol}$

Molar mass of NO_2: $M_{NO2} := 46.01 \frac{gm}{mol}$

Molar mass of Air: $M_{air} := 29 \frac{gm}{mol}$

Oxygen concentration in atmosphere (m/m): $\%O_{2.m/m} := 23.2\%$ (http://www.engineeringtoolbox.com/air-composition-d_212.html)

Oxygen concentration in atmosphere (v/v): $\%O_{2.v/v} := 20.95\%$

Latent heat of vaporization of water: $h_{H2O.vap} := 2270 \frac{kJ}{kg}$

Oxygen - flue gas density ratio: $\rho_{ratio} := \frac{32}{31} = 1.0322581$ (Molar Mass of Oxygen divided by Molar Mass of Flue Gas)

Mass balances

Unburnt carbon

Not all carbon takes part in the combustion reaction and some is contained in ash that leaves the furnace as fly ash or bottom ash. The amount of unburnt carbon from the ash analysis is interpreted below:

Mass of unburnt carbon per kg of coal: $C' := mf_{ash} \cdot \left[\left(\%C_{fa} \cdot \%FA \right) + \left(\%C_{ba} \cdot \%BA \right) \right] = 0.011$

Mass of unburnt carbon per kilogram of carbon: $C'' := \frac{C'}{mf_C} = 2.303 \cdot \%$

Energy in unburnt carbon per kJ of energy input: $C''' := \frac{CV_C \cdot mf_C \cdot C'}{CV_{coal}} = 0.882 \cdot \%$

Air and flue gas per kg of coal input

The minimum amount of air required for complete combustion is defined as the stoichiometric air required (SAR) and is dependent on the compostion of fuel.

Stoichiometric air required:

$$SAR := \frac{1}{\%O_{2.m/m}} \cdot \left[\frac{32}{12} \cdot \left(mf_C - C' \right) + 8 \cdot mf_H + 0.3 \cdot \frac{32}{14} mf_N + \frac{32}{32} \cdot mf_S - mf_O \right] = 6.0312 \quad \left(\frac{kg_{air}}{kg_{coal}} \right)$$

In order to ensure complete combustion, boilers are supplied with a certain amount of excess air. There is also ingress air which enters into the boiler at various locations. As a result, there is a certain amount of excess air contained in the flue gas leaving the control volume. To determine this amount of excess air, the oxygen concentration at the flue gas inlet of the air heater is used as a measure of the amount of excess air.

Excess air at A/H inlet: $$EA_{A/H.fg.inlet} := \frac{SAR + 1 - mf_{ash}}{SAR} \cdot \frac{\%O_{2.A/H.fg.inlet}}{\frac{\%O_{2.m/m}}{\rho_{ratio}} - \%O_{2.A/H.fg.inlet}} = 26.581 \cdot \%$$

Using the percentage of excess air in the furnace, it is possible to determine the amount of dry air entering the control volume:

Dry air required in the control volume: $DAR := SAR \cdot \left(1 + EA_{A/H.fg.inlet} \right) = 7.634 \quad \left(\frac{kg_{air}}{kg_{coal}} \right)$

However there is also some humidity in the air entering the control volume, so the total amount of air entering the control volume is defined as the humid air required (HAR):

Humid air required: $HAR := (1 + \omega) \cdot DAR = 7.642 \quad \left(\frac{kg_{air}}{kg_{coal}} \right)$

The flue gas composition per kilogram of coal is determined from the equations shown below (The equations assume that (i) Oxidation of carbon, sulphur and hydrogen is complete, (ii) 30% of the Nitrogen is oxidised as NO2)

Mass Flow Rate of Flue Gas per kg Coal: $\dot{m}_{fg} := \left(1 - mf_{ash} \right) - C' + HAR = 8.312 \quad \left(\frac{kg_{air}}{kg_{coal}} \right)$

Mass Flow Rate of Flue Gas per kg Coal: $\dot{m}_{fg} := \left(1 - mf_{ash}\right) - C' + HAR = 8.312 \left(\frac{kg_{air}}{kg_{coal}}\right)$

Flue gas composition by mass

Mass flow rate of CO_2 per kg coal: $\dot{m}_{CO2} := \frac{M_{CO2}}{M_C} \cdot \left(mf_C - C'\right) = 1.694$

Mass flow rate of N_2 per kg coal: $\dot{m}_{N2} := \left(1 - \%O_{2.m/m}\right) \cdot DAR + 0.7 \cdot \left(\frac{1}{2}\right) \cdot mf_N = 5.867$

Mass flow rate of H_2O per kg coal: $\dot{m}_{H2O} := mf_{H2O} + \omega \cdot DAR + \frac{2M_{H2O}}{4M_H} \cdot mf_H = 0.34647$

Mass flow rate of SO_2 per kg coal: $\dot{m}_{SO2} := \frac{M_{SO2}}{M_S} \cdot mf_S = 0.02$

Mass flow rate of NO_2 per kg coal: $\dot{m}_{NO2} := 0.3 \cdot \frac{M_{NO2}}{M_N} \cdot mf_N = 0.011$

Mass flow rate of O2 per kg coal: $\dot{m}_{O2} := \dot{m}_{fg} - \dot{m}_{CO2} - \dot{m}_{N2} - \dot{m}_{H2O} - \dot{m}_{SO2} - \dot{m}_{NO2} = 0.375$

Using the flue gas composition above, the mass percentages of flue gas constituents can be determined.

Mass fraction of O_2: $mf_{O2.fg} := \frac{\dot{m}_{O2}}{\dot{m}_{fg}} = 4.512 \cdot \%$

Mass fraction of CO_2: $mf_{CO2.fg} := \frac{\dot{m}_{CO2}}{\dot{m}_{fg}} = 20.375 \cdot \%$

Mass fraction of N_2: $mf_{N2.fg} := \frac{\dot{m}_{N2}}{\dot{m}_{fg}} = 70.58 \cdot \%$

Mass fraction of SO_2: $mf_{SO2.fg} := \frac{\dot{m}_{SO2}}{\dot{m}_{fg}} = 0.238 \cdot \%$

Mass fraction of NO_2: $mf_{NO2.fg} := \frac{\dot{m}_{NO2}}{\dot{m}_{fg}} = 0.127 \cdot \%$

Mass fraction of H_2O: $mf_{H2O.fg} := \frac{\dot{m}_{H2O}}{\dot{m}_{fg}} = 4.168 \cdot \%$

Flue gas compostion by volume

Volume of flue gas components m^3 per kg coal:

Volume of CO2: $v_{CO2.fg} := \left(\frac{\dot{m}_{CO2}}{44}\right) \cdot 22.4 = 0.862$

Volume of O2: $v_{O2.fg} := \left(\frac{\dot{m}_{O2}}{32}\right) \cdot 22.4 = 0.263$

Volume of N2: $v_{N2.fg} := \left(\frac{\dot{m}_{N2}}{28}\right) \cdot 22.4 = 4.694$

Volume of SO2: $v_{SO2.fg} := \left(\frac{\dot{m}_{SO2}}{64}\right) \cdot 22.4 = 6.938 \times 10^{-3}$

Volume of NO2: $v_{NO2.fg} := \left(\frac{\dot{m}_{NO2}}{46}\right) \cdot 22.4 = 5.137 \times 10^{-3}$

Volume of H2O: $v_{H2O.fg} := \left(\frac{\dot{m}_{H2O}}{18}\right) \cdot 22.4 = 0.431$

Volume of flue gas at STP: $v_{fg} := v_{CO2.fg} + v_{O2.fg} + v_{NO2.fg} + v_{SO2.fg} + v_{N2.fg} + v_{H2O.fg} = 6.262$

Using the mass fractions of the flue gas components, the molar mass of flue gas can be calculated.

Molar Mass of Flue Gas: $M_{fg} := mf_{O2.fg} \cdot M_{O2} + mf_{CO2.fg} \cdot M_{CO2} + mf_{N2.fg} \cdot M_{N2} \ldots + mf_{SO2.fg} \cdot M_{SO2} + mf_{NO2.fg} \cdot M_{NO2} + mf_{H2O.fg} \cdot M_{H2O} = 31.14941 \cdot \frac{gm}{mol}$

$$h_{air}(T) := \begin{cases} linterp\left(Air^{\langle 0 \rangle}, Air^{\langle 1 \rangle}, \frac{T}{K}\right) \cdot \frac{kJ}{kg} & \text{if } 200K < T < 2250K \\ error("Out of Range") & otherwise \end{cases} \qquad h_{air}(25\ °C) = 298.33$$

$$h_{N2}(T) := \begin{cases} linterp\left(N_2^{\langle 0 \rangle}, N_2^{\langle 1 \rangle}, \frac{T}{K}\right) \cdot \frac{J}{mol} \cdot \frac{1}{M_{N2}} & \text{if } 220K < T < 3250K \\ error("Out of Range") & otherwise \end{cases} \qquad h_{N2}(25\ °C) = 309.53$$

$$h_{O2}(T) := \begin{cases} linterp\left(O_2^{\langle 0 \rangle}, O_2^{\langle 1 \rangle}, \frac{T}{K}\right) \cdot \frac{J}{mol} \cdot \frac{1}{M_{O2}} & \text{if } 220K < T < 3250K \\ error("Out of Range") & otherwise \end{cases} \qquad h_{O2}(25\ °C) = 271.43$$

$$h_{CO2}(T) := \begin{cases} linterp\left(CO_2^{\langle 0 \rangle}, CO_2^{\langle 1 \rangle}, \frac{T}{K}\right) \cdot \frac{J}{mol} \cdot \frac{1}{M_{CO2}} & \text{if } 220K < T < 3250K \\ error("Out of Range") & otherwise \end{cases} \qquad h_{CO2}(25\ °C) = 212.8$$

$$h_{CO}(T) := \begin{cases} linterp\left(CO^{\langle 0 \rangle}, CO^{\langle 1 \rangle}, \frac{T}{K}\right) \cdot \frac{J}{mol} \cdot \frac{1}{M_{CO}} & \text{if } 220K < T < 3250K \\ error("Out of Range") & otherwise \end{cases} \qquad h_{CO}(25\ °C) = 309.64$$

$$h_{H2O}(T) := \begin{cases} linterp\left(H2O^{\langle 0 \rangle}, H2O^{\langle 1 \rangle}, \frac{T}{K}\right) \cdot \frac{J}{mol} \cdot \frac{1}{M_{H2O}} & \text{if } 220K < T < 3250K \\ error("Out of Range") & otherwise \end{cases} \qquad h_{H2O}(25\ °C) = 549.99$$

Taking into account the respective mass fractions of CO2, N2, H2O and O2 the enthalpy of flue gas can be expressed as:

$$h_{fg}(T) := mf_{CO2.fg} h_{CO2}(T) + mf_{N2.fg} h_{N2}(T) + mf_{H2O.fg} h_{H2O}(T) + mf_{O2.fg} h_{O2}(T)$$

Global boiler energy balances

Water and steam enthalpies

With reference to the IAPWS-IF97 worksheet, the enthalpies of the water-steam circuit are determined.

Enthalpy of feed water at economiser inlet: $h_{fw.econ.in} := h_{steam}(P_{fw}, T_{fw.econ.in}, "", "", "") = 778.404 \cdot \frac{kJ}{kg}$

Enthalpy at economiser outlet: $h_{fw.econ.out} := h_{steam}(P_{fw}, T_{fw.econ.out}, "", "", "") = 1254.21 \cdot \frac{kJ}{kg}$

Enthalpy of superheat attemporation water: $h_{sh.att} := h_{steam}(P_{sh.att}, T_{sh.att}, "", "", "") = 778.404 \cdot \frac{kJ}{kg}$

Enthalpy of saturated steam at drum outlet: $h_{steam.drum} := h_{steam}(P_{steam.drum}, "", "", 1, "") = 2697.64 \cdot \frac{kJ}{kg}$

Enthalpy of main steam (superheater outlet): $h_{stecm.sh.out} := h_{steam}(P_{steam.sh.out}, T_{steam.sh.out}, "", "", "") = 3454.569 \cdot \frac{kJ}{kg}$

Mass flowrate of coal:

Coal mass flowrate is determined by an energy balance over the boiler boundary.

Inputs consist of the energy of the CV of coal, the enthalpy of coal, the energy of the air (via the FD fans, ingress and seal air) going to the boiler, and the energy of other credits.

The outputs consist of the energy recovered by steam, flue gas losses, radiant losses, unburnt carbon losses, the energy lost in sensible heat in fly ash and bottom ash, and the energy lost due to evaporation of fuel moisture.

The net energy recovered by the steam can be accounted for by considering the enthalpies and flow rates of water/steam entering and leaving the control volume:

Net energy recovered by steam:

$$Q'_{out} := \left(\dot{m}_{fw.econ.in} + \dot{m}_{sh.att}\right) \cdot h_{steam.sh.out} - \left[\begin{matrix}\left(\dot{m}_{fw.econ.in} \cdot h_{fw.econ.in}\right) \cdots \\ + \left(\dot{m}_{sh.att} \cdot h_{sh.att}\right)\end{matrix}\right] = 532.95 \cdot MW$$

Energy from credits:

$$Q'_{credits} := P_{mills} + P_{fans} + P_{other} = 2063.794 \cdot kW$$

Mass flowrate of seal air to mills: $\dot{m}_{seal.air} := \rho_{air}\left(T_{amb}\right) \cdot V'_{seal.air} = 1 \frac{kg}{s}$

$$\dot{m}_{coal} := \frac{\left(Q'_{out} - Q'_{credits}\right) - \dot{m}_{seal.air} \cdot h_{air}(T_{amb}) + \dot{m}_{seal.air} \cdot h_{air}(T_{air.A/H.outlet})}{CV_{coal}\left(1 - C^{**} - Q_{insul.loss}\right) + h_{coal}(T_{amb}) + \left(HAR - HAR \cdot NAir_{mg}\right) \cdot h_{air}(T_{air.A/H.outlet}) + HAR \cdot NAir_{mg} \cdot h_{air}(T_{amb}) - mf_{fg} \cdot h_{fg}(T_{fg.A/H.inlet}) - mf_{ash} \cdot \%BA \cdot h_{ash}(T_{BA.exit}) - mf_{ash} \cdot \%FA \cdot h_{ash}(T_{fg.A/H.inlet}) - \left(mf_{H2O} \cdot h_{H2O.vap}\right)} = 30.55 \frac{kg}{s}$$

$$\dot{m}_{coal} = 30.55 \frac{kg}{s}$$

Mass flow rates of air and flue gas

Total air in the control volume: $\dot{m}_{air.total} := HAR \cdot \dot{m}_{coal} = 233.463 \frac{kg}{s}$

Ingress air flow: $\dot{m}_{air.ing} := \dot{m}_{air.total} \cdot \%Air_{ing} = 23.34628 \frac{kg}{s}$

Mass Flowrate of air leaving the air heater: $\dot{m}_{air.A/H.out} := \dot{m}_{air.total} - \dot{m}_{air.ing} - \dot{m}_{seal.air} = 209.117 \frac{kg}{s}$

Mass flowrate of flue gas at A/H inlet excluding ash and unburnt carbon: $\dot{m}_{fg.A/H.in} := \dot{m}_{coal} \cdot \dot{m}_{fg} = 253.944 \frac{kg}{s}$

Boiler efficiency analysis

Energy input

Fuel energy input: $Q'_{in} := \dot{m}_{coal} \cdot CV_{coal} = 584.225 \cdot MW$

Losses

Unburnt carbon energy loss: $Q_{loss.UBC} := C'''' \cdot Q'_{in} = 5.153 \cdot MW$

$$\%Q_{loss.UBC} := \left(\frac{Q_{loss.UBC}}{Q'_{in}} \right) = 0.882 \cdot \%$$

Heat loss to surroundings: $Q_{loss.rad} := Q_{insul.loss} \cdot Q'_{in} = 4.674 \cdot MW$

$$\%Q_{loss.rad} := \left(\frac{Q_{loss.rad}}{Q'_{in}} \right) = 0.8 \cdot \%$$

Exiting Flue Gas contains water in the vapour phase. If this water were to be condensed additional energy would be released. The loss due to not condensing this water is quantified below:

Flue Gas Humidity Loss: $Q_{loss.H2O} := \dot{m}_{fg.A/H.in} \cdot mf'_{H2O.fg} \cdot h_{H2O.vap} = 24.027 \cdot MW$

$$\%Q_{loss.H2O} := \left(\frac{Q_{loss.H2O}}{Q'_{in}} \right) = 4.113 \cdot \%$$

Sensible Heat Loss in Bottom Ash: $Q_{loss.ba} := \dot{m}_{coal} \cdot \left(mf_{ash} \cdot \%BA \right) \cdot h_{ash}\left(T_{BA.exit} \right) = 1.442 \cdot MW$

$$\%Q_{loss.ba} := \left(\frac{Q_{loss.ba}}{Q'_{in}} \right) = 0.247 \cdot \%$$

Sensible Heat Loss in Fly Ash:

$$Q_{loss.fa} := \dot{m}_{coal} \cdot \left(mf_{ash} \cdot \%FA\right) \cdot h_{ash}\left(T_{fg.A/H.inlet}\right) = 7.197 \cdot MW$$

$$\%Q_{loss.fa} := \left(\frac{Q_{loss.fa}}{Q'_{in}}\right) = 1.232 \cdot \%$$

Total Sensible Heat Loss in Ash:

$$Q_{loss.ash} := Q_{loss.ba} + Q_{loss.fa} = 8.639 \cdot MW$$

$$\%Q_{loss.ash} := \left(\frac{Q_{loss.ash}}{Q'_{in}}\right) = 1.479 \cdot \%$$

Energy is needed to evapcrate the moisture in coal, this energy loss is quantified below:

Fuel Moisture Loss:

$$Q_{loss.evap} := \dot{m}_{coal} \cdot mf_{H2O} \cdot h_{H2O.vap} = 5.062 \cdot MW$$

$$\%Q_{loss.evap} := \frac{Q_{loss.evap}}{Q'_{in}} = 0.867 \cdot \%$$

The Dry Flue Gas Loss is dirined as the net Energy Loss in the Flue Gas, i.e. the energy in the fluegas at the exit of the control volume minus the energy in the air and coal as they enter the control volume:

$$Q_{loss.fg} := \dot{m}_{fg.A/H.in} \cdot h_{fg}\left(T_{fg.A/H.inlet}\right) - \left[\dot{m}_{air.A/H.out} \cdot h_{air}\left(T_{air.A/H.outlet}\right) + \left(\dot{m}_{air.ing} + \dot{m}_{seal.air}\right) \cdot h_{air}\left(T_{amb}\right) + \dot{m}_{coal} \cdot h_{coal}\left(T_{amb}\right)\right] = 29.813 \cdot MW$$

$$\%Q_{loss.fg} := \frac{Q_{loss.fg}}{Q'_{in}} = 5.103 \cdot \%$$

Boiler Efficiency

LHV Boiler Efficiency (Direct Method):

$$\eta_{LHV.direct} := \frac{Q'_{out}}{Q'_{in} + Q'_{credits}} = 90.902 \cdot \%$$

LHV Boiler Efficiency (Losses Method):

$$Losses := Q_{loss.fg} + Q_{loss.UBC} + Q_{loss.rad} + Q_{loss.ash} + Q_{loss.evap} = 53.341 \cdot MW$$

$$\eta_{LHV.loss} := \frac{\left(Q'_{in} + Q'_{credits} - Losses\right)}{Q'_{in} + Q'_{credits}} = 90.902 \cdot \%$$

The HHV Boiler efficiency is an approximation taking into account the flue gas humidity losses.

HHV Boiler Efficiency (Losses Method):

$$\eta_{HHV.loss} := \frac{\left[Q'_{in} + Q'_{credits} - \left(Q_{loss.fg} + Q_{loss.UBC} + Q_{loss.rad} + Q_{loss.ash}\right) - Q_{loss.H2O}\right]}{Q'_{in} + Q'_{credits}} = 87.667 \cdot \%$$

Furnace Mass and Energy Balances

Energy input to the furnace:

$$E_{in} := \dot{m}_{cir.A/H.out} \cdot h_{air}\left(T_{air.A/H.outlet}\right) + \%Ingress_{furnace} \cdot \dot{m}_{air.ing} \cdot h_{air}\left(T_{amb}\right) \ldots + \dot{m}_{seal.air} \cdot h_{air}\left(T_{amb}\right) + \dot{m}_{coal} \cdot \left(CV_{coal} + h_{coal}\left(T_{amb}\right)\right) + Q'_{credits} = 712.056 \cdot MW$$

Energy transferred to furnace walls:

Percent of vaporization in furnace: $\alpha := 68\%$

$$Q_{cc} := \alpha \cdot \dot{m}_{fw.econ.in} \cdot \left(h_{steam.drum} - h_{fw.econ.out}\right) = 182.417 \cdot MW$$

Radiation calcuted by zonal method:

$$Q_{zonal} := 21765.672kW$$

Iterative furnace energy balance solution

Guess values for iteration

$$T_{fa.FE} := 1300K$$

$$temp := 1500K$$

$FET_f :=$ while $\left|T_{fa.FE} - FET\right| > 0.0001K$

$$T_{fa.FE} \leftarrow FET$$

$$E_{loss} \leftarrow \left(\frac{2}{3}\right) \cdot Q_{loss.rad} + Q_{loss.ba} + \dot{m}_{coal} \cdot \left(mf_{ash} \cdot \%FA\right) \cdot h_{ash}\left(T_{fa.FE}\right) + Q_{loss.UBC} + Q_{loss.evap} + Q_{zonal}$$

$$h_{FEf} \leftarrow \left(\frac{E_{in} - E_{loss} - Q_{cc}}{\dot{m}_{fg.A/H.in} - \%Ingress_{backpass} \cdot \dot{m}_{air.ing}}\right)$$

$$f(T) \leftarrow h_{fg}(T) - h_{FEf}$$

$$FET \leftarrow root(f(temp), temp)$$

FET

$$FET_f = 1338.295 \cdot °C$$

Backpass mass and energy balances

Energy transferred to economiser:

$$Q_{econ} := \dot{m}_{fw.econ.in} \cdot \left(h_{fw.econ.out} - h_{fw.econ.in}\right) = 88.429 \cdot MW$$

Energy transferred to the superheater:

$$Q_{superheaters} := \left(\dot{m}_{fw.econ.in} + \dot{m}_{sh.att}\right) \cdot h_{steam.sh.out} - \dot{m}_{fw.econ.in} \cdot h_{steam.drum} - \dot{m}_{sh.att} \cdot h_{sh.att} = 176.258 \cdot MW$$

Energy of flue gas leaving the control volume:

$$Q_{fg.A/H.in} := \dot{m}_{fg.A/H.in} \cdot h_{fg}\left(T_{fg.A/H.inlet}\right) = 155.58 \cdot MW$$

Energy transferred to the evaporator:

$$Q_{walls} := (1 - \alpha) \cdot \dot{m}_{fw.econ.in} \cdot \left(h_{steam.drum} - h_{fw.econ.out}\right) = 85.843 \cdot MW$$

Energy Losses:

$$Q_{loss} := Q_{loss.fa} + \left(\frac{1}{3}\right) \cdot Q_{loss.rad} = 8.755 \cdot MW$$

Iterative backpass energy balance solution

$FET_b :=$ while $\left|T_{fa.FE} - FET\right| > 0.0001K$

$T_{fa.FE} \leftarrow FET$

$Q_{fa.FE} \leftarrow \dot{m}_{coal} \cdot \left(mf_{ash} \cdot \%FA\right) \cdot h_{ash}\left(T_{fa.FE}\right)$

$$h_{FEb} \leftarrow \frac{Q_{superheaters} + Q_{econ} + Q_{walls} + Q_{fg.A/H.in} + Q_{loss} - Q_{zonal} - Q_{fa.FE} - \%Ingress_{backpass} \cdot \dot{m}_{air.ing} \cdot h_{air}\left(T_{amb}\right)}{\dot{m}_{fg.A/H.in} - \%Ingress_{backpass} \cdot \dot{m}_{air.ing}}$$

$f(T) \leftarrow h_{fg}(T) - h_{FEb}$

$FET \leftarrow root(f(temp), temp)$

FET

$$FET_b = 1338.295 \cdot °C$$

Summary of mass and energy balance results:

Global boiler mass balance results

Mass flow rate of coal: $\dot{m}_{coal} = 30.55 \frac{kg}{s}$

Total air mass flow rate into control volume (incl. ingress + seal air): $\dot{m}_{air.total} = 233.463 \frac{kg}{s}$

Mass flow rate of air at A/H outlet: $\dot{m}_{air.A/H.out} = 209.117 \frac{kg}{s}$

Mass flow rate of flue gas at A/H inlet: $\dot{m}_{fg.A/H.in} = 253.944 \frac{kg}{s}$

Global boiler energy balance results

Total energy input: $Q'_{in} = 584.225 \cdot MW$

Energy recovered by steam: $Q'_{out} = 532.948 \cdot MW$

Heat loss to surroundings: $Q_{loss.rad} = 4.674 \cdot MW$

Unburnt carbon loss: $Q_{loss.UBC} = 5.153 \cdot MW$

Sensible heat loss in ash: $Q_{loss.ash} = 8.639 \cdot MW$

Dry flue gas loss: $Q_{loss.fg} = 29.813 \cdot MW$

Fuel moisture loss: $Q_{loss.evap} = 5.062 \cdot MW$

Boiler efficiency (Direct method): $\eta_{LHV.direct} = 90.902 \cdot \%$

Boiler efficiency (Losses method): $\eta_{LHV.loss} = 90.902 \cdot \%$

HHV Boiler efficiency: $\eta_{HHV.loss} = 87.667 \cdot \%$

Furnace MEB results

Furnace Exit Temperature: $FET_f = 1338.295 \cdot °C$

Backpass MEB results

Furnace Exit Temperature: $FET_b = 1338.295 \cdot °C$

Appendix C. Uncertainty propagation programme

A Microsoft Excel Visual Basic for Applications (VBA) programme was developed to perform the uncertainty propagation task. The programme allows the user to specify input data and their uncertainties into a Mathcad model and retrieve the desired outputs in Excel with their uncertainties. Moreover, the programme is designed to be generic so that it can be applied to any Mathcad calculation model.

The user of the programme needs to make slight modifications to their Mathcad model to enable it to be used by the VBA programme. All input and extraction of data is handled from the Excel interface. Thus, the inputs should be specified in the Mathcad file as x1, x2, x3…etc. corresponding to the number in the Excel interface. Once that is done, the user now has a Mathcad file that is compatible with the VBA programme.

The Mathcad file can be loaded. The input names (as they are named in Mathcad), the values (in the units they are input into Mathcad), and the % uncertainty must be input. The output names need to be specified, and it should be noted that the output results retrieved from Mathcad will be in SI units.

The program calculates the uncertainties of the specified outputs as a result of each of the inputs alone, and also the overall uncertainty of the output due to all of the inputs combined.

Appendix D. Calculation of emissivity of furnace exit surface

The calculation of the emissivity of the furnace exit "surface" requires a consideration of the emissivities of both the particles and the gas

Gas emissivity

Consider first the gas phase:

The VDI Heat Atlas provides a method and several graphs which can be used to determine the flue gas emissivity, which is made up predominantly of the emissivity of CO_2 and H_2O.

The emissivity of the gas is given by:

$$\varepsilon_g = f_{p.CO2} \cdot \varepsilon'_{CO2} + f_{p.H2O} \cdot \varepsilon'_{H2O} - \Delta\varepsilon$$

where all of the values in the equation are dependant on the partial pressures, mean beam length and temperature of the gas

The ε' values represent values read off from graphs for a total pressure of 1atm, and the f_p values are correction factors for the actual pressures of the gases. Δε is a correction for the overlapping of CO_2 and H_2O wavelength bands

There are a few paramters that to be calculated first.

Total pressure of flue gas:

From DCS, furnace pressure is ~ -130Pa. So $P_{total} := 85kPa - 130Pa = 8.487 \times 10^4 Pa$

From MEB calculations, the volume fractions of H_2O and CO_2 in flue gas are calculated as:

$x_{CO2} := 13.28\%$

$x_{H2O} := 6.54\%$

By ideal gas relations, the ratio of volume fractions is equal to the ratio of partial pressures. Therefore:

$P_{CO2} := x_{CO2} \cdot P_{total} = 0.113 \cdot bar$

$P_{H2O} := x_{H2O} \cdot P_{total} = 0.056 \cdot bar$

Also required is the mean beam length, L_m, for the geometry beirg considered. In general:

$$L_m = 3.5 \cdot \frac{V}{A_{total}}$$

where V is the volume of the enclosure and A_{total} is the sum of the areas of all the enclosure surfaces.

For the cavity above the furnace:

$L := 14m$

$W := 9m$

$H := 18m$

Thus

$V := L \cdot W \cdot H = 2.268 \times 10^{3} \cdot m^{3}$

$A_{total} := 2 \cdot [(L \cdot W) + (L \cdot H) + (W \cdot H)] = 1.08 \times 10^{3}\ m^{2}$

And $L_m := \frac{V}{A_{total}} \cdot 3.5 = 7.35\ m$

The graphs for emissivity are plotted for specific (partial pressure x mean beam length) values so these need to be calculated

$P_{CO2} \cdot L_m = 0.828 \cdot bar \cdot m$

$P_{H2O} \cdot L_m = 0.414 \cdot bar \cdot m$

Using these values and a temperature of 1650K (because this calculation is for the furnace exit in particular), the values can be read off the graphs, as follows:

$T_g := 1650K$

Consider first CO_2

From the relevant graph in the VDI Heat Atlas::

$\varepsilon'_{CO2} := 0.15$

The correction factor for CO_2 can be calculated as follows:

$$A := \frac{\left[0.1 \cdot \left(\frac{T_g}{1000K}\right)^{-1.45} + 1\right] \cdot \frac{P_{total}}{bar} \cdot \left(1 + 0.28 \cdot \frac{P_{CO2}}{P_{total}}\right) + 0.23}{0.1 \cdot \left(\frac{T_g}{1000K}\right)^{-1.45} + \frac{P_{total}}{bar} \cdot \left(1 + 0.28 \cdot \frac{P_{CO2}}{P_{total}}\right) + 0.23} = 0.995$$

$$B := 0.225 \cdot \left(\frac{T_g}{1000K}\right)^{2} = 0.613$$

$$f_{p.CO2} := 1 + (A - 1) \cdot e^{\left[-0.5 \cdot \left(\log\left(\frac{B}{100 \cdot \frac{P_{CO2}}{bar} \cdot \frac{L_m}{m}}\right)\right)^{2}\right]} = 0.999$$

Since $f_{p.H2O}$ is greater than A $\quad f_{p.CO2} := A = 0.995$

From the relevant graph in the VDI Heat Atlas:

$\varepsilon'_{H2O} := 0.158$

The correction factor for H_2O can be found from as follows:

$$\tau := \frac{T_g}{1000K} = 1.65$$

$$A := \frac{(1.888 - 2.053\cdot\log(\tau))\cdot\frac{P_{total}}{bar}\cdot\left(1 + 4.9\cdot\frac{P_{H2O}}{P_{total}}\cdot\sqrt{\frac{273K}{T_g}}\right) + 1.10\cdot\left(\frac{T_g}{1000K}\right)^{-1.4}}{0.888 - 2.053\cdot\log(\tau) + \frac{P_{total}}{bar}\cdot\left(1 + 4.9\cdot\frac{P_{H2O}}{P_{total}}\cdot\sqrt{\frac{273K}{T_g}}\right) + 1.10\cdot\left(\frac{T_g}{1000K}\right)^{-1.4}} = 0.991$$

$$f_{p.H2O} := 1 + (A - 1)\cdot e^{\left[-0.5\cdot\left[\log\left[\frac{0.132\cdot\left(\frac{T_g}{1000K}\right)^2}{\frac{P_{H2O}}{bar}\cdot\frac{L_m}{m}}\right]\right]^2\right]} = 0.991$$

The overlapping correction factor is determined from the relevant graph in the VDI Heat Atlas:

$$\frac{P_{H2O}}{P_{H2O} + P_{CO2}} = 0.333 \qquad \text{and} \qquad P_{CO2}\cdot L_m + P_{H2O}\cdot L_m = 1.243\cdot bar\cdot m$$

$$\Delta\varepsilon := 0.0514$$

Therefore

$$\varepsilon_g := f_{p.CO2}\cdot\varepsilon'_{CO2} + f_{p.H2O}\cdot\varepsilon'_{H2O} - \Delta\varepsilon = 0.254$$

Particle emissivity:

First we establish the particle properties.

Using values from MEB for ash content and flue gas per kg coal

$\%Ash := (0.9)\cdot 31.87\% = 28.683\cdot\%$ (Assuming 90% fly ash)

$\dot{m}_{fg} := 8.642$ (Mass flow of flue gas per kg of coal)

Estimating densities

$$\rho_{fg} := \frac{(1bar - 130Pa)}{266.9\frac{J}{kg\cdot K}\cdot 1400\,°C} = 0.22364\frac{kg}{m^3}$$

$$\rho_p := 1500\frac{kg}{m^3}$$

$r_p := 35micron$ $d_p := 2\cdot r_p$

Mass fraction of particles in flue gas: $m_p := \frac{\%Ash}{\dot{m}_{fg}} = 0.033$

Volume fraction of particles: $fv := m_p \cdot \frac{\rho_{fg}}{\rho_p} = 4.948 \times 10^{-6}$

$V_p := \frac{4}{3} \cdot \pi \cdot r_p^{\,3} = 1.796 \times 10^{-13} \cdot m^3$ (Volume of single particle)

$N_p := \frac{fv}{V_p} = 2.755 \times 10^{7} \cdot \frac{1}{m^3}$

The emissivity of the particles is given by:

$\varepsilon_p := 1 - e^{\left(-1.5 \cdot fv \cdot \frac{L_m}{d_p}\right)} = 0.541$ (Verified from Gray and Muller)

Now, the total emissivity of the gas-particle mixture is not simply the sum of the emissivities. But rather, the total extinction coefficient of the gas particle mixture is the sum of the extinction coefficients.

So: $\beta_m = \beta_g + \beta_p$

where each β is related to the respective emissivty by: $\varepsilon = 1 - e^{-\beta \cdot L_m}$

Expressing all of the β values in terms of the emissivities and solving for the emissivity of the mixture yields:

$\varepsilon_m := \varepsilon_p + \varepsilon_g - \varepsilon_g \cdot \varepsilon_p = 0.658$

Appendix E. Temperature reconstruction code

```
clc
clear all
close all



%%%%GENERATION OF SIMULATED TIME OF FLIGHT DATA

%This part of script allows for the numerical determination of time of
%flight along any number of straight line paths over any specified
%temperature profile defined by T(x,y).

%Declare symbolic functions of x and y
syms T(x,y);
syms v(x,y);
syms f(x,y);

%INPUT
%Dimensions of furnace
x_dim=14;
y_dim=14;

%INPUT
%Flue gas properties
gam=1.28; %Specific heat ratio gamma
R=258;  %Gas constant



%INPUT
%Temperature profile. Any of the following temperature profiles is
%uncommented to be used

%One peak symmetrical distribution gradual gradient
T(x,y)=1100+300.*sin((pi/14)*x).*sin((pi/14)*y);

%One peak symmetrical distribution steep gradient
%T(x,y)=800+800.*sin((pi/14)*x).*sin((pi/14)*y);

%One peak asymmetrical distribution steep gradient
%T(x,y)=1000+600*(exp(1))^(-((x-7)^2+(y-4)^2)/100);

%2 peak asymmetrical distribution
%T(x,y)=800+800*(exp(1))^(-20*((x/14-1/3)^2+(y/12-2/3)^2))+800*(exp(1))^(-
(20*((x/14-2/3)^2)+15*(y/12-1/3)^2));



%INPUT
%The start and end coordinates of the acoustic paths must be specified.
%Here it is fetched from an Excel spreadsheet in the form of 4 vectors
x_start=xlsread('distance matrix config 2 rev 2','Sheet1','T2:T25');
x_end=xlsread('distance matrix config 2 rev 2','Sheet1','W2:W25');
```

```
y_start=xlsread('distance matrix config 2 rev 2','Sheet1','U2:U25');
y_end=xlsread('distance matrix config 2 rev 2','Sheet1','X2:X25');

%INPUT
%Number of paths
Nt=24;

%Calculations...

%The temperature function is used to determine a velocity function
v(x,y)=(gam*R.*T(x,y)).^(1/2);

%Slowness function (inverse of velocity)
f(x,y)=1./v(x,y);


%Each path is parametrized in terms of the path length in order to carry
%out the line intergation. This is executed 'Nt' times and k represents the
%path number

for k=1:Nt

    syms x(s);
    syms y(s);

    %Parametrizing the paths in terms of s which represents fraction of
    %total path length
    x(s)=x_start(k)+(x_end(k)-x_start(k))*s;
    y(s)=y_start(k)+(y_end(k)-y_start(k))*s;

    %Calculating path length
    L(k)=sqrt((x_end(k)-x_start(k))^2+(y_end(k)-y_start(k))^2);

    syms f_int(s);

    %Determine the integrand in terms of the parameter s
    f_int(s)=f(x(s),y(s))*L(k);

    %This specific statement is to allow the software to
    %recognize f_int(s) as a function that can be integrated
    fun=matlabFunction(f_int);

    format long

    %This statement carries out the numerical integration of the slowness
    %function along path the to calculate the time of flight which is
    %stored in the vector q
    q(k)=integral(fun,0,1);
    % This is done for every path.
end


%_____________________________________________________________________________
%_____________________________________________________________________________

%%%% ALGEBRAIC RECONSTRUCTION TECHNIQUE
```

```
%At this point the numerically determined time of flight data is used as if
%it was measured time of flight data to reconstruct the temperature
%profile by the ART

%The distance matrix of the path length in each discretised element has to
%be input. A spreadsheet input is utilised. Here it is loaded from an excel
%spreadsheet
D=xlsread('distance matrix config 2 rev 2','Sheet1','B2:Q25');

DT=transpose(D);

t=transpose(q);


%Initialise the solution vector
f=zeros(16,1);

%The number of rows of the distance matrix is determined.
m=size(D,1);

%A limit is placed on the maximum number of iterations as a fail safe if
%the solution does not converge
maxiter=20000;

%Relaxation factor
lambda=1;

%Initialize the iteration counter
k=0;

%Algebraic Reconstruction Technique algorithm
while (norm(D*f-t)>1e-6 && k<maxiter)
    ii=mod(k,m)+1;
    f = f + lambda*(t(ii) - D(ii,:)*f)*D(ii,:).'/norm(D(ii,:).')^2;
    k=k+1;
end

%The temperature in each discretised element is calculated
Ti=(1/(gam*R)).*(1./(f.^(2)));


%_____________________________________________________________________________
%_____________________________________________________________________________


%MULTIQUADRATIC RBF INTERPOLATION

%The centre points of the discretised elements are specified
xi=[1.75;5.25;8.75;12.25;1.75;5.25;8.75;12.25;1.75;5.25;8.75;12.25;1.75;5.25;8.7
5;12.25];
yi=[12.25;12.25;12.25;12.25;8.75;8.75;8.75;8.75;5.25;5.25;5.25;5.25;1.75;1.75;1.
75;1.75];


%Interpolation parameters are input
```

```
smooth=2.35;
beta=0.5;

%Number of discretised elements
Nd=16

%RBF calculations
for row=1:Nd
    for col=1:Nd
        phi(row,col)=(((xi(row)-xi(col))^2+(yi(row)-yi(col))^2)+smooth^2)^beta;
    end
end

w=inv(phi)*Ti

syms Tii(x,y);

%Interpolated temperature function is produced
Tii(x,y)=0
for i=1:Nd
    Tii(x,y)=Tii(x,y)+w(i)*(((x-xi(i))^2+(y-yi(i))^2)+smooth^2)^beta;
end


%_____________________________________________________________________________
%_____________________________________________________________________________

% OUTPUTS

%Original profile is plotted
figure;
ezsurf(T,[0,14,0,14])

%Reconstructed profile is plotted
figure;
ezsurf(Tii,[0,14,0,14])


%Error analysis is done to compare the reconstructed to the original on
%a discrete matrix of x-y co-ordinates

step=1;
[xii,yii]=meshgrid(0:step:14);

err=zeros()
errsum=0;
errsumbc=0;
err_max=0;
for j=1:225
   err(j)=(eval(Tii(xii(j),yii(j)))-
eval(T(xii(j),yii(j))))/eval(T(xii(j),yii(j)))*100;
   errsum=errsum+abs(err(j));
   if abs(err(j))>err_max
       err_max=err(j);
       loc_max=j;
   end
end
```

```
err_mean=errsum/225
err_max
loc_max
```

Appendix F. Time of flight detection code

```
clc;
close all;

%Choose path
path='G:\EPPEI\Unit 6 data\';

%Choos files to run
%
file_list=['crossa';'crossb';'crossc';'crossd';'crosse';'crossf';'crossg';'cross
h';'crossi';'crossj';'crossk';'crossl';'crossn';'crosso';'crossp';'crossq';'cros
sr';'crosst';'crossu';'crossv';'crossw';'crossx';'crossz']

file_array=cellstr(file_list);

Nfiles=length(file_array);


%Parameters
NN=2;
rip=0.001;
%Based on visualization of the spectrogram
%The frequency range to be analyzed further is specified
freq_range_lower=200;
freq_range_upper=1000;
%Ensure that band_min and band_max are specified correctly
%Threshold parameters
AST_thresh_factor=1.5;
ASR_thresh_factor=1.5;


% for k=1:Nfiles
    close all;

    full_path=char(strcat(path,file_array(1),'.xls'));

    %Set up excel file parameters
    sheet=1;
    ASTRange='B2:B4097';
    ASRRange='D2:D4097';

    %Specify time step, min and max times
    t_min=0;
    t_step=0.000025;
    t_max=0.102375;
    t=t_min:t_step:t_max;

    fs=40000; %Sample rate

    %Create vectors containing the AST and ASR signal data for each time step t
    AST=xlsread(full_path,sheet,ASTRange);
    ASR=xlsread(full_path,sheet,ASRRange);

    %FAST FOURIER TRANSFORM (FFT)
```

```
%The FFT of both the AST and ASR signals is done in this section
N=length(AST);      %Number of sample points per signal
AST_fft=abs(fft(AST));  %Magnitude of the AST FFT
ASR_fft=abs(fft(ASR));  %%Magnitude of the AST FFT

%FFT can only be performed for frequencies up to half the sampling
%frequency. So the redundant second half of the frequency range which
%is merely a mirror image of the first half is discarded
AST_fft=AST_fft(1:N/2);
ASR_fft=ASR_fft(1:N/2);

%A vector of the frequency values from 0Hz to 20000Hz is created
freq=(0:N/2-1)/0.102375;

%The fourier transform magnitudes are plotted as functions of frequency
figure;
plot(freq,AST_fft);
figure;
plot(freq,ASR_fft);


%The spectrogram plot is produced which plots frequency as a function of
%time, with the colour scale representing the how the power of the entire
%range of frequencie varies with time
nwin=128;
over=110;
nfft=2048;
figure;
spectrogram(ASR,nwin,over,freq,fs,'yaxis');




%The dominant frequency within the selected frequency range is determined
maxf=0;
i_lower=floor((freq_range_lower/(fs/2))*(N/2));
i_upper=ceil((freq_range_upper/(fs/2))*(N/2));
for i=drange(i_lower:i_upper)
    if ASR_fft(i)>maxf
        maxf=ASR_fft(i);
        dom_freq=freq(i); %This is the dominant frequency
    end
end

% %Design of a bandpass filter to filter at the dominat freq
band_min=dom_freq-1;
band_max=dom_freq+1;

D=fdesign.bandpass('N,Fp1,Fp2,Ap',NN,band_min*2/fs,band_max*2/fs,rip);

Hd=design(D);

%The chosen filter is applied to the ASR signal
ASR_filt=filter(Hd,ASR);
AST_filt=filter(Hd,AST);
```

```
%The filtered signal is then rectified for the threshold detection
ASR_pos=abs(ASR_filt);
AST_pos=abs(AST_filt);


%The original signal plus the rectified filtered signal is plotted
figure;
plot(t,ASR,'linewidth',0.5);
hold on;
plot(t,ASR_pos,'r','linewidth',2);

figure;
plot(t,AST);
hold on;
plot(t,AST_pos,'r','linewidth',2);

%THRESHOLD DETECTION
limit1=floor((25/102.375)*4096);
max1=0;
for i1=1:limit1
    if AST_pos(i1)>max1
        max1=AST_pos(i1);
    end
end
AST_threshold=AST_thresh_factor*max1;

limit2=floor((50/102.375)*4096);
max2=0;
for i2=1:limit2
    if ASR_pos(i2)>max2
        max2=ASR_pos(i2);
    end
end
ASR_threshold=ASR_thresh_factor*max2;


[ASTpk ASTloc]=findpeaks(AST,'MinPeakHeight',200);
AST_event=t(ASTloc(1))*1000

[ASRpks,ASRloc]=findpeaks(ASR_pos,'MinPeakHeight',ASR_threshold);
Time_correct=1.5*(t(ASRloc(2))-t(ASRloc(1)));
ASR_event=(t(ASRloc(1))-Time_correct)*1000

TOF=ASR_event-AST_event
```

Appendix G. Detailed time of flight measurement data

Outliers are highlighted.

Plant X Unit 2 Economiser

Date and time	Unit Load (MW)	Pyrometrix AST event (ms)	Pyrometrix ASR event (ms)	Pyrometrix Time of flight (ms)	Matlab AST event (ms)	Matlab ASR event (ms)	Matlab Time of flight (ms)
2014-05-16 10:39	159.98	38.550	68.950	30.400	38.550	69.338	30.788
2014-05-16 10:49	159.29	43.200	73.625	30.425	43.200	73.916	30.716
2014-05-16 10:50	159.26	36.400	66.975	30.575	36.400	67.041	30.641
2014-05-16 10:52	159.42	35.625	66.050	30.425	35.650	66.288	30.638
2014-05-16 10:53	159.75	36.375	78.650	42.275	36.375	66.877	30.502
2014-05-16 10:56	160.07	35.400	65.925	30.525	35.400	66.101	30.701
2014-05-16 10:57	160.18	35.350	65.975	30.625	35.350	66.091	30.741
2014-05-16 10:58	160.91	42.200	72.700	30.500	42.225	65.863	23.638
2014-05-16 10:59	160.81	42.275	156.325	114.050	42.275	73.049	30.774
2014-05-16 11:00	161.23	45.650	87.900	42.250	45.675	76.321	30.646
2014-05-16 11:14	160.31	40.325	70.975	30.650	40.325	71.084	30.759
2014-05-16 11:15	160.22	37.350	79.725	42.375	37.350	67.892	30.542
2014-05-16 11:17	160.48	42.150	72.875	30.725	42.175	67.662	25.487
2014-05-16 11:17	160.48	38.475	68.575	30.100	38.475	69.209	30.734
2014-05-16 11:19	161.05	38.025	68.575	30.550	38.025	68.692	30.667
2014-05-16 11:20	160.84	38.600	69.125	30.525	38.625	69.171	30.546
2014-05-16 11:21	160.87	40.300	70.625	30.325	40.325	70.926	30.601
2014-05-16 11:22	161.17	36.900	67.350	30.450	36.925	67.443	30.518
2014-05-16 11:23	161.06	46.025	75.750	29.725	46.025	72.218	26.193
2014-05-16 11:25	160.73	35.975	66.700	30.725	35.975	66.847	30.872
2014-05-16 11:25	160.73	39.400	70.025	30.625	39.425	70.047	30.622
2014-05-16 11:26	160.47	36.750	66.950	30.200	36.750	67.563	30.813

Plant X Unit 2 Furnace Front

Date and time	Unit Load (MW)	Pyrometrix AST event (ms)	Pyrometrix ASR event (ms)	Pyrometrix Time of flight (ms)	Matlab AST event (ms)	Matlab ASR event (ms)	Matlab Time of flight (ms)
2014-05-15 16:08	160.12	38.875	59.325	20.450	38.875	58.488	19.613
2014-05-15 16:11	160.14	36.800	57.400	20.600	36.800	57.450	20.650
2014-05-15 16:18	160.04	44.900	64.700	19.800	44.900	57.463	12.563
2014-05-15 16:22	160.19	38.425	58.275	19.850	38.425	59.450	21.025
2014-05-15 16:23	159.90	36.950	56.525	19.575	36.975	56.938	19.963
2014-05-15 16:24	160.06	38.025	58.125	20.100	38.050	58.000	19.950
2014-05-15 16:28	160.02	35.875	56.350	20.475	35.875	55.563	19.688
2014-05-15 16:29	160.01	35.175	55.725	20.550	35.175	54.813	19.638
2014-05-15 16:30	160.54	32.525	52.900	20.375	32.550	52.375	19.825

Plant X Unit 6 Furnace Front

Date and time	Unit Load (MW)	Pyrometrix AST event (ms)	Pyrometrix ASR event (ms)	Pyrometrix Time of flight (ms)	Matlab AST event (ms)	Matlab ASR event (ms)	Matlab Time of flight (ms)
2014-06-10 12:00	191.84	31.125	49.100	17.975	31.125	50.688	19.563
2014-06-10 12:02	192.31	38.275	56.325	18.050	38.300	57.525	19.225
2014-06-10 12:04	193.45	33.575	52.425	18.850	33.575	51.025	17.450
2014-06-10 12:05	192.87	34.025	52.525	18.500	34.050	54.263	20.213
2014-06-10 12:08	192.89	34.175	45.600	11.425	34.175	55.925	21.750
2014-06-10 12:20	192.13	30.900	48.750	17.850	30.900	50.113	19.213
2014-06-10 12:30	192.76	32.400	43.675	11.275	30.900	50.113	19.213
2014-06-10 12:40	191.77	33.400	51.650	18.250	33.425	51.413	17.988
2014-06-10 12:50	191.96	35.600	53.900	18.300	35.625	54.763	19.138
2014-06-10 12:53	192.21	33.700	46.950	13.250	33.725	52.125	18.400
2014-06-10 12:58	192.06	32.675	51.875	19.200	32.675	51.788	19.113
2014-06-10 13:24	191.77	40.300	59.450	19.150	40.300	59.513	19.213
2014-06-10 13:31	192.24	33.950	52.575	18.625	33.950	52.288	18.338
2014-06-10 13:35	192.52	33.325	51.200	17.875	33.325	52.363	19.038

Plant X Unit 6 Furnace Diagonal

Date and time	Unit Load (MW)	Pyrometrix AST event (ms)	Pyrometrix ASR event (ms)	Pyrometrix Time of flight (ms)	Matlab AST event (ms)	Matlab ASR event (ms)	Matlab Time of flight (ms)
2014-06-10 14:05	192.74	30.975	51.825	20.850	30.975	52.225	21.250
2014-06-10 14:06	192.14	37.225	58.025	20.800	37.250	58.475	21.225
2014-06-10 14:14	191.59	31.225	52.950	21.725	31.250	53.013	21.763
2014-06-10 14:21	192.93	42.975	64.575	21.600	42.975	64.525	21.550
2014-06-10 14:26	193.48	32.675	53.550	20.875	32.675	54.138	21.463
2014-06-10 14:30	191.71	41.725	55.600	13.875	41.750	63.113	21.363
2014-06-10 15:08	192.69	31.125	51.975	20.850	31.125	51.788	20.663
2014-06-10 15:12	193.59	30.200	51.050	20.850	30.225	51.500	21.275
2014-06-10 15:17	191.93	36.125	57.175	21.050	36.125	51.363	15.238
2014-06-10 15:22	192.68	32.750	53.600	20.850	32.775	54.113	21.338
2014-06-10 15:26	193.55	35.750	57.550	21.800	35.750	56.400	20.650
2014-06-10 15:30	191.74	31.600	32.900	1.300	31.625	52.963	21.338
2014-06-10 15:35	191.31	37.375	57.775	20.400	37.400	58.913	21.513
2014-06-11 00:06	140.00	33.475	54.975	21.500	33.475	55.238	21.763
2014-06-11 00:08	139.17	31.125	52.825	21.700	31.125	52.788	21.663
2014-06-11 00:11	140.15	36.550	58.725	22.175	36.550	58.488	21.938
2014-06-11 00:15	139.90	36.850	59.025	22.175	36.850	58.488	21.638
2014-06-11 00:29	140.10	41.525	61.925	20.400	41.525	63.175	21.650
2014-06-11 00:31	140.12	37.950	58.975	21.025	37.975	59.613	21.638
2014-06-11 00:45	139.95	38.625	59.325	20.700	38.625	60.788	22.163
2014-06-11 00:49	140.07	32.650	54.400	21.750	32.650	54.375	21.725
2014-06-11 00:57	140.11	30.725	124.700	93.975	30.725	52.675	21.950
2014-06-11 01:03	140.04	39.150	61.200	22.050	39.175	60.913	21.738

Appendix H. Radiation pyrometer results

Plant X Unit 2

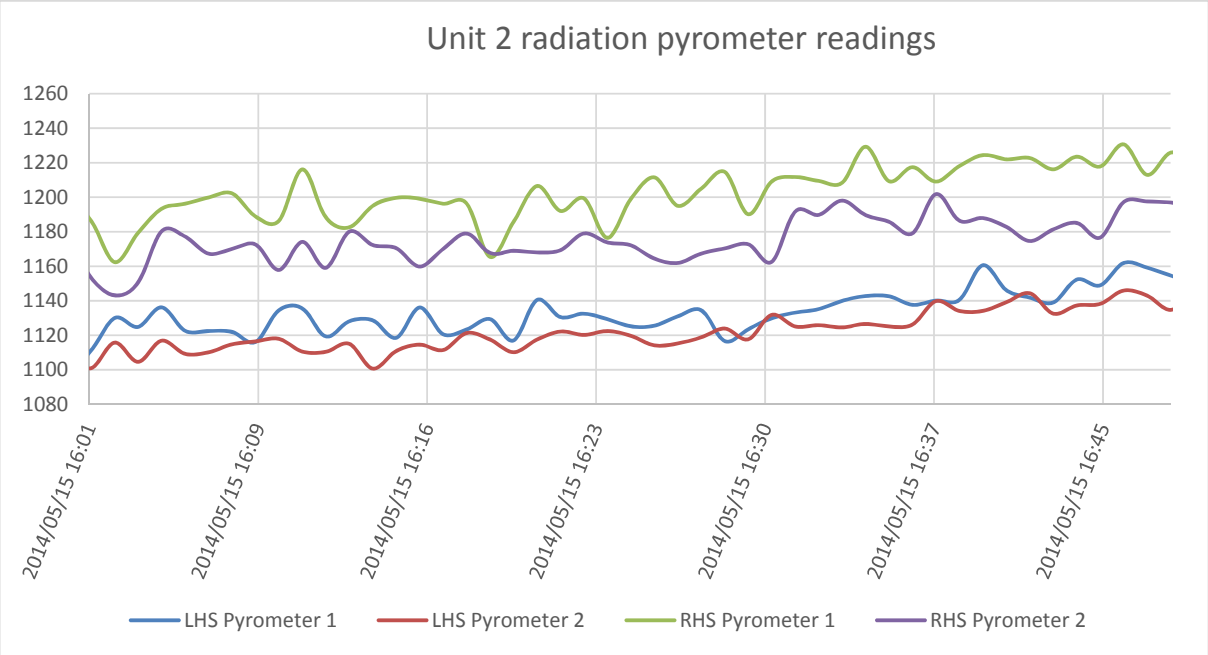

Plant X Unit 6 Full Load

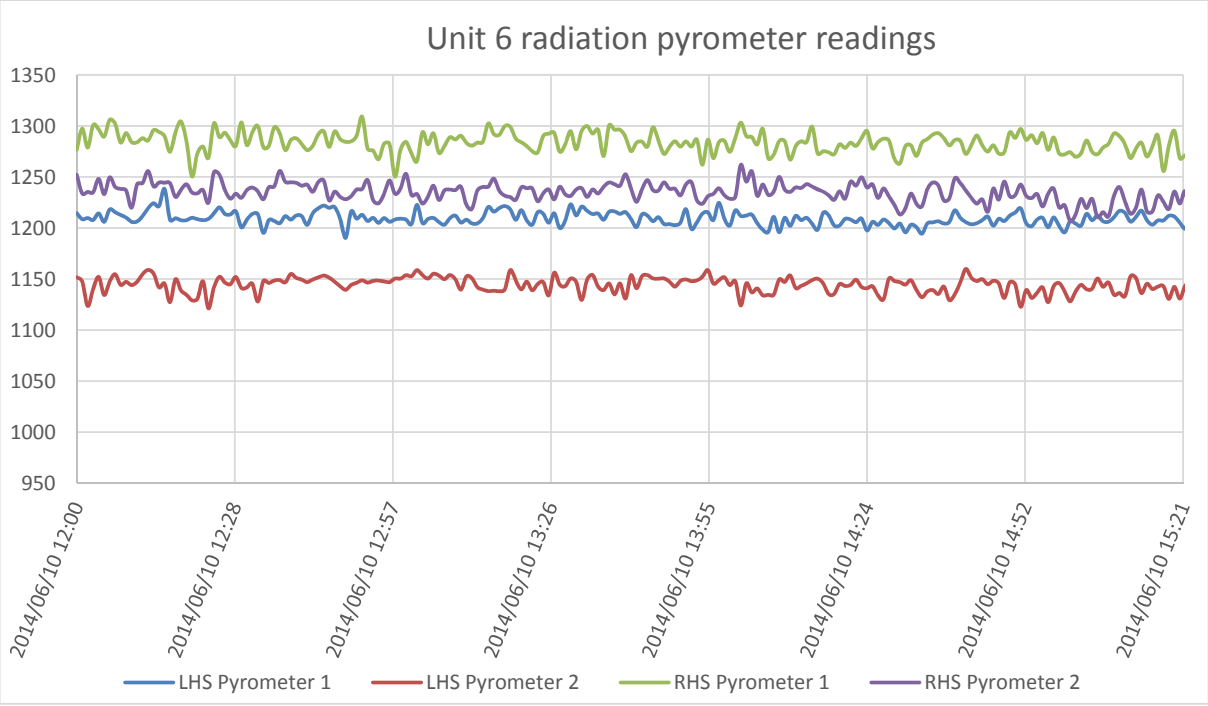

Plant X Unit 6 75% Load

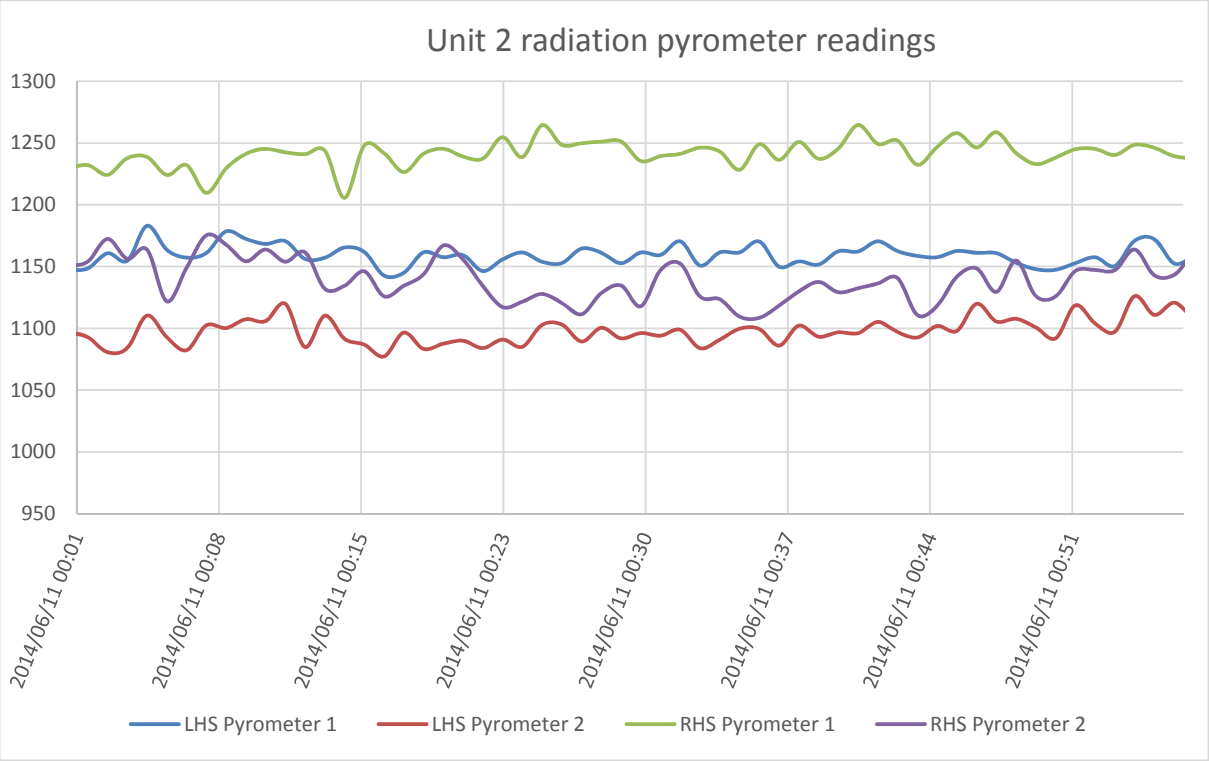

Appendix I. Calculation of flue gas-particle mixture properties

$R_{ideal} := 8.314 \frac{J}{mol \cdot K}$

Inputs

$M_{fg} := 31.15 \frac{gm}{mol}$

$\gamma_{fg} := 1.3$

$mass\%_{ash} := 0.9 \cdot 31.87\%$

$\dot{m}_{fg} := 8.642$

$mass\%_{CO2} := 20.375\%$

$mass\%_{N2} := 70.58\%$

$mass\%_{H2O} := 4.168\%$

$mass\%_{O2} := 4.512\%$

$T_{fg} := 1350\ °C$

$L_{path} := 16.26m$

$TOF := 22.077ms$

Pure gas properties:

$R_{fg} := \frac{R_{ideal}}{M_{fg}} = 266.902 \cdot \frac{J}{kg \cdot K}$

To calculate the C.p and C.v of the flue gas:

$a_{CO2} := 4.21 \cdot 10^{-1}$	$b_{CO2} := 1.89 \cdot 10^{-3}$	$c_{CO2} := -1.85 \cdot 10^{-6}$	$d_{CO2} := 1.02 \cdot 10^{-9}$
$a_{N2} := 1.11$	$b_{N2} := -4.64 \cdot 10^{-4}$	$c_{N2} := 9.53 \cdot 10^{-7}$	$d_{N2} := -4.62 \cdot 10^{-10}$
$a_{H2O} := 1.91$	$b_{H2O} := -7.2 \cdot 10^{-4}$	$c_{H2O} := 2.46 \cdot 10^{-6}$	$d_{H2O} := -1.94 \cdot 10^{-9}$
$a_{O2} := 9.98 \cdot 10^{-1}$	$b_{O2} := -8.89 \cdot 10^{-4}$	$c_{O2} := 2.85 \cdot 10^{-6}$	$d_{O2} := -2.85 \cdot 10^{-9.}$

$$a_{fg} := a_{CO2} \cdot mass\%_{CO2} + a_{N2} \cdot mass\%_{N2} + a_{H2O} \cdot mass\%_{H2O} + a_{O2} \cdot mass\%_{O2} = 0.994$$

$$b_{fg} := b_{CO2} \cdot mass\%_{CO2} + b_{N2} \cdot mass\%_{N2} + b_{H2O} \cdot mass\%_{H2O} + b_{O2} \cdot mass\%_{O2} = -1.252 \times 10^{-5}$$

$$c_{fg} := c_{CO2} \cdot mass\%_{CO2} + c_{N2} \cdot mass\%_{N2} + c_{H2O} \cdot mass\%_{H2O} + c_{O2} \cdot mass\%_{O2} = 5.273 \times 10^{-7}$$

$$d_{fg} := d_{CO2} \cdot mass\%_{CO2} + d_{N2} \cdot mass\%_{N2} + d_{H2O} \cdot mass\%_{H2O} + d_{O2} \cdot mass\%_{O2} = -3.277 \times 10^{-10}$$

$$C_{p.fg} := \left(a_{fg} + b_{fg} \cdot \frac{T_{fg}}{K} + c_{fg} \cdot \frac{T_{fg}^{2}}{K^{2}} + d_{fg} \cdot \frac{T_{fg}^{3}}{K^{3}} \right) \cdot \frac{kJ}{kg \cdot K} = 0.961 \cdot \frac{kJ}{kg \cdot K}$$

$$C_{v.fg} := \frac{C_{p.fg}}{\gamma_{fg}} = 0.739 \cdot \frac{kJ}{kg \cdot K}$$

Particle properties:

$$m_p := \frac{mass\%_{ash}}{\dot{m}_{fg}} = 0.033$$

$$C_{particle} := 1.38 \frac{kJ}{kg \cdot K}$$ (Assumed in MEB as well)

Mixture properties:

$$R' := \frac{R_{fg}}{1 + m_p} = 258.328 \cdot \frac{J}{kg \cdot K}$$

$$\gamma' := \frac{\left(\gamma_{fg} + \frac{C_{particle} \cdot m_p}{C_{v.fg}} \right)}{\left(1 + \frac{C_{particle} \cdot m_p}{C_{v.fg}} \right)} = 1.283$$

Appendix J. EBE Faculty: Assessment of Ethics in Research

EBE Faculty: Assessment of Ethics in Research Projects

Any person planning to undertake research in the Faculty of Engineering and the Built Environment at the University of Cape Town is required to complete this form before collecting or analysing data. When completed it should be submitted to the supervisor (where applicable) and from there to the Head of Department. If any of the questions below have been answered YES, and the applicant is NOT a fourth year student, the Head should forward this form for approval by the Faculty EIR committee: submit to Ms Zulpha Geyer (Zulpha.Geyer@uct.ac.za; Chem Eng Building, Ph 021 650 4791). Students must include a copy of the completed form with the thesis when it is submitted for examination.

Name of Principal Researcher/Student: NAEEM TOOTLA Department: MECHANICAL ENGINEERING

If a Student: Degree: MSc Supervisor: PROF LOUIS JESTIN

If a Research Contract indicate source of funding/sponsorship:

Research Project Title: MEASUREMENT AND MONITORING OF BOILER FLUE GAS TEMPERATUR

Overview of ethics issues in your research project:

Question 1: Is there a possibility that your research could cause harm to a third party (i.e. a person not involved in your project)?	YES	(NO)
Question 2: Is your research making use of human subjects as sources of data? If your answer is YES, please complete Addendum 2.	YES	(NO)
Question 3: Does your research involve the participation of or provision of services to communities? If your answer is YES, please complete Addendum 3.	YES	(NO)
Question 4: If your research is sponsored, is there any potential for conflicts of interest? If your answer is YES, please complete Addendum 4.	YES	(NO)

If you have answered YES to any of the above questions, please append a copy of your research proposal, as well as any interview schedules or questionnaires (Addendum 1) and please complete further addenda as appropriate.

I hereby undertake to carry out my research in such a way that

- there is no apparent legal objection to the nature or the method of research; and
- the research will not compromise staff or students or the other responsibilities of the University;
- the stated objective will be achieved, and the findings will have a high degree of validity;
- limitations and alternative interpretations will be considered;
- the findings could be subject to peer review and publicly available; and
- I will comply with the conventions of copyright and avoid any practice that would constitute plagiarism.

Signed by:

	Full name and signature	Date
Principal Researcher/Student:	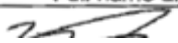	27/01/2015

This application is approved by:

Supervisor (if applicable):		29/01/2015
HOD (or delegated nominee): Final authority for all assessments with NO to all questions and for all undergraduate research.		27/02/2015
Chair : Faculty EIR Committee For applicants other than undergraduate students who have answered YES to any of the above questions.		